



THE UNIVERSITY
of ADELAIDE

Cu-based catalysts for electrochemical CO₂ reduction

Xianlong Zhou

A thesis submitted for the degree of Doctor of Philosophy

School of Chemical Engineering and Advanced Materials

The University of Adelaide

Table of contents

Abstract.....	1
Thesis Declaration.....	4
Acknowledgement.....	5
Chapter 1 Introduction.....	8
1.1 Significance of the Project.....	8
1.2 Research Objectives.....	8
1.3 Thesis Outline.....	9
1.4 References.....	10
Chapter 2 Literature review.....	11
2.1 Introduction of electrochemical CO ₂ reduction on Cu-based catalyst.....	11
2.2 The local environment of Cu-based catalyst.....	12
Chapter 3 Molecular scalpel to chemically cleave metal-organic frameworks for induced phase transition.....	34
3.1 Introduction and Significance.....	34
3.2 Molecular Cleavage of Metal-Organic Frameworks and Application to Energy Storage and Conversion.....	35
3.2 Mechanistic insight into molecular scalpel to chemically cleave metal-organic frameworks for induced phase transition.....	57
Chapter 4 Stabilizing Cu²⁺ ions by solid solutions to promote CO₂ electroreduction to methane.....	91
4.1 Introduction and Significance.....	91
4.2 Mechanistic insight into stabilizing Cu ²⁺ ions by solid solutions to promote CO ₂ electroreduction to methane.....	92
Chapter 5 Tuning molecular electrophilicity of Cu-MOF catalysts to steer CO₂	

electroreduction selectivity.....	124
5.1 Introduction and Significance.....	124
5.2 Mechanistic insight into tuning molecular electrophilicity of Cu-MOF catalysts to steer CO ₂ electroreduction selectivity.....	125
Chapter 6 Regulating interface water structure by solvation effects to promote electrochemical C-C coupling reactions.....	148
6.1 Introduction and Significance.....	148
6.2 Mechanistic insight into solvation effects regulating interface water structure of Cu catalysts to promote electrochemical C-C coupling reactions.....	149
Chapter 7 Conclusions and Perspectives.....	166
7.1 Conclusions.....	166
7.2 Perspectives.....	166
Appendix: Publications during PhD Candidature.....	169

Abstracts

Electrochemical CO₂ reduction (CRR) that converts CO₂ into high-value fuels and chemicals is one of critical approaches to achieving carbon-emissions-neutral processes. The first step in developing this technology is to design and synthesize high-performance CRR electrocatalysts. Because Cu binds to CRR intermediates *CO neither too weakly nor too strongly, it is the only metal catalyst to electrochemically transform CO₂ into various products, hydrocarbons and oxygenates. They are highly sought because of their large market volume and commercial value. However, CRR is a gas/solid/liquid three-phase interface reaction near the electrode in aqueous solution. Therefore, in addition to the composition and structure of various Cu catalysts, their catalytic activity and selectivity depend significantly on the local environment, including catalyst surface structure and electrolyte composition. Understanding the structure-activity relationship between catalyst composition and local environment with CRR activity and selectivity is crucial, which inspires researchers to synthesize the desired CRR catalysts. This thesis aims to solve this key scientific question from catalyst design and tuning electrolyte composition to steer CRR activity and selectivity of Cu-based catalysts.

First, we proposed a new method, molecular cleavage, to synthesize Cu-based MOFs. This strategy can precisely regulate the local coordination environment of a metal-organic framework (MOF) together with the derivation of a new topological structure. Importantly, this method is designed to circumvent limitations in hard and soft acids and bases (HSAB) theory to fabricate a new ordered Cu₂BDC (BDC = 1,4-benzenedicarboxylate) MOF composed of a soft acid metal and a hard base ligand. Starting from a reported CuBDC MOF, we demonstrated L-ascorbic Acid (LA) acting as a molecular scalpel to finely regulate the chemical state and coordination number of

Cu metal centres to cleave BDC linkers. A controlled phase transition from CuBDC to Cu₂BDC with resulting different chemical composition and topological structure was achieved. In comparison to the pristine CuBDC, the Cu₂BDC-derived sample can display a higher Faradaic efficiency (FE) for C₂ products (ethylene and ethanol). This improvement results from the formation of Cu₂O (111) and Cu (111) mixed phases, which can promote CRR activity and C₂ product selectivity in a synergistic way.

Second, a method was proposed to stabilize Cu²⁺ during catalytic operation through fabrication of a Cu-Ce-O_x solid solution, in which Cu ions are incorporated into CeO₂ matrix. In situ formed Ce³⁺ in solid solutions from electrochemical reduction can provide the rapid electron transport channel to suppress the accumulation of electrons around Cu²⁺ sites and protect them from reduction to Cu⁰. We also employed in situ attenuated total reflectance infrared spectroscopy (ATR-IR) to observe that the stable Cu²⁺ sites can significantly improve the initial *CO adsorption and facilitate the *CO hydrogenation to produce *OCH₃, which is a crucial intermediate of CH₄ generation. As a result, Cu-Ce-O_x delivered a high FE of CH₄ with significant suppression of the competing C₂ products (i.e., C₂H₄).

Third, a class of bipyridyl molecules work as linkers with tunable electrophilicity to steer CRR selectivity of Cu-MOFs. Theory calculations and in situ experiments confirm that the electrophilicity of the linker can tune the catalyst's proton availability, which can promote or inhibit the critical proton-coupled electron transfer (PCET) process in CRR. Catalyst with a low-electrophilicity linker exhibits fast proton transfer to *CO, accelerating its protonation to achieve a high FE of 58.2% for CH₄. By contrast, a high-electrophilicity linker can stabilize *CO and favor its C-C coupling step, resulting in a high FE of 65.9% for C₂H₄.

In the end, we engineered the solvated structure of metal cations to tune interfacial

water structure, which can fast PCET process of CO₂ activation and increase the absorption ability for *CO intermediate on Cu₂O during CRR operation, thereby promoting C-C coupling reaction during CRR. Dimethyl sulfoxide (DMSO) was employed as an electrolyte additive to tune the solvated structure of K ions because it can preferentially solvate with K ions over water. In situ spectroscopic characterizations revealed that the introduction of DMSO can form a higher percentage of 4-coordinated hydrogen-bonded water on the surface of Cu₂O catalyst, consequently building stronger hydrogen bonds to stabilize *CO and fast its dimerization.

Thesis Declaration

I certify that this thesis does not contain any material that has been accepted by any university or other institution of higher education to confer any other degree or diploma in my name and that, to the best of my knowledge and belief, this thesis does not contain any previously published or written material by another person, unless appropriately mentioned in the thesis. In addition, I warrant that, without the prior approval and application of the University of Adelaide, I will henceforth submit any other degree or diploma in my name at any university or other higher education institution to any institution responsible for the joint grant of that degree.

The author acknowledges that the copyright to the published works contained in this thesis belongs to the copyright holders of those works.

I acknowledge the support I have received for my research through the provision of an Australian Government Research Training Program Scholarship.

I allow digital versions of my thesis to be made available on the web through the University's Digital Research Repository, Library Search, and Web Search Engines, unless the University has allowed limited access for a period of time.

Xianlong Zhou

Signature:

Date: 10/11/2022

Acknowledgements

This thesis could not be completed without the careful guidance and great devotion from my principal supervisor Assoc. Prof. Yao Zheng and co-supervisor Prof. Shi-Zhang Qiao. During my candidature, they devoted much of time and effort to my selection of research topic, design and optimization experiment methodology, summary of the results, writing and polishing manuscripts. They also give me inspiring guidance, supportive encouragement and constructive opinions. I know that I could not complete any achievements without their guidance and support in my PhD study. Assoc. Prof. Yao Zheng teaches me how to think about scientific problems professionally. He always encourages me to address my shortcoming and become a great training researcher. I would like to thank Prof. Shi-Zhang Qiao. During my first program, I encountered great difficulties and did not know how to continue my research. He gives me great consolation and enlightens me not to give up. With their helps, I continue to my research and finish my thesis. Due to COVID-19, I can not go back to Australia, my supervisors give me strong supports so that I can conduct my research. I will benefit from their training as a researcher in my future career.

I am also grateful to all the members in Qiao's group who give me many supports and suggestions during my PhD study. Many thanks go to Assoc. Prof. Yan Jiao, Mr. Lin Chen, and Dr. Huan Li, Mr. Yilong Zhu for their great help in theoretical computations. Thanks to Dr. Anthony Vasileff and Dr. Chaochen Xu for their experimental help; many thanks to Dr. Jieqiong Shan and Miss. Min Zheng for in situ characterizations; many thanks to Dr. Huanyu Jin for his discussion, help and experiences on electrocatalysts. Also, I would liker to thanks all the group members from Qiao's group that share their research experiences and inspiration to me. For example, Prof. Dongliang Chao, Dr. Chao Ye, Dr. Fangxi Xie, Dr. Cheng Tang, Dr.

Jingrun Ran, Dr. Pengtang Wang, Dr. Junnan Hao, Dr. Laiquan Li, Dr. Bingquan Xia, Dr. Xin Liu, Dr., Xing Zhi, Dr. Biao Chen, Dr. Xuesi Wang, Dr. Yongqiang Zhao, Dr. Dongdong Zhu, Mr. Daozhi Yao, Mrs., Xin Xu, Mr. Ying Shi, Mr. Yanzhao Zhang, Mr. Hao Liu, Mr. Shaojian Zhang, Mr. Haifeng Shen, Mr. Junyu Zhang, Mr. Yiran Jiao, Miss. Jun Xu, Dr. Haobo Li and Dr. Xiaowan Bai. I also thanks to Dr. Qihong Hu for her strong experimental technical support, Dr. Xiaoguang Duan for his help and Dr. Kenneth Davey for his revisions my manuscripts.

I appreciate Prof. Bao Yu Xia from Huazhong University of Science and Technology for providing experimental conditions for me during the last two years of my PhD. Thanks to Prof. Xia for his support, trust, and guidance so that I can complete my thesis. My thanks to Assoc. Prof. Wei Guo, Dr. Fumin Li, Dr. Zhitong Wang, Dr. Lei Huang, Mr. Wensheng Fang, Mr. Chenfeng Xia, Mr. Song Yan, Miss. Huichao He, Miss. Huiting Niu, Mr. Deyu Zhu, and other members. Many thanks to Dr. Dafeng Yan and Dr. Shenghua Chen for their discussions. I also thank Prof. Bo You from Huazhong University of Science and Technology for his help, companionship and discussion. Many thanks to Mr. Zhiwei Zhu and Mr. Wenjie Xue for their experimental help. I also thank Prof. Xuan Yang from Huazhong University of Science and Technology and his student, Miss. Xiaoju Yang, for their help.

I appreciate my collaborators for their hard work. For example, Prof. Jingjing Duan and Mr. Kang Yang from Nanjing University of Science and Technology, Prof. Tao Lin and Miss. Jiaxing Guo from Tianjin University, Dr. Juncai Dong from Institute of High Energy Physics, Chinese Academy of Sciences, Prof. Yihan Zhu from Zhejiang University of Technology, Prof. Yu Han and Dr. Lingmei Liu from Abdullah University of Science and Technology, Prof. Qiang Xu from National Institute of Advanced Industrial Science and Technology, and Prof. Kostya (Ken) Ostrikov from Queensland

University of Technology.

I also thanks to my friends for their encouragements. For example, Prof. Tengfei Zhou, Prof. Yang Zheng, Dr. Renjie Wei, Dr. Keshuai Liu., Dr. Yiren Zhong, Dr. Mei Yang, and Mrs. Yuexian Chen. Thanks to their help and encourage during my PhD.

In addition, I acknowledge the Australian Government, The University of Adelaide, and Australia Research Council for their financial support.

Last but not the least, I would like to thank to my wife, Mrs. Jing Wu. Our baby, Mr. Yiming Zhou, was born during my PhD study. He brings us a lot of happiness in our daily life and also a great challenge to our life. Due to completion of my research, most of daily things are completed by Jing. Thanks for her selfless dedication and consideration. I also thanks to my parents, parents-in-law, brother, and brother-in-law for your support and encourage during my PhD study.

Chapter 1 introduction

1.1 Background

The development of viable technologies to convert CO₂ effectively into chemicals or fuels is rapidly gaining momentum. Indeed, these technologies not only reduce the overall CO₂ emissions by recycling the already burnt fossil fuels but also incentivize the exploration of new methods for CO₂ capture.¹ CRR is one of the particularly promising pathways for CO₂ conversion since it can store renewable electricity obtained from intermittent solar or wind energy.² However, at room temperature and atmospheric pressure, CRR requires large overpotentials to drive CO₂ hydrogenation for producing C₁ and even multi-carbon products. It is well known that the catalyst's activity depends mainly on its structure and the prevailing reaction conditions.³ In a typical solid-gas thermal catalytic reaction, the catalytic effects are limited by physicochemical properties and the electronic structure of the solid catalyst.⁴ Consequently, researchers focus on the development of various catalysts with high activity. In addition, CRR occurs on a gas/solid/liquid three-phase interface, and its reactivity is also sensitive to the local reaction environment of the catalysts, such as the specific electrolyte, pH, presence of metal cations, surface structure and composition of the catalyst, and some other factors.⁵

1.2 Aim and Objectives

The primary goal of this thesis is to discover the reaction mechanism of CRR on nanostructured catalysts and to find the activity origin on highly active catalysts. The objectives of this thesis are as follows:

- To discover the Cu(I)-MOFs resulted from cleavage of synthesized Cu(II)-MOFs that can build Cu-based catalyst with the mixed-phase interface, thereby promoting the efficacy of C-C coupling in CRR.

- To identify the mechanism of stabilizing Cu^{2+} through the formation of a solid solution and build electronic transfer network to build a platform to investigate the Cu^{2+} behaviors during CRR operation
- To break the conventional electronic structure engineering that tunes CRR activity and selectivity and propose a method to regulate the PCET process in CRR for tuning its selectivity.
- To rebuild the interfacial water structure for the formation of stronger hydrogen bonds to stabilize intermediates and improve CRR selectivity.

1.3 Thesis Layout

This thesis is partial outcomes of my PhD research presented in the form of journal publications. The chapters in this thesis are shown in the following sequence:

- **Chapter 1** introduces the general background and the significance of the project. Then, an outline and the research purpose of this thesis are provided.
- **Chapter 2** reviews the current development, reaction roadmap understanding and the designing and local environment regulation strategies of the Cu-based electrocatalysts for CRR.
- **Chapter 3** proposes a new method, molecular cleavage, to synthesize Cu-based MOFs, which can improve FE for ethylene and ethanol due to the formation of Cu_2O (111) and Cu (111) mixed phases.
- **Chapter 4** stabilizes Cu^{2+} during CRR operation by fabrication of a solid solution, building a platform for CRR to study Cu^{2+} behavior.
- **Chapter 5** tunes the molecular electrophilicity of Cu-MOFs to alter the PCET process in CRR, thereby regulating its selectivity towards CH_4 or C_2H_4 .
- **Chapter 6** engineers solvated structure of metal cations to tune interfacial water structure on catalyst surface to promote C-C coupling reaction during CRR.

- **Chapter 7** summarizes the key achievement of this thesis and provides perspectives for future work.

1.4 References

- (1) Wang, G.; Chen, J.; Ding, Y.; Cai, P.; Yi, L.; Li, Y.; Tu, C.; Hou, Y.; Wen, Z.; Dai, L., Electrocatalysis for CO₂ conversion: from fundamentals to value-added products. *Chem. Soc. Rev.* **2021**, *50* (8), 4993-5061.
- (2) Bushuyev, O. S.; De Luna, P.; Dinh, C. T.; Tao, L.; Saur, G.; van de Lagemaat, J.; Kelley, S. O.; Sargent, E. H., What Should We Make with CO₂ and How Can We Make It? *Joule* **2018**, *2* (5), 825-832.
- (3) Zheng, Y.; Jiao, Y.; Jaroniec, M.; Qiao, S. Z., Advancing the electrochemistry of the hydrogen-evolution reaction through combining experiment and theory. *Angew. Chem. Int. Ed.* **2015**, *54* (1), 52-65.
- (4) Zhou, X.; Liu, H.; Xia, B. Y.; Ostrikov, K.; Zheng, Y.; Qiao, S. Z., Customizing the microenvironment of CO₂ electrocatalysis via three-phase interface engineering. *SmartMat* **2022**, *3* (1), 111-129.
- (5) Wagner, A.; Sahm, C. D.; Reisner, E., Towards molecular understanding of local chemical environment effects in electro- and photocatalytic CO₂ reduction. *Nat. Catal.* **2020**, *3* (10), 775-786.

Chapter 2 Literature Review

2.1 Introduction

Electrochemical CO₂ reduction powered by reversible electricity provides an attractive technique for achieving carbon-emissions-neutral processes. It can transform CO₂ into various value-added chemicals or fuels, including carbon monoxide (CO), formic acid (HCOOH), methane (CH₄), methanol (CH₃OH), ethene (C₂H₄), or ethanol (C₂H₅OH). Cu is the only metal element to electrochemically catalyze CO₂ into hydrocarbons and oxygenates due to its binding to CRR intermediate *CO neither too weakly nor too strongly. Unfortunately, this unique physicochemical property of Cu also results in poor selectivity, heavily impeding their practical applications for CRR. Currently, tuning the electronic structure of Cu can significantly improve its adsorption ability of intermediates and then promote electrosynthesis of the desired reduction products. Furthermore, since CRR occurs on a gas/solid/liquid three-phase interface, in addition to the design of electrocatalysts, its reactivity is also sensitive to the local reaction environment of catalysts, such as electrolyte, pH, metal cation, catalyst's surface composition.

In this review we summarize various methods of tuning catalysts' surface/interface to optimize the microenvironment for CRR. We present different modification strategies on gas transport, electrolyte composition, controlling intermediate states, and catalyst structural engineering. Importantly, we focus on various chemical and engineering methods to increase local CO₂ concentration, lower the energetic barriers for CO₂ activation, decrease H₂O coverage, and stabilize intermediates to modulate the catalytic activity and selectivity delicately. In the end, we also provide some perspectives on the challenges and outlook for CRR through the three-phase interface engineering.

2.2 Customizing the microenvironment of CO₂ electrocatalysis via three-phase interface engineering

This chapter is included as a journal paper by Xianlong Zhou, Hao Liu, Bao Yu Xia, Kostya (Ken) Ostrikov, Yao Zheng, Shi-Zhang Qiao, Customizing the microenvironment of CO₂ electrocatalysis via three-phase interface engineering, SmartMat. 2022, 3, 111-129.

Statement of Authorship

Title of Paper	Customizing the microenvironment of CO ₂ electrocatalysis via three-phase interface engineering
Publication Status	<input checked="" type="checkbox"/> Published <input type="checkbox"/> Accepted for Publication <input type="checkbox"/> Submitted for Publication <input type="checkbox"/> Unpublished and Unsubmitted work written in manuscript style
Publication Details	Xianlong Zhou, Hao Liu, Bao Yu Xia, Kostya (Ken) Ostr kov, Yao Zheng,* and Shi-Zhang Qiao. SmartMat. 2022, 3, 111–129.

Principal Author

Name of Principal Author (Candidate)	Xianlong Zhou		
Contribution to the Paper	Proposed the review topic, reviewed and organised the literatures, and wrote the manuscript.		
Overall percentage (%)	80		
Certification:	This paper reports on original research I conducted during the period of my Higher Degree by Research candidature and is not subject to any obligations or contractual agreements with a third party that would constrain its inclusion in this thesis. I am the primary author of this paper.		
Signature		Date	09/09/2022

Co-Author Contributions

By signing the Statement of Authorship, each author certifies that:

- i. the candidate's stated contribution to the publication is accurate (as detailed above);
- ii. permission is granted for the candidate to include the publication in the thesis; and
- iii. the sum of all co-author contributions is equal to 100% less the candidate's stated contribution.

Name of Co-Author	Hao Liu		
Contribution to the Paper	Wrote part of manuscript		
Signature		Date	09/09/2022

Name of Co-Author	Bao Yu Xia		
Contribution to the Paper	Revised the manuscript		
Signature		Date	09/09/2022

Name of Co-Author	Kostya (Ken) Ostrikov		
Contribution to the Paper	Helped to edit the manuscript		
Signature		Date	09/09/2022




Name of Co-Author	Yao Zheng		
Contribution to the Paper	Supervised development of work, helped in manuscript evaluation and acted as corresponding author		
Signature		Date	09/09/2022

Name of Co-Author	Shi-Zhang Qiao		
Contribution to the Paper	Helped to revise the manuscript and organise the figures		
Signature		Date	09/09/2022

Please cut and paste additional co-author panels here as required.

REVIEW

Customizing the microenvironment of CO₂ electrocatalysis via three-phase interface engineering

Xianlong Zhou¹ | Hao Liu¹ | Bao Yu Xia^{2,3}  | Kostya (Ken) Ostrikov⁴ | Yao Zheng¹  | Shi-Zhang Qiao¹ 

¹School of Chemical Engineering and Advanced Materials, The University of Adelaide, Adelaide, South Australia, Australia

²Key Laboratory of Material Chemistry for Energy Conversion and Storage (Ministry of Education), Hubei Key Laboratory of Material Chemistry and Service Failure, Wuhan, China

³National Laboratory for Optoelectronics, School of Chemistry and Chemical Engineering, Huazhong University of Science and Technology (HUST), China

⁴School of Chemistry and Physics and Centre for Materials Science, Queensland University of Technology (QUT), Brisbane, Australia

Correspondence

Yao Zheng, School of Chemical Engineering and Advanced Materials, The University of Adelaide, Adelaide, SA 5005, Australia.
Email: yao.zheng01@adelaide.edu.au

Funding information

Australian Research Council, Grant/Award Numbers: FL170100154, FT200100062, DP220102596, DP210100472, DP190103472

Abstract

Converting CO₂ into high-value fuels and chemicals by renewable-electricity-powered electrochemical CO₂ reduction reaction (CRR) is a viable approach toward carbon-emissions-neutral processes. Unlike the thermocatalytic hydrogenation of CO₂ at the solid-gas interface, the CRR takes place at the three-phase gas/solid/liquid interface near the electrode surface in aqueous solution, which leads to major challenges including the limited mass diffusion of CO₂ reactant, competitive hydrogen evolution reaction, and poor product selectivity. Here we critically examine the various methods of surface and interface engineering of the electrocatalysts to optimize the microenvironment for CRR, which can address the above issues. The effective modification strategies for the gas transport, electrolyte composition, controlling intermediate states, and catalyst engineering are discussed. The key emphasis is made on the diverse atomic-precision modifications to increase the local CO₂ concentration, lower the energy barriers for CO₂ activation, decrease the H₂O coverage, and stabilize intermediates to effectively control the catalytic activity and selectivity. The perspectives on the challenges and outlook for the future applications of three-phase interface engineering for CRR and other gas-involving electrocatalytic reactions conclude the article.

KEYWORDS

catalytic selectivity, electrochemical CO₂ reduction, intermediates, microenvironment, three phase interface

This is an open access article under the terms of the Creative Commons Attribution License, which permits use, distribution and reproduction in any medium, provided the original work is properly cited.

© 2022 The Authors. *SmartMat* published by Tianjin University and John Wiley & Sons Australia, Ltd.

1 | INTRODUCTION

The development of viable technologies to effectively convert CO_2 into chemicals or fuels is rapidly gaining momentum. Indeed, these technologies not only reduce the overall CO_2 emissions by recycling the already burnt fossil fuels but also incentivize the exploration of new methods for CO_2 capture.^{1,2} Electrocatalytic CO_2 reduction reaction (CRR) is one of particularly promising pathways for CO_2 conversion since it can store renewable electricity obtained from intermittent solar or wind energy.^{3,4} However, CO_2 is a stable linear molecule, which is difficult to break due to the strong C–O bonds with the large energy barrier (Figure 1A).⁵ Thus, in a typical thermal catalysis process, external heat and pressure ($>180^\circ\text{C}$, 15 Pa) are supplied to activate molecular H_2 so that it can reduce CO_2 to generate C_1 products, such as methane (CH_4), carbon monoxide (CO), or methanol (CH_3OH).⁶ On the other hand, at room temperature and atmospheric pressure, CRR requires large overpotentials to drive CO_2 hydrogenation for producing C_1 and even multicarbon products.^{7,8} It is well known that the catalyst's activity depends mainly on its structure and the prevailing reaction conditions. In a typical solid–gas thermal catalytic reaction (Figure 1B), the catalytic effects are limited by physicochemical properties and the electronic structure of the solid

catalyst. Consequently, researchers focus on the development of various catalysts with high activity.^{9–11} Similarly, substantial efforts have been invested in the fabrication of different CRR catalysts, including single-atom,¹² alloy,^{13,14} surface oxidation state,^{15–17} grain boundaries,¹⁸ solid solutions,¹⁹ morphologies,^{20,21} chemical composition,²² and crystal facet engineering.²³ Nevertheless, differently to thermal catalysis, since CRR occurs on a gas/solid/liquid three-phase interface (Figure 1C),²⁴ its reactivity is also sensitive to the local reaction environment of the catalysts, such as the specific electrolyte,²⁵ pH,²⁶ presence of metal cations,²⁷ surface structure and composition of the catalyst,²⁸ and some other factors.

These differences bring some extra challenges for CRR. First, the low solubility (33 mmol/L) and diffusivity of CO_2 in water make CRR a diffusion-limited process (Figure 1D).²⁹ Specifically, the thickness of the mass-transfer boundary layers near the cathode in the H-type cell, for example, 60–160 μm , limits the current density on the order of 10 mA/cm^2 based on the geometrical area of the cathode, resulting in a low CRR activity.³⁰ Second, because of the typically large amount of water on the catalyst's surface, the competing hydrogen evolution reaction (HER) can significantly decrease the selectivity toward the CRR products (Figure 1E). Third, the CRR in an aqueous electrolyte involves multielectron/proton

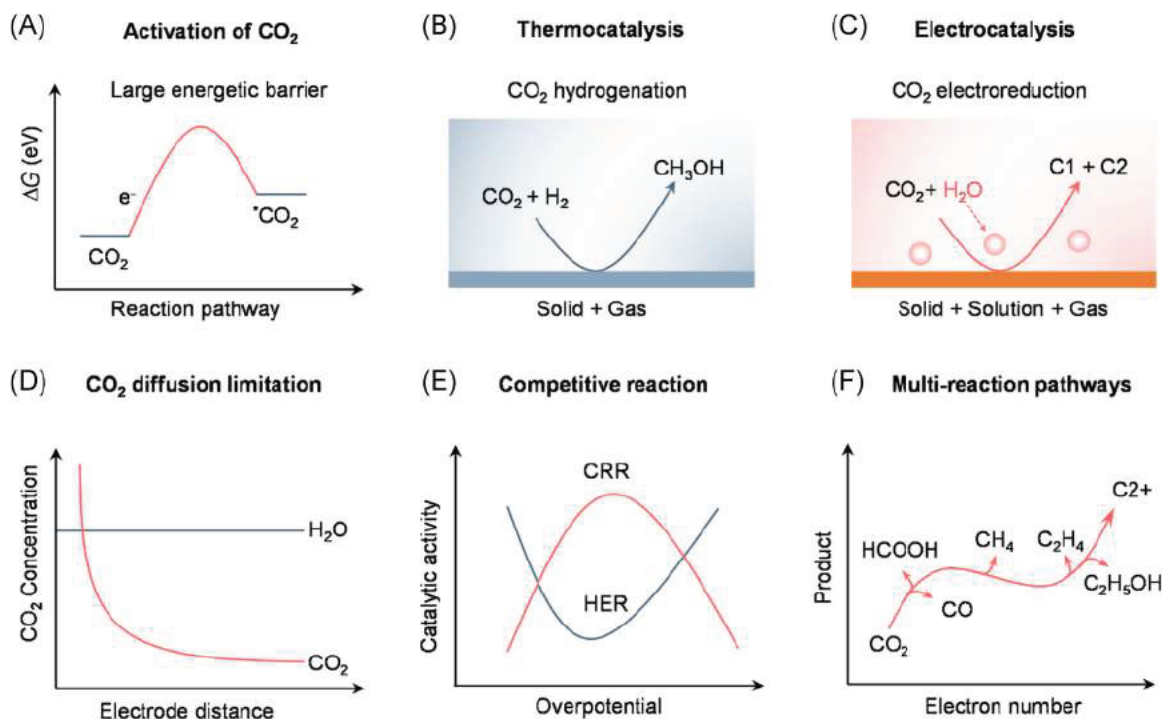


FIGURE 1 Schematics of (A) free energy diagrams for CO_2 activation; (B) thermochemical CO_2 hydrogenation; (C) CO_2 electrochemical reduction; (D) the CO_2 concentration near the electrode surface; (E) the catalytic activity relationship between CRR and HER; (F) pathways for CRR products. CRR, CO_2 reduction reaction; HER, hydrogen evolution reaction

transfer processes along with several distinct possible reaction intermediates (Figure 1F),³¹ in which various hydrocarbons and oxygenates, including CO, CH₄, formate (HCOOH), ethylene (C₂H₄), and ethanol (C₂H₅OH), can be produced.³² The multireaction pathways of CRR make it quite difficult to improve the selectivity of target products.

Through theoretical and experimental investigations, one can unveil the scaling relations for the binding energies of various intermediates on different catalytic active sites.^{33,34} These insights guide the development of a huge number of heterogeneous electrocatalysts with high CRR activity. Nevertheless, it is challenging to break the scaling relations and tune the catalytic selectivity by nanostructure engineering because it is difficult to optimize the binding of a specific intermediate without affecting another. On the other hand, the microenvironment of catalysts, including the electrode-electrolyte interface, the electrolyte composition, and the associated hydrodynamic boundary layers near the catalyst, has played a crucial role in determining the activity and selectivity of CRR.^{35,36} Since CRR is a typical three-phase (gas [CO₂]-solid [catalyst]-liquid [electrolyte]) reaction, customizing the microenvironment provides numerous opportunities to address the above issues without specific catalyst engineering.³⁵ For example, electrolyte cations affect the double electrical layer, thus enabling the possibility to regulate the reaction rates and selectivity of the CRR.³⁷ To date, excellent reviews on the design of electrocatalysts and reaction cells for CRR have

been published³⁸⁻⁴³; a comprehensive review focusing on tuning the catalyst microenvironment to promote the CRR is therefore timely.

In this review, we for the first time critically assess the various strategies for modulating the local reaction environment of catalysts to boost the activity and selectivity in the CRR. To highlight the recent advances in this rapidly developing field, we present them from the perspective of three-phase interface engineering (Figure 2A). First, we discuss in detail the methods to control gas transport (Figure 2B) and the thickness of diffusion layer near the catalyst surface (Figure 2C),⁴⁴ which can increase the CO₂ concentration while decreasing the HER reactivity, thereby accelerating the CO₂ reduction reaction. Second, the refined strategies to regulate the interfacial electric field by adjusting the electrolyte composition are discussed (Figure 2D). They allow to significantly stabilize the critical CRR intermediates to boost the activity and selectivity of the CRR. Third, we discuss the recent advances to functionalize the surface of the catalysts by coating organic molecules and polymers for effectively stabilizing or regulating the intermediate states (Figure 2E). Fourth, we assess different engineering examples of modulating the catalyst surface structure and composition (Figure 2F), which can also affect the local reaction environment of the catalysts. Finally, the challenges and perspectives for optimizing the microenvironment for CRR are presented. We envision that this review, based on the three-phase interface modulation engineering, can provide further

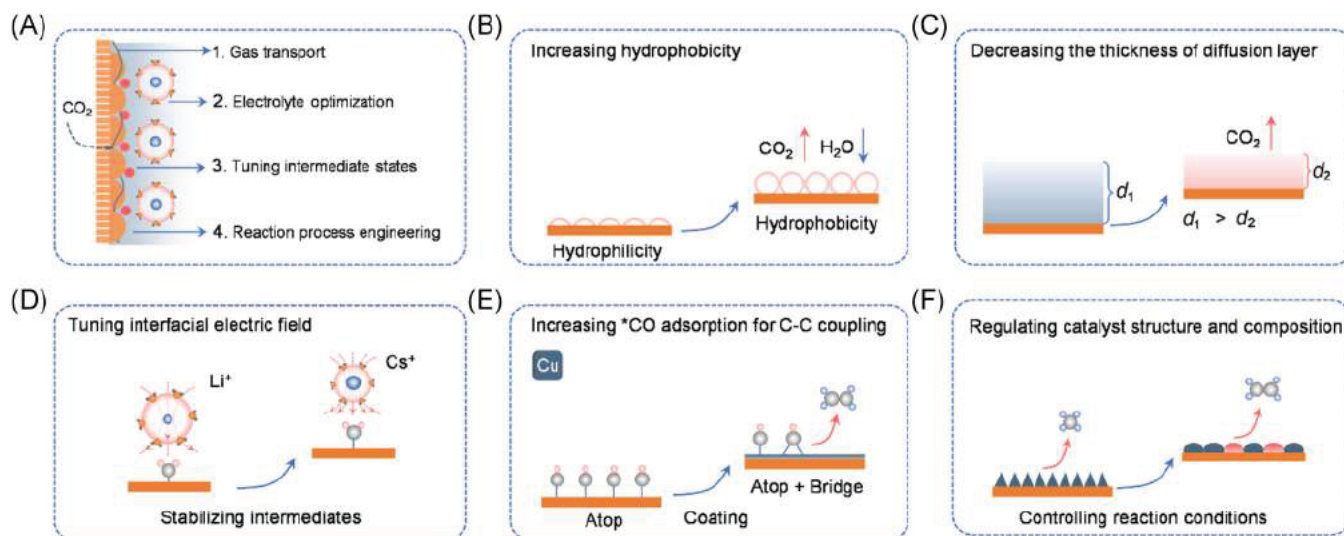


FIGURE 2 Schematics of (A) three phase interface and corresponding strategies to tune CRR activity and selectivity; (B) adjust the hydrophilicity of the catalyst surface to hydrophobicity to increase local CO₂ concentration and lower H₂O coverage; (C) decreasing the thickness of diffusion layer to improve CO₂ mass transport; (D) tuning interfacial electric field to stabilize CRR intermediates; (E) increasing *CO adsorption for C-C coupling to promote the formation of C₂₊ products; (F) controlling reaction conditions to modify the catalyst structure and composition. CRR, CO₂ reduction reaction

fundamental insights for a broad range of electrocatalytic processes challenged by the low gas solubility issues.

2 | GAS TRANSPORT AND UTILIZATION

To improve the gas transport efficiency, physical and chemical methods have been widely used, including tuning the catalyst surface from hydrophilic to hydrophobic for increasing CO_2 concentration, decreasing the thickness of diffusion layer to fast CO_2 mass transport, and lowering the CO_2 activation energy barrier, to accelerate the reaction rate of CRR.

2.1 | Hydrophobicity of catalyst

Wakerley et al.⁴⁵ developed a bioinspired method that involves constructing the hydrophobic surface of catalysts to improve local CO_2 concentration by providing more space to accommodate CO_2 (Figure 3A). After coating with

1-octadecanethiol, the normally wettable surface of Cu dendrites turns hydrophobic. The electrochemical results show that the H_2 evolution reaction is significantly suppressed, thereby boosting CRR selectivity. When the flow direction of CO_2 is turned from outside to inside, the hydrophobic surface can capture CO_2 more quickly. Consequently, the total Faradaic efficiency (FE) for C_2 products can drastically increase from 13% to 73%. In addition, Buckley et al.⁴⁷ found that the distribution of the products on Cu, for example, HCOOH and CO , depends on its hydrophobicity and hydrophilicity (Figure 3B), which is due to the different reaction mechanisms. For HCOOH formation, CO_2 firstly reacts with a surface Cu-H to form H bonded CO_2 . Then, HCOOH is generated after extraction of H from a H_2O , while CO is yielded after the twice hydrogenation by reacting with water. Thus, the hydrophilic species can facilitate the formation of HCOOH , while the hydrophobic species benefit CO generation. However, on Ag surface, the hydrophilicity for Ag is not the dominant factor determining the selectivity of CO .⁴⁸ The reason is when these modifiers have a similar hydrophobicity, the CO selectivity mainly depends on the ordering of the quaternary

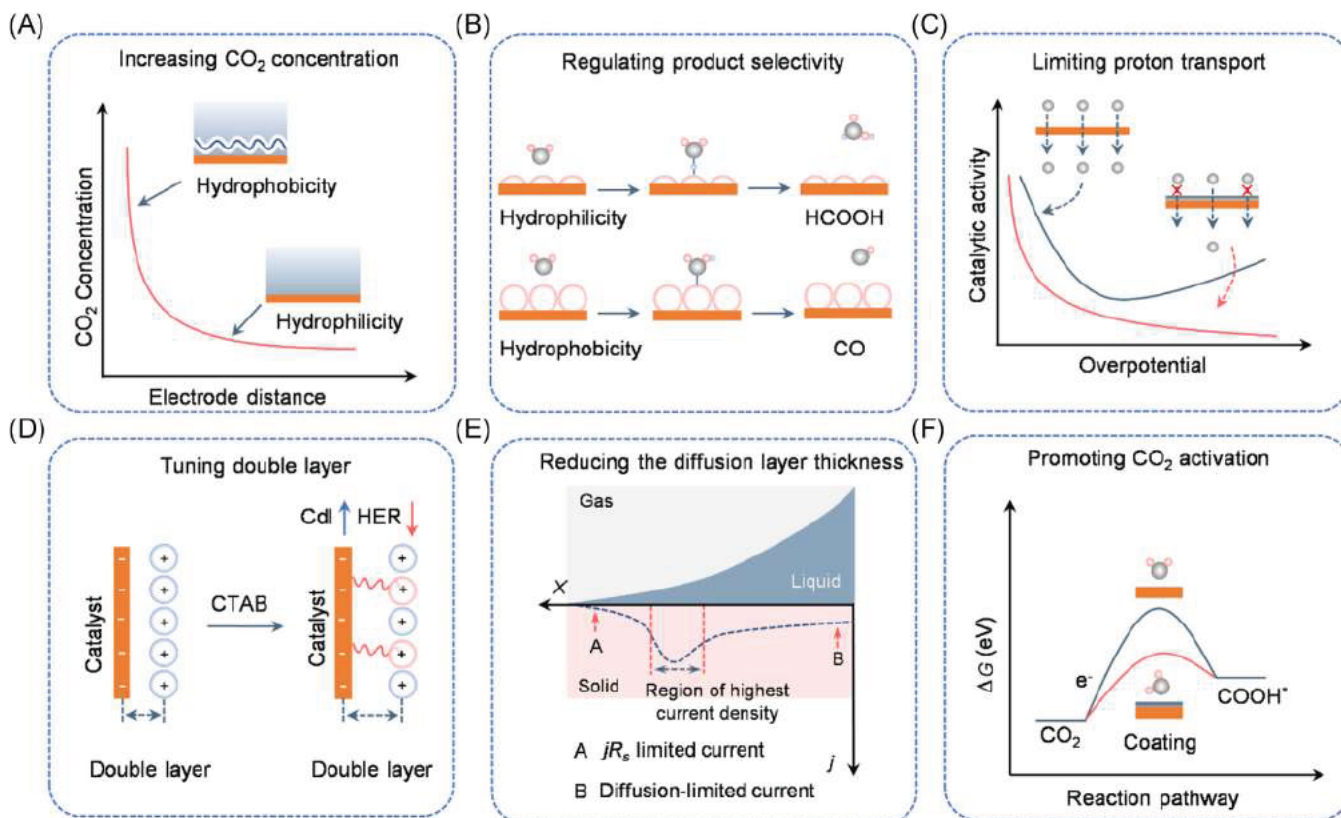


FIGURE 3 Schematics of (A) the relationship between the hydrophilicity/hydrophobicity of the catalyst surface and the local CO_2 concentration; (B) using the hydrophilicity/hydrophobicity of catalyst to tune CRR selectivity; (C) limiting proton transport to suppress HER; (D) tuning the EDL structure of catalysts by using CTAB to inhibit HER; (E) profile of the CRR current density near a three phase interface. Reproduced with permission: Copyright 2021, American Chemical Society.⁴⁶ (F) Coating molecules to lower the energetic barrier for CO_2 activation. CRR, CO_2 reduction reaction; EDL, electric double layer; HER, hydrogen evolution reaction

ammonium modifiers. The expanded structure can thus accommodate more CO₂ molecules at the electrode surface. After coating the quaternary ammonium surface additive, the current density for CO generation for Ag can significantly increase from 0.14 to 1.21 mA/cm². By contrast, the current density for H₂ generation reduces from 0.44 to 0.001 mA/cm².

In addition to enhancing the local CO₂ concentration, the surface hydrophilicity of the catalyst can also limit the proton and water transport. Liang et al.⁴⁹ used poly(vinylidene fluoride) (PVDF) to build the hydrophobic layer to restrict the water diffusion, thus creating a higher local pH near the Cu electrode surface. As a result, the hydrophobic polymers can significantly enhance the activity and selectivity for C₂H₄ on the CuO-derived sample. Organic film and carbon coating can also work as the hydrophobic layer to limit the water-related effects on the surface of CRR catalysts. However, they present different mechanisms to inhibit HER during CRR operation. Pyridinium-based organic film can limit proton but not CO₂ mass transport (Figure 3C).⁵⁰ It was found that the limiting effects depends on the applied potentials: when the potentials locate between -1.0 and -1.2 V, the hydrophobic layer on the Ag electrode surface can selectively limit proton transport but not CO₂. Zhang et al.⁵¹ fabricated a core-shell carbon layer as the hydrophobic interface to alter Cu CRR selectivity. Density functional theory (DFT) and experiments proved that the carbon layer can lower the H₂O coverage, thereby promoting the *CO hydrogenation to produce CH₄ instead of CO. In addition, cetyltrimethylammonium bromide (CTAB) was used to modulate the electronic double layer (EDL) of the electrode, which can also significantly suppress the HER and enhance the selectivity of CRR (Figure 3D).⁵² Specifically, the hydrophobic tails of CTAB can effectively replace the hydronium and hydrated metal cathode ions. The low hydronium concentration at the Ag surface can reduce the HER activity and promote the generation of HCOOH instead of CO. Zhang et al.⁵³ also used CTAB to modulate the surface of Cu electrode and found that the interfacial water molecules are replaced due to CTAB adsorption within the EDL, thereby inhibiting the HER. Importantly, the presence of CTAB can increase the *CO surface coverage and reduce the *CO adsorption. Consequently, the CRR activity of Cu electrode was significantly improved. By contrast, Lee et al.⁵⁴ employed the hydrophobic polytetrafluoroethylene (PTFE) as the binder to tune the local environment of the Au electrode. They found that F groups in PTFE can decrease the *H adsorption on the electrode surface, thereby creating more sites to produce the first reaction intermediate, *HOCO; thus, a ~97% FE of CO could be realized on modified Au electrode.

Apart from enriching CO₂ near the cathode and limiting water transport, hydrophobicity can also reduce the

thickness of the diffusion layer (Figure 3E). Xing et al.⁵⁵ used disperse hydrophobic PTFE nanoparticles to mix with commercial copper nanoparticles. Although this electrode design can significantly improve the CRR current density from 5 to 20 mA/cm², the total FEs for CRR products are ~30% in a H-cell. When the PTFE was used to tune the local environment of the gas-diffusion electrode for a flow cell, its CRR current density and the FEs for CRR were doubled, that is, 250 mA/cm² and ~70%, respectively. This result suggests that decreasing the thickness of the diffusion layer by using PTFE is also applicable in a flow cell. More importantly, PTFE can make the electrode surface hydrophobic after CRR operation for 2 h, which ensures the structural stability of the gas-diffusion electrode. The electrochemical impedance spectroscopy (EIS) was used to investigate the Nernst diffusion process in the flow cell and identify the thickness of the diffusion layer.⁴⁶ On Bi electrode, the diffusion layer thicknesses decrease from 20.6 ± 2.8 μm to 7.0 ± 1.5 μm for CRR on due to introduction of 30 wt% PTFE. Consequently, the FE of HCOOH is significantly improved from 50% to 80% at -0.7 V versus reversible hydrogen electrode (RHE). The authors ascribe this improvement to the formation of a three-phase interface due to the introduction of PTFE. The solid-liquid-gas interface can ensure that CO₂ molecules, protons, and ionic conductivity are available to drive the CRR. Zhang et al.⁵⁶ utilized confocal laser scanning microscopy to identify that the ideal three-phase structure for CRR is the Cassie-Wenzel coexistence wetting state, which ensures not only interfacial CO₂ transportation but also close contact between active catalytic sites and the electrolyte. Therefore, high current densities for CRR can be realized.

2.2 | CO₂ activation

CO₂ activation relies on chemisorbed rather than physisorbed CO₂ molecules. To accelerate the transformation from a physisorbed state to a chemisorbed state, cysteamine was used to modify the Ag catalyst for promoting CO₂ activation (Figure 3F).⁵⁷ Theoretical calculations confirmed that the NH₂ group of the cysteamine ligand can stabilize chemisorbed CO₂ by the hydrogen bond, thus reducing the CRR overpotential for CO formation. Therefore, the catalytic activity improvement of surface ligands is attributed to stabilizing chemisorbed CO₂ geometrically and electron-dislocation effects. Although this modification can effectively improve the catalytic activity, the active sites may be blocked by coating molecular. To address this issue, Cao et al.⁵⁸ chose a ring molecule, chelating tetradentate porphyrin ligand, to functionalize the Au nanoparticles because this molecule can provide the channel for CO₂ transport to

the surface of the catalyst. The experiment confirmed that, in comparison with the line molecule (e.g., oleylamine), the Au nanoparticles coating with the ring molecule presented a 110-fold enhancement for CO₂ to CO. Theoretical calculations revealed that the molecule can significantly lower the activation energy for CO₂ and facilitate the formation of the first intermediate, COOH*. This effect was also developed in the molecular catalysts.⁵⁹ The fac-Re(I)bipyridine(CO)₃Cl complex was modified by using a thiourea tether, which can serve as the second coordination sphere of the catalytic site to bind CO₂ via the hydrogen bond and directly as a local proton source, thereby together notably improving the activity. In addition to binding CO₂ by the hydrogen bond, the ligand can also be used to tune the local electron density at the active sites of catalysts to promote CO₂ activation and form the COOH* intermediate. Wei et al.⁶⁰ used thiocyanate to modify Ag nanofoams, which a higher density of localized unpaired electrons generate. It can stabilize surface adsorbed CO₂⁻ radical, which is beneficial for subsequent formation of COOH* after coupling with a proton. Thus, the modified Ag can present a high CO selectivity at a wide potential window from -0.5 to -1.2 V versus RHE.

3 | ELECTROLYTE OPTIMIZATION

It has been well known that the cation species and their concentration play an important role in affecting the selectivity and activity of electrocatalysis.^{61,62} For example, a too high near-surface cation concentration can result in near-surface cations blocking the surface of catalysts in alkaline solution, thereby lowering of the HER activity.⁶³ Therefore, tuning the presence of cation species and their concentration in the electrolyte can also affect the CRR kinetics.

3.1 | The effect of cations

Early CRR experiments used a copper electrode with the addition of different alkali metal cations in the electrolyte.⁶⁴ It was suggested that the ratio of C₂H₄ to CH₄ becomes greater with the increase of the cation size and that a larger cation radius is beneficial to suppress the HER. Consequently, this trend was rationalized by the variation of the potential of Out Helmholtz Plan (OHP) determined by cation species (Figure 4A). This effort can also be observed in Ag electrode. Thorson et al.⁶⁹ observed larger cations (e.g., Rb⁺, Cs⁺) inhibit HER, thereby promoting the selectivity of CO, reaching close to

100%. This phenomenon is explained as the extent of cation specific adsorption caused by the varied hydration ability of cations. Compared with small cation sizes, cations with larger radius possess weak hydration, thus being easily adsorbed on the surface of the electrode and resulting in a change in OHP. This feature can be used to tune the distribution of protons derived from the electrostatic effect, thereby altering the selectivity of CRR. In contrast, the small cations with a high hydration number, like Li⁺, have little impact on the OHP.

Except for the interpretation related to the potential change of OHP, another model based on the hydrolysis of cations was proposed (Figure 4B).⁶⁵ In the vicinity of the catalyst, the cations underwent hydrolysis resulting from Coulombic interactions with the negative charge; this effect improved with the increasing cathode potential. The hydrated cation near the cathode surface acted as a pH buffer. Different sizes of cations and charge lead to diverse pKa values. The pKa of cations near the catalyst decreased with the increasing cation size, whereby the buffering capability decreased in the following sequence Cs⁺ > Rb⁺ > K⁺ > Na⁺ > Li⁺. Therefore, the pH near the catalyst remained stable, and the CO₂ concentration increased in the presence of cations with low pKa. Consequently, this buffer effect decreased the selectivity toward the H₂ and CH₄, thus improving the selectivity of CO and C₂ products at -1.1 V versus RHE. However, this hydrolysis effect cannot be applied at much lower potentials as no hydrolysis of cations will occur under such conditions. Hussain et al.⁶⁶ used CO as the probe molecule to study the adsorption behaviors on Pt for identifying the effects of cation size on the location of OHP, which can determine the interfacial potential profile (Figure 4C). These results show that the smaller cations can enhance the polarizability of the intermediate CO_{ad}, thereby accumulating more electrons on the oxygen atom of CO_{ad}. This finding determines the following two aspects: (1) the CO_{ad} adsorption energy to tune the rates of reaction pathways, thereby affecting the reaction selectivity; (2) the degree of hydrogen bonding of interface water to CO_{ad}, which can affect the subsequent hydrogenation reaction.

To develop in-depth understanding of the reaction intermediates, new theories were developed to better understand the mechanisms of the effects of cations in the CRR. Resasco et al.³⁷ found that the larger cations have a positive effect on the selectivities of HCOO⁻ and CO, whereas that of H₂ remains unchanged (Figure 4D). The DFT computations verified that the dipole field created by hydrated cations in the OHP contributes to the adsorption of reaction intermediates with dipole moments (e.g., *CO₂, *CO, *OCCO). Furthermore, compared with small cations, the larger cations are

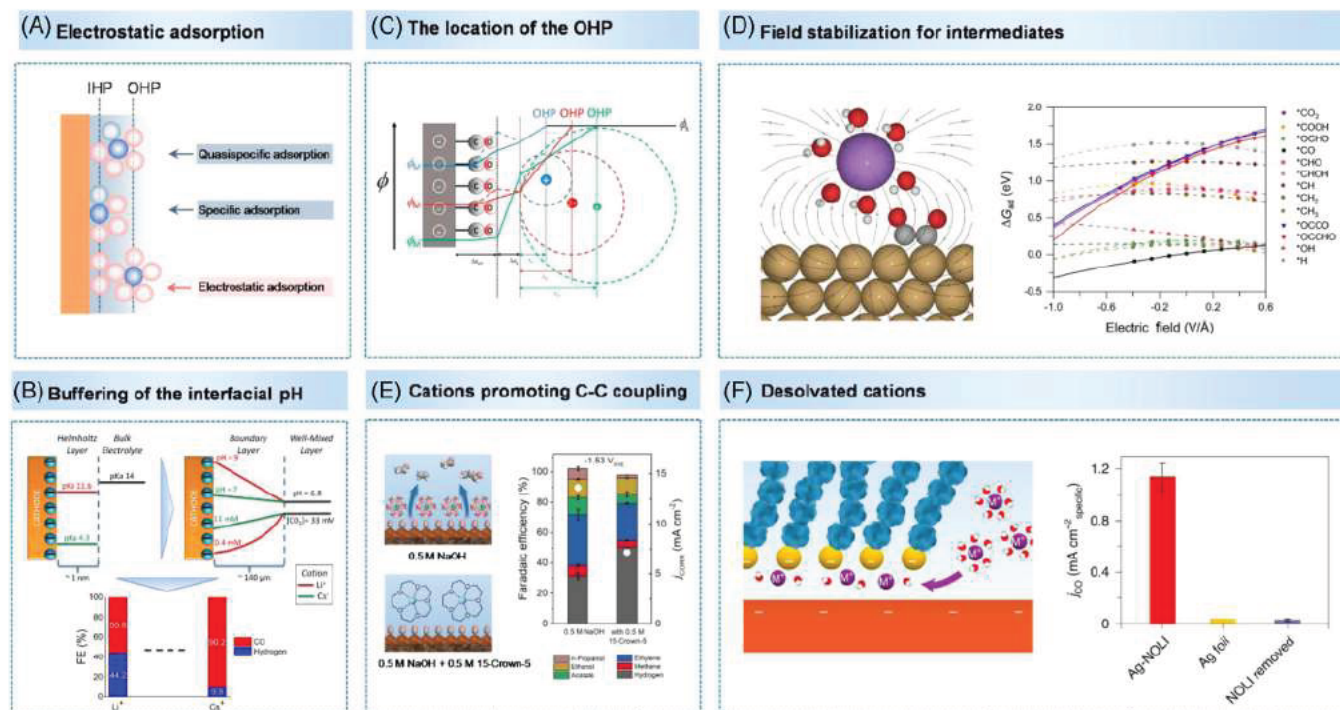


FIGURE 4 Schematics of (A) the EDL structure and distinct adsorption models. Reproduced with permission: Copyright 2019, AIP Publishing LLC.⁶¹ (B) Effect of cation hydrolysis on the CRR over Ag and the FEs for CO and H₂ in Li⁺ or Cs⁺ electrolyte. Reproduced with permission: Copyright 2016, American Chemical Society.⁶⁵ (C) Potential profile across the electrode electrolyte interface, and the effect of the cation size on the interfacial properties and on the polarizability of the CO adlayer. Reproduced with permission: Copyright 2019, Elsevier.⁶⁶ (D) Field effects on various CRR intermediates on Cu(111). Reproduced with permission: Copyright 2017, American Chemical Society.³⁷ (E) The decrease of cations in OHP owing to the chelation by 15 crown 5, CO electroreduction current densities and Faradaic efficiencies in 0.5 mol/L NaOH and in 1 mol/L NaOH chelated with 0.5 mol/L 15 crown 5 at 1.53 V_{SHE}. Reproduced with permission: Copyright 2017, John Wiley & Sons Inc.⁶⁷ (F) The structure of desolvated cations near the catalyst surface by coating with tetradecylphosphonic acid and the current density for different samples. Reproduced with permission: Copyright 2020, Nature Publishing Group.⁶⁸ CRR, CO₂ reduction reaction; EDL, electronic double layer; OHP, Out Helmholtz Plan

more energetically favored at the OHP, as they contribute to strengthening the dipole electrostatic field at the OHP and affect the product distribution. The cation effects to stabilize the *OCCO intermediate and to promote the C–C coupling have been revealed.⁶⁷ As shown in Figure 4E, when Na ions in electrolyte were chelated by 15-crown-5, the FE for C₂H₄ significantly decreased. This finding suggests that a higher concentration of cations facilitates the C–C coupling to boost the formation rate of C₂ products. To clarify which kind of cation effects (e.g., modification of OHP, buffering effect and stabilizing the reaction intermediate) dominates the CRR kinetics, the CRR was carried in acid solution.²⁷ It was found that in the absence of cations, no CRR was observed; the CO species were generated with the addition of cations. This result pointed out that the change of OHP and the buffering effect are not the primary roles of cations. Indeed, these two models indicated that the cations would only affect the CRR reaction rate. A combination of the experimental and

DTF results evidenced that partially desolvated metal cations can stabilize the negatively charged reaction intermediate, such as *CO₂⁻, and *OCCO⁻ through the short-range electrostatic interactions. In addition, the ability of cations to stabilize intermediates is in the following order Cs⁺ > K⁺ > Na⁺, indicating that the stabilization effect increases with the cation radius.

Tuning the solvated cation structure provides another way to alter the CRR catalytic activity. Kim et al.⁶⁸ developed a method to fabricate desolvated cations, which can be intercalated into the surface of Ag catalyst (Figure 4F). An anionic ligand, tetradecylphosphonic acid, and nanoparticles work together to build the nanoparticle/ordered-ligand interlayer (NOLI) structure through a chemisorbed bonding. Under a negative bias (−0.68 V versus RHE), the chemisorbed molecule transferred to a physisorbed state and formed a structural pocket on the surface of Ag nanoparticles.⁷⁰ These pockets allowed desolvated K⁺ to reach the surface of the Ag catalyst, which lowered the energy barrier of transforming

physically adsorbed CO_2 to a chemically adsorbed state by an electron transfer. As the electrochemical breaking of a nonpolar CO_2 is usually considered as an energetically demanding step for CRR, this detached layer of ligands significantly improved the catalytic turnover of Ag nanoparticles by two orders of magnitude over the Ag foil. When the NOLI of Ag nanoparticle surface was removed by washing with concentrated KOH, the current density decreases and was equal to that of the Ag foil.

3.2 | Enriching electrolyte cations

As discussed above, the presence of cations is an important physiochemical factor to promote the CRR by stabilizing the reaction intermediates. The CRR kinetics depends significantly on the cation concentration on the catalyst surface. Thus, some studies have also focused on altering the local environment by tuning cation concentration to promote the CRR selectivity. First, Liu et al.⁷¹ reported that fabricating Au needles can concentrate K^+ ions to accelerate the kinetics of CRR, thereby improving CRR's activity and selectivity

(Figure 5A). The DFT calculations revealed that the presence of adsorbed K^+ ions on the Au surface can lower the thermodynamic energy barrier for CRR, especially for CO_2 activation, and stabilize the COOH^* and CO^* intermediates (Figure 5B). The Gouy–Chapman–Stern model was used to map the surface adsorbed K^+ ion density in the Helmholtz layer of the electrical double layer directly adjacent to the electrode surface. The results proved that, due to an enhanced local electrostatic field, a 20-fold increase of surface adsorbed K^+ ion concentration at the Au needle tip was achieved. Therefore, the current density and FE for CO on the Au needles have been improved significantly compared to the Au rods and particles. In addition, functional groups can be introduced to improve the K^+ ion concentration at the catalyst surface. An ionomer bulk heterojunction architecture was synthesized to further improve the current density of CO in a flow cell to hundreds of mA/cm^2 ; the current density for multicarbon products even exceeded $1.0 \text{ A}/\text{cm}^2$ (Figure 5C).⁷² In this study, perfluorinated sulfonic acid (PFSA) ionomers, which include hydrophobic and hydrophilic functional groups, were used to change the local reaction environment of the catalysts.

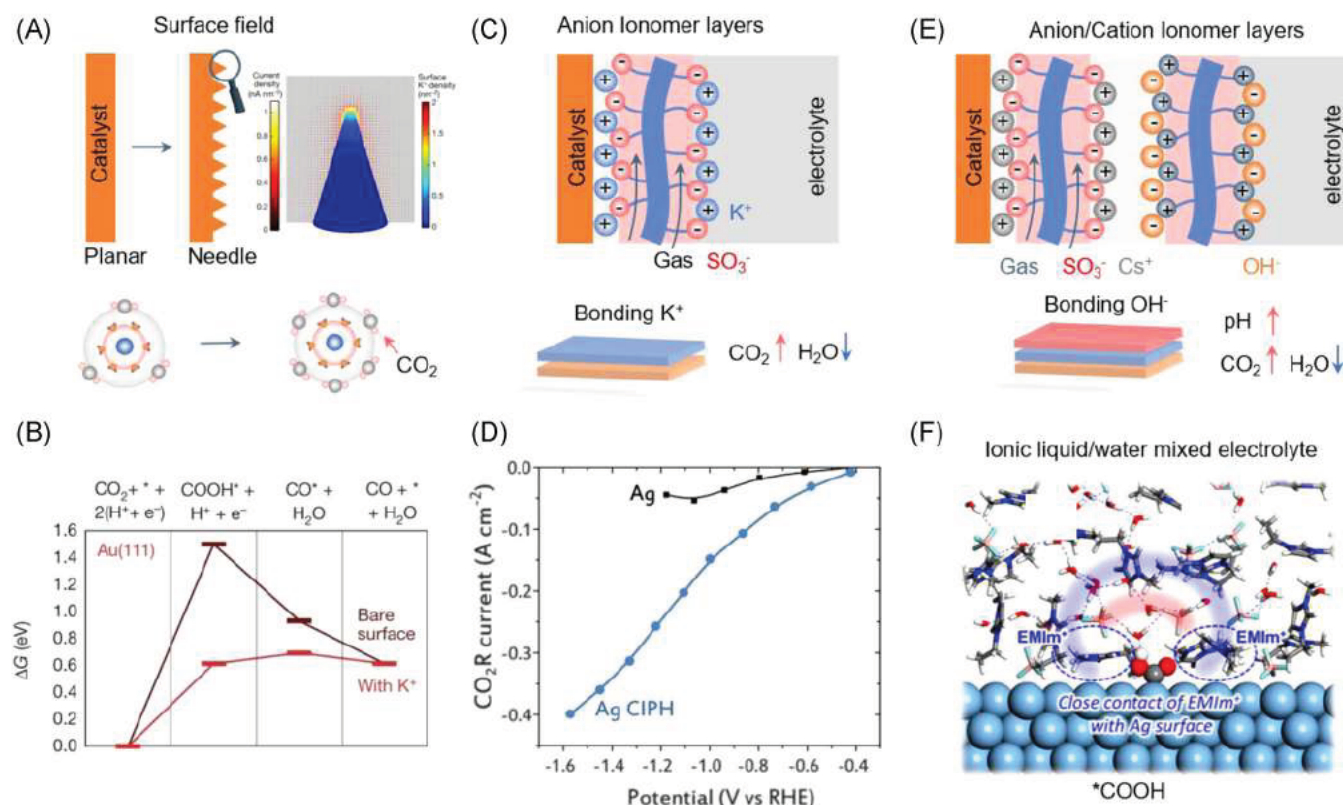


FIGURE 5 Schematics of (A) surface K^+ density and current density distributions on the surface of Au needles; (B) CRR thermodynamic barriers for CO_2 to CO on Au(111) under conditions with and without K^+ . Reproduced with permission: Copyright 2016, Nature Publishing Group.⁷¹ (C) Anion ionomer layer to modify the surface of catalyst; (D) the CRR current density of pristine and modified Ag under different potentials. Reproduced with permission: Copyright 2021, Science Publishing Group.⁷² (E) Anion and cation ionomer layer to modify the surface of catalyst. Reproduced with permission: Copyright 2021, Springer Nature.⁷³ (F) Solvent charge density and corresponding electronic polarization in the $^*\text{COOH}$ state. Reproduced with permission: Copyright 2018, American Chemical Society⁷⁴

The former ionomers increased the mass transport and CO₂ concentration while the latter functional groups provided numbers of SO₃⁻ groups to bind K⁺ ions, which benefit the CO₂ activation. When the ionomer loading of 3.3 mg/cm², the current density of C₂₊ products is over 1.2 A/cm² (Figure 5D), which is currently the highest CRR current density among the Cu-based catalysts. Although the current density of CRR was significantly improved by increasing the ratio of CO₂ to H₂O, improvement of C₂₊ product selectivity is still a critical challenge for Cu catalysts.

Kim et al.⁷³ further used double-layer ionomers to vary the local pH and CO₂ to H₂O ratio simultaneously to achieve a high C₂₊ production on Cu by coating two-layer ionomer (Figure 5E). The outer layer is Nafion (a perfluorosulfonic acid, a cation-exchange ionomer), which can hinder the HCO₃⁻ anion transport from the bulk electrolyte to the catalyst surface, thereby remaining a high pH to promote the C-C coupling for the formation of C₂₊ products. The inner layer is Sustainion (a polystyrene vinylbenzyl methylimidazolium, an anion ionomer layer), which behaves like the PFSA ionomers, that is, enhances the local ratio of CO₂ to H₂O due to its high CO₂ solubility.

3.3 | Addition of ionic liquid

In addition to improving the concentration of surface adsorbed K⁺ cations, the addition of ionic liquids on the catalyst surface is another way to adjust the local environment for boosting the CRR activity and selectivity. Lim et al.⁷⁴ used DFT to conclude that the thermodynamic barrier for CO₂ activation can be lowered by 310 mV when 1-ethyl-3-methylimidazolium [EMIM][BF₄] is added into water as the electrolyte. Compared with the aqueous system, a large number of metal Ag electrons are polarized toward *COOH direction in the mixed electrolyte system. Thus, a strong local field effect at the EDL of Ag electrode could be achieved, which stabilized the *COOH intermediate via the field-dipole interaction (Figure 5F). Ren et al.⁷⁵ utilized an ionic liquid with a high CO₂ solubility, that is, 600 mmol/kg in 1-butyl-3-methylimidazolium hexafluorophosphate, [BMIM][PF₆], which is significantly higher than in H₂O of 34 mmol/L, to improve the activity of Ni-N-C catalyst for CRR. The ionic liquid in the nanopores of Ni-N-C can mitigate the mass transport and conductivity issues. The DFT results proved that, due to the present of ionic liquid, the *d*-band center of Ni atoms is positively shifted to the Fermi level. Consequently, the thermodynamic barrier for CO₂ activation can be significantly lowered by 0.69 eV. Meanwhile, the ionic liquid on the surface of Cu is also conducive to *CO dimerization and generate C₂H₄. Sha et al.⁷⁶ used 1-butyl-3-methylimidazolium nitrate [BMIM]

[NO₃] to regulate local atomic coordination and electronic property of Cu₃(BTC)₂ (benzenetricarboxylate [BTC]) derived-Cu to realize negative charges of Cu. The DFT results proved that the modified Cu benefited the *CO dimerization toward C₂H₄ through lowering the thermodynamic barrier for C-C coupling. Moreover, the experimental results confirmed the FE for C₂H₄ rising from 31.2% to 77.3%. We emphasize that the above discussed results pinpoint on the two issues that need to be considered when using ionic liquids to adjust the local environment of catalysts. On one hand, the current research about the ionic liquid for CRR only focuses on promoting the formation of gaseous products without any liquid ones. On the other hand, long-operation stability (>100 h) of catalysts with the ionic liquid needs to be further explored.

4 | TUNING INTERMEDIATE STATES

Organic molecules have also been reported to modify the physicochemical properties of the catalyst sites because they can tune the intermediate states through weak interactions, for example, hydrogen bonding and electrostatic fields.

4.1 | Construction of proton donor

Pyridine has been reported as a homogeneous catalyst to drive CRR, in which pyridinium radicals (PyH⁺) are single-electron charge transfer mediators to generate methanol.⁷⁷ Dunwell et al.⁷⁸ found that the presence of pyridinium promotes the HCOOH pathway on Pt, whereas the absence of pyridinium can produce CO (Figure 6A). They used attenuated total reflectance surface-enhanced infrared absorption spectroscopy (ATR-SEIRAS) to find that unidentate carboxyl species (COOH_L) is the common intermediate for generation of CO and HCOOH. When pyridinium was added into the electrolyte, the proton from PyH⁺ transferred to the C of the COOH_L intermediate leading to the formation of HCOOH. By contrast, the proton from H₂O splitting transferred to the hydroxyl group of the COOH_L intermediate, generating CO. Fang et al.⁷⁹ used 4-pyridinylethanemercaptan to modify the Au electrodes and improved HCOOH formation efficiency. After coating this organic molecule, the modified Au presented a twofold increase in FE relative to Au foil. This improvement is because 4-pyridylethylmercaptan with an intermediate pKa can facilitate one proton to transfer to the key intermediate HCOO*, thereby accelerating the formation of HCOOH. However, this organic molecule

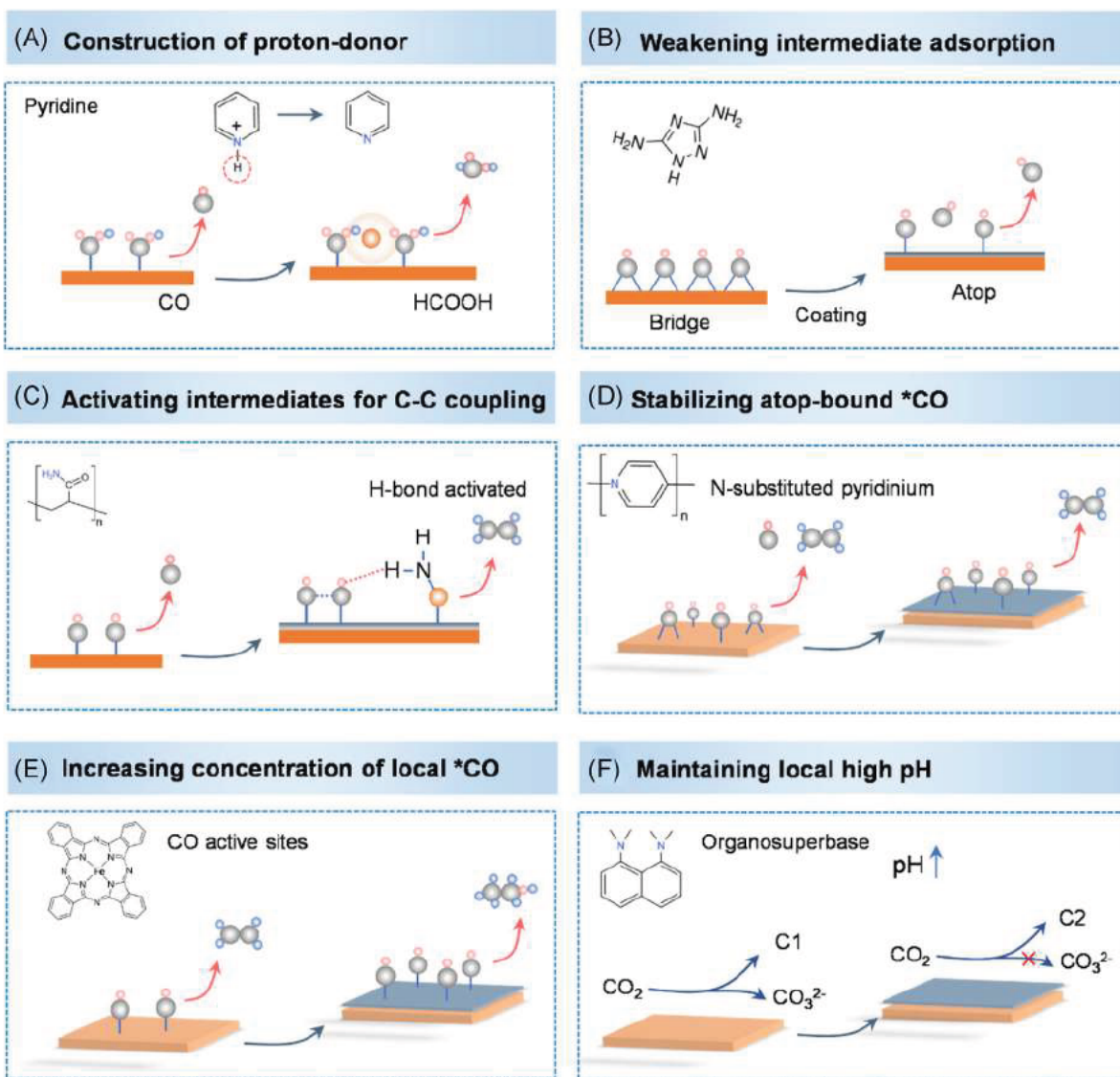


FIGURE 6 Schematics of (A) pyridine as the proton donor to tune the CRR selectivity; (B) coating organic molecule to weaken intermediate adsorption to promote CO formation; (C) H bond activating intermediates for C C coupling; (D) N substituted pyridinium to stabilize atop bound *CO intermediates to form C_2H_4 ; (E) inducing CO active sites to increase *CO coverage for C C coupling to promote the formation of C_2H_5OH ; (F) organosuperbase to create a high pH near the surface of electrode to improve the formation efficiency of C_2 products and maintain bulk electrolyte neutral to suppress carbonate formation. CRR, CO_2 reduction reaction

can be shed from the catalyst surface during the CRR reaction, a more stable structure to incorporate the pyridinium needs to be developed. Accordingly, Guo et al.⁸⁰ synthesized a new metal-organic framework (MOF) layer that is built by the ligand with pyridine group. The catalytic active sites, cobaltprotoporphyrin (CoP), have been induced into this MOFs by a postsynthesis method (e.g., carboxylate exchange with formate capping groups). In such a system, the pyridine group can form pyridinium species as secondary coordination spheres to bind CO_2 coupled with the metal Co sites via the hydrogen bonding, which can lower the energy barrier for CO_2 adsorption and facilitate

C–O bond cleavage, thereby enhancing the CRR activity with the high CO FE of 92.2%.

4.2 | Weakening intermediate adsorption

The early research showed that Ag is a candidate CRR catalyst to yield CO, however, a strong adsorption for *CO intermediate on Ag surface limits *CO desorption, thereby lowering the CRR activity. The organic 3,5-diamino-1,2,4-triazole (DAT) molecule was used to modify the surface of Ag electrode (Figure 6B).⁸¹ The in

situ surface-enhanced Raman spectroscopy (SERS) was utilized to rule out that the DAT promotes the transition of *CO intermediate from bridging and threefold hollow adsorption to atop binding, which can effectively accelerate the *CO desorption and promote the CO formation. Tao et al.⁸² also used CTAB to build the competitive adsorption on Cu for facilitating HCOO* desorption, resulting in a 56-fold increase in the partial current density for CRR to HCOOH.

In addition to weakening the adsorption strength of CRR intermediates, it has also been reported that decreasing the H binding on the surface of catalysts can inhibit HER to improve their CRR activity. The organic oleylamine molecule was used to functionalize the Ag nanoparticles, which can stabilize the *COOH intermediate and destabilize the hydrogen binding to eventually suppress the HER.⁸³ Consequently, the modified Ag electrode can present a high CO FE of 94.2% at a wide potential range from -0.5 to -1.0 V versus RHE in the CO₂-saturated 0.5 mol/L KHCO₃. In addition to stabilizing *COOH binding, the thiol group of dodecanethiol also promotes the hydrogen binding. As a result, both HER and CRR activities for this modification are significantly increased compared to the pure Ag electrode case.⁸³ However, the HER dominated at high negative potentials from -0.8 V versus RHE. Therefore, the judicious choice of organic molecules is the key step to improve the CRR activity of the catalysts. Zhao et al.⁸⁴ further developed this modification method by using different amine molecules, for example, the linear amine and branched polyamine, to tune the catalytic activity of ultrasmall Au nanoparticles, in which amine groups tend to be adsorbed on the undercoordinated corner Au sites. This adsorption molecule resulted in the surrounding sites favor the stabilization of *COOH intermediates, inhibiting the adsorption of *H and thus promoting the CO formation. Meanwhile, the molecule with an increased alkyl chain length could provide a stronger electron transfer to Au sites from amine groups, thereby boosting the promoted effect of the linear amine. By contrast, the branched molecule, polyethyleneimine (PEI), can significantly enhance the H₂ evolution and inhibit CO production. This is because the strong interaction between PEI and ultrasmall Au nanoparticles results in severe surface poisoning effects, which blocks the catalytic sites for CRR.

4.3 | Activating intermediates for C-C coupling

Compared to two-electron transfer products, for example, CO and HCOOH, formations of hydrocarbons and

oxygenates on Cu electrodes need a stronger adsorption of intermediates so that they can achieve the C-C coupling to yield C₂H₄ and C₂H₅OH.³⁸ Xie et al.⁸⁵ used amino-acid molecules, for example, glycine, to modify the surface of Cu nanowire films for improvement of hydrocarbon formation (Figure 6C). The DFT computation found that $-\text{NH}_3^+$ ends of the adsorbed glycine can stabilize the intermediate COOH* and CHO* via the formation of hydrogen binding, leading to lower thermodynamic energies of ~ 0.50 and ~ 0.20 eV, respectively. Consequently, the total FE of hydrocarbons can be significantly improved from 8.7% to 27.1%. Noted that such modified Cu foams improved the FEs for both CH₄ and C₂H₄. Ahn et al.⁸⁶ further developed this strategy to modify the Cu foam electrodeposited through adsorbing poly(acrylamide) on its surface. They used DFT modeling to find that two adjacent *CO intermediates can be activated through hydrogen binding interaction with $-\text{NH}_2$ groups. This method could increase the *CO coverage on the surface of Cu, thereby lowering the activation barriers of *CO dimerization and then promoting C₂H₄ formation, whereas the FE for CH₄ was unchanged. In addition, in situ ATR-SEIRAS was utilized to detect an increase in *CO coverage on the surface of Cu that was modified with polyaniline,⁸⁷ thereby facilitating the CO-CO coupling. As a result, the FE of C₂₊ hydrocarbons increased from 15% to 60% compared to the unmodified one.

Compared to the posttreatment methods to induce the organic molecules on the surface of Cu electrode, the coelectroplating method was used to prepare Cu-polyamine catalyst for fabrication of CRR gas-diffusion-layer electrode.⁸⁸ The in situ Raman measurements revealed that the amine groups can produce the higher CO content and more stabilized intermediates, which in turn facilitates the C₂₊ generation. Meanwhile, due to an acid-base equilibrium between the amine groups and HCO₃⁻ in the electrode, the local surface high pH was realized, which also facilitated the C-C coupling for the formation of C₂₊ hydrocarbons. The polyamine modified Cu achieved a maximum C₂H₄ FE of 72% at -0.97 V versus RHE in 1 mol/L KOH. When the electrode was 10 mol/L KOH, the value was improved to 87% at -0.47 V versus RHE, indicating that the local environment of the Cu electrode is critical for high C₂₊ hydrocarbon generation.

4.4 | Increasing CO coverage

N-substituted pyridinium is another organic molecule that can be transferred into the electrochemically deposited film on the Cu electrode. It had been firstly

reported to modify the polycrystalline Cu to promote the formation of C_{2+} hydrocarbons using a series of N-heterocyclic chloride salts as additives.⁸⁹ The pyridinium compounds with N-aryl substituents modified Cu show the highest increase in C_{2+} selectivity of 70%–80%, while tert-butyl substitution resulted in the increased H_2 production compared with pure Cu. Using in situ ATR-SEIRAS, it was found that the film formed by 1-(4-tolyl) (T-Pyr-) pyridinium can cause an increase in the surface local pH by limiting the mass transport to/from the interface.⁹⁰ The limited proton availability at the interface of the Cu improved the selectivity for C_{2+} products. By contrast, 1-(4-pyridyl) (P-Py-) pyridinium-derived film could selectively poison undercoordinated Cu sites by a lone pair on the N atom, thereby impeding the reduction of the *CO intermediate toward C_{2+} products. Similarly, Li et al.⁹¹ analyzed Bader charge of N atom in N-substituted pyridinium and synthesized different N-substituted pyridiniums to build a structure-performance relationship between the molecular structure and the selectivity for C_{2+} products on Cu catalyst (Figure 6D). DFT calculations predicted that *CO dimerization at atop and bridge sites needs a lower barrier than that of two bridge sites, whereas *CO dimerization at two atop sites is not favorable, indicating that the population of atop *CO is neither too large nor too small to promote C_{2+} selectivity. Therefore, an N-aryl-pyridinium-derived molecule with a moderate Bader charge was used to stabilize atop *CO on Cu and facilitate C–C coupling toward C_2H_4 . The modified Cu with T-Pyr-pyridinium could produce C_2H_4 with a FE of 72% at a partial current density of 230 mA/cm² in a flow cell.

Besides increasing the adsorption strength for *CO, induction of additional active sites for CO adsorption is another method to improve local CO concentration, thereby tuning the selectivity of C_2H_5OH . Li et al.⁹² found that a higher *CO coverage on the Cu promotes the formation of C_2H_5OH rather than C_2H_4 (Figure 6E). Therefore, they used a molecular catalyst, 5,10,15,20-tetraphenyl-21H,23H-porphine iron(iii) chloride, to modify the local environment of Cu. The increased local high-concentration CO has been observed by in situ Raman spectroscopy, resulting in a significantly improved FE ratio of C_2H_5OH to C_2H_4 .

4.5 | Maintaining a high local pH

Most studies in the flow cell were carried out in a highly concentrated KOH electrolyte, which leads to carbonate formation from gaseous CO_2 , decreasing the energy efficiency. To suppress the carbonate formation,

Fan et al.⁹³ used water-insoluble organosuperbases to modify the surface of Cu (Figure 6F). The organic molecule, that is, bis(dimethylamino)naphthalene, can provide strong alkaline environment for the Cu electrode, while the bulk electrode can maintain a neutral pH. Therefore, coating bis(dimethylamino)naphthalene can significantly lower the amount of dissolved CO_2 . The DFT results confirmed that the protonated organosuperbases can stabilize the *CO intermediate by local increased electrostatic fields, thereby improve the C–C coupling. After the modification, the C_{2+} product to C_1 ratio of commercial Cu nanoparticles was increased by a factor of 20 compared to its original performance.

4.6 | Tuning local CO_2 concentration

The kinetic rate of CRR depends on the local CO_2 concentration. However, it should be noted that a high CO_2 concentration at or near the catalyst surface could cause a higher population of unreacted * CO_2 , thereby reducing the surface *CO coverage, which may be unfavorable for *CO dimerization.⁹⁴ Although gas-diffusion electrodes can significantly decrease the distance of CO_2 mass transfer to ensure the industry-relevant current density for CRR, the local CO_2 concentration depends on the system parameters, for example, thickness and porosity of gas-diffusion electrodes, CO_2 feed concentration, and feed flow rate. Tan et al.⁹⁵ used Cu_2O nanoparticles as the model catalysts to tune these parameters to improve the efficiency for C–C coupling (Figure 7A). They observed that a high evaporation rate of the catalyst ink at a high temperature, for example, 75°C, can promote the formation of a thicker catalyst layer by using an airbrushing method, which can provide a moderate level of local CO_2 . In addition, decreasing the local CO_2 feed concentration from 100% to 50%–70% via mixing with N_2 or decreasing CO_2 feed flow could also realize an optimal *CO coverage, promoting the C–C coupling. The above results demonstrated that increasing the thickness of the catalyst layer or the porosity of gas-diffusion electrodes can indeed be used to optimize the surface concentration of intermediates, for example, * CO_2 , *CO, and *H, for the promotion of *CO dimerization.

5 | CATALYST SURFACE COMPOSITION

Catalyst restructuring always occurs due to the negative potential used to drive the CRR. For example, Lee et al.⁹⁸ used different reduction potentials to prepare Cu to tune

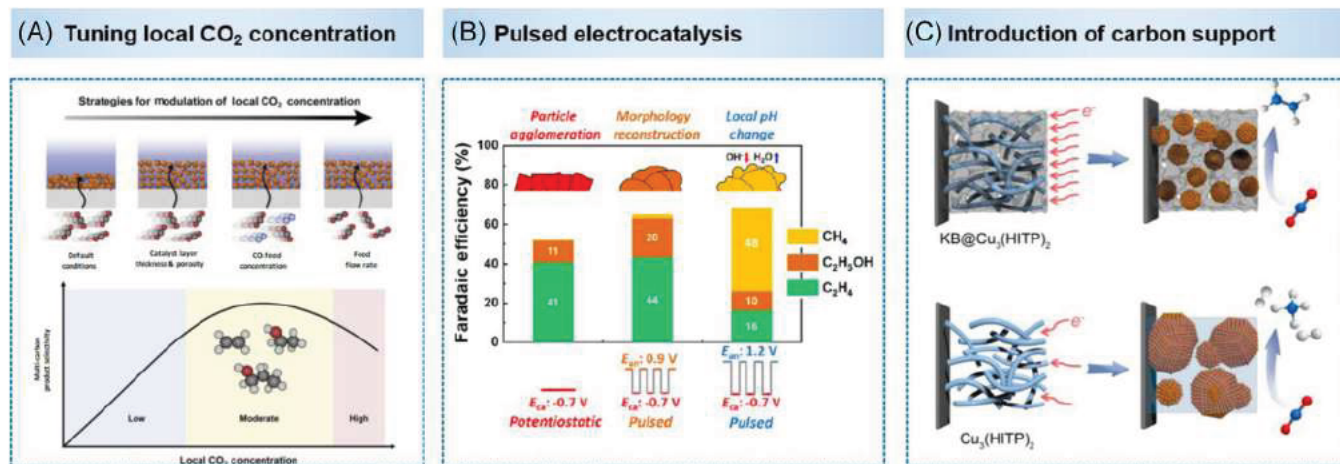


FIGURE 7 Schematics of (A) the relationship between the FEs for C₂₊ products and local CO₂ concentration. Reproduced with permission: Copyright 2020, Elsevier Inc.⁹⁵ (B) The FEs for C₂₊ products under potentiostatic and pulsed electrocatalysis. Reproduced with permission: Copyright 2016, American Chemical Society.⁹⁶ (C) Introduction of carbon support to suppress Cu nanoparticles growth derived from Cu₃(HITP)₂ and tuning the CRR selectivity. Reproduced with permission: Copyright 2021, Nature Publishing Group⁹⁷

its catalytic activity. Cu(OH)₂ worked as the original catalyst, which can transform into Cu under a reduction potential. These results demonstrated that the sample treated under a large negative potential, for example, -4.0 V versus Ag/AgCl, can ensure a longer stability for catalysis of C₂H₄ than that under a small negative potential, -1.15 V versus Ag/AgCl. Interestingly, X-ray photoelectron spectroscopy (XPS) and grazing incidence X-ray diffraction results revealed that, at a large negative potential, in addition to Cu⁰, there are some Cu²⁺ species found at the surface of the sample, which promote the C-C coupling.

Pulsed electrocatalysis is a method for the electrochemical oxidation of Cu⁰ to Cu¹⁺/Cu²⁺, thereby tuning its CRR selectivity because the surface Cu oxidation state significantly determines the CRR reaction pathways. Arán-Ais et al.⁹⁹ used this method to control the Cu morphology and oxidation states for improving the efficiency of C₂H₅OH production. Atomic force microscopy (AFM) confirmed that the Cu cubic islands with (100) facets can be formed under the pulsed potentials, whereas they could be converted into nanoparticles under potentiostatic conditions (Figure 7B). In addition, there were some Cu₂O species on the surface of Cu electrodes determined by in situ XPS measurements; an increased anode potential led to more Cu₂O. When this potential increased to 0.6 V versus RHE, the highest selectivity for C₂₊ products of 76% had been realized, if the anode potential was further increased to 0.8 V versus RHE, the selectivity of CH₄ has been significantly enhanced due to emergence of CuO. The CRR was further studied under the pulsed electrolysis conditions in a flow cell.⁹⁶ When the anode potential is 0.9 V versus

RHE, the total FEs for C₂H₅OH and C₂H₄ were increased by 10%, which is due to the presence of highly defective interfaces and grain boundaries on the catalyst surface. By contrast, when the anode potential was increased to 1.2 V versus RHE, the FEs for C₂H₅OH and C₂H₄ significantly decreased, whereas the main product was CH₄ with a FE of 48%. In another example, Sun et al.⁹⁷ introduced carbon support as conductive scaffolds to control the Cu growth, thereby promoting the C₂H₄ species formation (Figure 7C). The experimental results showed that the pristine MOF (Cu₃(HITP)₂, HITP = 2,3,6,7,10,11-hexamino-triphenylene) could be transferred into Cu particles, whereas Ketjen Black can significantly lower the size of the reconstructed Cu. Meanwhile, it was proposed the [101] Cu rectangular nanopyramid theoretical model with rich grain boundaries can promote C-C coupling and suppress the competitive HER reaction. Consequently, the FE for C₂H₄ and current density on modified MOF had been significantly improved. Meanwhile, the modified MOF can present a high FE for C₂H₄ at a wide potential range, whereas the FE for C₂H₄ decreases and the FE for CH₄ increases on the pristine MOF at a large negative potential. This result indicates that the composition and structure of the support material are critical for catalytic performance because they can significantly affect the reconstructed structure of the catalyst.

In addition, coating organic and polymeric molecules can also regulate the surface composition and morphology of the catalyst to steer its CRR activity and selectivity. Wu et al.¹⁰⁰ used thiadiazole and triazole derivatives to tune the Cu oxidation state of Ag-Cu electrode, thereby improving the CRR selectivity toward C₂₊ products. Due

to the electron-deficient property, the molecules can withdraw electrons from the surface Cu atoms with formation of $\text{Cu}^{\delta+}$ ($0 < \delta < 1$) species. They can favor the formation of atop adsorbed $^*\text{CO}$ during CRR operation, enhancing the efficiency of C–C coupling. When the modified Ag–Cu alloy was used in a membrane electrode-assembly electrolyzer, the catalyst can provide a high FE for C_{2+} products of $\approx 80\%$. Wang et al.¹⁰¹ fabricated Br-doped Cu catalysts, where the residual Br^- favors to adsorb the organic molecule, dodecanethiol (DDT). It can build a stable hydrophobic interface to decrease the coverage of $^*\text{H}$, thereby suppressing the competitive HER. In addition, the present of Br^- can stabilize high-valence Cu species, thus improve the selectivity toward C_2 products. DFT results showed that Br-doped Cu can provide a lower the formation energy of $^*\text{HC-CHOH}$ (precursor to ethanol) than that of $^*\text{C-CH}$ (precursor to ethylene). As a result, CuBr-DDT promotes ethanol formation and in turn inhibits ethylene formation.

Under CRR reduction potentials, single-crystal Cu (111) undergoes a surface reconstruction to generate Cu (100), which provides a lowest barrier for CO–CO coupling than Cu(111) and Cu(211).^{23,102} It is a challenge to stabilize the Cu(100) facets. To address this problem, Thevenon et al.¹⁰³ employed *N,N'*-ethylene-phenanthroline dibromide as molecular additive to protect the formation of cubic Cu with exposed (100) facets via corrosion of Cu film. They found that the organic additive can electrochemically convert to organic thin film, which is able to stabilize the nanostructure of the cubic Cu, thereby favoring the C–C coupling to generate C_{2+} products. The experiments proved that the modified Cu film can deliver a high FE for ethene and ethanol of 70%. The modified electrode can exhibit high structural stability for more than 40 h without significant change. Furthermore, in the absence of any protections, metal nanoparticles always transform to dendrites during CRR progress. However, this morphological transformation not only decreases the surface area, but also results in challenges to correlate the intrinsic activity to the nanostructures of nanoparticles. To prevent the nano-clustering of Au and Pd from formation of dendrites during CRR operation, Zhang et al.¹⁰⁴ used a copolymer consisting of poly(vinylbenzyl *N*-methylbenzimidazolium bicarbonate) and poly(vinylbenzyl *N*-methylbenzimidazolium carboxylate) to stabilize metal Au and Pd through the covalent metal–C bonds. The polymeric ligand not provides a hydrophobicity interface to inhibit proton reduction but enriches surface electron density of metal Au and Pd to improve their CRR activity. As a result, the modified Au nanoparticles can present an activity retention of 86% after CRR at -0.9 V versus RHE

for 11 h, which is significantly higher than that of unmodified Au of less than 10%.

6 | OUTLOOK AND FUTURE CHALLENGES

Modulating the local microenvironment of the catalyst has emerged as a promising strategy for improving the activity and selectivity of the CRR. This modification can provide a new direction to overcome the limitations of the catalyst design under the Sabatier volcano-like relations. Indeed, adjusting the local environment of the catalyst, for example, hydrophobicity, the size of cations in the electrolyte, and organic molecule/polymer modification, can provide additional opportunities to significantly modulate the intrinsic and extrinsic catalytic activities. For instance, tuning the size of cations can increase the interfacial electric field, thereby stabilizing the key intermediates to promote the CRR. In addition, decreasing the thickness of the diffusion layer can significantly increase the mass transport of CO_2 , thereby improving its concentration near the surface of the electrode. While several methods have been employed to regulate the local environment of the catalyst, significant practical challenges remain for CRR to various applications, namely:

- (1) Flow cell reactors have been widely used in CRR because it can decrease the thickness of the diffusion layer and sustain the industry-relevant current densities. However, the electrode flooding is a great challenge for its practical applications. It usually leads to the destruction of the gas diffusion layer during the reaction. One promising approach to resolve this issue is to use a hydrophobic Cu electrode to mitigate the electrode flooding for CRR, which can ensure the flow cell stable working for 45 h at the 300 mA/cm^2 .¹⁰⁵ More studies should be pursued to improve the stability of the electrode in the flow cell.
- (2) Organic molecules and polymers can offer a certain freedom degree to adjust the local environment of the electrodes. However, those molecules and polymers may be shed from the surface of the electrodes, decreasing the stability of the electrode. In addition, the thickness of the modification materials should be precisely controlled since a thicker layer can limit the mass transport of CO_2 , thereby decreasing the CRR current density. In comparison, a thinner layer cannot stabilize the intermediates. Therefore, the stable organic molecules and polymers should be further explored.

- (3) Modulating the local environment of the catalyst is a surface and interface issue. Although there are some studies on the electrical double layer of the electrodes, little attention has been paid to investigating the relationship between the catalytic activity and the electrical double layer of the electrodes. Electrochemical impedance spectroscopy (EIS) is an effective tool to carry out research on the surface and interface of electrodes. However, most studies focus on calculating the impedance/resistance of the electrodes; a detailed analysis of the EIS may help to fully understand the change of electrode interface and modify it to optimize CRR through different approaches.
- (4) The theoretical modeling and simulations are vital to understand the catalytic processes. Based on the catalyst design, one can investigate the effects of the various modification strategies on catalytic activity and selectivity at the molecular or atomic scales. The theoretical calculations can provide additional opportunities to investigate the interface science of the CRR. Currently there are few theoretical studies on the physical surface and interface of the catalyst. Further research needs to be directed to reveal the relationship between the catalyst's local micro-environment and the catalytic performance.
- (5) Tuning the interfacial electric field has been widely used to regulate the local environment of the catalysts because it can provide additional means to stabilize intermediates, thereby promoting the CRR. Indeed, external fields, for example, electric, and magnetic fields, have been used to improve the catalytic activity in other energy electrochemical catalysis, for instance, HER and oxygen evolution reaction.¹⁰⁶ Very recently, the synergistic electric-thermal field has been used to accelerate the CRR toward the C_{2+} products.¹⁰⁷ However, there are few studies on the effects of the external fields on the CRR activity and selectivity from the perspective of tuning the local microenvironment.
- (6) Currently, a high FE for C_{2+} products usually requires a robust alkaline solution, which can consume a large number of CO_2 molecules to form carbonates, thereby decreasing the energy efficiency of CRR. There are some studies on CRR in strong acid,^{108–110} which can avoid the formation of carbonate in the bulk electrolyte. However, the complete HER and a low FE for C_{2+} products seriously limit the development of CRR in acid solutions. Surface modification through tuning the local environment of the catalyst has been addressed similar issues of CRR in alkaline solution, which may shed new insights for CRR in acid.

While the field of CRR mainly focuses on the development of high-performance catalysts and new reactors, we urge that the understanding of micro-environment can provide more opportunities to tune the CRR activity and selectivity. We suggest that, in addition to fabricating new catalysts, the seamless collaborations among operando techniques to character the reaction intermediates and catalyst surface structure, real-time products detection, and theoretical computations can benefit us to optimize the micro-environment of CRR catalysts.

ACKNOWLEDGMENTS

This study was financially supported by the Australian Research Council through the Discovery Project Programs (Nos. FL170100154, FT200100062, DP220102596, DP210100472, and DP190103472) and the Australian Government through Research Training Program Scholarships.

CONFLICTS OF INTEREST

The authors declare no conflicts of interest.

ORCID

Bao Yu Xia  <https://orcid.org/0000-0002-2054-908X>

Yao Zheng  <https://orcid.org/0000-0002-2411-8041>

Shi-Zhang Qiao  <https://orcid.org/0000-0002-4568-8422>

REFERENCES

1. Ross MB, De Luna P, Li Y, et al. Designing materials for electrochemical carbon dioxide recycling. *Nat Catal.* 2019; 2(8):648–658.
2. Tackett BM, Gomez E, Chen JG. Net reduction of CO_2 via its thermocatalytic and electrocatalytic transformation reactions in standard and hybrid processes. *Nat Catal.* 2019;2(5):381–386.
3. Koshy DM, Nathan SS, Asundi AS, et al. Bridging thermal catalysis and electrocatalysis: catalyzing CO_2 conversion with carbon based materials. *Angew Chem Int Ed.* 2021;60(32):17472–17480.
4. Zhou H, Chen Z, López AV, et al. Engineering the Cu/ Mo_2CT_x (MXene) interface to drive CO_2 hydrogenation to methanol. *Nat Catal.* 2021;4(10):860–871.
5. Fan L, Xia C, Yang F, Wang J, Wang H, Lu Y. Strategies in catalysts and electrolyzer design for electrochemical CO_2 reduction toward C_{2+} products. *Sci Adv.* 2020;6(8):eaay3111.
6. Zhong J, Yang X, Wu Z, Liang B, Huang Y, Zhang T. State of the art and perspectives in heterogeneous catalysis of CO_2 hydrogenation to methanol. *Chem Soc Rev.* 2020;49(5):1385–1413.
7. Li J, Chen G, Zhu Y, et al. Efficient electrocatalytic CO_2 reduction on a three phase interface. *Nat Catal.* 2018;1(8):592–600.
8. Zhao X, Du L, You B, Sun Y. Integrated design for electrocatalytic carbon dioxide reduction. *Catal Sci Technol.* 2020;10(9):2711–2720.

9. Hu J, Yu L, Deng J, et al. Sulfur vacancy rich MoS₂ as a catalyst for the hydrogenation of CO₂ to methanol. *Nat Catal*. 2021;4(3):242–250.
10. Li H, Wang L, Dai Y, et al. Synergetic interaction between neighbouring platinum monomers in CO₂ hydrogenation. *Nat Nanotechnol*. 2018;13(5):411–417.
11. Wang Z, Zhou Y, Xia C, Guo W, You B, Xia BY. Efficient electroconversion of carbon dioxide to formate by a reconstructed amino functionalized indium organic framework electrocatalyst. *Angew Chem Int Ed*. 2021;60(35):19107–19112.
12. Su X, Yang XF, Huang Y, Liu B, Zhang T. Single atom catalysis toward efficient CO₂ conversion to CO and formate products. *Acc Chem Res*. 2019;52(3):656–664.
13. Vasileff A, Zhi X, Xu C, et al. Selectivity control for electrochemical CO₂ reduction by charge redistribution on the surface of copper alloys. *ACS Catal*. 2019;9(10):9411–9417.
14. Ma S, Sadakiyo M, Heima M, et al. Electroreduction of carbon dioxide to hydrocarbons using bimetallic Cu Pd catalysts with different mixing patterns. *J Am Chem Soc*. 2017;139(1):47–50.
15. Wang J, Tan HY, Zhu Y, Chu H, Chen HM. Linking the dynamic chemical state of catalysts with the product profile of electrocatalytic CO₂ reduction. *Angew Chem Int Ed*. 2021;60(32):17254–17267.
16. Zhou X, Dong J, Zhu Y, et al. Molecular scalpel to chemically cleave metal organic frameworks for induced phase transition. *J Am Chem Soc*. 2021;143(17):6681–6690.
17. Deng P, Yang F, Wang Z, et al. Metal organic framework derived carbon nanorods encapsulating bismuth oxides for rapid and selective CO₂ electroreduction to formate. *Angew Chem Int Ed*. 2020;59(27):10807–10813.
18. Mariano RG, McKelvey K, White HS, Kanan MW. Selective increase in CO₂ electroreduction activity at grain boundary surface terminations. *Science*. 2017;358(6367):1187–1192.
19. Zhou X, Shan J, Chen L, et al. Stabilizing Cu²⁺ ions by solid solutions to promote CO₂ electroreduction to methane. *J Am Chem Soc*. 2022;144(5):2079–2084.
20. Gao FY, Hu SJ, Zhang XL, et al. High curvature transition metal chalcogenide nanostructures with a pronounced proximity effect enable fast and selective CO₂ electroreduction. *Angew Chem Int Ed*. 2020;59(22):8706–8712.
21. Yang PP, Zhang XL, Gao FY, et al. Protecting copper oxidation state via intermediate confinement for selective CO₂ electroreduction to C₂₊ fuels. *J Am Chem Soc*. 2020;142(13):6400–6408.
22. Chi LP, Niu ZZ, Zhang XL, et al. Stabilizing indium sulfide for CO₂ electroreduction to formate at high rate by zinc incorporation. *Nat Commun*. 2021;12(1):5835.
23. Sandberg RB, Montoya JH, Chan K, Nørskov JK. CO CO coupling on Cu facets: coverage, strain and field effects. *Surf Sci*. 2016;654:56–62.
24. Weekes DM, Salvatore DA, Reyes A, Huang A, Berlinguette CP. Electrolytic CO₂ reduction in a flow cell. *Acc Chem Res*. 2018;51(4):910–918.
25. Lv JJ, Jouny M, Luc W, Zhu W, Zhu JJ, Jiao F. A highly porous copper electrocatalyst for carbon dioxide reduction. *Adv Mater*. 2018;30(49):1803111.
26. Zhang F, Co AC. Direct evidence of local pH change and the role of alkali cation during CO₂ electroreduction in aqueous media. *Angew Chem Int Ed*. 2020;59(4):1674–1681.
27. Monteiro MCO, Dattila F, Hagedoorn B, García Muelas R, López N, Koper MTM. Absence of CO₂ electroreduction on copper, gold and silver electrodes without metal cations in solution. *Nat Catal*. 2021;4(8):654–662.
28. He M, Li C, Zhang H, et al. Oxygen induced promotion of electrochemical reduction of CO₂ via co electrolysis. *Nat Commun*. 2020;11(1):3844.
29. Larrazábal GO, Ma M, Seger B. A comprehensive approach to investigate CO₂ reduction electrocatalysts at high current densities. *Acc Chem Res*. 2021;2(4):220–229.
30. Weng LC, Bell AT, Weber AZ. Modeling gas diffusion electrodes for CO₂ reduction. *Phys Chem Chem Phys*. 2018;20(25):16973–16984.
31. Zheng Y, Jiao Y, Zhu Y, et al. Molecule level g C₃N₄ coordinated transition metals as a new class of electrocatalysts for oxygen electrode reactions. *J Am Chem Soc*. 2017;139(9):3336–3339.
32. Kortlever R, Shen J, Schouten KJ, Calle Vallejo F, Koper MT. Catalysts and reaction pathways for the electrochemical reduction of carbon dioxide. *J Phys Chem Lett*. 2015;6(20):4073–4082.
33. Nitopi S, Bertheussen E, Scott SB, et al. Progress and perspectives of electrochemical CO₂ reduction on copper in aqueous electrolyte. *Chem Rev*. 2019;119(12):7610–7672.
34. Zhi X, Vasileff A, Zheng Y, Jiao Y, Qiao S Z. Role of oxygen bound reaction intermediates in selective electrochemical CO₂ reduction. *Energy Environ Sci*. 2021;14(7):3912–3930.
35. Sa YJ, Lee CW, Lee SY, Na J, Lee U, Hwang YJ. Catalyst electrolyte interface chemistry for electrochemical CO₂ reduction. *Chem Soc Rev*. 2020;49(18):6632–6665.
36. Ye K, Zhang G, Ma X Y, et al. Resolving local reaction environment toward an optimized CO₂ to CO conversion performance. *Energy Environ Sci*. 2022;15(2):749–759.
37. Resasco J, Chen LD, Clark E, et al. Promoter effects of alkali metal cations on the electrochemical reduction of carbon dioxide. *J Am Chem Soc*. 2017;139(32):11277–11287.
38. Vasileff A, Xu C, Jiao Y, Zheng Y, Qiao S Z. Surface and interface engineering in copper based bimetallic materials for selective CO₂ electroreduction. *Chem*. 2018;4(8):1809–1831.
39. Wang G, Chen J, Ding Y, et al. Electrocatalysis for CO₂ conversion: from fundamentals to value added products. *Chem Soc Rev*. 2021;50(8):4993–5061.
40. Chen C, Khosrowabadi KJF, Sheehan SW. Progress toward commercial application of electrochemical carbon dioxide reduction. *Chem*. 2018;4(11):2571–2586.
41. Zhou X, Jin H, Xia BY, Davey K, Zheng Y, Qiao SZ. Molecular cleavage of metal organic frameworks and application to energy storage and conversion. *Adv Mater*. 2021;33(51):2104341.
42. Niu Z Z, Chi L P, Liu R, Chen Z, Gao M R. Rigorous assessment of CO₂ electroreduction products in a flow cell. *Energy Environ Sci*. 2021;14(8):4169–4176.
43. Gao F Y, Wu Z Z, Gao M R. Electrochemical CO₂ reduction on transition metal chalcogenide catalysts: recent advances

- and future perspectives. *Energy Fuels*. 2021;35(16):12869 12883.
44. Zheng Y, Vasileff A, Zhou X, Jiao Y, Jaroniec M, Qiao SZ. Understanding the roadmap for electrochemical reduction of CO₂ to multi carbon oxygenates and hydrocarbons on copper based catalysts. *J Am Chem Soc*. 2019;141(19):7646 7659.
45. Wakerley D, Lamaison S, Ozanam F, et al. Bio inspired hydrophobicity promotes CO₂ reduction on a Cu surface. *Nat Mater*. 2019;18(11):1222 1227.
46. Xing Z, Hu X, Feng X. Tuning the microenvironment in gas diffusion electrodes enables high rate CO₂ electrolysis to formate. *ACS Energy Lett*. 2021;6(5):1694 1702.
47. Buckley AK, Lee M, Cheng T, et al. Electrocatalysis at organic metal interfaces: identification of structure reactivity relationships for CO₂ reduction at modified Cu surfaces. *J Am Chem Soc*. 2019;141(18):7355 7364.
48. Buckley AK, Cheng T, Oh MH, et al. Approaching 100% selectivity at low potential on Ag for electrochemical CO₂ reduction to CO using a surface additive. *ACS Catal*. 2021;11(15):9034 9042.
49. Liang H Q, Zhao S, Hu X M, Ceccato M, Skrydstrup T, Daasbjerg K. Hydrophobic copper interfaces boost electro reduction of carbon dioxide to ethylene in water. *ACS Catal*. 2021;11(2):958 966.
50. Thevenon A, Rosas Hernández A, Fontani HAM, Agapie T, Peters JC. Dramatic HER suppression on Ag electrodes via molecular films for highly selective CO₂ to CO reduction. *ACS Catal*. 2021;11(8):4530 4537.
51. Zhang H, Yang Y, Liang Y, et al. Selective methane electrosynthesis enabled by a hydrophobic carbon coated copper core shell architecture. *Energy Environ Sci*. 2022;15(1):234 243.
52. Banerjee S, Han X, Thoi VS. Modulating the electrode electrolyte interface with cationic surfactants in carbon dioxide reduction. *ACS Catal*. 2019;9(6):5631 5637.
53. Zhang ZQ, Banerjee S, Thoi VS, Shoji HA. Reorganization of interfacial water by an amphiphilic cationic surfactant promotes CO₂ reduction. *J Phys Chem Lett*. 2020;11(14):5457 5463.
54. Lee JH, Kattel S, Xie Z, et al. Understanding the role of functional groups in polymeric binder for electrochemical carbon dioxide reduction on gold nanoparticles. *Adv Funct Mater*. 2018;28(45):1804762.
55. Xing Z, Hu L, Ripatti DS, Hu X, Feng X. Enhancing carbon dioxide gas diffusion electrolysis by creating a hydrophobic catalyst microenvironment. *Nat Commun*. 2021;12(1):136.
56. Shi R, Guo J, Zhang X, et al. Efficient wettability controlled electroreduction of CO₂ to CO at Au/C interfaces. *Nat Commun*. 2020;11(1):3028.
57. Wang Z, Wu L, Sun K, et al. Surface ligand promotion of carbon dioxide reduction through stabilizing chemisorbed reactive intermediates. *J Phys Chem Lett*. 2018;9(11):3057 3061.
58. Cao Z, Zacate SB, Sun X, et al. Tuning gold nanoparticles with chelating ligands for highly efficient electrocatalytic CO₂ reduction. *Angew Chem Int Ed*. 2018;57(39):12675 12679.
59. Haviv E, Azaiza Dabbah D, Carmieli R, Avram L, Martin JML, Neumann R. A thiourea tether in the second coordination sphere as a binding site for CO₂ and a proton donor promotes the electrochemical reduction of CO₂ to CO catalyzed by a rhenium bipyridine type complex. *J Am Chem Soc*. 2018;140(39):12451 12456.
60. Wei L, Li H, Chen J, et al. Thiocyanate modified silver nanofoam for efficient CO₂ reduction to CO. *ACS Catal*. 2019;10(2):1444 1453.
61. Waegle MM, Gunathunge CM, Li J, Li X. How cations affect the electric double layer and the rates and selectivity of electrocatalytic processes. *J Chem Phys*. 2019;151(16):160902.
62. Subbaraman R, Tripkovic D, Strmcnik D, et al. Enhancing hydrogen evolution activity in water splitting by tailoring Li⁺ Ni(OH)₂ Pt interfaces. *Science*. 2011;334(6060):1256 1260.
63. Goyal A, Koper MTM. The interrelated effect of cations and electrolyte pH on the hydrogen evolution reaction on gold electrodes in alkaline media. *Angew Chem Int Ed*. 2021;60(24):13452 13462.
64. Murata A, Hori Y. Product selectivity affected by cationic species in electrochemical reduction of CO₂ and CO at a Cu electrode. *Bull Chem Soc Jpn*. 1991;64(1):123 127.
65. Singh MR, Kwon Y, Lum Y, Ager JWI, Bell AT. Hydrolysis of electrolyte cations enhances the electrochemical reduction of CO₂ over Ag and Cu. *J Am Chem Soc*. 2016;138(39):13006 13012.
66. Hussain G, Pérez Martínez L, Le J B, et al. How cations determine the interfacial potential profile: relevance for the CO₂ reduction reaction. *Electrochim Acta*. 2019;327:135055.
67. Li J, Wu D, Malkani AS, et al. Hydroxide is not a promoter of C₂₊ product formation in the electrochemical reduction of CO on copper. *Angew Chem Int Ed*. 2020;59(11):4464 4469.
68. Kim D, Yu S, Zheng F, et al. Selective CO₂ electrocatalysis at the pseudocapacitive nanoparticle/ordered ligand interlayer. *Nat Energy*. 2020;5(12):1032 1042.
69. Thorson MR, Siil KI, Kenis PJA. Effect of cations on the electrochemical conversion of CO₂ to CO. *J Electrochem Soc*. 2012;160(1):F69 F74.
70. Yu S, Kim D, Qi Z, et al. Nanoparticle assembly induced ligand interactions for enhanced electrocatalytic CO₂ conversion. *J Am Chem Soc*. 2021;143(47):19919 19927.
71. Liu M, Pang Y, Zhang B, et al. Enhanced electrocatalytic CO₂ reduction via field induced reagent concentration. *Nature*. 2016;537(7620):382 386.
72. García de Arquer FP, Dinh CT, Ozden A, et al. CO₂ electrolysis to multicarbon products at activities greater than 1 A cm⁻². *Science*. 2020;367(6478):661 666.
73. Kim C, Bui JC, Luo X, et al. Tailored catalyst microenvironments for CO₂ electroreduction to multicarbon products on copper using bilayer ionomer coatings. *Nat Energy*. 2021;6(11):1026 1034.
74. Lim H K, Kwon Y, Kim HS, et al. Insight into the microenvironments of the metal ionic liquid interface during electrochemical CO₂ reduction. *ACS Catal*. 2018;8(3):2420 2427.
75. Ren W, Tan X, Chen X, et al. Confinement of ionic liquids at single ni sites boost electroreduction of CO₂ in aqueous electrolytes. *ACS Catal*. 2020;10(22):13171 13178.
76. Sha Y, Zhang J, Cheng X, et al. Anchoring ionic liquid in copper electrocatalyst for improving CO₂ conversion to

- ethylene. *Angew Chem Int Ed.* 2022;61:e202200039. doi:10.1002/anie.202200039
77. Barton Cole EE, Baruch MF, L'Esperance RP, et al. Substituent effects in the pyridinium catalyzed reduction of CO₂ to methanol: further mechanistic insights. *Top Catal.* 2014;58(1):15–22.
78. Dunwell M, Yan Y, Xu B. In situ infrared spectroscopic investigations of pyridine mediated CO₂ reduction on Pt electrocatalysts. *ACS Catal.* 2017;7(8):5410–5419.
79. Fang Y, Flake JC. Electrochemical reduction of CO₂ at functionalized Au electrodes. *J Am Chem Soc.* 2017;139(9):3399–3405.
80. Guo Y, Shi W, Yang H, et al. Cooperative stabilization of the [pyridinium CO₂ Co] adduct on a metal organic layer enhances electrocatalytic CO₂ reduction. *J Am Chem Soc.* 2019;141(44):17875–17883.
81. Schmitt KG, Gewirth AA. In situ surface enhanced Raman spectroscopy of the electrochemical reduction of carbon dioxide on silver with 3,5 diamino 1,2,4 triazole. *J Phys Chem C.* 2014;118(31):17567–17576.
82. Tao Z, Wu Z, Wu Y, Wang H. Activating copper for electrocatalytic CO₂ reduction to formate via molecular interactions. *ACS Catal.* 2020;10(16):9271–9275.
83. Kim C, Eom T, Jee MS, et al. Insight into electrochemical CO₂ reduction on surface molecule mediated Ag nanoparticles. *ACS Catal.* 2016;7(1):779–785.
84. Zhao Y, Wang C, Liu Y, MacFarlane DR, Wallace GG. Engineering surface amine modifiers of ultrasmall gold nanoparticles supported on reduced graphene oxide for improved electrochemical CO₂ reduction. *Adv Energy Mater.* 2018;8(25):1801400.
85. Xie MS, Xia BY, Li Y, et al. Amino acid modified copper electrodes for the enhanced selective electroreduction of carbon dioxide towards hydrocarbons. *Energy Environ Sci.* 2016;9(5):1687–1695.
86. Ahn S, Klyukin K, Wakeham RJ, et al. Poly amide modified copper foam electrodes for enhanced electrochemical reduction of carbon dioxide. *ACS Catal.* 2018;8(5):4132–4142.
87. Wei X, Yin Z, Lyu K, et al. Highly selective reduction of CO₂ to C₂₊ hydrocarbons at copper/polyaniline interfaces. *ACS Catal.* 2020;10(7):4103–4111.
88. Chen X, Chen J, Alghoraibi NM, et al. Electrochemical CO₂ to ethylene conversion on polyamine incorporated Cu electrodes. *Nat Catal.* 2020;4(1):20–27.
89. Han Z, Kortlever R, Chen HY, Peters JC, Agapie T. CO₂ reduction selective for C₂₊ products on polycrystalline copper with N substituted pyridinium additives. *ACS Cent Sci.* 2017;3(8):853–859.
90. Ovalle VJ, Waegle MM. Understanding the impact of N arylpyridinium ions on the selectivity of CO₂ reduction at the Cu/electrolyte interface. *J Phys Chem C.* 2019;123(40):24453–24460.
91. Li F, Thevenon A, Rosas Hernández A, et al. Molecular tuning of CO₂ to ethylene conversion. *Nature.* 2020;577(7791):509–513.
92. Li F, Li YC, Wang Z, et al. Cooperative CO₂ to ethanol conversion via enriched intermediates at molecule metal catalyst interfaces. *Nat Catal.* 2019;3(1):75–82.
93. Fan L, Liu C Y, Zhu P, et al. Proton sponge promotion of electrochemical CO₂ reduction to multi carbon products. *Joule.* 2022;6(1):205–220.
94. Ma S, Sadakiyo M, Luo R, Heima M, Yamauchi M, Kenis PJA. One step electroreduction of ethylene and ethanol from CO₂ in an alkaline electrolyzer. *J Power Sources.* 2016;301:219–228.
95. Tan YC, Lee KB, Song H, Oh J. Modulating local CO₂ concentration as a general strategy for enhancing C–C coupling in CO₂ electroreduction. *Joule.* 2020;4(5):1104–1120.
96. Jeon HS, Timoshenko J, Rettenmaier C, et al. Selectivity control of Cu nanocrystals in a gas fed flow cell through CO₂ pulsed electroreduction. *J Am Chem Soc.* 2021;143(19):7578–7587.
97. Sun H, Chen L, Xiong L, et al. Promoting ethylene production over a wide potential window on Cu crystallites induced and stabilized via current shock and charge delocalization. *Nat Commun.* 2021;12(1):6823.
98. Lee SY, Jung H, Kim N K, Oh H S, Min BK, Hwang YJ. Mixed copper states in anodized Cu electrocatalyst for stable and selective ethylene production from CO₂ reduction. *J Am Chem Soc.* 2018;140(28):8681–8689.
99. Arán Ais RM, Scholten F, Kunze S, Rizo R, Roldan CB. The role of in situ generated morphological motifs and Cu(I) species in C₂₊ product selectivity during CO₂ pulsed electroreduction. *Nat Energy.* 2020;5(4):317–325.
100. Wu H, Li J, Qi K, et al. Improved electrochemical conversion of CO₂ to multicarbon products by using molecular doping. *Nat Commun.* 2021;12(1):7210.
101. Wang J, Yang H, Liu Q, et al. Fastening Br⁻ ions at copper molecule interface enables highly efficient electroreduction of CO₂ to ethanol. *ACS Energy Lett.* 2021;6(2):437–444.
102. Kim Y G, Javier A, Baricuatro JH, et al. Reprint of: surface reconstruction of pure Cu single crystal electrodes under CO reduction potentials in alkaline solutions: a study by serially ECSTM DEMS. *J Electrochem Soc.* 2017;793:113–118.
103. Thevenon A, Rosas Hernandez A, Peters JC, Agapie T. In situ nanostructuring and stabilization of polycrystalline copper by an organic salt additive promotes electrocatalytic CO₂ reduction to ethylene. *Angew Chem Int Ed.* 2019;58(47):16952–16958.
104. Zhang L, Wei Z, Thanneer S, et al. A polymer solution to prevent nanoclustering and improve the selectivity of metal nanoparticles for electrocatalytic CO₂ reduction. *Angew Chem Int Ed.* 2019;58(44):15834–15840.
105. Niu ZZ, Gao FY, Zhang XL, et al. Hierarchical copper with inherent hydrophobicity mitigates electrode flooding for high rate CO₂ electroreduction to multicarbon products. *J Am Chem Soc.* 2021;143(21):8011–8021.
106. Yao J, Huang W, Fang W, et al. Promoting electrocatalytic hydrogen evolution reaction and oxygen evolution reaction by fields: effects of electric field, magnetic field, strain, and light. *Small Methods.* 2020;4(10):2000494.
107. Yang B, Liu K, Li H, et al. Accelerating CO₂ electroreduction to multicarbon products via synergistic electric thermal field on copper nanoneedles. *J Am Chem Soc.* 2022;144(7):3039–3049.
108. Huang JE, Li F, Ozden A, et al. CO₂ electrolysis to multicarbon products in strong acid. *Science.* 2021;372(6546):1074–1078.
109. Monteiro MCO, Philips MF, Schouten KJP, Koper MTM. Efficiency and selectivity of CO₂ reduction to CO on gold gas diffusion electrodes in acidic media. *Nat Commun.* 2021;12(1):4943.
110. Bondue CJ, Graf M, Goyal A, Koper MTM. Suppression of hydrogen evolution in acidic electrolytes by electrochemical CO₂ reduction. *J Am Chem Soc.* 2021;143(1):279–285.

AUTHOR BIOGRAPHIES



Xianlong Zhou received his ME degree from Nankai University (China). Currently, he is a PhD candidate under the supervision of Assoc. Prof. Yao Zheng and Prof. Shi-Zhang Qiao at the School of Chemical Engineering and Advanced Materials of the

University of Adelaide. His research focuses on Cu-based catalyst design for electrochemical reduction of CO₂.



Yao Zheng received his PhD degree in 2014 from the University of Queensland (Australia). He is currently an Associate Professor at The University of Adelaide. His current research

focuses on fundamental studies of some key electrocatalysis processes by combining experiments and theoretical computations, and the development of advanced electrocatalysts for electrocatalytic refinery processes. He has published >120 papers with a total citation of 28,000 times (h index = 68) and 48 ESI highly cited papers.

How to cite this article: Zhou X, Liu H, Xia BY, Ostrikov K(K), Zheng Y, Qiao S-Z. Customizing the microenvironment of CO₂ electrocatalysis via three-phase interface engineering. *SmartMat*. 2022; 3:111-129. doi:10.1002/smm2.1109

Chapter 3 Molecular scalpel to chemically cleave metal-organic frameworks for induced phase transition

3.1 Introduction and Significance

Metal-organic frameworks (MOFs) comprised of metal nodes and organic linkers are a class of significant crystalline porous materials. MOFs present significant practical potential therefore for applications including gas separation, catalysis, chemical sensing and energy storage. Coupling between metal centres and ligands during the synthesis of MOFs must aligns with the qualitative hard and soft acids and bases (HSAB) theory. This means a hard acid prefers to coordinate with a hard base, and vice versa. Cu^{1+} has been widely investigated as CRR catalysts due to its high selectivity for C_2 products. It is a great challenge to prepare Cu(I)-MOFs as CRR catalysts because of the limit of HSAB theory.

In this chapter, there are two parts to introduce the synthesis of Cu(I)-MOFs as CRR catalysts through molecular cleavage of MOFs. In the first part, we describe the development of molecular cleavage of MOFs and also highlight their application of energy storage and conversion. In the second part, we present a molecular cleavage of Cu(II)-MOFs to synthesize Cu(I)-MOFs. The obtained MOFs can show a higher catalytic selectivity of C_2 products. The highlights of this work include:

1. New method. We conceive a top-down strategy to break the limitation of HSAB theory via the structure cleavage of MOFs, CuBDC (BDC = 1,4-benzenedicarboxylate), to trigger a phase transition by a 'molecular scalpel'.
2. New MOF. Controlled phase transition was achieved by a series of redox steps to regulate the chemical state and coordination number of Cu ions, resulting in the formation of a new MOF, Cu_2BDC .
3. Universality. We also prove this strategy can be extended to general Cu-based

MOFs and supra-molecules for nanoscopic casting of unique architectures from existing ones.

4. New catalytic structure. The improved C₂ product-selectivity on Cu₂BDC-derived sample belongs to Cu₂O (111) and Cu (111) mixed phases.

3.2 Molecular Cleavage of Metal-Organic Frameworks and Application to Energy Storage and Conversion.

This part is included as a journal paper by Xianlong Zhou, Huanyu Jin, Bao Yu Xia, Kenneth Davey, Yao Zheng, Shi-Zhang Qiao, Molecular Cleavage of Metal-Organic Frameworks and Application to Energy Storage and Conversion, *Advanced Materials* 2021, 33, 2104341.

3.3 Molecular Scalpel to Chemically Cleave Metal-Organic Frameworks for Induced Phase Transition.

This part is included as a journal paper by Xianlong Zhou, Juncai Dong, Yihan Zhu, Lingmei Liu, Yan Jiao, Huan Li, Yu Han, Kenneth Davey, Qiang Xu, Yao Zheng, Shi-Zhang Qiao, Molecular Scalpel to Chemically Cleave Metal-Organic Frameworks for Induced Phase Transition, *Journal of the American Chemical Society*, 2021, 143, 6681–6690.

Statement of Authorship

Title of Paper	Molecular Cleavage of Metal-Organic Frameworks and Application to Energy Storage and Conversion
Publication Status	<input checked="" type="checkbox"/> Published <input type="checkbox"/> Accepted for Publication <input type="checkbox"/> Submitted for Publication <input type="checkbox"/> Unpublished and Unsubmitted work written in manuscript style
Publication Details	Xianlong Zhou, Huanyu Jin, Bao Yu Xia, Kenneth Davey, Yao Zheng,* and Shi-Zhang Qiao*, Advanced Materials, 2022, 144, 2079–2084.

Principal Author

Name of Principal Author (Candidate)	Xianlong Zhou		
Contribution to the Paper	Proposed the review topic, reviewed and organised the literatures, and wrote the manuscript.		
Overall percentage (%)	85		
Certification:	This paper reports on original research I conducted during the period of my Higher Degree by Research candidature and is not subject to any obligations or contractual agreements with a † in its inclusion in this thesis. I am the primary author of this paper.		
Signature		Date	09/09/2022

Co-Author Contributions

By signing the Statement of Authorship, each author certifies that:

- i. the candidate's stated contribution to the publication is accurate (as detailed above);
- ii. permission is granted for the candidate to include the publication in the thesis; and
- iii. the sum of all co-author contributions is equal to 100% less the candidate's stated contribution.

Name of Co-Author	Huanyu Jin		
Contribution to the Paper	Revised the manuscript		
Signature		Date	09/09/2022

Name of Co-Author	Bao Yu Xia		
Contribution to the Paper	Revised the manuscript		
Signature		Date	09/09/2022

Name of Co-Author	Kenneth Davey		
Contribution to the Paper	Helped to edit the manuscript		
Signature	_____	Date	09/09/2022

Name of Co-Author	Yao Zheng		
Contribution to the Paper	Helped to revise the manuscript and organise the figures, and acted as the corresponding author		
Signature	_____	Date	09/09/2022

Name of Co-Author	Shi-Zhang Qiao		
Contribution to the Paper	Supervised development of work, helped in manuscript evaluation and acted as corresponding author		
Signature	_____	Date	09/09/2022

Please cut and paste additional co-author panels here as required.

Molecular Cleavage of Metal-Organic Frameworks and Application to Energy Storage and Conversion

Xianlong Zhou, Huanyu Jin, Bao Yu Xia, Kenneth Davey, Yao Zheng,* and Shi-Zhang Qiao*

The physicochemical properties of metal-organic frameworks (MOFs) significantly depend on composition, topology, and porosity, which can be tuned via synthesis. In addition to a classic direct synthesis, postsynthesis modulations of MOFs, including ion exchange, installation, and destruction, can significantly expand the application. Because of a limitation of the qualitative hard and soft acids and bases (HSAB) theory, posttreatment permits regulation of MOF structure by cleaving chemical bonds at the molecular level. Here, methods of coordination bond scission to tailor the structure are critically appraised and the application to energy storage and conversion is assessed. MOF structures synthesized by molecular-level coordination bond cleavage are described and the corresponding MOFs for electrocatalysis and renewable battery applications are evaluated. Significant emphasis is placed on various coordination bond cleavage to tune properties, including chemical groups, electronic structures, and morphologies. The review concludes with a critical perspective on practical application, together with challenges and future outlook for this emerging field.

1. Introduction

Metal-organic frameworks (MOFs) composed of metal nodes and organic linkers are a class of significant crystalline porous materials. Research interest has grown over the past two decades because of the tailorable structure, uniform porosity, and record-high surface area of MOFs.^[1] MOFs exhibit significant practical potential therefore for applications, including gas separation, catalysis, chemical sensing, and energy storage.^[2] The properties exhibited by MOFs depend on composition,

topology, and pore structure. This has led to research via various chemical approaches to control precisely chemical moieties within the structure of MOFs.^[3] However, the direct (bottom-up) synthesis of MOFs from metal ions and ligands is not always feasible due to factors, including limited reactant concentration, lack of solvent, improper reaction temperature, and undesired side reactions.^[4] Therefore, postsynthesis (top-down) methods are receiving increased research attention. This approach is seen as being flexible to modulate the structure of as-synthesized MOFs.^[5] For example, the synthesis of defects via missing clusters can regulate the pore volume of derived MOFs to boost CO₂ capture from flue gas.^[6] Additionally, missing linkers not only create vacancy sites in MOF-808 (Zr₆O₅(OH)₃(BTC)₂(HCOO)₅(H₂O)₂, BTC = 1,3,5-benzenetricarboxylate) and UiO-66 (University in Oslo, Zr₆O₄(OH)₄(BDC)₆, BDC = terephthalic acid) but introduce OH groups, which work as Brønsted bases to facilitate tertbutyl alcohol catalytic dehydration.^[7]

Weakening of the energy of metal-linker coordination bonds provides an opportunity to achieve postsynthesis of MOFs.^[8] Using simple thermal pyrolysis, derivatives such as transition-metal-based materials, single-atom catalysts, and carbon materials have been prepared for catalysis and energy-related applications.^[9] However, the structure of MOFs is destroyed during many of these treatments. As a result, MOFs serve only as precursors for the derivatives rather than the direct active materials in catalytic application.^[1] Here, we focus on postsynthesis methods involving selective chemical bond cleavage to tailor composites and create new MOF structures. This method is advantageous because the reticular chemistry structure of the parent is not destroyed.

Posttreatment of MOFs can be conveniently categorized as one of each of three distinct methods: 1) introduction of foreign metal ions or ligands into a pristine structure via exchange reactions;^[4] 2) solvent-assisted incorporation of linkers on vacant/labile sites into the structure;^[11] and 3) partial destruction to a new structure.^[12] Generally, for the first two, the insertion of linkers with desired functional groups is not always trivial because these groups coordinate to metal sites during synthesis, losing functionalities.^[13] The destruction of MOFs by cleavage of coordination bonds between metal and solvent molecules/linkers to precisely tune structures generates opening of metal sites, defects, hierarchical pores, or

X. Zhou, H. Jin, K. Davey, Y. Zheng, S.-Z. Qiao
School of Chemical Engineering and Advanced Materials
The University of Adelaide
Adelaide, SA 5005, Australia
E-mail: yao.zheng01@adelaide.edu.au; s.qiao@adelaide.edu.au

B. Y. Xia
Key Laboratory of Material Chemistry for Energy Conversion and Storage
(Ministry of Education)
Hubei Key Laboratory of Material Chemistry and Service Failure
Wuhan 430074, China

B. Y. Xia
National Laboratory for Optoelectronics
School of Chemistry and Chemical Engineering
Huazhong University of Science and Technology (HUST)
1037 Luoyu Road, Wuhan 430074, China

 The ORCID identification number(s) for the author(s) of this article can be found under <https://doi.org/10.1002/adma.202104341>.

DOI: 10.1002/adma.202104341

new morphologies. Because these methods involve controlled chemical bond cleavage at the molecular level, we use the term “molecular cleavage.” Although there are several reviews of postsynthetic MOFs,^[12,14] modification from the perspective of molecular cleavage has not been treated in any detail. Additionally, the electronic structure of metal sites is tuned following molecular cleavage and improves intrinsic activity for catalytic application.^[15]

In this timely review, we for the first time critically assess postsynthesis methods involving selective chemical bond cleavage to tailor composites and structures without destroying the reticular chemistry of the MOFs parent matrices. We summarize and evaluate methods of molecular-level coordination bonds between metal and solvent molecules/linkers for tailoring MOF structures, including: exposing Lewis acid sites by removal of coordination solvent molecules; building missing-linker defects by labile linker cleavage; creating hierarchical pores by directly etching MOFs or labile linkers; synthesizing 2D nanosheets by exfoliation layered MOFs; and constructing hollow architecture by selectively etching 3D MOFs. The mechanisms of coordination bond cleavage and details of MOF structural transition originating from composition change are presented. These engineered MOFs exhibit boosted activity and broad application to energy conversion and storage, including oxygen evolution reaction (OER), carbon dioxide reduction reaction (CRR), Li–sulfur battery, Li–metal battery, and aqueous zinc batteries. We assess examples of tailoring MOF electronic structures to accelerate electrocatalytic processes and exploit pores and open metal sites to regulate ion confinement and transport for boosted performance in reversible batteries. We conclude with a critical perspective on practical application and challenges and a future outlook for this important and developing field.

2. Molecular Cleavage to Regulate MOFs

As-synthesized MOFs can be prepared by bottom-up methods, including, conventional electric heating, electrochemistry, microwave heating, mechanochemistry, and ultrasonic method.^[3b] An advantage is selective control of the composition and growth direction of MOF crystals. It is not always practical however because of drawbacks including limited reactant concentration, lack of solvent, improper reaction temperature, and undesired side reactions. In contrast to bottom-up methods, top-down methods, including thermal, chemical, mechanical and photolytic stimulus, can destroy MOFs by cleaving coordination bonds between metal and solvent molecules/linkers.^[12] This results in the generation of open metal sites, defects, and hierarchical pores or new morphologies.

2.1. Open Metal Sites

In the synthesis of MOFs, metal atoms are weakly coordinated with solvent molecules such as DMF (dimethylformamide) or H₂O to decrease porosity. Given that the thermal stability of metal–solvent coordination bonds is generally lower than that

for metal–linker bonds, a physical or chemical stimulus can remove solvent molecules. The resultant unsaturated Lewis acid sites in MOFs can therefore be exploited with alternative properties.^[16] Kaskel et al. reported that uncoordinated Cu sites in [Cu₃(BTC)₂(H₂O)₃] (HKUST-1) are created by the removal of coordinated H₂O molecules at 120 °C in a vacuum.^[17] If particular high boiling-point solvents are used to synthesize pristine MOFs, a more significant temperature, or a longer treatment time is required to remove solvent molecules because of the more stable metal–solvent coordination bonds. However, this change of temperature or treatment time can lead to a collapse of MOFs. To address this, Yaghi et al. applied a solvent-exchange reaction to remove solvent molecules of MOF-505 ([Cu₂(bptc)(H₂O)₂(DMF)₃(H₂O)], bptc = 3,3',5,5'-biphenyletracarboxylic acid) at mild-condition. Low boiling-point acetone replaced high boiling-point DMF in as-synthesized MOF-505. An intermediate temperature (e.g., 120 °C) activation step removes coordinated acetone, which results in the opening of metal sites.^[18]

To obviate what is a time-consuming step, Maspoch et al. used a single-step cleavage of solvent molecules via a photo-thermal effect. When irradiated with high-intensity ultraviolet and visible (UV–vis) light, HKUST-1 is rapidly heated to a high temperature of >120 °C. This localized heat facilitates the removal of trapped and coordinated DMF from HKUST-1 to promote the generation of open metal sites in a (record) short time of 30 min.^[19] These authors demonstrated this method is suitable for additional MOFs, including ZIF-67 (Co(mim)₂, mim = 2-methylimidazole), MOF-74 ([Zn₂(DHBC)(DMF)₂·(H₂O)₂), UiO-66–NH₂ ([Zr₆O₄(OH)₄(NH₂-BDC)₆], NH₂-BDC = 2-aminoterephthalic acid) and Fe–MIL-101–NH₂ ([Fe₃O(H₂O)₂F·(NH₂-BDC)₂]·14.5H₂O).

Jeong et al. optimized the solvent-exchange method without introducing external thermal energy. Methylene chloride (CH₂Cl₂) was applied to activate HKUST-1. They proposed a mechanism for this chemical activation via Raman spectroscopy (Figure 1a).^[20] CH₂Cl₂ replaces the chemisorbed H₂O to coordinate Cu²⁺ center via a Cl-bridge, which is concomitantly de-coordinated from the frameworks when deposited in a vacuum for 120 min. Trichloromethane (CHCl₃) was reported to have weaker coordination bonds than CH₂Cl₂. Therefore, this lower bonding decreases activation time to 30 min when the reduced external thermal energy of 55 °C and 2.6 meV is supplied.^[21] This modified method can therefore be applied practically to particular thermal-sensitive MOF-polymer composites without destroying structural integrity.

2.2. Defect Engineering

In contrast to removing coordinated solvent molecules without destroying reticular chemistry structure, breaking metal-linker coordination bonds creates missing and/or dislocated atoms/linkers. This change in structure can increase catalytic sites and/or introduce new functional properties into MOFs.^[14b] Through tailored cleavage of metal-linker bonds, researchers have synthesized various types of defects, including missing linkers and missing clusters.

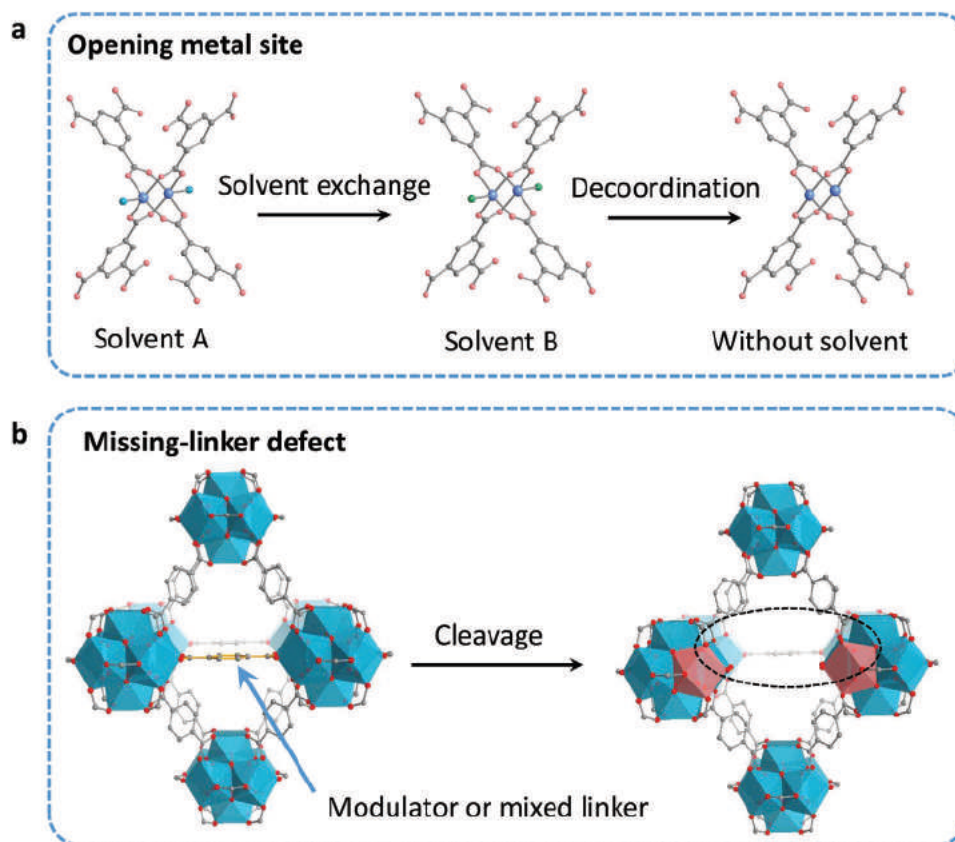


Figure 1. Schematic of a) chemical activation to yield open metal sites; b) missing-linker defects through cleavage of modulators or mixed linkers.

2.2.1. Missing-Linker Defects

De Vos et al. employed trifluoroacetic acid (TFA) to substitute a part of BDC during the synthesis of UiO-66(Zr).^[22] Because of the lower stability of coordination bonds between Zr and TFA, the trifluoroacetic groups are readily removed at 320 °C. This temperature is less than that typical for a deconstruction of UiO-66(Zr), and forms defects in postsynthetic UiO-66(Zr). Zhou et al. identified the defect type via high-resolution neutron powder diffraction.^[23] Refined results of linker occupancies revealed that about 1 in 12 linkers was missing in the pristine UiO-66 matrix. Acetic acid was used as a modulator to tune the linker vacancies by varying synthesis conditions systematically. The optimal sample showed significantly increased pore volume and surface area because of missing linkers.

Missing linkers and clusters in the treatment of MOFs can occur concomitantly, leading to difficulty in ruling out any structure-activity relationship from defects. To address this, De Vos et al. modified this method by applying a thermolabile linker, trans-1,4-cyclohexane-dicarboxylate (CBC), to replace BDC (Figure 1b).^[24] Because of the similarity between CBC and BDC in geometry, length, and steric bulk, CBC in UiO-66(Zr) is readily embedded during synthesis. Because of its distinct thermal stability (275 °C vs 450 °C in air, respectively), UiO-66(Zr) with a greater concentration of defects of ≈ 4.3 in 12 linkers is obtained in cleaving CBC from UiO-66(Zr). An identical specific surface area following missing linkers

underscores that the high porosity in defected UiO-66(Zr) arises from missing clusters rather than missing linkers.

Theoretical computation shows that the maximum number of defects in UiO-66 is 6.0 missing linkers per cluster. A greater concentration of defects destroys the MOF network.^[25] To achieve this number Voort et al. employed 4-sulfonatobenzoate (PSBA) as a hemilabile linker to replace parts of BDC in synthesizing hemilabile UiO-66.^[26] Because the coordination strength of sulfonates to Zr_6 clusters is weaker than that for carboxyl groups, the coordination bonds between sulfonate and Zr are more readily broken to remove PSBA from the hemilabile UiO-66 framework. Additionally, some sulfonates in the remaining PSBA linkers are protonated to form free-dangling linkers. These work as a coligand to boost the stability of the defective framework by hydrogen bonding with optimal distance. The number of defects, therefore, reaches 6.0 missing BDC linkers per cluster. In some cases, the missing linker causes the collapse of MOFs. Consequently, it is essential to control precisely the number of missing linkers.

Wang et al. applied an H₂O-etching method to construct HKUST-1 with three-coordinated Cu, which can boost the structural stability of the product.^[27] Based on the thermodynamic and kinetic conditions that arise during the catalytic reaction, theoretical computations showed that three-coordinated Cu-carboxylic species possess greater structural robustness than that of one-, two- and four-coordinated counterparts. There is also a smaller gap between the highest occupied molecular orbital, and the lowest unoccupied molecular orbital, compared with

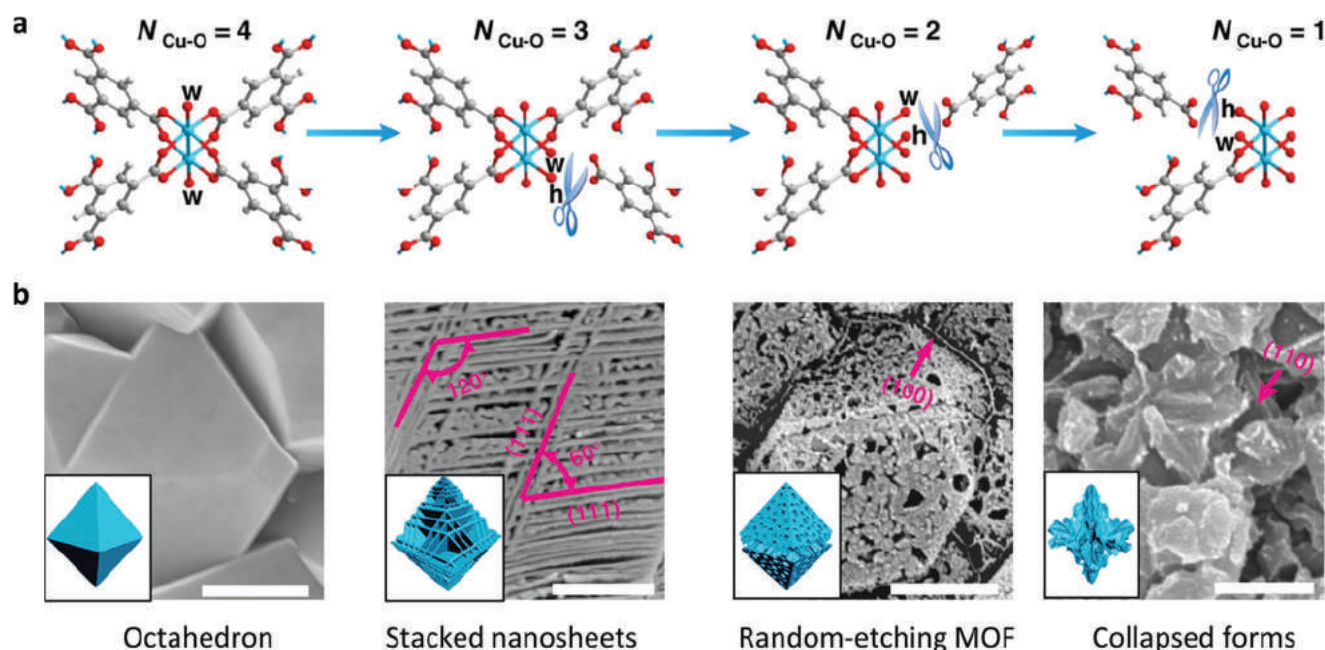


Figure 2. a) Schematic of etching transition of four-coordinated Cu atoms in HKUST-1 to three-, two- and one-coordinated Cu atoms with organic ligands and corresponding morphologies. b) Real morphologies of the four MOF crystal states following cleavage. Scale bars represent 500 nm for the octahedron, stacked nanosheets, and collapsed forms, 200 nm for random-etching MOF. Reproduced with permission.^[27] Copyright 2019, Nature Publishing Group.

others. This suggested it works as active sites to coordinate soft bases. Through control of etching time, the carboxylic groups of four-coordinated Cu sites are successively replaced by water molecules (Figure 2a). The initial octahedron morphology of HKUST-1 is gradually transferred to stacked 2D nanosheets, random-etching MOF, and collapsed derivatives (Figure 2b). The mechanism for this cleavage is surface energy-driven, ordered cleaving. Because of lower surface energy, the cleavage favors the (111) plane, thereby forming stacked 2D nanosheets. When external stress is applied to one side of the triangle, the other two sides act as counteracting stresses to ensure deformation of the nanosheets under external stress is minimized. This three-coordinated Cu-carboxylic species in stacked 2D nanosheets, therefore, has greater stability than that of the octahedron, random-etching MOF, and collapsed derivatives.

2.2.2. Missing-Cluster Defects

During the synthesis of UiO-66 when the applied modulator or linker is inhomogeneously mixed, the type of defects are transferred from the missing linker into the missing cluster. Because the 2-amino-1,4-benzenedicarboxylate (BDC-NH₂) is readily removed under a low-temperature thermal treatment, Zhou et al. used it as a thermolabile linker to replace a part of BDC. In this way, they investigated the relationship between distribution conditions of mixed linkers and the type of defects through the cleavage of labile linkers.^[28] In principle, when two linkers are mixed to synthesize multivariate MOFs, the labile one is nondominant and is considered disperse in a matrix formed by the dominant. Based on the size of domain linkers, four types of multivariate MOFs can be categorized.

Inhomogeneous mixing of linkers produces large and small domains, while a well-mixed distribution of linkers produces random and ordered domain-free models (Figure 3). Following cleavage of thermolabile linkers, the large and small domains result as missing-cluster defects with mesopores, while the random and ordered models result as missing-linker defects without the formation of mesopores.

Goodwin et al. reported missing-cluster defects through a synthesis of correlated nanoregions of a *reo* topology.^[29] In this work, formic acid as a modulator promoted the formation of a defective *reo* phase in which the linker connectivity decreased to 8. This compares with 12 in pristine UiO-66. Additionally, the coherence length and volume fraction of defect nanoregions can be tuned by controlling the relative concentration of the modulator and linker components. Lillerud et al. reported that missing-cluster defects are the primary defects in UiO-66 based on experimental nitrogen adsorption isotherms and simulations.^[25] These researchers systematically investigated four monocarboxylic acids (trifluoroacetic, difluoroacetic, acetic, and formic) as modulators to synthesize defects in UiO-66. They found that the defect concentration depends on acidity (pKa) and/or the concentration of monocarboxylic acid. For example, when trifluoroacetic acid was applied, it had the lowest pKa value among all monocarboxylic acids. Therefore, there are more deprotonated trifluoroacetic molecules compared to deprotonated linker molecules in a synthesis solution. Trifluoroacetic acid dominates the competition for carboxylate sites in Zr₆(OH)₄O₄(CO₂)₁₂ clusters to yield a significantly high concentration of missing-cluster defects in treated samples. On the contrary, acetic acid with the greatest pKa value results in the lowest deprotonated modulator molecule, thereby yielding UiO-66 with the lowest concentration of defects.

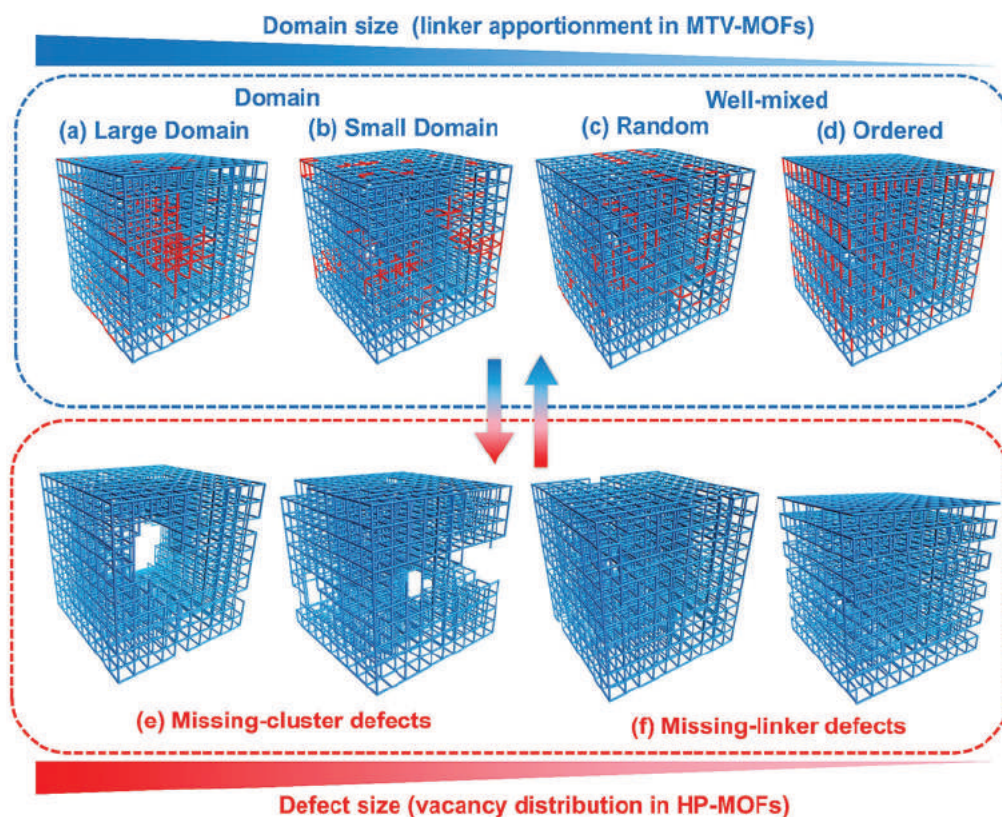


Figure 3. Schematic of four types of MOFs with different domain sizes: large, small, random, and ordered distribution and resultant MOFs with missing-cluster as well as missing-linker defects. Missing-cluster defects in hierarchically porous MOFs origin from linker domain model in MOFs following removal of labile linkers inside frameworks. Missing-linker defects in hierarchically porous origin from linker well-mixed model in MOFs following removal of labile linkers inside frameworks. Reproduced with permission.^[28] Copyright 2018, American Chemical Society.

Additionally, changes in the chemical state of the metal can generate missing clusters in MOFs. Jeong et al. reported an HKUST-1 with Cu vacancies via partially reducing Cu^{2+} ions to Cu^{1+} .^[30] The coordination of hydroquinone with Cu^{2+} ions results in a "single" electron transfer from hydroquinone to Cu^{2+} . This reaction triggers a reduction of Cu^{2+} ($\approx 30\%$) to Cu^{1+} within the framework. The proton from hydroquinone subsequently causes the protonation of carboxylate, which leads to the dissociation of half Cu^{1+} species from the framework and the formation of metal vacancies. As a result, an oxygen-rich negatively charged coordination environment is created, with the remaining Cu nodes having a high coordination strength. The defective HKUST-1, therefore, exhibits significant hydrolytic stability following exposure to humid air for two years.

2.2.3. Phase Transition

Compared with disordered defects, ordered ones are more readily investigated for a relationship between structure and activity. However, it remains practically challenging to synthesize MOFs with ordered defects because of difficulties in precisely controlling defects to be at specific locations. Li et al. employed a phase transition method to address this in which a single-crystal to the single-crystal transition of $\text{Zn}_4\text{O}(\text{PyC})_3$ ($\text{PyC} = 4\text{-pyrazolecarboxylate}$) promoted the generation of

ordered defects and linker vacancies in derived MOF.^[31] As is shown schematically in Figure 4a, initially a quarter of Zn^{2+} and a half of PyC linker are removed from Zn-MOF by water immersion. Zn^{2+} ions around the missing PyC are saturated by H_2O molecules to yield Structure 1. Following the filling of these vacancies with new metals and linkers, a new single-crystalline structure, Structure 2, with ordered multicomponent results. Importantly, this method is different from conventional ion exchange for at least two reasons: 1) there is precise control of linker and metal sites, and 2) the new, complex MOF cannot be made using more conventional methods.

We recently reported a molecular scalpel to chemically cleave CuBDC with controlled phase transition.^[32] This method breaks the classic hard and soft acids and bases (HSAB) theory to synthesize a new Cu_2BDC MOF composed of a soft acid (Cu^{1+}) and a hard base (BDC). High-resolution transmission electron microscopy (HRTEM) image confirmed that Cu_2BDC nanocrystals are highly crystalline (Figure 4b) in which CuO_x polyhedral sheets are bridged by BDC linkers. L-ascorbic acid as a chemical scalpel triggers four redox steps for the regulation of the chemical state and coordination number of Cu ions (Figure 4c) namely: 1) bulk $\text{CuBDC}\cdot 2\text{H}_2\text{O}$ is chemically exfoliated into nanosheets via breaking of partial H-bonds; 2) Cu^{2+} ions in $\text{CuBDC}\cdot 2\text{H}_2\text{O}$ sheet are chemically reduced to Cu^{1+} (the consequent lowered coordination number yields a transition sample of $\text{Cu}_2\text{BDC}\cdot \text{H}_2\text{O}$ and cleaved H_2BDC);

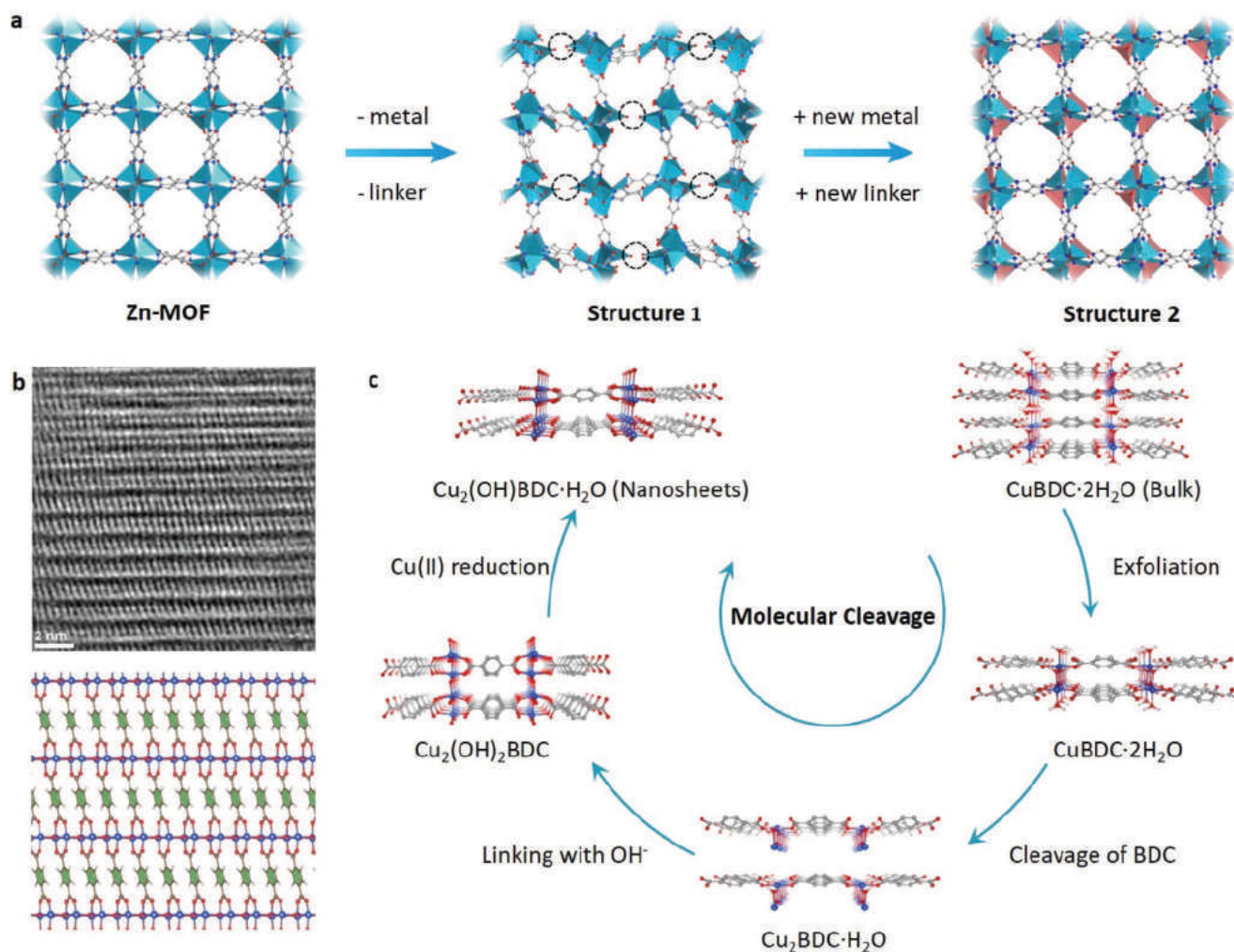


Figure 4. a) Schematic of one-fourth of Zn^{2+} and a half of PyC of Zn-MOF are removed to create a MOF with ordered metal and linker vacancies (Structure 1). Following the incorporation of new metals and linkers, a new Zn/Co-MOF results (Structure 2). Reproduced with permission.^[31] Copyright 2014, American Chemical Society. b) Proposed structural model for Cu_2BDC projected along the [010] projection and its HRTEM image. c) Reaction processes of four-step molecular cleaving. Reproduced with permission.^[32] Copyright 2021, American Chemical Society.

3) dehydrogenated LA ($\text{C}_6\text{H}_6\text{O}_6$) oxidizes Cu^+ into Cu^{2+} forming OH groups, which bridge two $\text{Cu}_2\text{BDC}\cdot\text{H}_2\text{O}$ molecules (this results in a $\text{Cu}_2(\text{OH})_2\text{BDC}$ structure with compression of the metal oxide interlayer spacing); 4) with additional LA half of the Cu^{2+} ions in $\text{Cu}_2(\text{OH})_2\text{BDC}$ are reduced to Cu^+ and half of the OH bridges are removed to yield final $\text{Cu}_2(\text{OH})\text{BDC}\cdot\text{H}_2\text{O}$ as the product.

2.3. Pore Structure Engineering

Removal of metal ions or linkers can create defects by breaking metal-linker coordination bonds in MOFs. If the linker size or the cleaving area increases, it generates hierarchical pores. These benefit diffusion of large molecules and enzyme immobilization.^[1] There are two methods to build hierarchical pores in MOFs without deconstructing crystal structures, namely, 1) indiscriminative and 2) discriminative, cleavage.^[33]

2.3.1. Indiscriminative Cleavage

Because of low chemical and thermal stability, metal-linker coordination bonds can be readily broken by H_2O /acid etching and thermolysis without destroying the network.

Kim et al. synthesized mesoporous yttrium MOF ($[\{\text{Y}_4(\text{H}_2\text{O})_3\}(\text{hmtt})_8](\text{OH})_6(\text{NO}_3)_6\cdot 70\text{ DMF}\cdot 67\text{ H}_2\text{O}$, hmtt = methyl-substituted truxene tricarboxylic acid, POST-66(Y), via H_2O etching to partially replace metal ions and ligands.^[34] In this, H_2O molecules replace parts of linkers and bind with metal ions. Because the size of an H_2O molecule is smaller than that of the linker, mesoporous POST-66(Y) MOF is generated following etching. By controlling the reaction temperature and time, the ratio of micropores to mesopores can be finely tuned without destroying structural integrity. Sun et al. synthesized a hierarchical porous HKUST-1 using Cu redox species as intermediates.^[35] A change in chemical valence leads to a change of coordination number of Cu ions, resulting in the breaking of metal-linker coordination bonds. Methanol vapor

was applied to reduce a part of Cu^{2+} to Cu^{+} . The Cu coordination number decreased from 6 (or 5) to 4 (2) during which part of the linkers in HKUST-1 is cleaved and removed, thereby generating hierarchical pores.

Although chemical etchings can be used to tune the MOF structure and morphology, pore size following destruction is uncontrollable. A result is that it is difficult to tune the porosity of hierarchical MOFs finely. Kim et al. applied phosphoric acid as an etching agent to selectively break the metal-linker coordination bonds of MIL-100(Fe) ($[\text{Fe}_3\text{O}(\text{X})(\text{H}_2\text{O})_2(\text{BTC})_2] \cdot n\text{H}_2\text{O}$, X = OH, F).^[36] Because the appropriate size of phosphoric acid (0.61 nm) is less than the cage size of MIL-100(Fe) (0.49 to 0.89 nm), it means the latter acts as an acid diffusion access in which phosphoric acid selectively passes through the cages during treatment. The inherent crystallinity and external morphology of formed MIL-100(Fe) can therefore be maintained. Because the ratio of mesopores to micropores in these two methods is low, 1.80 for H_2O and 1.11 for H_3PO_4 etching, Kim et al. applied a chemical etching induced decarboxylation to improve the ratio of mesopores to micropores in HKUST-1.^[37] Ag(III)/Ag(I) worked as a redox pair to reduce $\text{K}_2\text{S}_2\text{O}_8$ to sulfate ion (SO_4^{2-}) in which the process linker is cleaved into CO_2 and

a benzene ring. Resultant SO_4^{2-} replaces carboxylic group coordinating to original Cu^{2+} ions and consequently forms Cu-sulfate complex. Mesopores and macropores then result, while the micropores in HKUST-1 are preserved. The ratio of mesopores to micropores increases to 3.88. Significantly, this method can be extended to other MOFs, including MIL-53(Al) $[\text{Al}(\text{OH})(\text{BDC})(\text{H}_2\text{O})]$ and MIL-100(Al).

In addition to linker oxidative decomposition, thermolysis can induce decarboxylation for the linkers. Huang et al. utilized a thermal method to obtain hierarchical porosity via decarboxylation on MIL-121 in which the surface area of targeted MOF highly increased from 13 to $908 \text{ m}^2 \text{ g}^{-1}$.^[38] As is shown in Figure 5a, free carboxylate groups on the benzene ring undergo condensation with the formation of anhydride groups at 380°C . With the temperature rising to 410°C , all carboxylate groups undergo decarboxylation, which leads to parts of linkers clipping from the adjacent metal clusters. This results in five-coordinated AlO_5 clusters with open metal sites. At 440°C , another linker is cleaved from the AlO_5 clusters with the formation of AlO_4 units. With the removal of some aluminum, the mesopore size and volume further increase and construct hierarchical pores. Although indiscriminate cleavage can create a

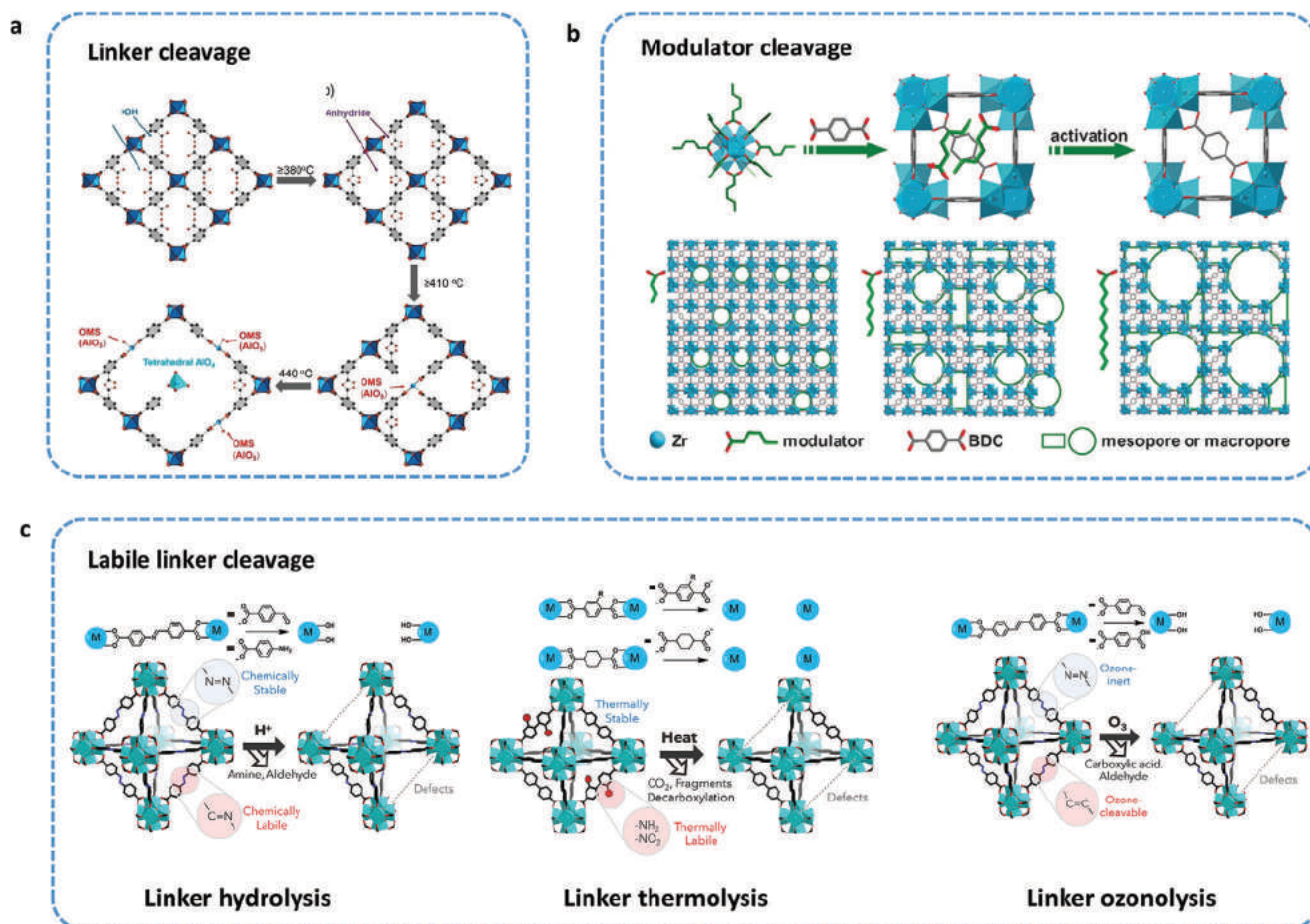


Figure 5. Schematic of a) proposed linker decarboxylation in MIL-121. Reproduced with permission.^[38] Copyright 2019 American Chemical Society; b) synthesis of hierarchically porous MOFs with adjustable porosity using UiO-66 and modulators with various lengths. Reproduced with permission.^[39] Copyright 2017, Wiley-VCH; c) removal of labile linkers in mixed-linker Zr-MOFs through different routes: hydrolysis; thermolysis; ozonolysis. Reproduced with permission.^[40] Copyright 2020, Elsevier Inc.

hierarchical pore structure, it is practically difficult to tune the pore size precisely because of the breakage of chemical bonds with non-selectivity.

2.3.2. Discriminative Cleavage

Cai and Jiang applied a modulator-induced defect method to synthesize hierarchical pores in UiO-66 by controlling the size of the modulator.^[39] A correct amount of BDC linker together with the presence of suitable modulators are the two prerequisites for the formation of hierarchical pores. As is shown in Figure 5b, modulators with diverse alkyl chains are initially used to synthesize parent UiO-66. When the modulator is an elongated alkyl chain, it could occupy a large space and cause steric hindrance that blocks the coordination between Zr⁴⁺ and BDC around the modulator. Following activation, modulators can be removed from the framework, in which mesopores and macropores form. Tuning the alkyl chain length in monocarboxylic acids from 2 to 12 carbon atoms systematically regulates pore size from about 3 to 8.6 nm.

One of the practical difficulties in discriminative cleavage is to distribute modulators uniformly. This arises because of the difference in chemical properties between the modulators and the linkers. Linker labilization provides a means to address this because the structure of specific linkers is similar to that of the primary linker. There are three methods used to cleave labile linkers, 1) hydrolysis, 2) thermolysis, and 3) ozonolysis (Figure 5c).^[40] An imine-based linker was installed into Zr-MOFs through an exchange reaction. These imine groups in the labile linker (4-carboxybenzylidene-4-aminobenzoate) readily dissociate into 4-formylbenzoic acid and 4-amino benzoic acid fragments in a single hydrolysis reaction.^[41] Following cleaving of these fragments via acetic acid treatment, defective Zr-MOF is produced. The pore size can be tuned to within the range of 1.5 to 18 nm by controlling the ratio of the labile linker to acetic acid. To obviate any additional procedures to eliminate linker fragments formed during the acid treatment, Zhou et al. investigated the direct elimination of labile linker by thermolysis.^[28] BDC-NH₂ was employed as a labile linker during the synthesis of UiO-66. Following heating at a temperature of 300 °C, the linker, with poor thermal stability, was cleaved whereas the crystallinity of the MOF remained.^[28]

Maspoch et al. used a solid-gas phase reaction to cleave unstable linkers at room temperature with high selectivity.^[42] During the synthesis of pristine UiO-66(Zr), the linker with olefin bonds was used. These were selectively broken into fragments following the reaction with ozone. Because the length of the unstable linker is about 13.3 Å, cleavage results in a structural transformation from micropores to mesopores. Additionally, this cleavage precisely controls the concentration of defects by tuning the ratio of special ligands during synthesis. The resultant mesopores work as sites for installing other metals for synergistic catalysis. For example, Lin et al. used ozone to cleave olefin ligands of DUT-5 (DUT = Dresden University of Technology), which consists of Al³⁺, 2,2'-bipyridine-5,5' dicarboxylate, and 1,4-benzenediacrylate, to generate Al₂(OH)(OH₂) sites for installing homogeneous Lewis acidic centers, e.g., trimethylsilyl triflate.^[43] Consequently, the incorporated groups

played a synergistic role with in situ reductions metallic Pd produced for conversion of renewable biomass to hydrocarbon feedstocks.

2.4. Morphological Regulation

In addition to creating hierarchical pores, the cleavage of chemical bonds regulates morphological change, e.g., the synthesis of 2D nanosheets, and hollow architecture for exposing increased numbers of active sites for catalysis.^[44] The two main molecular cleavage methods to tune the morphology of MOFs are exfoliation and etching.

2.4.1. 2D Nanosheets

Because of the unique physical and chemical properties, 2D MOFs are attractive for applications in gas-sieving membranes and heterogeneous electrocatalysts. Yang et al. reported the exfoliation of poly[Zn₂(benzimidazole)₄] (Zn₂(bim)₄) MOF via a soft-physical route that yielded a 2D ultrathin sheet with a uniform thickness of 1.12 nm.^[45] These researchers utilized low speed (60 rpm) ball milling followed by exfoliation in a volatile solvent with ultrasonication to break van der Waals interaction between interlayers. However, this facile method is suitable only for MOFs with weak layered interactions.

Zhou et al. used an intercalation and chemical cleaving method to produce 2D ultrathin MOFs. They intercalated a labile dipyriddy ligand, 4,4'-dipyriddy disulfide (DPDS), into a 2D layered Zn₂(PdTCPP) (TCPP = 4-(phenyldithio)pyridine) MOF (Figure 6a).^[46] The disulfide bonds in the linker were selectively broken, forming 2D ultrathin nanosheets with a uniform thickness of ≈1 nm under a high-yield (≈57%) exfoliation. In addition to breaking the van der Waals interaction or labile dipyriddy ligand, the cleavage of strong metal–ligand bonds of 3D MOFs synthesized 2D layered MOF nanosheets. Grey et al. used a ligand-deficient layered UiO-67 ([Hf₆O₄(OH)₄](BDC)₆, BPDC = biphenyl-4,4'-dicarboxylate) to synthesize 2D hexagonal lattice (hxl) nanosheets by cleaving metal-carboxylate bonds between metal oxide layers.^[47] They used a high-concentration formic acid to form a ligand-deficiency UiO-67(Hf) with a double cluster (Hf₁₂O₈(OH)₁₄). They reported two routes to break the metal-carboxylate bonds. 1) As-synthesized UiO-67(Hf) was left under ambient conditions for one week to obtain a complete transition to hxl UiO-67(Hf) following missing linkers along the [110] direction. The resultant, stacked UiO-67(Hf) sheets are delaminated into 2D nanosheets under grinding or sonication–exfoliation. 2) Parent UiO-67(Hf) was directly delaminated into 2D nanosheets under grinding, or sonication–exfoliation, through missing the linkers between different metal oxide layers. The as-synthesized 2D UiO-67(Hf) nanosheets were ≈11 nm thick. This corresponded to some four-unit cells of hxl UiO-67(Hf) lattice.

In addition to these mechanical and chemical methods, an electrochemical method can be applied to cleave linkers.^[48] For example, a 2,3-dihydroxy-1,4-benzenedicarboxylic acid (H₄dhbdc) was used as a labile linker in the synthesis of parent Co-MOF, (H₃O)₂[Co₆O(dhbdc)₂(H₂dhbdc)₂(EtOH)₄]·2 EtOH.

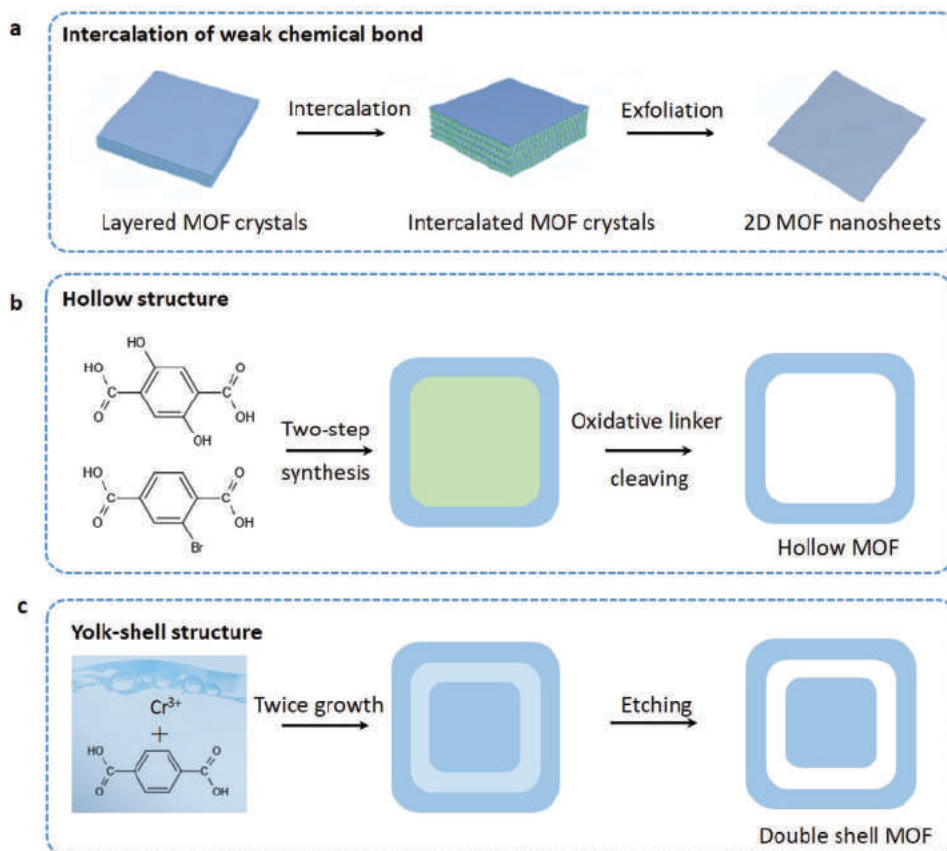


Figure 6. Schematic of a) a process developed to generate 2D MOF nanosheets by intercalation and chemical exfoliation; b) preparation of hollow MOFs by oxidative linker cleaving; c) synthesis of yolk-shell MOFs by acid etching.

This is because this linker can be oxidized into cyclopenta-2,4-dienone under applied potential. Compared to the original linker with electron-donating hydroxy groups, the oxidation products own electron-withdrawing carbonyl groups and a flexural bridging angle. These two features reduce the coordination ability of the oxidized linkers, making them be readily dissociated from bulk to form 2D nanosheets.

2.4.2. Hollow Architectures

Recently, hollow architectures with high active sites and low diffusion distances have received increased attention. Via exploiting distinct chemical composition in exposed crystallographic planes, Maspoeh et al. devised a wet-chemical method to anisotropically etch ZIF-8 ($\text{Zn}(\text{mim})_2$, mim = 2-methylimidazole) and ZIF-67 to engineer morphologies, without losing porosity.^[49] This chemical etching relies on an acid-based reaction and a metal ion sequestration to break the metal-linker coordination bonds. Xylenol orange (XO), a weak acid, was used as a chelating agent to generate a water-soluble metal-XO complex and induce missing linkers. The complex prevents resultant metal from coordinating with the linker in the solution and consequently, etches ZIF-8 and ZIF-67. Two reasons are hypothesized for the morphological change during this posttreatment, namely: 1) etching preferentially carves the

external crystal surfaces with greater density of metal-linker coordination bonds—which results in cubes forming from the parent ZIF-8 and ZIF-67 dodecahedra, and 2) pH of the tuning etchant solution optimizes etching rate in a single direction, in which the starting rhombic dodecahedra are morphed into tetrahedrons, or hollow boxes. This morphological evolution improves surface-area-to-volume ratios of ZIF-8 and ZIF-67 to be advantageous for application to heterogeneous catalysis.

Additionally, linkers with different chemical properties can be used to synthesize hollow MOFs. Tsung et al. used an oxidative linker cleaving to synthesize hollow structures (Figure 6b).^[50] They applied a two-step method to prepare a core-shell UiO-66-(OH)₂@UiO-66 with 2,5-dihydroxyterephthalic acid as a sacrificial linker. Following etching, the core UiO-66-(OH)₂ is removed either from shell to core, or from core to shell. When redox-active Pd nanoparticles are pre-embedded in the UiO-66 the oxidative linker etching is initiated and localized. The Pd nanoparticles are confined in the single crystalline UiO-66 particle, forming a multiyolk-shell structure. This design protects Pd from agglomeration and affords size-selective catalysis.

In comparison with this single-shelled hollow architecture, a multishelled structure exhibits new and improved functions and properties. The practical difficulty is to remove the intermediate layer in the multilayer nanoparticles. Huo et al. reported a method to prepare multishelled hollow MIL-101 to significantly boost catalytic activity for styrene oxidation (Figure 6c).^[51]

Inhomogeneous MIL-101 crystals provide possibilities for practical synthesis of hollow structure because its shell is more stable than the inner core. Consequently, the inner core can be selectively etched by acid. In this work, growth-etching was repeated two- or three times using MIL-101 crystals as a template. By varying the initial concentration of reactants, the multilayer MIL-101 crystals with different sizes of 120, 200, and 300 nm can be synthesized. Following etching of these particles by acetic acid for 4 h, multishelled hollow MIL-101 with cavity sizes of 70, 110, and 140 nm was obtained, with corresponding shell thickness 25, 45, and 80 nm. Due to these structural advantages, these multi-shelled hollow structures provide increased active sites in each layer to boost the catalytic performance of styrene oxidation. To address the limitation of MOF micronized pores and narrow channels, Liu et al. synthesized a hollow mesoporous MOF with a macroporous core and mesoporous shell to accelerate the diffusion of reactants.^[52] They chose solid Cr and Al-bimetallic MIL-101 as a precursor. The less stable core and Al uniform distribution in the shell were readily removed following selective etching. The resultant hollow mesoporous MOF as a Pd nanoparticles carrier significantly boosted mass diffusion within the framework to facilitate benzyl alcohol oxidation reaction.

3. Application of Cleaved MOFs to Energy Technologies

3.1. Electrocatalysis

Electrocatalytic refinery is an emerging method to obtain fuel and chemical products from fossil fuels to renewable energy sources.^[53] A critical step in practically realizing this method is the need to develop suitable electrocatalysts with high activity and selectivity for targeted chemical conversions. There are three main steps in typical heterogeneous electrocatalysis:

1) chemical adsorption of the reactant on the electrocatalyst surface; 2) transformation from reactant to product, through a series of intermediates, and; 3) desorption of product from active sites.^[54] Generally, the adsorption energy of intermediates determines the corresponding reaction activities. This is because the adsorption interaction of intermediates on active sites should neither be too weak nor too strong. If this adsorption interaction is too weak, the reactant is difficult to adsorb, thereby limiting the following reactions. If the adsorption interaction is too strong, however, it will hinder the removal of products.^[55] The tuning of intrinsic activities of electrocatalysts can be achieved by adjusting the adsorption energy of intermediates on active sites.

Compared with nanomaterials, MOFs have become a platform to develop advanced electrocatalysts because of unique structural features, including the highly ordered structure and tunable metal nodes/linkers as active sites.^[56] Additionally, MOFs have inherently high porosity. This allows high accessibility of interior active species and promotes kinetics of electrocatalysis that benefit from the open channel, spatial confinement, and host-guest interactions of the pores.^[57] Through molecular cleavage, the size/shape of pores and metal sites coordination environment, MOFs accelerate electrocatalysis (Figure 7).^[1] This includes synthesizing coordinatively unsaturated sites as catalytic centers, strain engineering to change the electronic structure of metal sites, regulation of the coordinative environment, and optimizing coordination number of catalysts to accelerate the generation of reaction intermediates for OER and CRR.

3.1.1. Oxygen Evolution Reaction (OER)

OER is the anodic reaction in a water electrolysis cell to generate pure oxygen. Tang et al. reported ultrathin NiCo-BDC nanosheets (≈ 3.1 nm) with an abundance of unsaturated metal

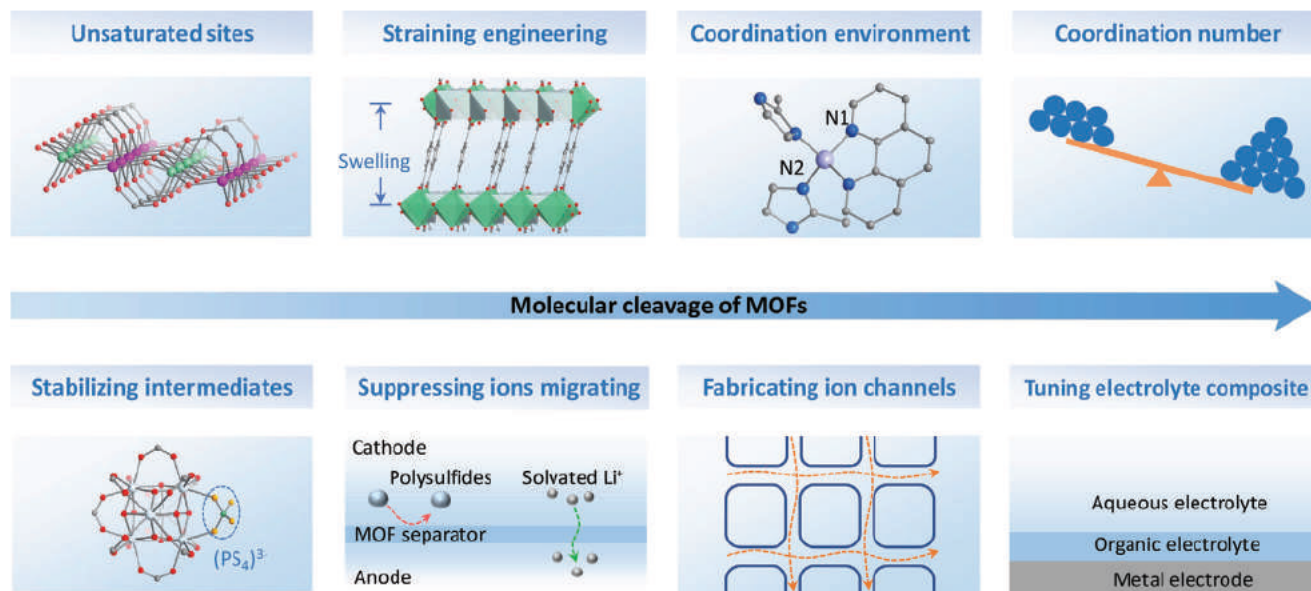


Figure 7. Structural designs in cleaved MOFs to tune electronic structure of electrocatalysts, and ions confinement and transport in electrode and electrolyte for reversible batteries.

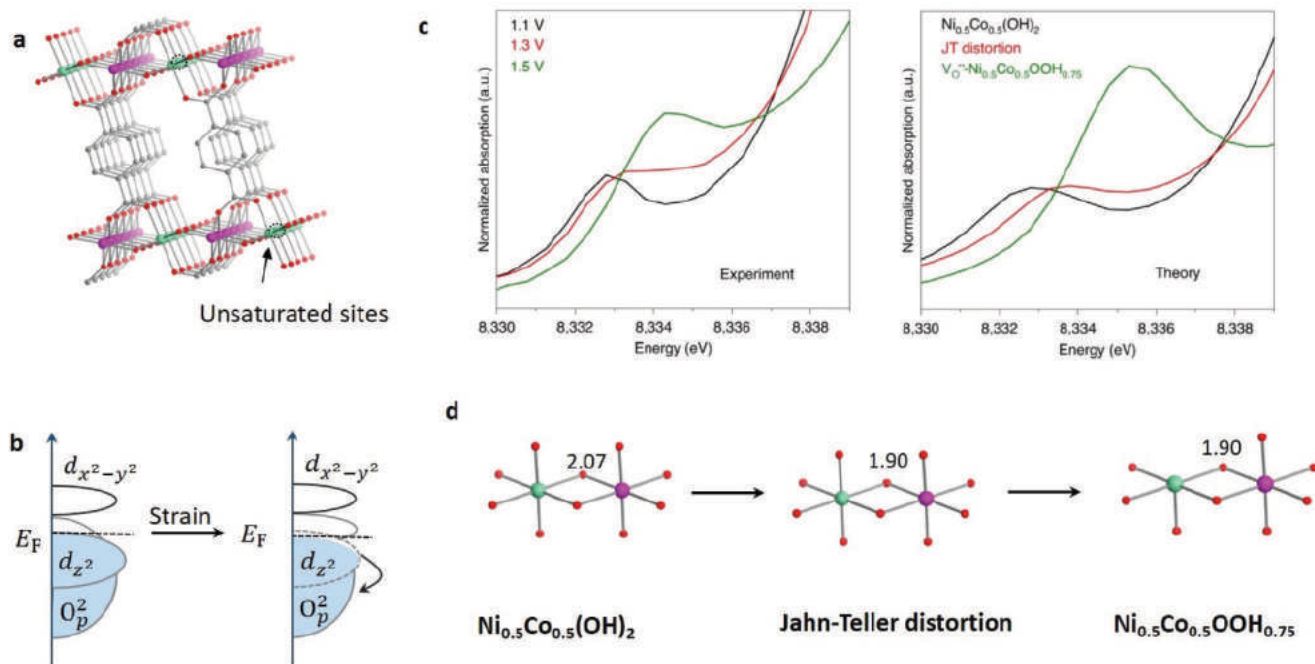


Figure 8. Schematic of a) unsaturated and partially saturated models for the metals on surfaces of NiCo-MOF nanosheets; b) electron exchange for lattice-strained NiCo-MOF. Reproduced with permission.^[62] Copyright 2019, Nature Publishing Group. c) Experimental and theoretical pre-edge peaks of the Ni K-edge at different potentials. d) Structural transformation of NiCo-MOF under certain potentials during OER. Reproduced with permission.^[65] Copyright 2020, Nature Publishing Group.

sites for OER in alkaline conditions (Figure 8a).^[58] Through judiciously combining X-ray absorption near-edge structure (XANES) characterization and density functional theory (DFT) computation, the unsaturated metal sites on the surface of NiCo-BDC nanosheets were confirmed as the main active sites for OER. Additionally, the partial density of states analyses showed that a bimetal coupling increases, or decreases, the unoccupied e_g filling for Ni or Co. Consequently, NiCo-BDC with bimetal coupling has a stronger π donation and a weaker e^-e^- repulsion than that of fully coordinated metals in single-metal-Ni-BDC and Co-BDC, thereby boosting electrocatalytic activity.

Subsequently, Wang et al. applied N_2 plasma to cleave part of linkers in ZIF-67 to synthesize coordinately unsaturated Co atoms as catalytic sites.^[59] They reported that the missing linker can lead to charge redistribution of active sites, enabling Co atoms with higher positive charges. This change strengthens the interaction between Co atoms with reactive intermediates and accelerates OER. Despite possessing highly active sites, the poor electrical conductivity of MOFs hinders charge transfer during electrocatalysis. Li et al. applied a missing-linker method to boost the electrical conductivity of CoBDC-Fc (Fc = carboxyferrocene) to improve catalytic activity.^[60] DFT results showed that there are newly formed electronic states near the Fermi level following missing linkers. The rate-determining step then transfers from the oxidation of H_2O to OH^* with an energy difference of 3.74 eV, to the oxidation of OH^* to O^* with an energy barrier of 1.85 eV. Therefore defective CoBDC exhibits a boosted OER greater than for the pristine state. Recently, Li et al. developed an alternative method to increase the electrical conductivity of NiBDC via the synthesis of partial charge

transfer.^[61] These researchers used an alkali-etch method to obtain missing-linker defects in which extra K^+ was introduced into the framework. These K^+ couples with Ni^{2+} , resulting in an increased valance of the Ni metal center. This partial charge transfer improved the electronic conductivity of the MOF, and consequently, the OER activity of NiBDC.

Cleavage of linkers in MOFs gives not only missing-linker defects but additionally the compression, or expansion, of surface atom geometry, i.e., strain effect to tune the electronic structure of metal atoms within frameworks. As an example, Liu et al. applied a photochemical method to expand the lattice of NiFe-MOF along the [100] direction.^[62] Because of the tensile lattice strain, the O 2p band is upshifted and promotes electron exchange from the Ni 3d orbital. This leads to a greater covalency in the Ni-O coordination bond. In this case, the surface oxo species thermodynamically benefits binding with neighboring Ni atoms to boost the high oxygen-involved catalytic activity (Figure 8b). Importantly, the operando synchrotron spectroscopies were employed to observe a key *OOH intermediate on Ni^{4+} sites during OER and oxygen reduction reaction (ORR). This intermediate is thermodynamically beneficial to O-O bond breakage/formation during the four-electron catalysis. Similarly, Yan et al. used monocarboxylic acids as the linker scission to replace part of binary carboxylic acids for building the lattice strain in NiFe-MOF.^[63] They found that this defect can optimize the Ni 3d e_g -orbital, facilitating the generation of *OOH intermediate to accelerate OER.

Chen et al. used a cation-substitution method to introduce Co^{2+} into Zn-based zeolite imidazole frameworks (Zn-ZIF) arrays on Ni foam in which ligand vacancies and mesopores form.^[64] Relying on the hydrolysis of Co^{2+} the hydrated

protons produced gradually cleave the Zn–N coordination bonds with the formation of free dimethyl imidazole. Following, Co^{2+} ions coordinate with the released dimethyl imidazole and enter into the Zn–ZIF. This leads to mismatched crystal growth and forming mesopores through the missing ligand. Experiments highlighted that the ligand vacancies generate unoccupied 3d orbitals at metal sites to lower the energy barrier of the OER reaction. The bimetal coupling promotes a partial charge transfer from Zn towards Co. This lowers the energy level of Co d orbitals to improve ORR activity of Zn–ZIF. Additionally, mesopores ensure efficient transport of the reactant and product toward, and away from, catalytic sites. This accelerates OER and ORR kinetics to give high-performance rechargeable Zn–air batteries.

It is established that a high anodic overpotential cleaves coordination bonds and drives a structural transition of MOFs during OER. With reliance on interpreting operando XAS spectroscopy and high-resolution transmission electron microscopy (TEM), Tang et al. reported a structural transformation of NiCo–MOF under OER.^[65] With a combined ab initio X-ray absorption near edge structure simulations and experimental spectra under two typical potentials (Figure 8c), they reported that NiCo–MOF undergoes a two-step transition during OER, namely, when the potential is 1.3 V versus RHE, the bond length of Ni–O and Co–O in NiCo–MOF decreases and a Jahn–Teller distorted model occurs (Figure 8d); when the potential increases to 1.5 V, O vacancies form through cleaving one of the Ni–O bonds of the Jahn–Teller distorted $\text{Ni}_{0.5}\text{Co}_{0.5}(\text{OH})_2$, thereby yielding in situ the $\text{Ni}_{0.5}\text{Co}_{0.5}\text{OOH}_{0.75}$ phase. These are the actual active sites for OER. Additionally, TEM characterization of NiCo–MOF following OER disclosed that its crystal structure remained. When the sample following OER was placed in air for 15 d, it reverted to primal $\text{Ni}_{0.5}\text{Co}_{0.5}(\text{OH})_2$ phase. They concluded, therefore, that this biphasic reconstruction occurs at the local metal nodes inside the pores and not from the total deconstruction of the MOF crystal structure.

3.1.2. Electrochemical CO_2 Reduction (CRR)

Electrochemical reduction of CO_2 produces high energy-density oxygenates and hydrocarbons via renewable energy input.^[66] It was established that sp^2 C atoms of the imidazolate linker in ZIF-8 electrochemically convert CO_2 to CO.^[67] Wang et al. reported an alternative method to boost CRR for ZIF-8 via coordinating an electron-donating molecule to Zn atoms (Figure 9a).^[68] The solvent molecule on Zn centers was cleaved by a methanol activation process to expose unsaturated metal sites. Phenanthroline was introduced to cooperate with unsaturated Zn atoms to accomplish charge transfer from phenanthroline plural to sp^2 C atoms in the imidazolate linker. DFT computations revealed that, after the modification with phenanthroline, the rate-determining step is converting CO_2 to $^*\text{COOH}$ with a smaller energy difference of 0.686 eV. This transition consequently generates $^*\text{COOH}$ to boost the CRR activity of ZIF-8.

Additionally, tuning linkers in MOFs strengthens CO_2 physisorption together with regulating the intermediate binding to improve CO selectivity.^[69] Sargent et al. applied a chemical

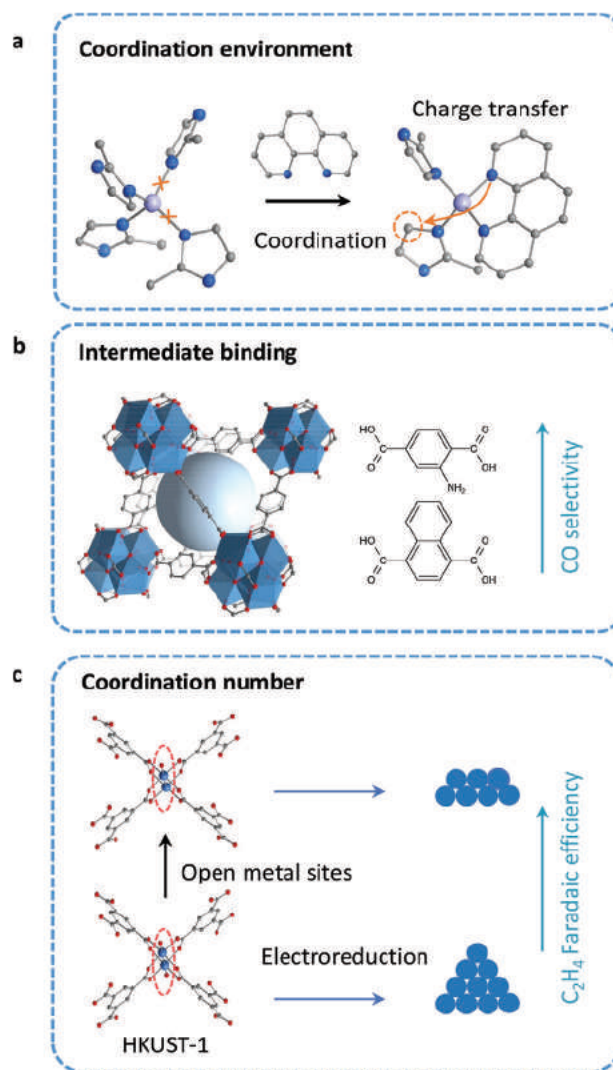


Figure 9. Schematic of a) Phenanthroline-doped ZIF-8; b) UiO-66(Zr) with the various linkers to regulate intermediate structure; c) controlling the structure of the Cu dimer in HKUST-1 to tune Cu–Cu coordination number of derived Cu clusters to obtain greater C_2H_4 FE.

reduction method to incorporate in situ Ag nanoparticles into pores of Zr–MOFs in which the local CO_2 concentration was significantly increased (Figure 9b). Ag nanoparticles work as active centers to promote the electrochemical reduction of CO_2 to CO. At the same time, the amine acts as functional groups in the organic linker to continuously capture CO_2 for the reaction. In situ Raman spectroscopy confirmed that modulating linkers regulates the binding modes of CO intermediates from the bridge to atop and pore size confinement. This increases CO selectivity. In contrast to this incorporation of nanoparticles into pores of MOFs, Hod et al. applied a MOF membrane to boost Ag catalyst activity. This involved three steps: 1) the porous membrane MOF physically lowers the mass transport of reactants (H^+) to Ag electrocatalyst. The local concentrations of reactants in the vicinity of catalytic sites are significantly altered compared to those in the bulk solution, thereby accelerating CRR and inhibiting HER side-reaction; 2) due to missing

clusters, there are several OH groups in the defective UiO-66. This works as a membrane to modify the Ag active surface. The electrocatalysis of CO from CO₂ is sped up via stabilizing *COO intermediates, and 3) a positively charged ligand, (3-carboxypropyl) trimethylammonium (TMA), is introduced into the MOF framework with a postsynthesis modification. This linker serves as an electrostatic ionic gating to fine control the H⁺ flux towards the Ag surface and to inhibit HER. As a result, the selectivity of CO is significantly boosted from 43% (for pure Ag) to 89% at a potential of -0.8 V versus RHE.

As with OER, a particular potential can reduce some electrochemically unstable MOFs to the metallic phase, such as Cu-MOFs. Sargent et al. found that by tuning the Cu–Cu coordination number (CN) in HKUST-1 the activity, selectivity, and efficiency for CRR were optimized simultaneously (Figure 9c).^[70] A thermal treatment was used to partially remove some coordinating water molecules in HKUST-1 from symmetrical Cu centers. The local atomic structure, oxidation state, and bonding strain of Cu dimers are modulated by varying processing times. This thereby regulates the Cu–Cu CN of Cu dimers resulting from electroreduction. These authors reported that the Cu clusters with reduced Cu–Cu CN significantly boosted catalytic activity for C₂H₄ production.

Recently we reported using molecular cleavage to tune the Cu cooperation environment of CuBDC to synthesize Cu₂BDC with mixed Cu²⁺ and Cu¹⁺. This is used to regulate the CRR activity of derived samples.^[32] Following cleaving half of the linkers from pristine CuBDC via reduction of Cu²⁺ to Cu¹⁺, the ratio of Cu to BDC increased from 1 to 2 to yield Cu₂BDC. When Cu₂BDC is used as the catalyst for CRR, in situ Cu K-edge extended X-ray absorption fine structure characterization confirms that it has decomposed and converted to mainly Cu, together with a little Cu₂O. Ex situ powder X-ray diffraction revealed that following an electrochemical reduction, Cu₂BDC obtains the Cu₂O (111) and Cu (111) mixed phases, which is typically different from pure Cu₂O (111) derived from the pristine CuBDC. The quantum mechanics calculations have confirmed that the Cu¹⁺ and Cu⁰ regions facilitate C–C coupling for CRR synergistically.^[71] This boosts C₂ products selectivity. The sample derived from Cu₂BDC exhibited a significant increase in catalytic activity for ethylene and ethanol over that for CuBDC.

3.2. Renewable Batteries

A market that is expected to grow in demand for portable electronics and electric vehicles will require high-performance, renewable batteries with high power/energy density and long-term cycling stability.^[72] Current commercial Li-ion batteries are based on the use of a transition metal oxide cathode, e.g., LiCoO₂, LiFePO₄, or LiNi_{1/3}Mn_{1/3}Co_{1/3}O₂ and a graphite anode, both of which rely on reversible intercalation/insertion of Li⁺ ions and charge transition during cycling.^[73] However, the batteries deliver low specific energy. There is significant research interest therefore in the development of high-capacity cathode/anode materials. Conversion reaction cathode materials, including S or organic electrode and metallic Li anode, have been proposed for next-generation electrode materials because

of high theoretical capacity and low cost. It is essential therefore to develop new electrode materials, and compatible electrolytes, and functional separators. In contrast to traditional inorganic and organic materials, MOFs not only possess a significant number of cavities and high specific surface area but additionally inherent structural advantages, including highly ordered pores, tunable pore sizes and topologies, and a hybrid inorganic–organic nature.^[74] Because of these intrinsic properties, a high density of charged species can be stored in a small geometric volume. This structure facilitates closely packed cation hopping sites to lower the activation energy for ion transport and increase ion conductivity.^[75] Additionally, the anions in the electrolyte can be docked on significant numbers of coordinatively unsaturated cationic sites. These result from removing solvent molecules to build single cation ion transport in the electrolyte for regulation of metal stripping.^[76] There are presently four methods to tune the structure of MOFs for rechargeable batteries: 1) stabilize intermediates; 2) use MOF-based separators to block polysulfides; 3) synthesize ion channels; and (4) tune electrolyte composite to control metal plating/stripping (Figure 7).

3.2.1. Li/Na–S Batteries

Metal anodes such as Li or Na, coupling with S cathode, can assemble into metal–sulfur batteries with a high theoretical energy density. The shutter effect caused by the migration of polysulfide intermediates lowers Coulombic efficiency, leading to a rapid capacity decay.^[77] MOFs materials however have a practical advantage for use as sulfur hosts because these immobilize polysulfides within porous structures and polar surfaces. Xiao et al. reported a new Ni₆(BTB)₄(BP)₃/S (BTB = benzene-1,3,5-tribenzoate and BP = 4,4'-bipyridyl) cathode in which mesopores and micropores of Ni₆(BTB)₄(BP)₃ are used as a matrix to confine polysulfides via molecular-level physical and chemical interactions.^[78] Strong Lewis acid–base interactions between Ni(II) center and polysulfides significantly slow migration of soluble polysulfides out of the pores to give significant cycling performance of the Ni₆(BTB)₄(BP)₃/S composite cathodes. Unlike 3D framework structures, 2D MOF nanosheets with abundant exposed active sites also confine polysulfides via weak interaction. We reported a mechanical exfoliation to break weak interaction between distinct layers and prepare a 2D Ni-MOF with Ni nodes and 2-mer-captopyrimidine ligands.^[79] The dynamic electron states of Ni centers were used to tune the interaction between polysulfides and Ni sites during discharge/charge. This results in strong adsorption together with rapid conversion kinetics of polysulfides. The electron states of Ni centers are changed from an electron accumulation state (Na₂S₅) to an electron depletion state (Na₂S). As a result, the polysulfides are confined in 2D Ni MOF. This design, therefore, is a practical solution to address the shuttle effect in metal–sulfur batteries. Thoi et al. reported a chemical method to stabilize polysulfides (Figure 10a). Li₃PS₄ worked as a host to anchor polysulfides through the formation of Li_{3+y}PS_{4+x} via S–S bonds. Li₃PS₄ is soluble in the electrolyte, resulting in loss of active material from the cathode and reduced cell capacity. To address this, Li₃PS₄ is incorporated into unsaturated sites

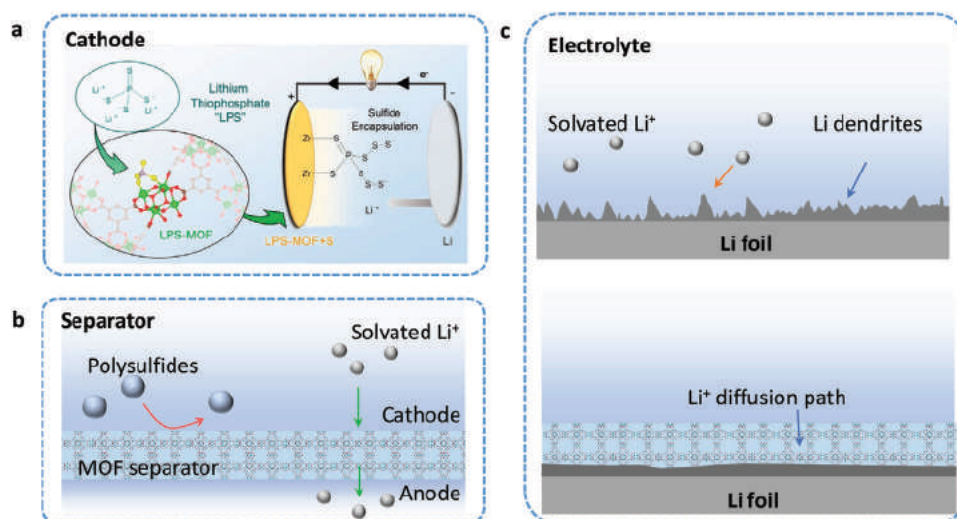


Figure 10. Schematic of a) anchoring Li_3PS_4 to achieve stable and reversible cycling via the introduction of polysulfides in Li–S battery cathodes. Reproduced with permission.^[80] Copyright 2019, American Chemical Society; b) MOF separator to block polysulfides; c) Li-metal electrode under (top) pristine electrolytes and (bottom) MOF-modified electrolyte.

of UiO-66, resulting from cleavage of the coordination bonds between the metal and linker. The open sites immobilize soluble PS_4^{3-} to facilitate $\text{Li}_2\text{S}/\text{Li}_2\text{S}_2$ deposition in the cathode.^[80] A high-rate capacity and long-cycling performance have thereby resulted in Li–S batteries.

Li et al. reported synthesis of a MOF host for stable Li–S batteries determined by pore and particle size.^[81] Pore size needs to be less than the diameter of an S_8 ring (6.9 Å) so that the MOF can immobilize polysulfides. Reported experiments confirmed via comparison with three MOFs, MIL-53 (Al), NH_2 -MIL-53 (Al), and HKUST-1, ZIF-8 stores and immobilizes polysulfides due to pore size of 3.4 Å. Downsized MOFs, from 3 μm to 150 nm, have a shorter diffusion length for Li^+ . This facilitates additional sulfur becoming electrochemically active with additional Li^+/e per S atom and results in greater reversible capacity.

MOFs can act as functional separators to obviate the shuttle effect. This is because the average size of 3D ordered micropores in MOFs is typically smaller than the size of lithium polysulfides. Zhou et al. reported a MOF-based separator in which thermal activation was used to remove solvent molecules from HKUST-1 (Figure 10b).^[82] It sieves Li^+ ions and blocks polysulfides. Graphene oxide (GO) is introduced to build a MOF@GO membrane to overcome the intrinsic mechanical brittleness of the MOF crystals. Compared with a pristine GO membrane this ionic sieve prevents polysulfides from migrating to the anode whilst having a negligible influence on the transfer of Li^+ ions across the separator. There is no meaningful capacity fading with this MOF-based separator following an initial 100 cycles for Li–S batteries. Importantly, it retains its structural stability under electrochemical cycling.

Although a MOF membrane can sieve Li^+ ions and block polysulfides, conventional functional membranes are synthesized by incorporating the MOF particles into a polymer matrix. An incompatibility between MOF particles and the polymer matrix leads to MOFs inhomogeneous dispersions and significant interfacial gaps, however, that form nonselective permeation

pathways. To obviate this, Kang et al. used a sol–gel to synthesis a MOF-gel membrane that was free of a matrix or binders.^[83] This freestanding membrane with homogeneous micropores gave permselective channels for targeted intermediates in rechargeable organic batteries and obviated serious electrode dissolution issues and the migration of organic redox intermediates. A battery synthesized with MOF-gel separator and 5,5'-dimethyl-2,2'-bis-*p*-benzoquinone as the cathode reportedly delivered high cycle stability with capacity retention of 82.9% after 2000 cycles.

3.2.2. Lithium-Ion and Lithium–Metal Batteries

A current drawback for the continued development of lithium-ion (Li-ion) batteries is a low specific capacity, and therefore low energy density. Another drawback is the formation of Li-dendrites during cycling, that leads to catastrophic short-circuit and significant safety hazard.^[84] MOFs exhibit practical promise however to obviate this in both Li-ion and Li–metal batteries. Dinca et al. reported that Cu-MOF undergoes a reversible phase transition as an anode in Li-ion batteries. The Li-ions are bound to the Cu sites, while the cations of electrolyte migrate freely within the pores of the MOF.^[76] Based on this finding, Dunn et al. used HKUST-1 as a host material to synthesize a pseudo-solid-state electrolyte as a superionic conductor for a Li-ion battery.^[85] A normal thermal activation was used to cleave the coordinating solvent molecule of HKUST-1 and obtain opened Cu sites. These coordinate with ClO_4^- anions of electrolyte and result in the electrolyte with biomimetic ionic channels. Electrochemical testing confirmed that this electrolyte exhibits high ambient conductivity, low activation energy, and a boosted Li^+ transference number. These features give Li-based batteries an excellent rate of performance and cycling stability.

Additionally, MOFs can serve as hosts to synthesize an ionic-liquid-impregnated MOF-based electrolyte for solid-state Li batteries. The large interfacial impedance from poor Li^+ transport

kinetics between the electrode materials was solved by Pan et al.^[86] HKUST-1, following cleavage of the coordinating solvent molecule, is a significant 3D-connected Li⁺ transport network. It has high ionic conductivity and nano-wetted interfaces, which lower the interfacial impedance to improve the migration of Li⁺ ions. Zhou et al. applied open metal sites of HKUST-1 to modify an organic electrolyte to regulate Li plating/stripping (Figure 10c).^[87] They reported that well-ordered MOF pores limit TFSI⁻ (trifluoromethanesulfonyl) anion migration by the interaction of TFSI⁻ and Cu sites. Electrostatic forces between TFSI⁻ and Li⁺ can restrain TFSI⁻ diffusion, which results in a homogeneous Li-ion flux. This design avoids the formation of Li-dendrites and gives a stable Li plating/stripping. Wang et al. developed this method to conduct a single ion electrolyte for control of Li-growth.^[88] They claimed that this modified electrolyte gave highly efficient Li⁺ transport within the pores of MOF-74 (Cu) via a Grotthuss-type mechanism. The charge is transported through the coordinated transition of Li⁺ between the ClO₄⁻ groups. This unimpeded Li-ion transport restrains irregular deposition of metallic Li and, consequently, suppresses the formation of Li-dendrites. However, MOFs particles in these electrolytes randomly distribute. To address this, Lu et al. synthesized a MOF-based hybrid polymer electrolyte by in situ growth of Cu(BDC) on poly(vinylidene fluoride) (PVDF).^[89] This electrolyte gives a high ambient Li⁺ conductivity of 0.24 ms cm⁻¹. This is because of ordered 1D Li⁺ channel via anchoring ClO₄⁻ anions on open metal sites of CuBDC and 3D continuous Li⁺ pathways, together with the CuBDC/PVDF interface. When the resultant electrolyte was used in an all-solid-state Li-Li(Ni_{0.8}Co_{0.1}Mn_{0.1})O₂ (NCM-811) full cell, it exhibited a high reversible capacity with cycling stability.

In conventional liquid electrolytes, the state of Li⁺ ions is solvated through coordination with the solvent. Before Li⁺ ions are inserted and deposited on the cathode (for example NCM-811), solvated Li⁺ ions undergo desolvation on the cathode surface. This produces highly reactive free solvent molecules that

can cause solvent-related decomposition during cycling. As a result, it can reduce electrochemical stability windows and form unstable cathode–electrolyte interface layers on the cathode surface. Zhou et al. synthesized a liquid electrolyte with desolvated Li⁺ ions by mechanically coating ZIF-7 on the surface of NCM-811 and a high-energy-battery full cell.^[90] Electrolyte analysis showed that a similar solid-state form of DME (dimethyl ether) molecules exists in MOF channels. Li⁺ ions in the MOF channels are in close contact with TFSI⁻ (bistrifluoromethanesulfonimide) and form a similar crystal-like LiTFSI salt. This means that this configuration makes the desolvated Li⁺ ions occur within MOF channels, rather than on the cathode surface. As a result, the electrochemical stability window can be significantly improved from 3.8 to 4.5 V for these electrolytes. Importantly, no cathode–electrolyte interface layer is found on the surface of the cycled NCM-811.

3.2.3. Aqueous Zinc-Ion Batteries

There are two problems of capacity decline in aqueous zinc batteries: 1) growth of nonuniform Zn dendrites, and 2) side reaction of HER on Zn anode surface.^[91] Xia et al. used an annealed ZIF-8 as a host material to regulate Zn plating and stripping and suppress HER on Zn anode surface (Figure 11a).^[92] They optimized the annealing temperature to cleave part of Zn–O coordinated bonds and obtain trace amounts of metal Zn without disturbing the inherent porous structure of ZIF-8. These metal Zn sites provide uniform nuclei for Zn growth. The Zn@ZIF-8 host exhibited a high over-potential for HER and, consequently, reduced undesired decomposition of H₂O. Zhou et al. added ZIF-7 into the electrolyte to synthesize a surface super-saturated electrolyte on the anode to regulate Zn growth (Figure 11b).^[93] In this work, open metal sites in ZIF-7 were host to coordinate anions (SO₄²⁻) of the electrolyte, in which a supersaturated electrolyte was generated

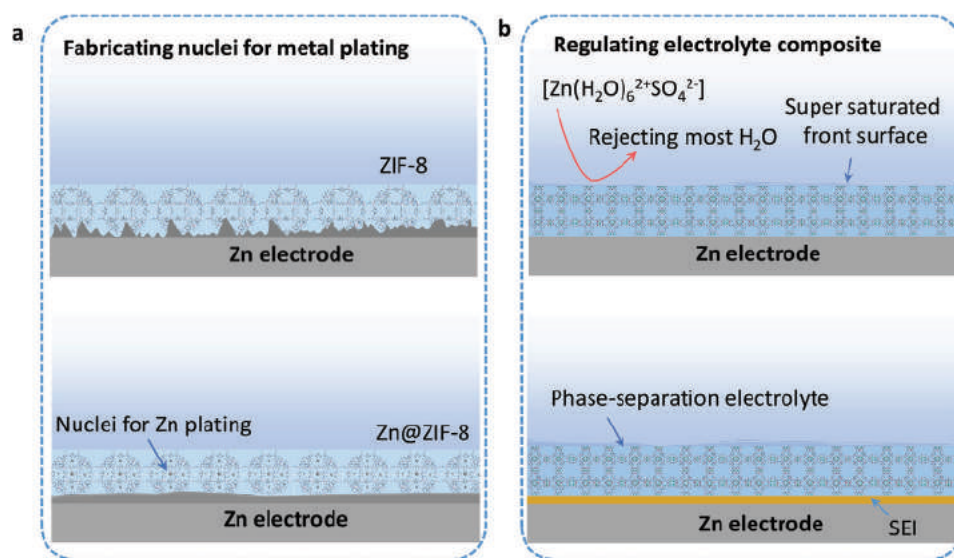


Figure 11. Schematic of a) (top) Zn dendrite formation on ZIF-8 modified Zn-foil and (bottom) Zn@ZIF-8 modified Zn-foil; b) (top) MOF coating layer to reject H₂O and synthesize a supersaturated front surface, (bottom) SEI formation in HKUST-1 confined organic electrolyte that is immiscible with an aqueous electrolyte. Reproduced with permission.^[94] Copyright 2020, Wiley-VCH.

on the Zn anode surface. This electrolyte ensured a homogeneous Zn deposition and avoided the formation of dendrites. The MOF channels allowed migration of highly coordinated ion complexes of $\text{H}_2\text{O}\text{-Zn}^{2+}\text{-SO}_4^{2-}$ through the pore size, which reduced the formation of solvable $[\text{Zn}(\text{H}_2\text{O})_6]^{2+}$. Therefore the Zn anode exhibited an ultralong lifespan, without noticeable voltage fluctuation over 3000 h. Both Fourier transform infrared and Raman spectra confirmed that the supersaturated electrolyte restrained the formation of by-product ZnO and $\text{Zn}(\text{OH})_2$ on the Zn anode surface and improved cycling stability. Because the size of cations and anodes are smaller than the pore size of those of HKUST-1 ordered micropores, they confine the organic electrolyte and produce a phase-separation electrolyte to protect the Zn anode (Figure 11b). Wang et al. introduced $\text{Zn}(\text{TFSI})_2$ -tris(2,2,2-trifluoroethyl)-phosphate organic electrolyte into pores of MOFs following cleavage of solvent molecules from HKUST-1.^[94] Because the organic electrolyte is immiscible with aqueous $\text{Zn}(\text{TFSI})_2\text{-H}_2\text{O}$ bulk electrolyte, a hydrophobic layer formed. During battery cycling with this modified electrolyte, a $\text{ZnF}_2\text{-Zn}_3(\text{PO}_4)_2$ SEI was formed in situ to boost Zn plating/stripping significantly and inhibit water decomposition.

4. Summary and Outlook

Molecular cleavage can be used to tune the structure and morphology of MOFs. Through cleavage of metal–solvent coordination bonds, MOFs with open metal sites are synthesized. Following removal of linkers or clusters by coordination bond breakdown, missing-linker or missing-cluster defects are formed in MOFs. These allow tuning of electronic structure and optimization of catalytic activity. When the missed linker size increases, hierarchical pores in MOFs are generated to enlarge pore size and then promote mass transfer within the framework. The exploitation of the pores and open metal sites of MOFs regulate ion confinement and transport for high performance in reversible batteries.

While several methods have been used to cleave coordination bonds of MOFs, significant practical challenges remain for molecular cleavage of MOFs to diversify application, namely:

1. Synthesis of high-porosity MOFs requires minimal processing, which is attractive for practical application. Although the chemical activation of MOFs to open metal sites does not need heat energy, a significant amount of toxic solvents, such as methylene chloride, is required. A drawback however is that solvent-exchange pre-treatment is time-consuming. A green method that is simple in time and energy therefore should be investigated.
2. Because missing-linker and missing-cluster defects simultaneously occur, the types of defects in engineered MOFs need to be precisely controlled. An explicit defect structure provides a platform to investigate the structural–catalytic property relationship. Despite labile linkers giving a practical method to build missing-linker defects by breaking special chemical bonds, unevenly mixed linker leads to product missing-cluster defects following removal of labile linkers. Therefore, the main catalytic sites when defective MOFs work as catalysts need to be identified.
3. Synthesis of highly ordered mesoporous or macroporous crystal materials on various length scales with different structural coherence is a critical path to increase MOF pore size. Although a significant number of MOFs with hierarchical pores have been synthesized by postsynthesis methods, the design of MOFs with ordered macropores remains practically difficult because harsh synthetic conditions are needed to maintain the ordered arrangement of hard templates.^[95] Selective cleavage of carboxylate-based MOFs might therefore provide new routes to MOFs with ordered macropores.
4. Advanced in situ characterization techniques can be reliably used to aid understanding of catalysis and mechanism(s) in catalytic reductions. However, with usual characterization techniques, it is practically challenging to detect cleaving detail. Development of in situ characterizations is therefore needed to fully understand coordination bond cleavage and for the design of new methods to cleave metal–coordination bonds in MOFs.
5. Reconstruction of electrocatalysts is commonly observed during catalysis, in which new catalytic centers are produced in situ. Although a significant number of MOFs have been investigated as electrocatalysts, there are few reliable data that aid disclosure of structural transition by cleavage of coordination bonds. To permit continued development of MOFs, investigative research will need to be directed to revealing structure during catalytic reaction mechanisms.
6. For reversible battery application, modified MOFs that coat on metal anodes or regulate electrolyte composites can lower the cation migration to control Li and Zn plating/stripping at a relatively low current density. However, they hinder the rapid migration of ions at a high current density. This decreases the rate performance of electrodes that is essential for the power battery application. Alternate methods that not only control the growth of metal dendrites but achieve high-rate performance, therefore, need to be investigated for the application of MOFs to energy storage application.

Acknowledgements

This work was financially supported by the Australian Research Council through the Discovery Project programs (FL170100154, DP160104866, and DP190103472) and the Australian Government through Research Training Program Scholarships.

Conflict of Interest

The authors declare no conflict of interest.

Keywords

batteries, coordination bonds, electrocatalysis, metal-organic frameworks, molecular cleavage

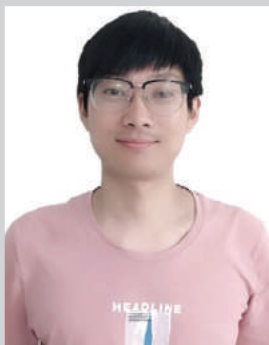
Received: June 7, 2021

Revised: August 10, 2021

Published online:

- [1] H. F. Wang, L. Chen, H. Pang, S. Kaskel, Q. Xu, *Chem. Soc. Rev.* **2020**, *49*, 1414.
- [2] a) M. J. Kalmutzki, N. Hanikel, O. M. Yaghi, *Sci. Adv.* **2018**, *4*, eaat9180; b) X. F. Lu, B. Y. Xia, S. Q. Zang, X. W. D. Lou, *Angew. Chem., Int. Ed.* **2020**, *59*, 4634; c) X. Xiao, L. Zou, H. Pang, Q. Xu, *Chem. Soc. Rev.* **2020**, *49*, 301.
- [3] a) J. D. Evans, C. J. Sumby, C. J. Doonan, *Chem. Soc. Rev.* **2014**, *43*, 5933; b) N. Stock, S. Biswas, *Chem. Rev.* **2012**, *112*, 933.
- [4] M.-M. Xu, Q. Chen, L.-H. Xie, J.-R. Li, *Coord. Chem. Rev.* **2020**, *421*, 213421.
- [5] L. Jiao, J. Y. R. Seow, W. S. Skinner, Z. U. Wang, H.-L. Jiang, *Mater. Today* **2019**, *27*, 43.
- [6] E. López-Maya, C. Montoro, V. Colombo, E. Barea, J. A. R. Navarro, *Adv. Funct. Mater.* **2014**, *24*, 6130.
- [7] D. Yang, C. A. Gaggioli, D. Ray, M. Babucci, L. Gagliardi, B. C. Gates, *J. Am. Chem. Soc.* **2020**, *142*, 8044.
- [8] R. E. Morris, J. Cejka, *Nat. Chem.* **2015**, *7*, 381.
- [9] a) J. Liu, D. Zhu, C. Guo, A. Vasileff, S.-Z. Qiao, *Adv. Energy Mater.* **2017**, *7*, 1700518; b) P. Deng, F. Yang, Z. Wang, S. Chen, Y. Zhou, S. Zaman, B. Y. Xia, *Angew. Chem., Int. Ed.* **2020**, *59*, 10807; c) Y. Qu, Z. Li, W. Chen, Y. Lin, T. Yuan, Z. Yang, C. Zhao, J. Wang, C. Zhao, X. Wang, F. Zhou, Z. Zhuang, Y. Wu, Y. Li, *Nat. Catal.* **2018**, *1*, 781; d) A. Han, B. Wang, A. Kumar, Y. Qin, J. Jin, X. Wang, C. Yang, B. Dong, Y. Jia, J. Liu, X. Sun, *Small Methods* **2019**, *3*, 1800471.
- [10] a) H. Zhang, J. Nai, L. Yu, X. W. Lou, *Joule* **2017**, *1*, 77; b) Q. Wang, D. Astruc, *Chem. Rev.* **2020**, *120*, 1438; c) X. F. Lu, Y. Fang, D. Luan, X. W. D. Lou, *Nano Lett.* **2021**, *21*, 1555.
- [11] P. Deria, J. E. Mondloch, E. Tyliranakis, P. Ghosh, W. Bury, R. Q. Snurr, J. T. Hupp, O. K. Farha, *J. Am. Chem. Soc.* **2013**, *135*, 16801.
- [12] L. Feng, K. Y. Wang, G. S. Day, M. R. Ryder, H. C. Zhou, *Chem. Rev.* **2020**, *120*, 13087.
- [13] O. Karagiari, W. Bury, J. E. Mondloch, J. T. Hupp, O. K. Farha, *Angew. Chem., Int. Ed.* **2014**, *53*, 4530.
- [14] a) Ü. Kökçam-Demir, A. Goldman, L. Esrafilı, M. Gharib, A. Morsali, O. Weingart, C. Janiak, *Chem. Soc. Rev.* **2020**, *49*, 2751; b) S. Dissegna, K. Epp, W. R. Heinz, G. Kieslich, R. A. Fischer, *Adv. Mater.* **2018**, *30*, 1704501; c) L. Feng, K. Y. Wang, J. Willman, H. C. Zhou, *ACS Cent. Sci.* **2020**, *6*, 359.
- [15] a) A. De Vos, K. Hendrickx, P. Van Der Voort, V. Van Speybroeck, K. Lejaeghere, *Chem. Mater.* **2017**, *29*, 3006; b) J. L. Mancuso, A. M. Mroz, K. N. Le, C. H. Hendon, *Chem. Rev.* **2020**, *120*, 8641.
- [16] X. Zhang, Z. Chen, X. Liu, S. L. Hanna, X. Wang, R. Taheri-Ledari, A. Maleki, P. Li, O. K. Farha, *Chem. Soc. Rev.* **2020**, *49*, 7406.
- [17] K. Schlichte, T. Kratzke, S. Kaskel, *Microporous Mesoporous Mater.* **2004**, *73*, 81.
- [18] B. Chen, N. W. Ockwig, A. R. Millward, D. S. Contreras, O. M. Yaghi, *Angew. Chem., Int. Ed.* **2005**, *44*, 4745.
- [19] J. Espín, L. Garzón-Tovar, A. Carné-Sánchez, I. Imaz, D. Maspoch, *ACS Appl. Mater. Interfaces* **2018**, *10*, 9555.
- [20] H. K. Kim, W. S. Yun, M. B. Kim, J. Y. Kim, Y. S. Bae, J. Lee, N. C. Jeong, *J. Am. Chem. Soc.* **2015**, *137*, 10009.
- [21] J. S. Choi, J. Bae, E. J. Lee, N. C. Jeong, *Inorg. Chem.* **2018**, *57*, 5225.
- [22] F. Vermoortele, B. Bueken, G. Le Bars, B. Van de Voorde, M. Vandichel, K. Houthoofd, A. Vimont, M. Daturi, M. Waroquier, V. Van Speybroeck, C. Kirschhock, D. E. De Vos, *J. Am. Chem. Soc.* **2013**, *135*, 11465.
- [23] H. Wu, Y. S. Chua, V. Krungleviciute, M. Tyagi, P. Chen, T. Yildirim, W. Zhou, *J. Am. Chem. Soc.* **2013**, *135*, 10525.
- [24] B. Bueken, N. Van Velthoven, A. Krajnc, S. Smolders, F. Taulelle, C. Mellot-Draznieks, G. Mali, T. D. Bennett, D. De Vos, *Chem. Mater.* **2017**, *29*, 10478.
- [25] G. C. Shearer, S. Chavan, S. Bordiga, S. Svelle, U. Olsbye, K. P. Lillerud, *Chem. Mater.* **2016**, *28*, 3749.
- [26] X. Feng, J. Hajek, H. S. Jena, G. Wang, S. K. P. Veerapandian, R. Morent, N. De Geyter, K. Leyssens, A. E. J. Hoffman, V. Meynen, C. Marquez, D. E. De Vos, V. Van Speybroeck, K. Leus, P. Van Der Voort, *J. Am. Chem. Soc.* **2020**, *142*, 3174.
- [27] C. Huang, J. Dong, W. Sun, Z. Xue, J. Ma, L. Zheng, C. Liu, X. Li, K. Zhou, X. Qiao, Q. Song, W. Ma, L. Zhang, Z. Lin, T. Wang, *Nat. Commun.* **2019**, *10*, 2779.
- [28] L. Feng, S. Yuan, L. L. Zhang, K. Tan, J. L. Li, A. Kirchon, L. M. Liu, P. Zhang, Y. Han, Y. J. Chabal, H. C. Zhou, *J. Am. Chem. Soc.* **2018**, *140*, 2363.
- [29] M. J. Cliffe, W. Wan, X. Zou, P. A. Chater, A. K. Kleppe, M. G. Tucker, H. Wilhelm, N. P. Funnell, F. X. Coudert, A. L. Goodwin, *Nat. Commun.* **2014**, *5*, 4176.
- [30] D. Song, J. Bae, H. Ji, M. B. Kim, Y. S. Bae, K. S. Park, D. Moon, N. C. Jeong, *J. Am. Chem. Soc.* **2019**, *141*, 7853.
- [31] B. Tu, Q. Pang, D. Wu, Y. Song, L. Weng, Q. Li, *J. Am. Chem. Soc.* **2014**, *136*, 14465.
- [32] X. Zhou, J. Dong, Y. Zhu, L. Liu, Y. Jiao, H. Li, Y. Han, K. Davey, Q. Xu, Y. Zheng, S. Z. Qiao, *J. Am. Chem. Soc.* **2021**, *143*, 6681.
- [33] a) J. B. DeCoste, J. A. Rossin, G. W. Peterson, *Chem. - Eur. J.* **2015**, *21*, 18029; b) M. K. Albolqany, C. Liu, Y. Wang, C. H. Chen, C. Zhu, X. Chen, B. Liu, *Angew. Chem., Int. Ed.* **2021**, *60*, 14601; c) J. Y. Wang, L. Feng, T. H. Yan, S. Wu, E. A. Joseph, H. C. Zhou, *Angew. Chem., Int. Ed.* **2020**, *59*, 11349; d) H. Huang, J. R. Li, K. Wang, T. Han, M. Tong, L. Li, Y. Xie, Q. Yang, D. Liu, C. Zhong, *Nat. Commun.* **2015**, *6*, 8847.
- [34] Y. Kim, T. Yang, G. Yun, M. B. Ghasemian, J. Koo, E. Lee, S. J. Cho, K. Kim, *Angew. Chem., Int. Ed.* **2015**, *54*, 13273.
- [35] S. C. Qi, X. Y. Qian, Q. X. He, K. J. Miao, Y. Jiang, P. Tan, X. Q. Liu, L. B. Sun, *Angew. Chem., Int. Ed.* **2019**, *58*, 10104.
- [36] J. Koo, I. C. Hwang, X. Yu, S. Saha, Y. Kim, K. Kim, *Chem. Sci.* **2017**, *8*, 6799.
- [37] G. Y. Jeong, A. K. Singh, M. G. Kim, K. W. Gyak, U. Ryu, K. M. Choi, D. P. Kim, *Nat. Commun.* **2018**, *9*, 3968.
- [38] S. Chen, S. Mukherjee, B. E. G. Lucier, Y. Guo, Y. T. A. Wong, V. V. Tersikh, M. J. Zaworotko, Y. Huang, *J. Am. Chem. Soc.* **2019**, *141*, 14257.
- [39] G. Cai, H. L. Jiang, *Angew. Chem., Int. Ed.* **2017**, *56*, 563.
- [40] L. Feng, G. S. Day, K.-Y. Wang, S. Yuan, H.-C. Zhou, *Chem* **2020**, *6*, 2902.
- [41] S. Yuan, L. Zou, J. S. Qin, J. Li, L. Huang, L. Feng, X. Wang, M. Bosch, A. Alsalmeh, T. Cagin, H. C. Zhou, *Nat. Commun.* **2017**, *8*, 15356.
- [42] V. Guillerme, H. Xu, J. Albalad, I. Imaz, D. Maspoch, *J. Am. Chem. Soc.* **2018**, *140*, 15022.
- [43] Y. Song, X. Feng, J. S. Chen, C. Brzezinski, Z. Xu, W. Lin, *J. Am. Chem. Soc.* **2020**, *142*, 4872.
- [44] H. Jin, Q. Gu, B. Chen, C. Tang, Y. Zheng, H. Zhang, M. Jaroniec, S.-Z. Qiao, *Chem* **2020**, *6*, 2382.
- [45] Y. Peng, Y. Li, Y. Ban, H. Jin, W. Jiao, X. Liu, W. Yang, *Science* **2014**, *346*, 1356.
- [46] Y. Ding, Y. P. Chen, X. Zhang, L. Chen, Z. Dong, H. L. Jiang, H. Xu, H. C. Zhou, *J. Am. Chem. Soc.* **2017**, *139*, 9136.
- [47] M. J. Cliffe, E. Castillo-Martinez, Y. Wu, J. Lee, A. C. Forse, F. C. N. Firth, P. Z. Moghadam, D. Fairen-Jimenez, M. W. Gaultois, J. A. Hill, O. V. Magdysyuk, B. Slater, A. L. Goodwin, C. P. Grey, *J. Am. Chem. Soc.* **2017**, *139*, 5397.
- [48] J. Huang, Y. Li, R. K. Huang, C. T. He, L. Gong, Q. Hu, L. Wang, Y. T. Xu, X. Y. Tian, S. Y. Liu, Z. M. Ye, F. Wang, D. D. Zhou, W. X. Zhang, J. P. Zhang, *Angew. Chem., Int. Ed.* **2018**, *57*, 4632.
- [49] C. Avci, J. Arinez-Soriano, A. Carne-Sanchez, V. Guillerme, C. Carbonell, I. Imaz, D. Maspoch, *Angew. Chem., Int. Ed.* **2015**, *54*, 14417.
- [50] L. Luo, W. S. Lo, X. Si, H. Li, Y. Wu, Y. An, Q. Zhu, L. Y. Chou, T. Li, C. K. Tsung, *J. Am. Chem. Soc.* **2019**, *141*, 20365.

- [51] W. Liu, J. Huang, Q. Yang, S. Wang, X. Sun, W. Zhang, J. Liu, F. Huo, *Angew. Chem., Int. Ed.* **2017**, *56*, 5512.
- [52] Y. Qin, X. Han, Y. Li, A. Han, W. Liu, H. Xu, J. Liu, *ACS Catal.* **2020**, *10*, 5973.
- [53] C. Tang, Y. Zheng, M. Jaroniec, S.-Z. Qiao, *Angew. Chem., Int. Ed.* **2021**, <https://doi.org/10.1002/anie.202101522>.
- [54] D. D. Zhu, J. L. Liu, S. Z. Qiao, *Adv. Mater.* **2016**, *28*, 3423.
- [55] Z. Li, R. Gao, M. Feng, Y. P. Deng, D. Xiao, Y. Zheng, Z. Zhao, D. Luo, Y. Liu, Z. Zhang, D. Wang, Q. Li, H. Li, X. Wang, Z. Chen, *Adv. Energy Mater.* **2021**, *11*, 2003291.
- [56] W. Cheng, H. Zhang, D. Luan, X. W. D. Lou, *Sci. Adv.* **2021**, *7*, eabg25.
- [57] X. Wang, X. Li, S. Dou, *ACS Mater. Lett.* **2020**, *2*, 1251.
- [58] S. Zhao, Y. Wang, J. Dong, C.-T. He, H. Yin, P. An, K. Zhao, X. Zhang, C. Gao, L. Zhang, J. Lv, J. Wang, J. Zhang, A. M. Khattak, N. A. Khan, Z. Wei, J. Zhang, S. Liu, H. Zhao, Z. Tang, *Nat. Energy* **2016**, *1*, 16184.
- [59] L. Tao, C.-Y. Lin, S. Dou, S. Feng, D. Chen, D. Liu, J. Huo, Z. Xia, S. Wang, *Nano Energy* **2017**, *41*, 417.
- [60] Z. Xue, K. Liu, Q. Liu, Y. Li, M. Li, C. Y. Su, N. Ogiwara, H. Kobayashi, H. Kitagawa, M. Liu, G. Li, *Nat. Commun.* **2019**, *10*, 5048.
- [61] J. Zhou, Y. Dou, X. Q. Wu, A. Zhou, L. Shu, J. R. Li, *Small* **2020**, *16*, 1906564.
- [62] W. Cheng, X. Zhao, H. Su, F. Tang, W. Che, H. Zhang, Q. Liu, *Nat. Energy* **2019**, *4*, 115.
- [63] Q. Ji, Y. Kong, C. Wang, H. Tan, H. Duan, W. Hu, G. Li, Y. Lu, N. Li, Y. Wang, J. Tian, Z. Qi, Z. Sun, F. Hu, W. Yan, *ACS Catal.* **2020**, *10*, 5691.
- [64] Y. Jiang, Y. P. Deng, R. Liang, J. Fu, R. Gao, D. Luo, Z. Bai, Y. Hu, A. Yu, Z. Chen, *Nat. Commun.* **2020**, *11*, 5858.
- [65] S. Zhao, C. Tan, C.-T. He, P. An, F. Xie, S. Jiang, Y. Zhu, K.-H. Wu, B. Zhang, H. Li, J. Zhang, Y. Chen, S. Liu, J. Dong, Z. Tang, *Nat. Energy* **2020**, *5*, 881.
- [66] Y. Zheng, A. Vasileff, X. Zhou, Y. Jiao, M. Jaroniec, S. Z. Qiao, *J. Am. Chem. Soc.* **2019**, *141*, 7646.
- [67] X. Jiang, H. Li, J. Xiao, D. Gao, R. Si, F. Yang, Y. Li, G. Wang, X. Bao, *Nano Energy* **2018**, *52*, 345.
- [68] S. Dou, J. Song, S. Xi, Y. Du, J. Wang, Z. F. Huang, Z. J. Xu, X. Wang, *Angew. Chem., Int. Ed.* **2019**, *58*, 4041.
- [69] D. H. Nam, O. Shekhah, G. Lee, A. Mallick, H. Jiang, F. Li, B. Chen, J. Wicks, M. Eddaoudi, E. H. Sargent, *J. Am. Chem. Soc.* **2020**, *142*, 21513.
- [70] D. H. Nam, O. S. Bushuyev, J. Li, P. De Luna, A. Seifitokaldani, C. T. Dinh, F. P. Garcia de Arquer, Y. Wang, Z. Liang, A. H. Proppe, C. S. Tan, P. Todorovic, O. Shekhah, C. M. Gabardo, J. W. Jo, J. Choi, M. J. Choi, S. W. Baek, J. Kim, D. Sinton, S. O. Kelley, M. Eddaoudi, E. H. Sargent, *J. Am. Chem. Soc.* **2018**, *140*, 11378.
- [71] H. Xiao, W. A. Goddard, T. Cheng, Y. Liu, *Proc. Natl. Acad. Sci. USA* **2017**, *114*, E7045.
- [72] D. Chao, W. Zhou, C. Ye, Q. Zhang, Y. Chen, L. Gu, K. Davey, S.-Z. Qiao, *Angew. Chem., Int. Ed.* **2019**, *58*, 7823.
- [73] S. H. Yu, X. Feng, N. Zhang, J. Seok, H. D. Abruna, *Acc. Chem. Res.* **2018**, *51*, 273.
- [74] J. Liu, D. Xie, W. Shi, P. Cheng, *Chem. Soc. Rev.* **2020**, *49*, 1624.
- [75] Y. He, Y. Qiao, Z. Chang, H. Zhou, *Energy Environ. Sci.* **2019**, *12*, 2327.
- [76] S. S. Park, Y. Tulchinsky, M. Dinca, *J. Am. Chem. Soc.* **2017**, *139*, 13260.
- [77] C. Ye, D. Chao, J. Shan, H. Li, K. Davey, S.-Z. Qiao, *Matter* **2020**, *2*, 323.
- [78] J. Zheng, J. Tian, D. Wu, M. Gu, W. Xu, C. Wang, F. Gao, M. H. Engelhard, J. G. Zhang, J. Liu, J. Xiao, *Nano Lett.* **2014**, *14*, 2345.
- [79] C. Ye, Y. Jiao, D. Chao, T. Ling, J. Shan, B. Zhang, Q. Gu, K. Davey, H. Wang, S.-Z. Qiao, *Adv. Mater.* **2020**, *32*, 1907557.
- [80] A. E. Baumann, X. Han, M. M. Butala, V. S. Thoi, *J. Am. Chem. Soc.* **2019**, *141*, 17891.
- [81] J. Zhou, R. Li, X. Fan, Y. Chen, R. Han, W. Li, J. Zheng, B. Wang, X. Li, *Energy Environ. Sci.* **2014**, *7*, 2715.
- [82] S. Bai, X. Liu, K. Zhu, S. Wu, H. Zhou, *Nat. Energy* **2016**, *1*, 16094.
- [83] S. Bai, B. Kim, C. Kim, O. Tamwattana, H. Park, J. Kim, D. Lee, K. Kang, *Nat. Nanotechnol.* **2021**, *16*, 77.
- [84] a) T. Li, X.-Q. Zhang, P. Shi, Q. Zhang, *Joule* **2019**, *3*, 2647; b) X. Zhang, Y. Yang, Z. Zhou, *Chem. Soc. Rev.* **2020**, *49*, 3040.
- [85] L. Shen, H. B. Wu, F. Liu, J. L. Brosmer, G. Shen, X. Wang, J. I. Zink, Q. Xiao, M. Cai, G. Wang, Y. Lu, B. Dunn, *Adv. Mater.* **2018**, *30*, 1707476.
- [86] Z. Wang, R. Tan, H. Wang, L. Yang, J. Hu, H. Chen, F. Pan, *Adv. Mater.* **2018**, *30*, 1704436.
- [87] S. Bai, Y. Sun, J. Yi, Y. He, Y. Qiao, H. Zhou, *Joule* **2018**, *2*, 2117.
- [88] S. Yuan, J. L. Bao, J. Wei, Y. Xia, D. G. Truhlar, Y. Wang, *Energy Environ. Sci.* **2019**, *12*, 2741.
- [89] J. Yu, T. Guo, C. Wang, Z. Shen, X. Dong, S. Li, H. Zhang, Z. Lu, *Nano Lett.* **2021**, *21*, 5805.
- [90] Z. Chang, Y. Qiao, H. Deng, H. Yang, P. He, H. Zhou, *Joule* **2020**, *4*, 1776.
- [91] D. Chao, W. Zhou, F. Xie, C. Ye, H. Li, M. Jaroniec, S.-Z. Qiao, *Sci. Adv.* **2020**, *6*, eaba4098.
- [92] Z. Wang, J. H. Huang, Z. W. Guo, X. L. Dong, Y. Liu, Y. G. Wang, Y. Y. Xia, *Joule* **2019**, *3*, 1289.
- [93] H. Yang, Z. Chang, Y. Qiao, H. Deng, X. Mu, P. He, H. Zhou, *Angew. Chem., Int. Ed.* **2020**, *59*, 9377.
- [94] L. Cao, D. Li, T. Deng, Q. Li, C. Wang, *Angew. Chem., Int. Ed.* **2020**, *59*, 19292.
- [95] K. Shen, L. Zhang, X. Chen, L. Liu, D. Zhang, Y. Han, J. Chen, J. Long, R. Luque, Y. Li, B. Chen, *Science* **2018**, *359*, 206.



Xianlong Zhou received his M.E. degree from Nankai University (China). Currently, he is a Ph.D. candidate under the supervision of Assoc. Prof. Yao Zheng and Prof. Shi-Zhang Qiao at the School of Chemical Engineering and Advanced Materials of the University of Adelaide. His research focuses on Cu-based catalyst design for electrochemical reduction of CO₂.



Yao Zheng received his Ph.D. degree in 2014 from The University of Queensland (Australia). He is currently an associate professor at The University of Adelaide. His research focuses on fundamental studies of some key electrocatalytic refinery processes by combining experiments and theoretical computations, and the development of advanced electrocatalysts for energy conversion processes.



Shi-Zhang Qiao received his Ph.D. degree in Chemical Engineering from the Hong Kong University of Science and Technology in 2000. He is currently a chair professor and Australian Laureate Fellow at The University of Adelaide. His research interests include synthesis and characterization of nanomaterials as well as their applications in catalysis, energy storage, and conversion (fuel cells, batteries, supercapacitors, electrocatalysis, and photocatalysis).

Statement of Authorship

Title of Paper	Molecular Scalpel to Chemically Cleave Metal–Organic Frameworks for Induced Phase Transition
Publication Status	<input checked="" type="checkbox"/> Published <input type="checkbox"/> Accepted for Publication <input type="checkbox"/> Submitted for Publication <input type="checkbox"/> Unpublished and Unsubmitted work written in manuscript style
Publication Details	Xianlong Zhou, Juncai Dong, Yihan Zhu, Lingmei Liu, Yan Jiao, Huan Li, Yu Han, Kenneth Davey, Qiang Xu, Yao Zheng,* and Shi-Zhang Qiao*, Journal of the American Chemical Society, 2021, 143, 6681–6690.

Principal Author

Name of Principal Author (Candidate)	Xianlong Zhou		
Contribution to the Paper	Conducted material synthesis, carried out electrochemical tests and wrote the paper		
Overall percentage (%)	70		
Certification:	This paper reports on original research I conducted during the period of my Higher Degree by Research candidature and is not subject to any obligations or contractual agreements with a third party that would constrain its inclusion in this thesis. I am the primary author of this paper.		
Signature		Date	09/09/2022

Co-Author Contributions

By signing the Statement of Authorship, each author certifies that:

- i. the candidate's stated contribution to the publication is accurate (as detailed above);
- ii. permission is granted for the candidate to include the publication in the thesis; and
- iii. the sum of all co-author contributions is equal to 100% less the candidate's stated contribution.

Name of Co-Author	Juncai Dong		
Contribution to the Paper	Conducted X-ray absorption spectroscopy characterization and analysis		
Signature		Date	09/09/2022

Name of Co-Author	Yihan Zhu		
Contribution to the Paper	Conducted low-dose high-resolution transmission electron microscopy analysis		
Signature		Date	09/09/2022

Name of Co-Author	Lingmei Liu		
Contribution to the Paper	Conducted low-dose high-resolution transmission electron microscopy characterization		
Signature		Date	09/09/2022

Name of Co-Author	Yan Jiao		
Contribution to the Paper	Conducted Density Functional Theory computations		
Signature		Date	09/09/2022

Name of Co-Author	Huan Li		
Contribution to the Paper	Conducted XRD simulations		
Signature		Date	09/09/2022

Name of Co-Author	Yu Han		
Contribution to the Paper	Conducted low-dose high-resolution transmission electron microscopy and analysis		
Signature		Date	09/09/2022

Name of Co-Author	Kenneth Davey		
Contribution to the Paper	Helped to revise the manuscript		
Signature		Date	09/09/2022

Name of Co-Author	Qiang Xu		
Contribution to the Paper	Helped to evaluate and edit the manuscript		
Signature		Date	09/09/2022

Name of Co-Author	Yao Zheng		
Contribution to the Paper	Discussion of research plan, manuscript revision, and acted as corresponding author		
Signature		Date	09/09/2022

Name of Co-Author	Shi-Zhang Qiao		
Contribution to the Paper	Supervised development of work, helped in manuscript evaluation and revision, and acted as corresponding author		
Signature		Date	09/09/2022

Please cut and paste additional co-author panels here as required.

Molecular Scalpel to Chemically Cleave Metal–Organic Frameworks for Induced Phase Transition

Xianlong Zhou,[†] Juncai Dong,[†] Yihan Zhu,[†] Lingmei Liu,[†] Yan Jiao, Huan Li, Yu Han, Kenneth Davey, Qiang Xu, Yao Zheng,* and Shi-Zhang Qiao*

Cite This: *J. Am. Chem. Soc.* 2021, 143, 6681–6690

Read Online

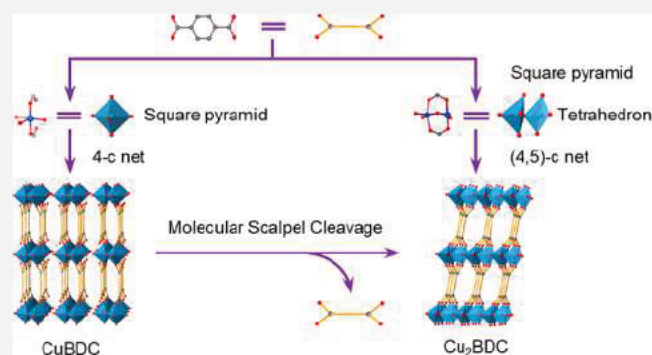
ACCESS |

Metrics & More

Article Recommendations

Supporting Information

ABSTRACT: A bottom up chemical synthesis of metal–organic frameworks (MOFs) permits significant structural diversity because of various combinations of metal centers and different organic linkers. However, fabrication generally complies with the classic hard and soft acids and bases (HSAB) theory. This restricts direct synthesis of desired MOFs with converse Lewis type of metal ions and ligands. Here we present a top down strategy to break this limitation via the structural cleavage of MOFs to trigger a phase transition using a novel “molecular scalpel”. A conventional CuBDC MOF (BDC = 1,4 benzenedicarboxylate) prepared from a hard acid (Cu^{2+}) metal and a hard base ligand was chemically cleaved by L ascorbic acid acting as chemical scalpel to fabricate a new Cu_2BDC structure composed of a soft acid (Cu^{1+}) and a hard base (BDC). Controlled phase transition was achieved by a series of redox steps to regulate the chemical state and coordination number of Cu ions, resulting in a significant change in chemical composition and catalytic activity. Mechanistic insights into structural cleavage and rearrangement are elaborated in detail. We show this novel strategy can be extended to general Cu based MOFs and supramolecules for nanoscopic casting of unique architectures from existing ones.



of redox steps to regulate the chemical state and coordination number of Cu ions, resulting in a significant change in chemical composition and catalytic activity. Mechanistic insights into structural cleavage and rearrangement are elaborated in detail. We show this novel strategy can be extended to general Cu based MOFs and supramolecules for nanoscopic casting of unique architectures from existing ones.

INTRODUCTION

Metal–organic frameworks (MOFs) made with metal ion nodes and organic linkers are an interesting class of crystalline materials. Porous structure and high surface area permit widespread application in material science and nanotechnology.^{1,2} Because properties of MOFs depend strongly on topology of the framework and pore size, synthetic strategies have been developed to fabricate new structures.³ However, coupling between metal centers and ligands, in principle, must align with the qualitative hard and soft acids and bases (HSAB) theory. This means a hard acid prefers to coordinate with a hard base, and vice versa.^{4,5} For example, hard acidic metal ions such as Al^{3+} , Fe^{3+} , Ti^{4+} , and Zr^{4+} are used to fabricate stable MOFs with carboxylate based linkers that act as hard bases, such as MIL 100, MIL 125, and UiO 66.⁶ It is practically difficult to obtain a class of MOFs fabricated with soft acids and hard bases via conventional hydrothermal or solvothermal methods. For example, Cu^{1+} as a typical soft acid is likely to be oxidized and undergoes disproportionation reaction in aqueous media;⁷ stable single phase Cu(I) MOFs are always formed with soft bases, such as nitrogen or sulfur containing ligands.^{8,9} The bond energy of Cu–O is typically greater than that for Cu–N coordination. Cu MOFs fabricated with the carboxylate based ligands display a thermal stability and have broad catalytic applications.¹⁰ For this reason, it is

desirable to fabricate new MOFs with soft acid metals and hard base ligands. HSAB theory, however, acts to limit categories of functional MOFs and applications.

In contrast to direct synthesis, post treatment methods are critical in creating new MOFs because they permit introduction of additional chemical functions into structures.^{11,12} An important effect of post treatment is the introduction of abundant vacancies into the framework (e.g., missing metals or linkers). These are widely used to regulate electrical structure of MOFs to boost catalytic performance.^{13–15} There are two general postsynthetic strategies: (1) physical or chemical etching by water or acid to create metal/linker defects and hierarchical pores,^{16–18} and; (2) exfoliating bulk crystals into ultrathin nanosheets.^{19–21} However, etching treatments are random and uncontrollable at the molecular level. This results in formation of disordered defects or pores in a complicated structure. Significantly, morphology and structure of derived MOFs are highly dependent on those of

Received: March 4, 2021

Published: April 23, 2021



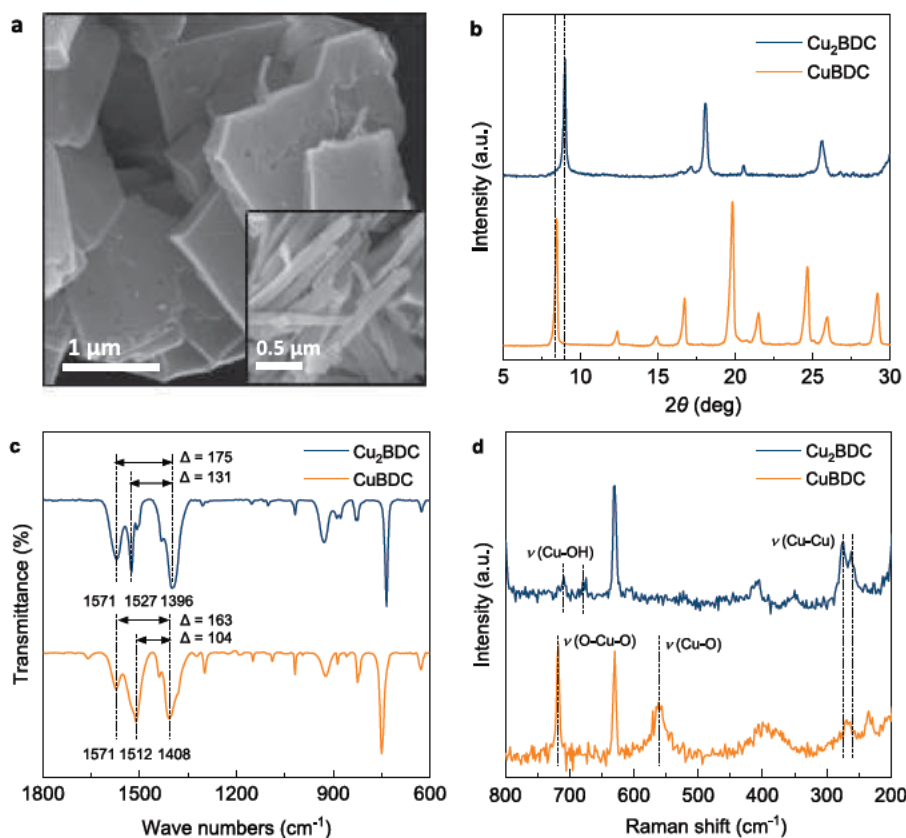


Figure 1. (a) SEM images of CuBDC and Cu₂BDC (inset); (b) XRD patterns of CuBDC and Cu₂BDC. CuBDC is iso structural to that reported (no. 141928, space group of *Pmc2₁*, Cambridge Crystallographic Data Centre);³⁶ (c) FTIR spectra of CuBDC and Cu₂BDC. (d) Raman spectra of CuBDC and Cu₂BDC.

initial ones. In consequence, these strategies do not permit creation of new categories of MOF because of unachievable phase transition control.

Phase transition has been reported for many crystalline MOFs. This is especially the case for flexible and dynamic ones exposed to stimuli (e.g., temperature, pressure, light, ad/desorption of a gas or solvent and a modulator).²² For example, Farha et al. reported formic acid as a modulator facilitates a phase transition between NU 1008 and NU 906.²³ In situ characterizations were employed to demonstrate this transition as being realized by dissolution/reprecipitation. This type of phase transition, however, only induces change in pore volume and bond angle. Overall chemical composition of the MOF and connection mode between metals and linkers remains unchanged.²⁴ An intrinsic reason is the lack of practical control in breaking of old chemical bonds and concomitant reforming of new ones for the new structure. To date only solvent assisted metal/linker exchange has been reported to achieve full phase transition between different compounds.^{25,26} These ion exchanges, however, must conform to HSAB theory. This therefore limits choice of metal/linker. In contrast to conventional phase transition that results from a rearrangement of the entire structure, the linker cleaving method can regulate the MOF's local bonds via chemical, thermal, or etching treatment. This includes clipping parts of linkers to introduce specific defects, cleavage of labile linkers to tailor the size of pores, and net clipping to deconstruct ligand symmetry.^{13,18,27–30} However, these cleaving strategies alter only the local coordinated environment, resulting in slight changes in the overall topology of the MOF.

Here, we report a novel, chemical molecular scalpel cleaving as a strategy to precisely regulate the local coordination environment of an MOF, together with derivation of a new topological structure. It is designed to circumvent limitations in HSAB theory to fabricate a new ordered Cu₂BDC (BDC = 1,4 benzenedicarboxylate) MOF composed of a soft acid metal and a hard base ligand. Starting with a reported CuBDC MOF, we demonstrate L ascorbic acid (LA) acting as a molecular scalpel to finely regulate the chemical state and coordination number of Cu metal centers to cleave BDC linkers. A controlled phase transition from CuBDC to Cu₂BDC with resulting different chemical composition and topological structure was achieved. Mechanistic insights into successive structural cleavage are elaborated based on combined high resolution microscopy imaging and vibrational spectrum. We discuss applications to general Cu based MOFs and supra molecules for nanoscopic casting of unique architectures from existing ones.

RESULTS AND DISCUSSION

Structural Characterization. CuBDC was synthesized via a combined solvothermal method coupled with solvent exchange.³¹ Scanning electron microscopy (SEM) images showed that the as prepared CuBDC was a micrometer scaled sheet shape. In contrast, following LA treatment it exhibited ordered nanoribbon structure, together with a highly significant reduction in width from 2 to 0.2 μm (Figure 1a). Thickness was highly significantly reduced from 600 to 60 nm (Figure S1). This highly significant change in morphology resulted from modulation of the MOF structure (discussed in

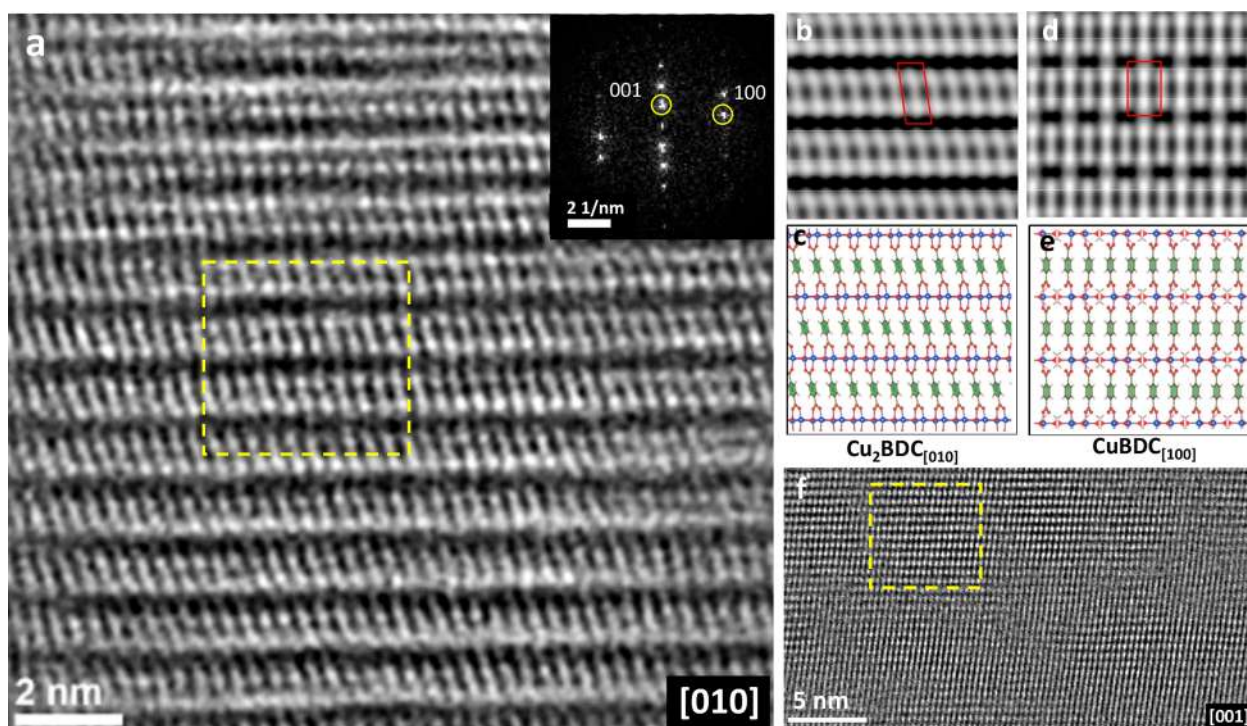


Figure 2. (a) CTF corrected HRTEM image of Cu_2BDC and FFT pattern (inset) along the $[010]$ projection; (b, c) simulated potential map of highlighted area shown in (a) and proposed structural model for Cu_2BDC projected along the $[010]$ projection; (d, e) simulated potential map and structural model for CuBDC along the $[100]$ projection; (f) HRTEM image of Cu_2BDC taken near the Scherzer defocus along the $[001]$ projection.

following sections). Thermogravimetric (TGA) analysis showed the ratio of Cu and BDC changed from 1 to 2 following LA treatment (Figure S2, see detailed analysis in the Supplementary Note). Therefore, the as synthesized MOF was denoted as Cu_2BDC . The phase transition was confirmed by power X ray diffraction (XRD) patterns (Figure 1b), which show a decreased (001) crystallographic plane from 1.05 (CuBDC) to 0.97 nm (Cu_2BDC), indicating a compression of the metal oxide interlayer spacing.

Fourier transform infrared spectroscopy (FTIR) was employed to investigate the coordination mode of Cu and carboxylate linker in the forms of chelating, bridging, ionic or monodentate.³² The splitting value of asymmetric and symmetric stretch of carboxylic vibration, $\Delta = \nu_{\text{as}}(\text{COO}^-) - \nu_{\text{s}}(\text{COO}^-)$, was used to determine the mode of binding (Figure S3).³³ As is shown in Figure 1c two antisymmetric peaks appear in Cu_2BDC and CuBDC . For Cu_2BDC , O atoms of carboxylate groups connect with two different Cu atoms respectively, yielding two peaks of 1571 and 1527 cm^{-1} .^{34,35} In contrast in CuBDC , two O atoms connect to two different atoms. One O atom connects to Cu metal to yield an antisymmetric peak at 1571 cm^{-1} . The other O atom connects to H from the coordinated H_2O in the structure, and results in formation of hydrogen bonds (Figure S4). Therefore, the values of 175 and 131 cm^{-1} on Cu_2BDC are consistent with a bridging character that is greater than 163 and 104 cm^{-1} on CuBDC for a monodentate mode.³⁶ These two values are lower than those of a normal monodentate mode because the inherent hydrogen bond withdraws the electron density of the C–O bond to the oxygen atom, resulting in the frequency of the antisymmetric peaks of CuBDC shifting to a lower wavenumber. Additionally, the hydrogen bond broadens the

peak at 1512 cm^{-1} to contrast with the sharp peak at 1527 cm^{-1} in Cu_2BDC .

In Raman spectroscopy (Figure 1d), the pair of peaks at 718 and 561 cm^{-1} in CuBDC can be assigned to $(\text{H}_2\text{O})\text{O}-\text{Cu}-\text{O}(\text{H}_2\text{O})$ and $\text{Cu}-\text{O}(\text{H}_2\text{O})$ stretching, respectively.³⁷ The disappearance of them from Cu_2BDC indicates that the coordinated water in the framework of CuBDC had been cleaved. Additionally, the new pair of peaks at 709 and 678 cm^{-1} in Cu_2BDC can be attributed to $\text{Cu}(\text{OH})_x$ species,^{38,39} indicating a mixed state of $\text{Cu}^{1+}/\text{Cu}^{2+}$ ions. The initial peak at 268 cm^{-1} in CuBDC split into two at 275 and 263 cm^{-1} . This finding shows that the Cu sites of Cu_2BDC underwent a rearrangement and became two kinds of Cu–Cu stretches⁴⁰ that agree well with those from FTIR.

Atomic Structural Analyses by High-Resolution Transmission Electron Microscopy (HRTEM). The vibrational spectroscopic investigations showed distinct structures of CuBDC and Cu_2BDC . The recent breakthroughs in low dose HRTEM imaging techniques permit direct structural elucidation of atomic structure.^{41,42} As is shown in Figure S5, the nanoribbon shaped Cu_2BDC is assembled by small, thin nanocrystals along the $[001]$ projection, which typically differs from bulk thick CuBDC in Figure S6. A high magnification TEM image and corresponding fast Fourier transform (FFT) patterns confirmed that these nanocrystals are highly crystalline (Figure 2a). It is therefore that Cu_2BDC adopts a layered structure similar to that of CuBDC , i.e., CuO_x polyhedral sheets bridged by BDC linkers (Figure 2b–e).

However, there is a significant difference between the layering of polyhedral sheets in Cu_2BDC with that of its parent CuBDC . Instead of two split dark dot contrast, mainly arising from well separated neighboring H_2O terminated CuO_x polyhedral columns in CuBDC along the $[100]$ projection,

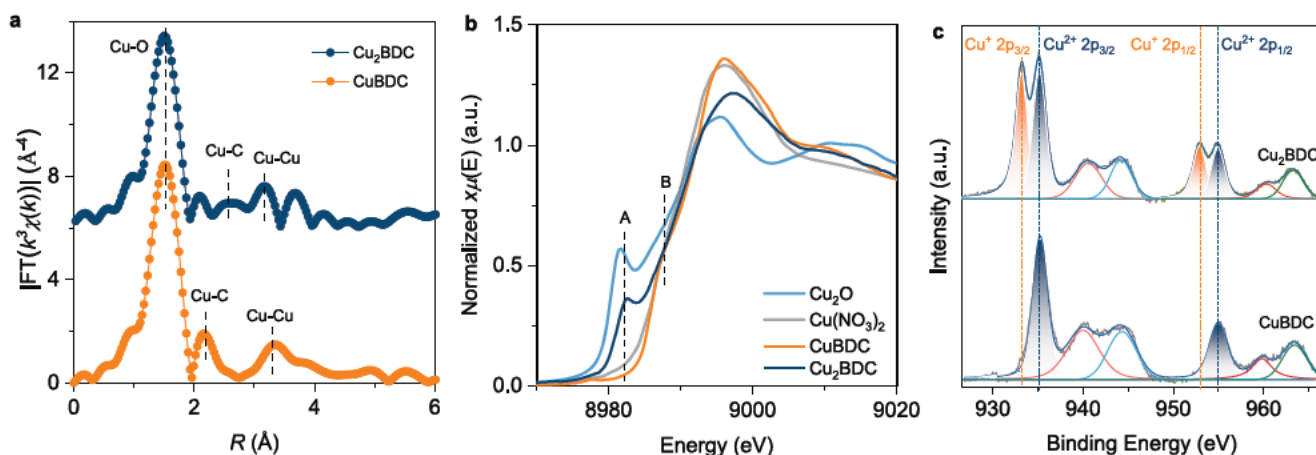


Figure 3. (a) Fourier transformed magnitudes of experimental K edge EXAFS signals for CuBDC and Cu₂BDC. The Fourier transforms are not corrected for phase shift. (b) Comparison between experimental XANES spectra of CuBDC, Cu₂BDC, and reference materials. (c) XPS spectra for Cu 2p. The fitted peaks at 933.21 and 935.20 eV are assigned to Cu¹⁺ and Cu²⁺ species, respectively.⁴⁴

Cu₂BDC exhibits a broadened and merged dark dot contrast for CuO_x polyhedral columns along the [010] projection (Figure 2b–e). This is indicative of the decreased Cu–Cu projected distance arising from dehydration and condensation of neighboring CuO_x polyhedral in CuBDC, as was observed in the Raman spectra. Therefore, a structural model for Cu₂BDC can be proposed and optimized by density functional theory (DFT) methods. The structural projection and simulated potential of the optimized model agreed well with the CTF corrected HRTEM image along the [010] projection (Figure 2a–c). The HRTEM image from an additional [001] projection was taken (Figure 2f), which is also consistent with the projected structure and potential of the proposed structural model (Figure S7). Taken together low dose HRTEM along with FTIR and Raman spectroscopy, allow the unambiguous structural determination of the new Cu₂BDC phase that is formed via dehydration and condensation of CuO_x polyhedral by the chemical cleavage.

Atomic Structural Analyses by Spectroscopies. The coordination environment and chemical state of the Cu atoms in Cu₂BDC were explored by Cu K edge extended X ray absorption fine structure (EXAFS) and X ray absorption near edge structure (XANES). In the R space EXAFS, both samples contained a major Cu–O peak together with two minor peaks. These are attributed to the higher coordination shells of Cu–C and Cu–Cu, respectively.¹⁶ Compared with pristine CuBDC the Cu₂BDC spectrum has an identifiable shift of the Cu–C and Cu–Cu peaks to the larger and lower R directions (Figure 3a). In the XANES spectra (Figure 3b), both samples exhibited a shoulder peak at 8987 eV arises from the 1s → 4p transition of Cu²⁺ (peak B), whereas in the spectrum of Cu₂BDC, a new and pronounced peak at 8983 eV is present attributed to the 1s → 4p transition of Cu¹⁺ (peak A).⁴³ This difference indicates a significant fraction of Cu¹⁺ ions in Cu₂BDC in contrast to overall Cu²⁺ ions in CuBDC, agree with Raman analysis.

This finding was confirmed by X ray photoelectron spectra (XPS). In contrast to overall Cu²⁺ ion in CuBDC a mixed state of Cu¹⁺/Cu²⁺ was observed in Cu₂BDC with a Cu¹⁺/Cu²⁺ ratio of 1 (Figure 3c).⁴⁴ Moreover, a slow scan XRD data set of the as synthesized MOF was subject to Le Bail whole pattern fitting, which confirms Cu₂BDC as the major phase and traces amount of CuBDC as the impurity phase along with their refined unit cell parameters (Figure S8, Table S1). It is thus

concluded, from the combination of HRTEM, XAS, and XRD results that a new and stable Cu₂BDC structure with metastable Cu¹⁺ ions was successfully synthesized.

Structure Description of Cu₂BDC. Different to CuBDC (Figure S9, see details in the Supplementary Note), Cu₂BDC crystallizes in the triclinic system with space group *P*1. In the structure, the asymmetric unit contains a Cu²⁺ ion (Cu1), a Cu¹⁺ ion (Cu2), and two BDC linkers (Figure S9a). The coordinated Cu1 is completed by two carboxylic oxygen atoms (O1 and O2) of two BDC linkers, one μ₂ oxygen atom (O5) of one water molecule and two μ₃ oxygen atoms (O6, O6B) of two OH units. Therefore, the Cu1 is pyramidally coordinated by five O atoms, forming a square pyramid. In contrast the coordinated Cu2 is completed by two carboxylic oxygen atoms (O3 and O4) of two BDC ligands, one μ₂ oxygen atom (O5A) of one water molecule and one μ₃ oxygen atom (O6B) of one OH unit. Therefore, the Cu2 is quadrilaterally coordinated by four O atoms, forming a tetrahedron. Each square pyramid is corner connected with each other along the [100] direction (Figure S9b) to form parallel copper based chains. Chains are separated by tetrahedrons via corner connecting along the [010] direction to form metal oxide layers. They are separated by the BDC linkers along the [001] direction. The topological analysis of Cu₂BDC shows that every [Cu₂(OH)(H₂O)]²⁺ unit is coordinated with two bridged BDC linkers to form a 4, 5 connected node.

Cleavage Mechanism for CuBDC to Cu₂BDC. A series of ex situ spectra were used to investigate the mechanism of phase transition from CuBDC to Cu₂BDC. This was achieved by controlled synthesis of transition samples during cleavage. The reaction stoichiometry between CuBDC and LA was first established (Figures S10 and S11, see details in the Supplementary Note). To understand this transition, we used complete chemical formulas of each sample. Through reducing LA treatment to 0.06 g, the first transition sample was obtained. The coexistence of two phases is clearly observed on XRD patterns, Figure 4a. From the SEM image, it is observed the microstructure is composed of nanoparticles and nano sheets (Figure S12a). A finding is consistent with TEM (Figure S12b, c). HRTEM images determine the *d* spacing of these nanoparticles is 0.98 nm, Figure S12d. This is consistent with the layer distance of Cu₂BDC (but not for CuBDC at 1.05 nm). The fast Fourier transform (FFT) pattern confirms that

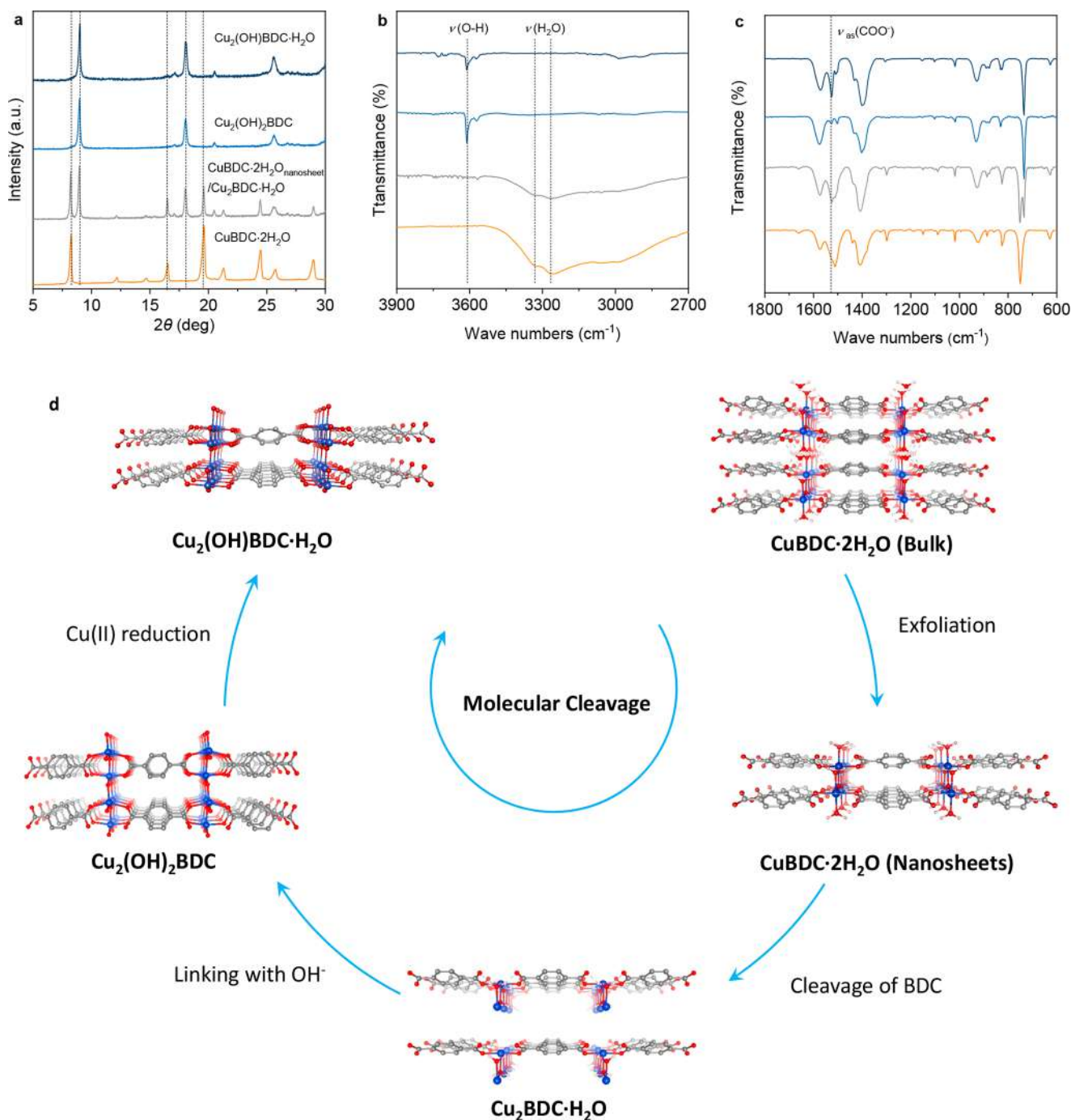


Figure 4. Proposed molecular cleaving mechanism. (a–c) XRD patterns and FTIR spectra of various transition samples; (d) Reaction processes of four step molecular cleaving. The most likely reaction equation for each step is (Step I) $\text{Cu(II)BDC}\cdot 2\text{H}_2\text{O} + 1/2\text{LA} \rightarrow \text{Cu(II)BDC}(\text{LA})_{1/2}\cdot 2\text{H}_2\text{O}$; (Step II) $2\text{Cu(II)BDC}(\text{LA})_{1/2}\cdot 2\text{H}_2\text{O} \rightarrow \text{Cu(I)}_2\text{BDC}\cdot\text{H}_2\text{O} + \text{H}_2\text{BDC} + \text{C}_6\text{H}_8\text{O}_6$; (Step III) $\text{C}_6\text{H}_8\text{O}_6 \leftrightarrow \text{C}_6\text{H}_6\text{O}_6 + 2\text{H}^+ + 2\text{e}^-$; $\text{Cu(I)}_2\text{BDC}\cdot\text{H}_2\text{O} + \text{H}_2\text{O} + \text{C}_6\text{H}_6\text{O}_6 \rightarrow \text{Cu(II)}_2(\text{OH})_2\text{BDC} + \text{C}_6\text{H}_8\text{O}_6$; (Step IV) $\text{Cu(II)}_2(\text{OH})_2\text{BDC} + \text{C}_6\text{H}_8\text{O}_6 \rightarrow \text{Cu}_2(\text{OH})\text{BDC}\cdot\text{H}_2\text{O} + \text{C}_6\text{H}_7\text{O}_6$.

the crystal system of nanoparticles is triclinic, rather than orthorhombic in CuBDC (Figure S12e). This finding suggests the final Cu_2BDC nanoribbons result from growth of these nanoparticles. AFM profile revealed the thickness of nano sheets is ~ 150 nm, Figure S12f. This is a value significantly less than that for CuBDC . It indicates an exfoliation occurred. On the basis of the fact that the pristine $\text{CuBDC}\cdot 2\text{H}_2\text{O}$ crystal structure is connected by these coordinated waters via H bonding, we hypothesized that this step is the chemical exfoliation of bulk $\text{CuBDC}\cdot 2\text{H}_2\text{O}$ into nanosheets via the

breaking of partial H bonds. The DFT computed exfoliation energies (definition can be found in the Supplementary Note) underscored that the bulk model with less coordinated water is more readily exfoliated (Figure S13).

Following the coordination with LA, Cu^{2+} ions in the $\text{CuBDC}\cdot 2\text{H}_2\text{O}$ sheet were chemically reduced, resulting in a decreased valence, and consequently, a lowered coordination number.⁴⁵ The latter triggers breaking the Cu carboxylate coordination together with cleaving of BDC ligands, yielding the second transition samples of $\text{Cu}_2\text{BDC}\cdot\text{H}_2\text{O}$ and H_2BDC in

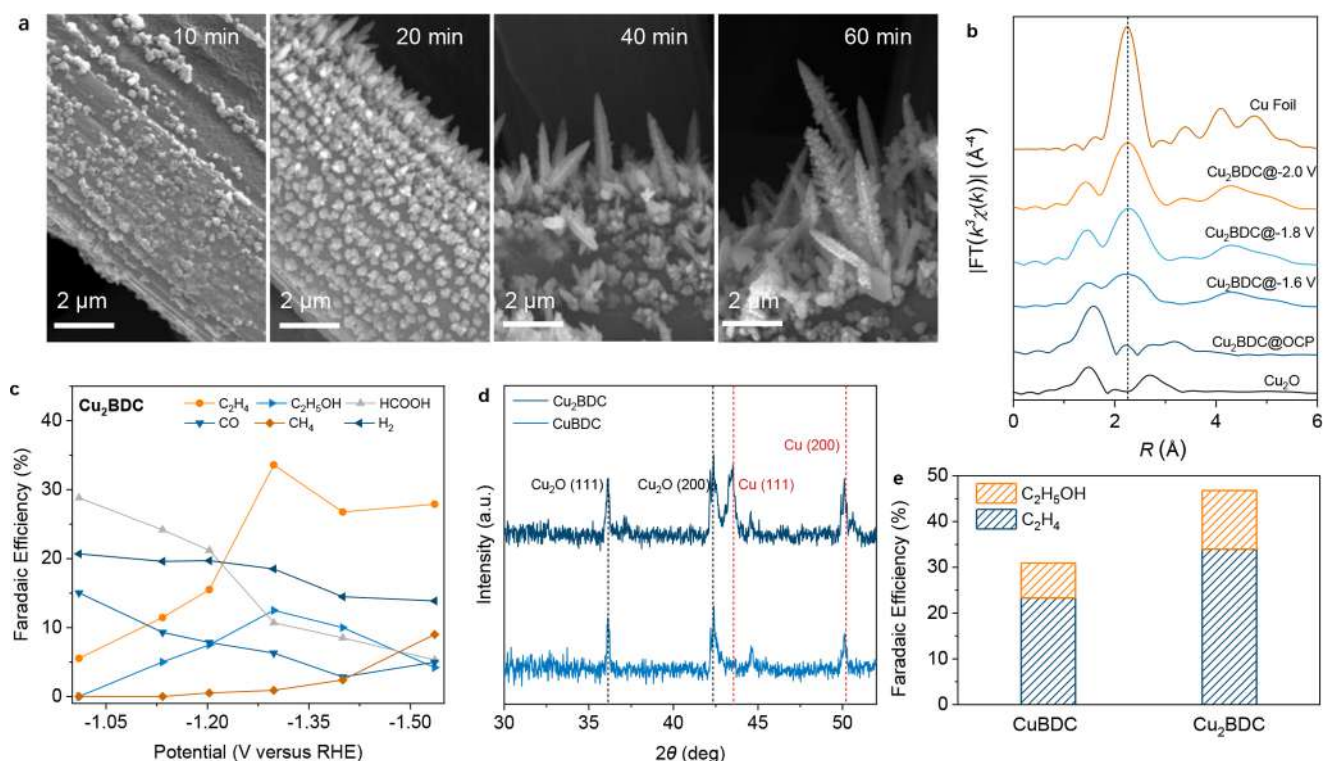


Figure 5. CRR performance on CuBDC and Cu₂BDC derived electrocatalysts. (a) SEM images of Cu₂BDC derived samples under different reduction times at a constant potential of -1.30 V vs RHE. (b) In situ Cu EXAFS spectra of Cu₂BDC under distinct applied potentials vs Ag/AgCl. Cu₂O and Cu foil work as reference samples. (c) Faradaic efficiencies (FE) of CRR products for Cu₂BDC derived sample over a range of applied potentials. (d) XRD patterns for Cu₂BDC and CuBDC derived samples following CRR testing after 60 min at a constant potential of -1.30 V vs RHE. (e) Comparison of FE of C₂ products on different derived electrocatalysts at a constant potential of -1.30 V vs RHE.

solution (Figure 4d, Figure S14). This process is rapid and cannot be controlled by the amount of LA. Additionally, this process is accomplished due to the unique molecular configuration of LA, i.e., two oxygen atoms in the adjacent hydroxyls can attach with two Cu atoms in the CuBDC·2H₂O framework. A slight configuration change results in a more ready cleaving of H₂BDC than that by another hydroquinone (HQ) reductant as a control (Figures S15 and S16). This was confirmed via experiment in which there was no phase or structural change observed in CuBDC·2H₂O as a result of HQ treatment (Figure S17). Additionally, it was found that the traditional acid etching also cannot facilitate the phase transition because it cannot reduce the chemical state of Cu to regulate its coordination number, and consequently, to cleave the BDC linkers (Figure S18). In contrast, as a strong reductant NaBH₄ reduced the CuBDC structure to pure Cu (Figure S19). This finding confirmed the special phase transition function of LA during cleaving.

When missing linkers Cu₂BDC·H₂O is unstable because of the interaction of Cu¹⁺ with H₂O.⁷ LA, however, is readily oxidized into dehydrogenated LA (C₆H₆O₆), which further oxidizes Cu¹⁺ into Cu²⁺ with formation of OH groups in the interlayer (Figure 4d). Specifically, two Cu₂BDC·H₂O molecules are bridged with each other by triple μ_3 OH groups (Figure S20). This results in a Cu₂(OH)₂BDC structure with compression of the metal oxide interlayer spacing, as is evidenced in the XRD patterns (Figure 4a). Given there is no obvious difference in Cu₂(OH)₂BDC and the final Cu₂(OH)BDC·H₂O in XRD patterns, FTIR was employed to determine distinctive local structures. As is shown in Figure 4b the Cu₂(OH)₂BDC structure was confirmed by formation of a

new, sharp OH peak (3611 cm^{-1}) together with the disappearance of H₂O stretching peaks (3330 and 3270 cm^{-1}).⁴⁶ A $\Delta\nu$ value of 175 cm^{-1} confirms a bridging mode of Cu and BDC coordination, rather than a monodentate one in CuBDC·2H₂O (Figure 4c). With additional LA some of the Cu²⁺ ions in Cu₂(OH)₂BDC were reduced to Cu¹⁺ with removal of the OH bridge to form the final Cu₂(OH)BDC·H₂O (Figure 4d). The peak for OH species in the FTIR spectrum is significantly weaker than that for Cu₂(OH)₂BDC (Figure 4b). In addition, a new, strong peak at 1527 cm^{-1} was observed in Cu₂(OH)BDC·H₂O spectrum compared to that of Cu₂(OH)₂BDC. This can be assigned to Cu¹⁺ coordination with carboxylate (Figure 4c),³⁴ which agrees well with the XANES and XPS results.

Following cleaving, the Cu₂(OH)BDC·H₂O nanocrystalline material self assembled into nanoribbons along the [001] direction because of the interaction between Cu ions and carboxylic acid of 2,3 diketo L gulonic acid (C₆H₈O₇) derived from oxidative LA. This oriented growth is attributed to the fact that the BDC ligands and C₆H₈O₇ have the same carboxylate functionality. The latter works as the capping reagent in the self assembly processing.⁴⁷ This impedes the coordination mode of Cu and BDC in the [100] direction and facilitates crystal growth in the [001] direction.

Catalytic Activity for CRR. It is widely reported that the oxidation state of the surface Cu sites can regulate product distribution of CO₂ reduction reaction (CRR). For example, both theoretical and experimental work has demonstrated that the mixed Cu¹⁺/Cu⁰ species promotes CRR activity and C₂ product selectivity in a synergistic way.⁴⁸ Given that there is Cu²⁺/Cu¹⁺ that is two different Cu atoms in the Cu₂BDC

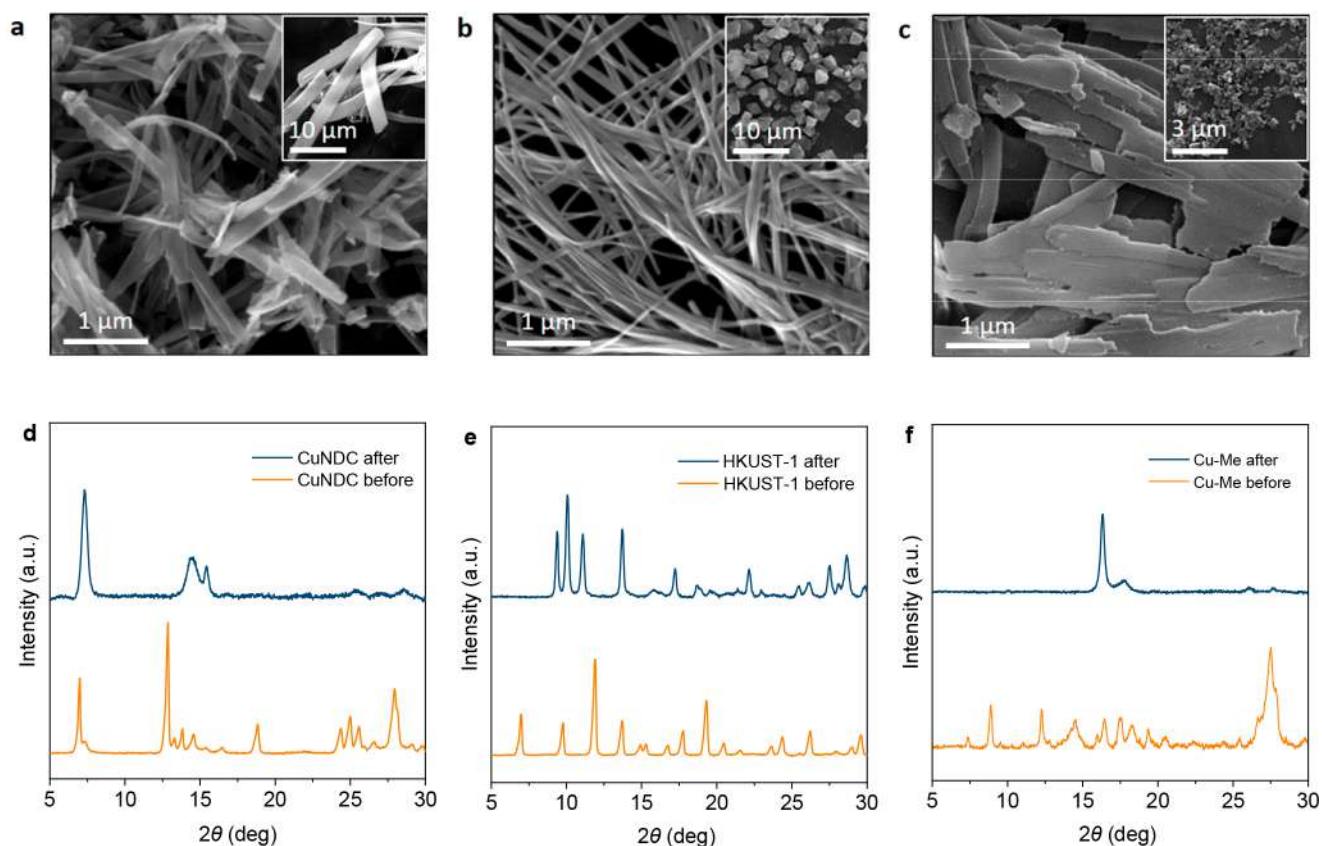


Figure 6. SEM images and XRD patterns of (a, d) CuNDC; (b, e) HKUST 1; (c, f) Cu Me before (insets in panels a–c) and after LA treatment.

framework, we expect that these will be converted into target $\text{Cu}^{1+}/\text{Cu}^0$ species under a negative potential of CRR. The ex situ SEM images indicate a structure reconstruction occurred following electrochemical reduction at constant potential. In this, the original nanoribbon morphology evolved into nanoneedles (Figure 5a, Figure S21). As is shown by the in situ Cu EXAFS characterization, under low potentials of CRR pristine Cu_2BDC is decomposed and converted into, mainly, Cu and a small amount of Cu_2O (Figure 5b).

Electrochemical testing showed that the Cu_2BDC derived sample gave greater C_2 products (ethylene and ethanol) and lower CO and H_2 Faradaic efficiencies (FE) when compared with derived CuBDC (Figure 5c, Figure S22) and MOF derived Cu based CRR electrocatalysts, Table S2. The improved C_2 product selectivity on Cu_2BDC derived samples is attributed to Cu_2O (111) and Cu (111) mixed phases. However, there is no such couple in derived CuBDC (Figure 5d). As a result, Cu_2BDC derived samples exhibited a FE of 46.8% for ethylene and ethanol. Significantly, this is a greater value than for the derived CuBDC (Figure 5e).

Generalization to Other Linkers. To assess generalization of the molecular scalpel cleavage, we tested three additional linker formed MOFs and supramolecules. A long dicarboxylic linker was used to prepare CuNDC (NDC = 2, 6 naphthalenedicarboxylic acid). Following LA treatment the initial bulk sheets converted into thicker, nanobelts with a phase transition. This is a similar finding to CuBDC (Figure 6a, d). FTIR spectra exhibited a stronger peak at 1702 cm^{-1} following treatment. This finding is attributed to the stretching of free $-\text{COOH}$ species as a result of Cu–O bond cleavage (Figure S23a). In addition to dicarboxylic linkers, we

confirmed that the tricarboxylic 1,3,5 benzenetricarboxylate (TA) based HKUST 1 can be cleaved into nanowires that are narrower than those for Cu_2BDC (Figure 6b). XRD patterns and FTIR spectra showed clearly a phase transition with a change in coordination of Cu and carboxylates (Figure 6e, Figure S23b). Importantly, this cleavage can be extended to a nitrogen containing soft base melamine formed Cu melamine complex (Cu Me) (Figure 6c, f).^{49,50} FTIR spectra indicated the formation of Cu^{1+} Me complex after cleavage, evidenced by a peak splitting from 1476 cm^{-1} into 1480 and 1464 cm^{-1} (Figure S23c).⁵¹ The width of the nanosheets significantly increased compared with that for the initial nanoparticle, and was greater than that for Cu_2BDC . This finding likely results because of the difference of carboxylate in melamine and because $\text{C}_6\text{H}_8\text{O}_7$ cannot work as a capping reagent to impede the growth of Cu Me along any one specific direction.

In addition to the Cu based MOFs, we investigated application of the novel molecular cleavage to metal ions based MOFs including NiBDC and FeBDC. Both of these have a structure similar to CuBDC. For NiBDC there was no phase transition and its size became less after treatment (Figure S24). We hypothesize that this change is because of completion of the first step of etching but without linker cleaving because of lack of $\text{Ni}^{2+}/\text{Ni}^{1+}$ redox. For FeBDC, the initial spindle morphology was broken following treatment to generate bulk H_2BDC only (Figure S25). The reason, most likely, is that there were no stable chemical bonds forming between Fe^{2+} and nearby BDC to complete steps similar to Step III and IV of Figure 4d. This finding emphasizes that to fabricate a new structure using molecular scalpel cleaving, the metal center in parent MOF should possess not only a redox

pair but also be capable of forming new chemical bonds with adjacent linkers.

CONCLUSIONS

A novel molecular scalpel strategy for controlled cleaving of MOFs via a series of chemical bond breaking, generation, and rearrangement is presented. It relies on a novel redox reaction to accomplish phase transition and breaks with HSAB theory to construct new MOFs with soft acid and hard base type coordination bonds. We demonstrated this with chemical cleaving of CuBDC by LA to fabricate a new Cu₂BDC structure where LA precisely cleaved the BDC linkers and facilitated new chemical bonds formation. During this process we achieved precise regulation of the local bond environment together with the creation of a new topological structure. The atomic structure of the resultant Cu₂BDC was confirmed via low dose HRTEM imaging and vibrational spectroscopies. Cu₂BDC derived material acting as a CRR catalyst exhibited greater FE for C₂ products because of the formation of additional Cu (111) compared with its parent CuBDC. This new strategy appears generalizable to other linkers of Cu MOFs or to supramolecules. It could therefore be used to controllably clip off various macromolecule materials for broad applications in nanotechnology and catalysis.

EXPERIMENTAL SECTION

Materials Synthesis. Pristine CuBDC was synthesized according to the literature.³¹ Two millimoles of Cu(NO₃)₂·6H₂O and 2 mmol of H₂BDC were dissolved in 45 mL of dimethylformamide (DMF). This was placed in a closed three necked bottle in an oil bath at 110 °C for 24 h. The teal colored precipitate powder was washed with DMF three times and then vacuum dried at 80 °C overnight. The as synthesized powder was washed with deionized water three times and freeze dried for 48 h to obtain a final product. For a standard molecular cleaving treatment, 0.2 g of CuBDC was dispersed in 8 mL of deionized water with sonication for 10 min; 0.12 g of LA was added to the solution at room temperature. Following sonication for 1 h (135 W, 42 KHZ) the precipitate was washed with, respectively, DMF and deionized water three times. Cu₂BDC powder was obtained after freeze drying for 48 h. The controlled synthesis of additional transition samples and the synthesis of additional MOFs can be found in the [Supporting Information](#).

Materials Characterization. The phase and structure of as synthesized samples were analyzed by power X ray diffraction on a Rigaku MiniFlex 600 X ray diffractometer ($\lambda = 1.5406 \text{ \AA}$, scan rate = 5° min^{-1}). SEM images were obtained on a FEI QUANTA 450 electron microscope. FTIR spectra were collected on a Nicolet 6700 spectrometer. TGA profiles were obtained from a TGA/SETARAM thermogravimetric analyzer from 25 to 800 °C with a heating rate of $10^\circ \text{ C min}^{-1}$ in air flow. Raman spectra were collected on a confocal Raman microscope (Horiba LabRAM HR Evolution) with a 532 nm solid laser as an excitation source ($100\text{--}2000 \text{ cm}^{-1}$). XPS measurements were conducted on Kratos Axis Ultra XPS (mono Al K α 1486.6 eV) and recorded by a hemispherical analyzer with a step size of 0.05 eV.

HRTEM. Low dose HRTEM experiments were carried out on a Cs corrected FEI cubed G2 Titan 60–300 electron microscope operated at 300 kV. Specimen searching, zone axis alignment, and defocusing were carried out at 9800 \times magnification. Selected area electron diffraction (SAED) patterns were obtained using a Gatan Ultrascan CCD camera. HRTEM images were obtained at 55 000 \times magnification using a Gatan K2 direct detection camera in electron counting mode with dose fractionation function. Each image stack was composed of 120 frames using 0.05 s exposure for each frame. The HRTEM images containing periodic structural information are denoised by average background subtraction filter (ABSF).⁵² The contrast inversion arising from contrast transfer function (CTF) of

the objective lens is corrected at a defocus value of 260 nm for the [010] zone axis HRTEM image according to previous reports.^{41,42} The projected potential maps are simulated using QSTEM code with a point spread function (PSF) width of 0.3 Å.

X-ray Absorption Spectroscopy (XAS) Analysis. Cu K edge X ray absorption spectra were obtained under ambient condition in fluorescence mode at beamline 1W2B in the Beijing Synchrotron Radiation Facility (BSRF), China, using a Si (111) double crystal monochromator. The energy was calibrated using Cu foil, both the incident and fluorescence X ray intensities were monitored using respectively standard ion chambers and Ar filled Lytle type detector. The XAS raw data were background subtracted, normalized and Fourier transformed using standard procedures with ATHENA.⁵³ A customized reaction H cell was adopted to conduct in situ absorption spectroscopy measurements of the Cu K edge in total fluorescence mode. The measurements were carried out using a typical three electrode setup with the same conditions as the electrochemical measurement but performed in a specially designed Teflon container with a window sealed by Kapton tape.

Electrochemistry Measurement. The CRR catalytic activity of different samples was investigated by a standard H cell in CO₂ saturated 0.1 M KI electrolyte. The volume of both anode and cathode chamber electrolyte was 50 mL. To prepare the working electrode 5 mg of catalyst was dispersed by sonication in 600 μL of methanol, 350 μL of deionized water, and 50 μL of 5 wt % of Nafion for 30 min. 50 μL of ink was dipped onto a carbon fiber paper (loading mass 0.5 mg cm⁻²). Prior to CRR a constant potential of -1.3 V vs reversed hydrogen electrode (RHE) was applied for 60 min. This was to electrochemically reduce the working electrodes and to form active catalysts. The reference and counter electrodes were, respectively, Ag/AgCl (3.0 M KCl) and RuO₂ coated Ti mesh electrode connected to a 760E potentiostat (CH Instruments). CO₂ was continuously purged at 10 $\mu\text{L min}^{-1}$. The gas product was detected by a gas chromatograph (GC, 7890B, Agilent, USA) equipped with TCD and methanizer/FID detectors. H¹ nuclear magnetic resonance spectroscopy (NMR, AS00a DD2 500 MHz, Agilent, USA) was used to analyze liquid products. Phenol and DMSO as known internal standards were utilized to obtain a calibration curve to quantifying the liquid products.

ASSOCIATED CONTENT

Supporting Information

The Supporting Information is available free of charge at <https://pubs.acs.org/doi/10.1021/jacs.1c02379>.

Synthesis of other samples, characterization, DFT calculations, etc. (PDF)

AUTHOR INFORMATION

Corresponding Authors

Yao Zheng – School of Chemical Engineering and Advanced Materials, The University of Adelaide, Adelaide, South Australia 5005, Australia; [orcid.org/0000 0002 2411 8041](https://orcid.org/0000-0002-2411-8041); Email: yao.zheng01@adelaide.edu.au

Shi Zhang Qiao – School of Chemical Engineering and Advanced Materials, The University of Adelaide, Adelaide, South Australia 5005, Australia; [orcid.org/0000 0002 4568 8422](https://orcid.org/0000-0002-4568-8422); Email: s.qiao@adelaide.edu.au

Authors

Xianlong Zhou – School of Chemical Engineering and Advanced Materials, The University of Adelaide, Adelaide, South Australia 5005, Australia

Juncal Dong – Beijing Synchrotron Radiation Facility, Institute of High Energy Physics, Chinese Academy of Sciences, Beijing 100049, China; [orcid.org/0000 0001 8860 093X](https://orcid.org/0000-0001-8860-093X)

Yihan Zhu – Center for Electron Microscopy, State Key Laboratory Breeding Base of Green Chemistry Synthesis Technology and College of Chemical Engineering, Zhejiang University of Technology, Hangzhou 310014, China; [orcid.org/0000 0003 0183 8350](https://orcid.org/0000-0003-0183-8350)

Lingmei Liu – Physical Sciences and Engineering Division, Advanced Membranes and Porous Materials Centre, King Abdullah University of Science and Technology, Thuwal 23955 6900, Saudi Arabia; [orcid.org/0000 0002 3273 9884](https://orcid.org/0000-0002-3273-9884)

Yan Jiao – School of Chemical Engineering and Advanced Materials, The University of Adelaide, Adelaide, South Australia 5005, Australia; [orcid.org/0000 0003 1329 4290](https://orcid.org/0000-0003-1329-4290)

Huan Li – School of Chemical Engineering and Advanced Materials, The University of Adelaide, Adelaide, South Australia 5005, Australia

Yu Han – Physical Sciences and Engineering Division, Advanced Membranes and Porous Materials Centre, King Abdullah University of Science and Technology, Thuwal 23955 6900, Saudi Arabia; [orcid.org/0000 0003 1462 1118](https://orcid.org/0000-0003-1462-1118)

Kenneth Davey – School of Chemical Engineering and Advanced Materials, The University of Adelaide, Adelaide, South Australia 5005, Australia

Qiang Xu – AIST Kyoto University Chemical Energy Materials Open Innovation Laboratory (ChEM OIL), National Institute of Advanced Industrial Science and Technology (AIST), Kyoto 606 8501, Japan; [orcid.org/0000 0001 5385 9650](https://orcid.org/0000-0001-5385-9650)

Complete contact information is available at:
<https://pubs.acs.org/10.1021/jacs.1c02379>

Author Contributions

[†]X.Z., J.D., Y.Z., and L.L. contributed equally to this work.

Notes

The authors declare no competing financial interest.

ACKNOWLEDGMENTS

This work was financially supported by the Australian Research Council through Discovery Project programs (FL170100154 and DP190103472). J.D. acknowledges financial support from Youth Innovation Promotion Association CAS. Y.Z. acknowledges financial support from the National Natural Science Foundation of China (Grant 21771161, 22075250).

REFERENCES

- (1) Wang, Q.; Astruc, D. State of the art and prospects in metal organic framework (MOF) based and MOF derived nanocatalysis. *Chem. Rev.* **2020**, *120*, 1438–1511.
- (2) Diercks, C. S.; Liu, Y.; Cordova, K. E.; Yaghi, O. M. The role of reticular chemistry in the design of CO₂ reduction catalysts. *Nat. Mater.* **2018**, *17*, 301–307.
- (3) Xiao, X.; Zou, L.; Pang, H.; Xu, Q. Synthesis of micro/nanoscaled metal organic frameworks and their direct electrochemical applications. *Chem. Soc. Rev.* **2020**, *49*, 301–331.
- (4) Chattaraj, P. K.; Lee, H.; Parr, R. G. HSAB principle. *J. Am. Chem. Soc.* **1991**, *113*, 1855–1856.
- (5) Yuan, S.; Feng, L.; Wang, K.; Pang, J.; Bosch, M.; Lollar, C.; Sun, Y.; Qin, J.; Yang, X.; Zhang, P.; Wang, Q.; Zou, L.; Zhang, Y.; Zhang, L.; Fang, Y.; Li, J.; Zhou, H. C. Stable metal organic frameworks: design, synthesis, and applications. *Adv. Mater.* **2018**, *30*, 1704303.

- (6) Howarth, A. J.; Liu, Y.; Li, P.; Li, Z.; Wang, T. C.; Hupp, J. T.; Farha, O. K. Chemical, thermal and mechanical stabilities of metal organic frameworks. *Nat. Rev. Mater.* **2016**, *1*, 15018.

- (7) Blumberger, J. Cu(aq)⁺/Cu(aq)²⁺ redox reaction exhibits strong nonlinear solvent response due to change in coordination number. *J. Am. Chem. Soc.* **2008**, *130*, 16065–16068.

- (8) Coskun, A.; Hmadeh, M.; Barin, G.; Gandara, F.; Li, Q.; Choi, E.; Strutt, N. L.; Cordes, D. B.; Slawin, A. M.; Stoddart, J. F.; Sauvage, J. P.; Yaghi, O. M. Metal organic frameworks incorporating copper complexed rotaxanes. *Angew. Chem., Int. Ed.* **2012**, *51*, 2160–2163.

- (9) Troyano, J.; Castillo, O.; Martínez, J. I.; Fernández Moreira, V.; Ballesteros, Y.; Maspoch, D.; Zamora, F.; Delgado, S. Reversible thermochromic polymeric thin films made of ultrathin 2D crystals of coordination polymers based on copper(I) thiophenolates. *Adv. Funct. Mater.* **2018**, *28*, 1704040.

- (10) Yaghi, O. M.; O’Keeffe, M.; Ockwig, N. W.; Chae, H. K.; Eddaoudi, M.; Kim, J. Reticular synthesis and the design of new materials. *Nature* **2003**, *423*, 705–714.

- (11) Cohen, S. M. The postsynthetic renaissance in porous solids. *J. Am. Chem. Soc.* **2017**, *139*, 2855–2863.

- (12) Wang, Z.; Cohen, S. M. Postsynthetic modification of metal organic frameworks. *Chem. Soc. Rev.* **2009**, *38*, 1315–1329.

- (13) Cheng, W.; Zhao, X.; Su, H.; Tang, F.; Che, W.; Zhang, H.; Liu, Q. Lattice strained metal organic framework arrays for bifunctional oxygen electrocatalysis. *Nat. Energy* **2019**, *4*, 115–122.

- (14) Xue, Z.; Liu, K.; Liu, Q.; Li, Y.; Li, M.; Su, C. Y.; Ogiwara, N.; Kobayashi, H.; Kitagawa, H.; Liu, M.; Li, G. Missing linker metal organic frameworks for oxygen evolution reaction. *Nat. Commun.* **2019**, *10*, 5048.

- (15) Fu, Q.; Xie, K.; Tan, S.; Ren, J. M.; Zhao, Q.; Webley, P. A.; Qiao, G. G. The use of reduced copper metal organic frameworks to facilitate CuAAC click chemistry. *Chem. Commun.* **2016**, *52*, 12226–12229.

- (16) Huang, C.; Dong, J.; Sun, W.; Xue, Z.; Ma, J.; Zheng, L.; Liu, C.; Li, X.; Zhou, K.; Qiao, X.; Song, Q.; Ma, W.; Zhang, L.; Lin, Z.; Wang, T. Coordination mode engineering in stacked nanosheet metal organic frameworks to enhance catalytic reactivity and structural robustness. *Nat. Commun.* **2019**, *10*, 2779.

- (17) Wang, K. Y.; Feng, L.; Yan, T. H.; Wu, S.; Joseph, E. A.; Zhou, H. C. Rapid generation of hierarchically porous metal organic frameworks through laser photolysis. *Angew. Chem., Int. Ed.* **2020**, *59*, 1–7.

- (18) Luo, L.; Lo, W. S.; Si, X.; Li, H.; Wu, Y.; An, Y.; Zhu, Q.; Chou, L. Y.; Li, T.; Tsung, C. K. Directional engraving within single crystalline metal organic framework particles via oxidative linker cleaving. *J. Am. Chem. Soc.* **2019**, *141*, 20365–20370.

- (19) Cliffe, M. J.; Castillo Martinez, E.; Wu, Y.; Lee, J.; Forse, A. C.; Firth, F. C. N.; Moghadam, P. Z.; Fairen Jimenez, D.; Gaultois, M. W.; Hill, J. A.; Magdysyuk, O. V.; Slater, B.; Goodwin, A. L.; Grey, C. P. Metal organic nanosheets formed via defect mediated trans formation of a hafnium metal organic framework. *J. Am. Chem. Soc.* **2017**, *139*, 5397–5404.

- (20) Huang, J.; Li, Y.; Huang, R. K.; He, C. T.; Gong, L.; Hu, Q.; Wang, L.; Xu, Y. T.; Tian, X. Y.; Liu, S. Y.; Ye, Z. M.; Wang, F.; Zhou, D. D.; Zhang, W. X.; Zhang, J. P. Electrochemical exfoliation of pillared layer metal organic framework to boost the oxygen evolution reaction. *Angew. Chem., Int. Ed.* **2018**, *57*, 4632–4636.

- (21) Ding, Y.; Chen, Y. P.; Zhang, X.; Chen, L.; Dong, Z.; Jiang, H. L.; Xu, H.; Zhou, H. C. Controlled intercalation and chemical exfoliation of layered metal organic frameworks using a chemically labile intercalating agent. *J. Am. Chem. Soc.* **2017**, *139*, 9136–9139.

- (22) Morris, R. E.; Brammer, L. Coordination change, lability and hemilability in metal organic frameworks. *Chem. Soc. Rev.* **2017**, *46*, 5444–5462.

- (23) Lyu, J.; Gong, X.; Lee, S. J.; Gnanasekaran, K.; Zhang, X.; Wasson, M. C.; Wang, X.; Bai, P.; Guo, X.; Gianneschi, N. C.; Farha, O. K. Phase transitions in metal organic frameworks directly monitored through in situ variable temperature liquid cell trans

mission electron microscopy and in situ X ray diffraction. *J. Am. Chem. Soc.* **2020**, *142*, 4609–4615.

(24) Lo, S. H.; Feng, L.; Tan, K.; Huang, Z.; Yuan, S.; Wang, K. Y.; Li, B. H.; Liu, W. L.; Day, G. S.; Tao, S.; et al. Rapid desolvation triggered domino lattice rearrangement in a metal organic framework. *Nat. Chem.* **2020**, *12*, 90–97.

(25) Yu, D.; Shao, Q.; Song, Q.; Cui, J.; Zhang, Y.; Wu, B.; Ge, L.; Wang, Y.; Zhang, Y.; Qin, Y.; Vajtai, R.; Ajayan, P. M.; Wang, H.; Xu, T.; Wu, Y. A solvent assisted ligand exchange approach enables metal organic frameworks with diverse and complex architectures. *Nat. Commun.* **2020**, *11*, 927.

(26) Lalonde, M. B.; Mondloch, J. E.; Deria, P.; Sarjeant, A. A.; Al Juaid, S. S.; Osman, O. I.; Farha, O. K.; Hupp, J. T. Selective solvent assisted linker exchange (SALE) in a series of zeolitic imidazolate frameworks. *Inorg. Chem.* **2015**, *54*, 7142–7144.

(27) Song, Y.; Feng, X.; Chen, J. S.; Brzezinski, C.; Xu, Z.; Lin, W. Multistep engineering of synergistic catalysts in a metal organic framework for tandem C O bond cleavage. *J. Am. Chem. Soc.* **2020**, *142*, 4872–4882.

(28) Chen, S.; Mukherjee, S.; Lucier, B. E. G.; Guo, Y.; Wong, Y. T. A.; Terskikh, V. V.; Zaworotko, M. J.; Huang, Y. Cleaving carboxyls: understanding thermally triggered hierarchical pores in the metal organic framework MIL 121. *J. Am. Chem. Soc.* **2019**, *141*, 14257–14271.

(29) Guillerm, V.; Xu, H.; Albalad, J.; Imaz, I.; Maspoch, D. Postsynthetic selective ligand cleavage by solid gas phase ozonolysis fuses micropores into mesopores in metal organic frameworks. *J. Am. Chem. Soc.* **2018**, *140*, 15022–15030.

(30) Ortin Rubio, B.; Ghasempour, H.; Guillerm, V.; Morsali, A.; Juanhuix, J.; Imaz, I.; Maspoch, D. Net clipping: an approach to deduce the topology of metal organic frameworks built with zigzag ligands. *J. Am. Chem. Soc.* **2020**, *142*, 9135–9140.

(31) Carson, C. G.; Hardcastle, K.; Schwartz, J.; Liu, X.; Hoffmann, C.; Gerhardt, R. A.; Tannenbaum, R. Synthesis and structure characterization of copper terephthalate metal organic frameworks. *Eur. J. Inorg. Chem.* **2009**, *2009*, 2338–2343.

(32) Zelenak, V.; Vargova, Z.; Gyoryova, K. Correlation of infrared spectra of zinc(II) carboxylates with their structures. *Spectrochim. Acta, Part A* **2007**, *66*, 262–272.

(33) Verpoort, F.; Haemers, T.; Roose, P.; Maes, J. P. Characterization of a surface coating formed from carboxylic acid based coolants. *Appl. Spectrosc.* **1999**, *53*, 1528–1534.

(34) Young, D. M.; Geiser, U.; Schultz, A. J.; Wang, H. H. Hydrothermal synthesis of a dense metal organic layered framework that contains Cu(I) olefinic bonds, $Cu_2(O_2CCH=CHCO_2)$. *J. Am. Chem. Soc.* **1998**, *120*, 1331–1332.

(35) An, B.; Li, Z.; Song, Y.; Zhang, J.; Zeng, L.; Wang, C.; Lin, W. Cooperative copper centres in a metal–organic framework for selective conversion of CO_2 to ethanol. *Nat. Catal.* **2019**, *2*, 709–717.

(36) Deakin, L.; Arif, A. M.; Miller, J. S. Observation of ferromagnetic and antiferromagnetic coupling in 1 D and 2 D extended structures of copper(II) terephthalates. *Inorg. Chem.* **1999**, *38*, 5072–5077.

(37) Prestipino, C.; Regli, L.; Vitillo, J. G.; Bonino, F.; Damin, A.; Lamberti, C.; Zecchina, A.; Solari, P. L.; Kongshaug, K. O.; Bordiga, S. Local structure of framework Cu(II) in HKUST 1 metallorganic framework: spectroscopic characterization upon activation and interaction with adsorbates. *Chem. Mater.* **2006**, *18*, 1337–1346.

(38) Chan, H. Y. H.; Takoudis, C. G.; Weaver, M. J. Oxide film formation and oxygen adsorption on copper in aqueous media as probed by surface enhanced raman spectroscopy. *J. Phys. Chem. B* **1999**, *103*, 357–365.

(39) Zhao, Y.; Chang, X.; Malkani, A.; Yang, X.; Thompson, L.; Jiao, F.; Xu, B. Speciation of Cu surfaces during the electrochemical CO reduction reaction. *J. Am. Chem. Soc.* **2020**, *142*, 9735–9743.

(40) Woertink, J. S.; Smeets, P. J.; Groothaert, M. H.; Vance, M. A.; Sels, B. F.; Schoonheydt, R. A.; Solomon, E. I. A $[Cu_2O]^{2+}$ core in Cu ZSM 5, the active site in the oxidation of methane to methanol. *Proc. Natl. Acad. Sci. U. S. A.* **2009**, *106*, 18908–18913.

(41) Zhu, Y.; Ciston, J.; Zheng, B.; Miao, X.; Czarnik, C.; Pan, Y.; Sougrat, R.; Lai, Z.; Hsiung, C. E.; Yao, K.; Pinnau, I.; Pan, M.; Han, Y. Unravelling surface and interfacial structures of a metal organic framework by transmission electron microscopy. *Nat. Mater.* **2017**, *16*, 532–536.

(42) Zhang, D.; Zhu, Y.; Liu, L.; Ying, X.; Hsiung, C. E.; Sougrat, R.; Li, K.; Han, Y. Atomic resolution transmission electron microscopy of electron beam sensitive crystalline materials. *Science* **2018**, *359*, 675–679.

(43) Kau, L. S.; Spira Solomon, D. J.; Penner Hahn, J. E.; Hodgson, K. O.; Solomon, E. I. X ray absorption edge determination of the oxidation state and coordination number of copper. Application to the type 3 site in *Rhus vernicifera* laccase and its reaction with oxygen. *J. Am. Chem. Soc.* **1987**, *109*, 6433–6442.

(44) Duke, A. S.; Dolgoplova, E. A.; Galhenage, R. P.; Ammal, S. C.; Heyden, A.; Smith, M. D.; Chen, D. A.; Shustova, N. B. Active sites in copper based metal organic frameworks: understanding substrate dynamics, redox processes, and valence band structure. *J. Phys. Chem. C* **2015**, *119*, 27457–27466.

(45) Song, D.; Bae, J.; Ji, H.; Kim, M. B.; Bae, Y. S.; Park, K. S.; Moon, D.; Jeong, N. C. Coordinative reduction of metal nodes enhances the hydrolytic stability of a paddlewheel metal organic framework. *J. Am. Chem. Soc.* **2019**, *141*, 7853–7864.

(46) Huang, Z. L.; Drillon, M.; Masciocchi, N.; Sironi, A.; Zhao, J. T.; Rabu, P.; Panissod, P. Ab initio XRPD crystal structure and giant hysteretic effect ($H_c = 5.9$ T) of a new hybrid terephthalate based cobalt(II) magnet. *Chem. Mater.* **2000**, *12*, 2805–2812.

(47) Tsuruoka, T.; Furukawa, S.; Takashima, Y.; Yoshida, K.; Isoda, S.; Kitagawa, S. Nanoporous nanorods fabricated by coordination modulation and oriented attachment growth. *Angew. Chem., Int. Ed.* **2009**, *48*, 4739–4743.

(48) Zheng, Y.; Vasileff, A.; Zhou, X.; Jiao, Y.; Jaroniec, M.; Qiao, S. Z. Understanding the roadmap for electrochemical reduction of CO_2 to multi carbon oxygenates and hydrocarbons on copper based catalysts. *J. Am. Chem. Soc.* **2019**, *141*, 7646–7659.

(49) Gao, J.; Wang, J.; Qian, X.; Dong, Y.; Xu, H.; Song, R.; Yan, C.; Zhu, H.; Zhong, Q.; Qian, G.; Yao, J. One pot synthesis of copper doped graphitic carbon nitride nanosheet by heating Cu melamine supramolecular network and its enhanced visible light driven photo catalysis. *J. Solid State Chem.* **2015**, *228*, 60–64.

(50) Chen, C.; Yeh, C. W.; Chen, J. D. Syntheses, structures and thermal properties of two new copper(II) melamine complexes. *Polyhedron* **2006**, *25*, 1307–1312.

(51) Wiles, A. B.; Bozzuto, D.; Cahill, C. L.; Pike, R. D. Copper (I) and (II) complexes of melamine. *Polyhedron* **2006**, *25*, 776–782.

(52) Kilaas, R. Optimal and near optimal filters in high resolution electron microscopy. *J. Microsc.* **1998**, *190*, 45–51.

(53) Ravel, B.; Newville, M. ATHENA, ARTEMIS, HEPHAESTUS: data analysis for X ray absorption spectroscopy using IFEFFIT. *J. Synchrotron Radiat.* **2005**, *12*, 537–541.

A Molecular Scalpel to Chemically Cleave Metal-Organic Frameworks for Induced Phase Transition

Xianlong Zhou,^{1#} Juncai Dong,^{2#} Yihan Zhu,^{3#} Lingmei Liu,^{4#} Yan Jiao,¹ Huan Li,¹ Yu Han,⁴
Kenneth Davey,¹ Qiang Xu,⁵ Yao Zheng,^{1*} Shi-Zhang Qiao^{1*}

¹ School of Chemical Engineering and Advanced Materials, The University of Adelaide, Adelaide, SA 5005, Australia.

² Beijing Synchrotron Radiation Facility, Institute of High Energy Physics, Chinese Academy of Sciences, Beijing 100049, China.

³ Center for Electron Microscopy, State Key Laboratory Breeding Base of Green Chemistry Synthesis Technology and College of Chemical Engineering, Zhejiang University of Technology, Hangzhou 310014, China.

⁴ Physical Sciences and Engineering Division, Advanced Membranes and Porous Materials Centre, King Abdullah University of Science and Technology, Thuwal 23955-6900, Saudi Arabia.

⁵ AIST-Kyoto University Chemical Energy Materials Open Innovation Laboratory (ChEM-OIL), National Institute of Advanced Industrial Science and Technology (AIST), Sakyo-ku, Kyoto 606-8501, Japan.

These authors contributed equally.

* Email: yao.zheng01@adelaide.edu.au; s.qiao@adelaide.edu.au

SUPPLEMENTARY NOTES

1. Materials synthesis

Cleavage of CuBDC with different amount of LA. 0.2 g of CuBDC was dispersed in 8 mL of water with sonication for 10 min. Different amount of LA (0.03, 0.06, 0.09, 0.12, and 0.15 g) was added into this mixture. Following sonication for 60 min the precipitate was washed respectively with dimethylformamide (DMF) and deionized water three times. All samples were obtained following freeze-drying for 48 h.

Cleavage of other MOFs with LA. The treatment of other MOFs was similar to that for CuBDC. Typically, 0.2 g of as-prepared CuNDC, HKUST-1, Cu-Me, FeBDC or NiBDC samples and 0.12 g of LA were mixed in 8 mL of deionized water. Following sonication for 1 h, the resultant powder(s) was collected following washing three times with solvent. CuNDC and NiBDC were washed with DMF and deionized water; HKUST-1 and Cu-Me washed with methanol and deionized water; FeBDC washed with deionized water. Samples were collected following freeze-drying for 48 h.

Cleavage of CuBDC with HQ. 0.2 g of CuBDC was dispersed in 8 mL of water with sonication for 10 min. 0.12 g of HQ was added into this mixture. Following sonication for 60 min the precipitate was washed respectively with DMF and deionized water three times. The products were obtained following freeze-drying for 48 h. Different concentrations, temperatures or solvents for HQ treatment are considered to promote the cleavage. Different concentrations mean that 0.12, 0.24 or 0.48 g HQ was used to cleave CuBDC in water, respectively, while the reaction temperature is at 40 °C. Different temperatures mean that 0.12 g HQ was used to cleave CuBDC in water, while the reaction temperature is at 40, 60, or 80 °C. Different solvents mean that 0.12 g HQ was used to cleave CuBDC at 40 °C, while the solvent is water, DMF or CH₃CN, respectively.

Cleavage of CuBDC with HCOOH. 0.2 g of CuBDC was dispersed in 8 mL of water with sonication for 10 min. 0.12 g of HCOOH was added into this mixture. Following sonication for 60 min the

precipitate was washed respectively with DMF and deionized water three times. The products were obtained following freeze-drying for 48 h.

Cleavage of CuBDC with NaBH₄. 0.2 g of CuBDC was dispersed in 8 mL of water with sonication for 10 min. 0.12 g of NaBH₄ was added into this mixture. Following sonication for 60 min the precipitate was washed respectively with DMF and deionized water three times. The products were obtained following freeze-drying for 48 h.

Synthesis of CuNDC. 2 mmol of Cu(NO₃)₂·6H₂O and 2 mmol of 2, 6-Naphthalenedicarboxylic acid were dissolved in 45 mL of DMF and placed in a closed three-necked bottle in an oil-bath under magnetic stirring at 110 °C for 24 h. The resulting powder was collected by washing with DMF three times and then vacuum drying at 80 °C overnight. Through solvent exchange in deionized water CuNDC crystals were collected following freeze-drying for 48 h.

Synthesis of HKUST-1. 2 mmol of Cu(NO₃)₂·6H₂O and 2 mmol of trimesic acid were respectively dissolved in 50 mL of methanol. Following formation of homogeneous solution, the two solutions were mixed and stirred for 2 h at room temperature.¹ Blue precipitate powder was acquired following washing with methanol three times and then vacuum drying at 80 °C overnight. Through solvent exchange in deionized water HKUST-1 crystals were collected following freeze-drying for 48 h.

Synthesis of NiBDC. Preparation of NiBDC was similar to that for CuBDC, in which Cu(NO₃)₂·6H₂O was replaced with Ni(NO₃)₂·6H₂O (2 mmol).

Synthesis of FeBDC. Synthesis of FeBDC followed that reported in the literature.² 0.5 mmol of Fe(NO₃)₃·9H₂O and 2 mmol of H₂BDC were dissolved in 60 mL of DMF in a 100 mL Teflon vessel to form a dark-yellow solution. The vessel was put into a stainless-steel autoclave and kept at 150 °C for 3 h. The resulting powder was obtained following washing respectively with ethanol and water three times. The FeBDC crystals were collected following freeze-drying for 48 h.

Synthesis of Cu-melamine. Synthesis of Cu-melamine (Cu-Me) followed that in the literature.³ 5 mmol of CuCl₂·2H₂O, 5 mmol of melamine and 100 mL of methanol were mixed in a 250 mL closed, three-necked bottle. The solution was refluxed under magnetic stirring at 70 °C for 3 h, before cooling

to room temperature. A resultant green-coloured powder was obtained following washing with diethyl ether three times and then dried under vacuum oven at 80 °C overnight. Through solvent exchange in deionized water the Cu-Me crystals were obtained following freeze-drying for 48 h.

2. Computation models and methods

To investigate the thermodynamics of CuBDC exfoliation Density Functional Theory (DFT) computations were carried out. All electronic structure computations were carried out by Perdew-Burke-Ernzerhof (PBE) exchange-correlation functional using a projector augmented-wave method by VASP.⁴⁻⁶ For the plane-wave expansion a 400 eV kinetic energy cut-off was used - following testing a series of different cut-off energies. The convergence criterion for electronic structure iteration was set to 10^{-5} eV, and that for geometry optimization was set at 0.01 eV/Å. A Gaussian smearing of 0.05 eV was applied during geometry optimization and total energy computations, whilst for accurate density of states computation a tetrahedron method with Blochl correction was employed. The K-points were set to be 2 x 3 x 4 for pristine CuBDC and 2 x 1 x 4 for cleaved CuBDC unit cells. The Tkatchenko-Scheffler method was applied during all computations to address properly the van der Waals interactions between atoms.⁷ The unit cell of CuBDC was optimized to be, respectively, 10.88 Å, 7.49 Å, 5.81 Å on *a*, *b*, *c* directions.

To compute the exfoliation energy with different numbers of coordinated water, the unit cells were cut perpendicular to *b* direction. A 15 Å vacuum space was put between two cleaved CuBDC layers, making the new *b* lattice constant 22.49 Å. The exfoliation energy is defined as

$$E_{\text{exfoliation}} = E_{\text{cleaved}} - E_{\text{bulk}}$$

where E_{cleaved} = energy of a E_{cleaved} model and E_{bulk} = energy of pristine CuBDC models. To compute the cleavage energy across *a* direction a supercell of 2 x 1 x 1 was created to give a cell size of 21.76 Å x 22.49 Å x 5.81 Å. The connecting benzene ring was replaced by one and two LA/HQ molecules to investigate thermodynamic stability and degree of difficulty for cleavage with the aid of the solvent molecules. To ensure comparability, atom types and numbers for each investigated system were

strictly kept the same. The reference energy level was set to be that for the initial state based on pristine CuBDC unit cell.

3. TGA Analysis

Taking the pristine CuBDC·2H₂O as an example, which was oxidized into CuO under air atmosphere for the TGA test. An experimental CuO mass percentage of 30.00 % (Figure S2) was observed, closing to the theoretical value of 30.30 % based on the following equation.

$$\frac{M(\text{CuO})}{M(\text{CuBDC}) + M(\text{H}_2\text{O}) \times 2} = \frac{80}{264} \times 100\% = 30.30\%$$

Afterwards, we propose the chemical formula of final products is Cu_xBDC (x > 1). If all of Cu²⁺ in CuBDC was reduced to Cu¹⁺, the ratio of Cu to BDC would be 2 when the principle of valence balance is considered. Therefore, the calculated CuO mass percentage would be 54.79 % based on the following equation.

$$\frac{M(\text{CuO})}{M(\text{Cu}_2\text{BDC})} = \frac{160}{292} \times 100\% = 54.79\%$$

Noted that this value is higher than that of experimental value of 49.70 % (Figure S2). Besides, according to the FTIR results (Figure 4b), there are some OH and H₂O groups in the framework on Cu₂BDC. XPS results prove that the ratio of Cu¹⁺ to Cu²⁺ in Cu₂BDC is 1 (Figure 3c), suggesting the ratio of BDC²⁻ to OH⁻ is 1. Therefore, we propose its chemical formula of final products is Cu₂(OH)BDC·H₂O, which has a theoretical CuO mass percentage of 48.93 % based on

$$\frac{M(\text{CuO}) \times 2}{M(\text{Cu}_2(\text{OH})\text{BDC} \cdot \text{H}_2\text{O})} = \frac{160}{327} \times 100\% = 48.93\%$$

This value is much closer to the experimental value (49.70 %), validating our proposed formula.

4. Structure Description of CuBDC

CuBDC crystallizes in the orthorhombic system with space group *Pmc*2₁. In the structure, the asymmetric unit contains a unique Cu²⁺ ion and two BDC linker. The coordinated Cu is completed by two carboxylic oxygen atoms (O1, O2) of two BDC linkers, two μ₂-oxygen atoms (O3, O4) of two bridged water molecules and one oxygen atom (O5) of one water molecule (Figure S8c). Thus, the Cu atom is pyramidally coordinated by five O atoms, forming a square pyramid. The pyramids are

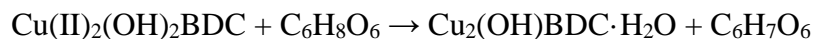
corner connected with each other along the [001] direction to construct zigzagging chains of $[\text{Cu}(\text{H}_2\text{O})_2(\text{COO})_2]_n$. Different chains are separated by the BDC linkers along the [100] direction, forming 2D layer structures (Figure S8d), which is connected by hydrogen bindings along the [010] direction. Topological analysis of CuBDC reveals that every $[\text{Cu}(\text{H}_2\text{O})]^{2+}$ unit is coordinated with two bridged water molecules and two monodentate BDC linkers to form a 4-connected node.

5. Reaction Stoichiometry

We establish the reaction stoichiometry between CuBDC and LA from the perspective of chemical reaction equations. The molar amounts of 0.2 g CuBDC and 0.12 g LA are both ~ 0.65 mmol. The phase transition in this work undergoes two processes. The first step is the cleavage of all CuBDC molecules by half amount of LA (0.325 mmol), yielding $\text{Cu}(\text{II})_2(\text{OH})_2\text{BDC}$, H_2BDC and oxidized LA ($\text{C}_6\text{H}_8\text{O}_7$).



While the second step is that half of Cu^{2+} ion in $\text{Cu}(\text{II})_2(\text{OH})_2\text{BDC}$ reduced into Cu^{1+} via an one-electron reduction, yielding $\text{Cu}_2(\text{OH})\text{BDC} \cdot \text{H}_2\text{O}$ ($\text{Cu}^{2+}/\text{Cu}^{1+} = 1$), which was labelled as Cu_2BDC in the manuscript.



Based on above XRD, FTIR and XPS analysis (Figure S9, S10), we propose the final product Cu_2BDC is a pure phase when 0.12 g LA was used to realize the cleavage of 0.2 g CuBDC.

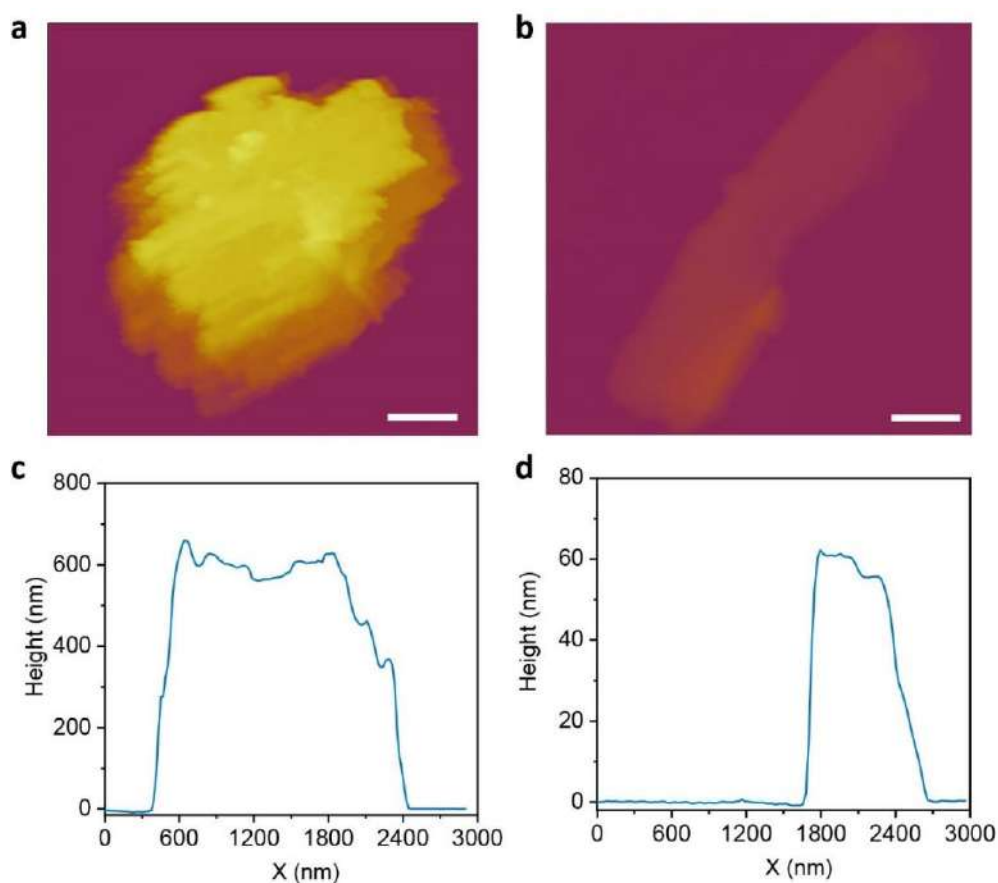


Figure S1. AFM images of (a) CuBDC and (b) Cu₂BDC. Corresponding height profile of (c) CuBDC and (d) Cu₂BDC. Scale bar is 0.5 μm in panels (a) and (b).

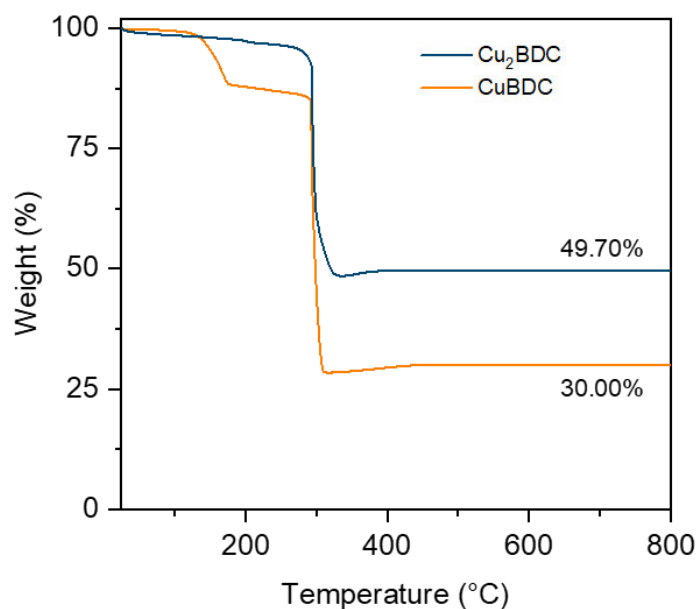


Figure S2. TGA curves for CuBDC and Cu₂BDC under air atmosphere. For the range: < 300 °C the mass difference of two samples results from removal of coordinated water in Cu₂BDC; > 300 °C the mass difference results from removal of H₂BDC in Cu₂BDC.

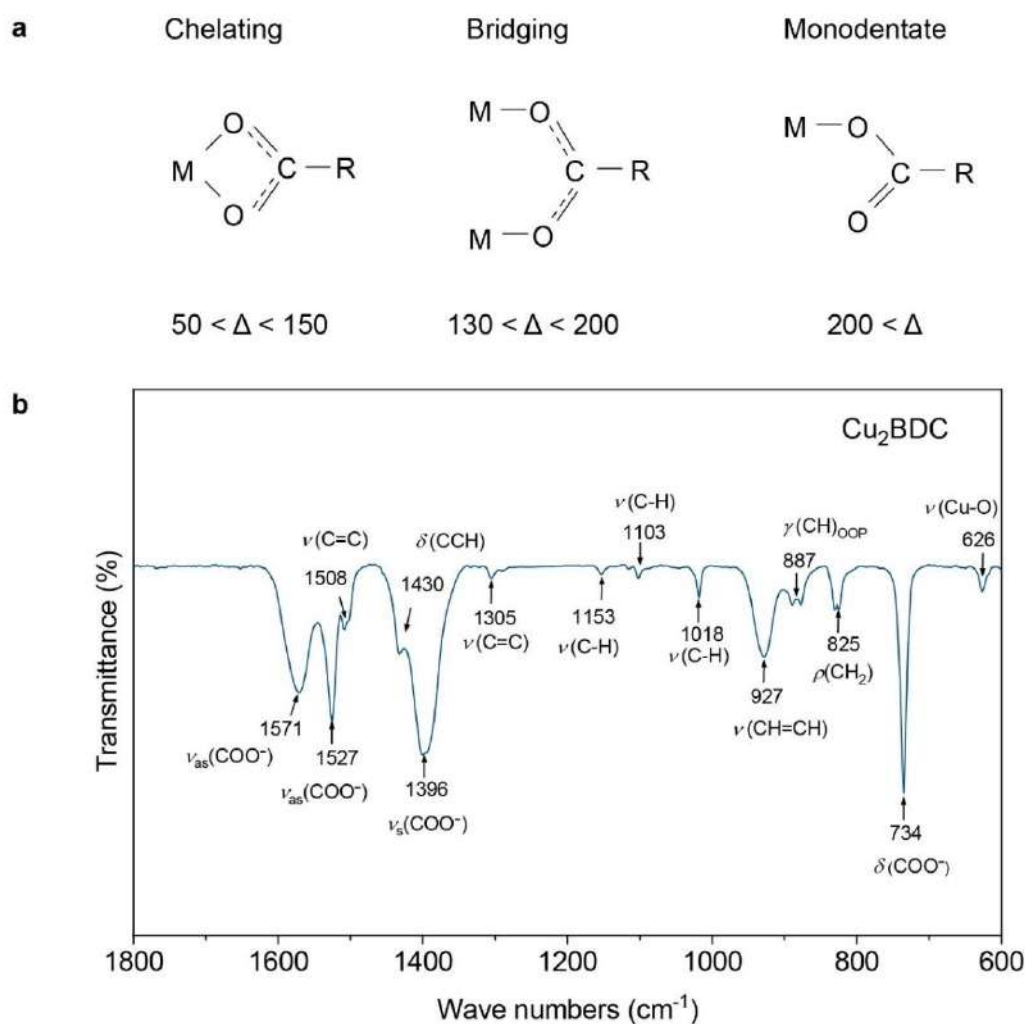


Figure S3. (a) Three coordination modes and corresponding Δ values for carboxylate ion and metal (M). (b) FTIR spectrum of Cu_2BDC and assignment of typical peaks.

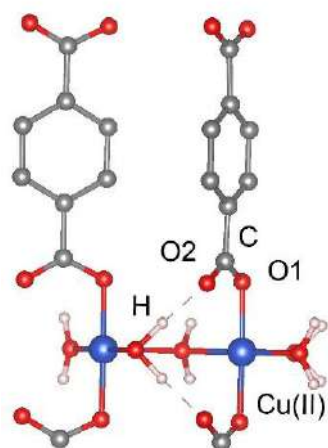


Figure S4. The coordination structure of carboxylate binding in CuBDC .

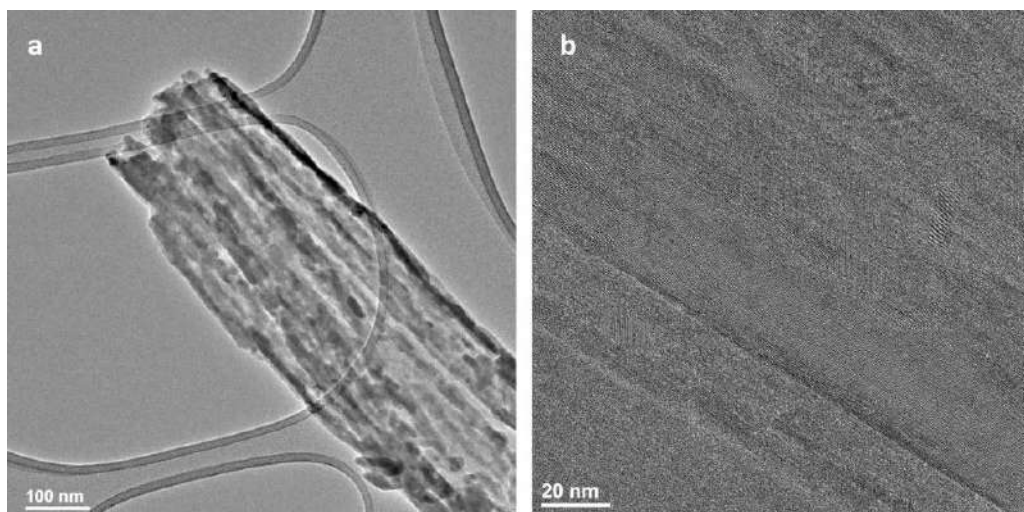


Figure S5. (a) TEM and (b) HRTEM images of Cu_2BDC .

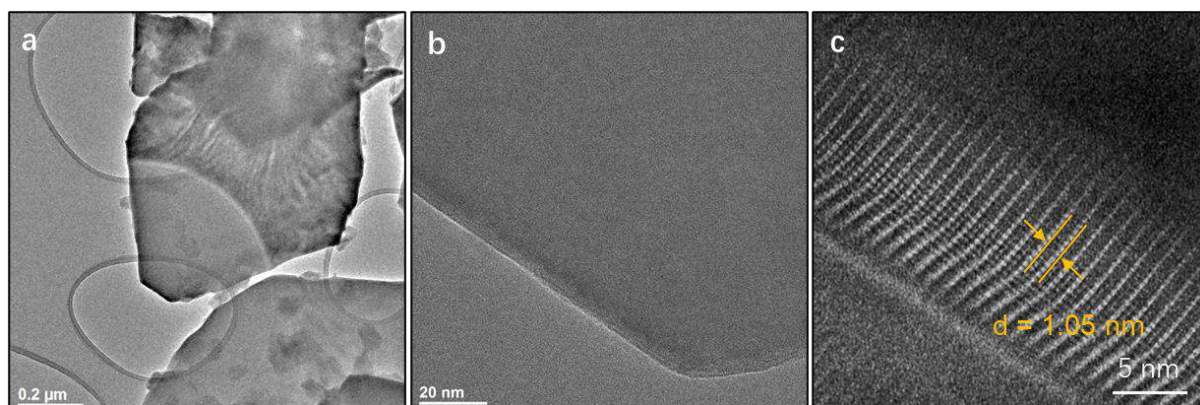


Figure S6. (a) TEM and (b, c) HRTEM images of CuBDC .

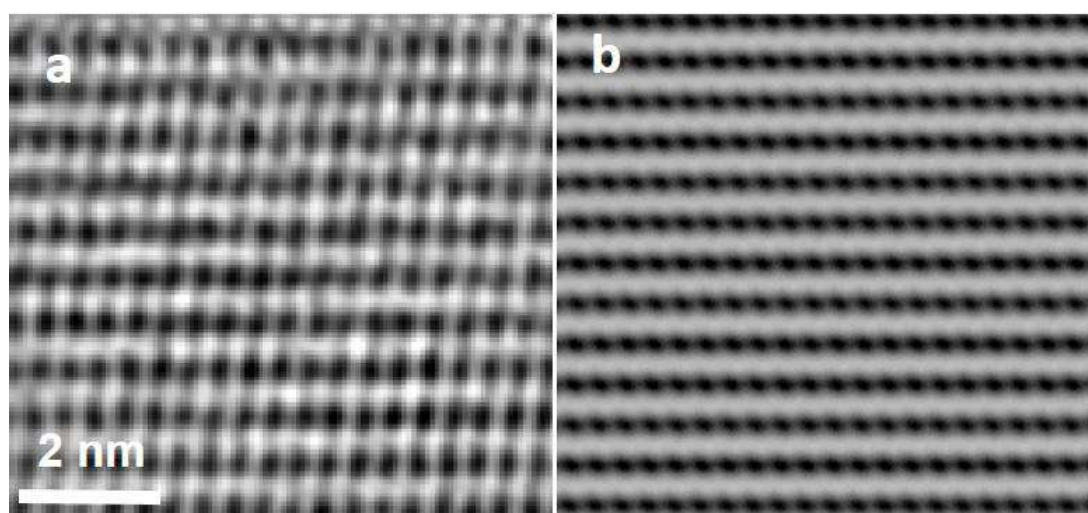


Figure S7. (a) CTF-corrected HRTEM image and (b) corresponding simulated projected potential map of the area highlighted in Figure 2f.

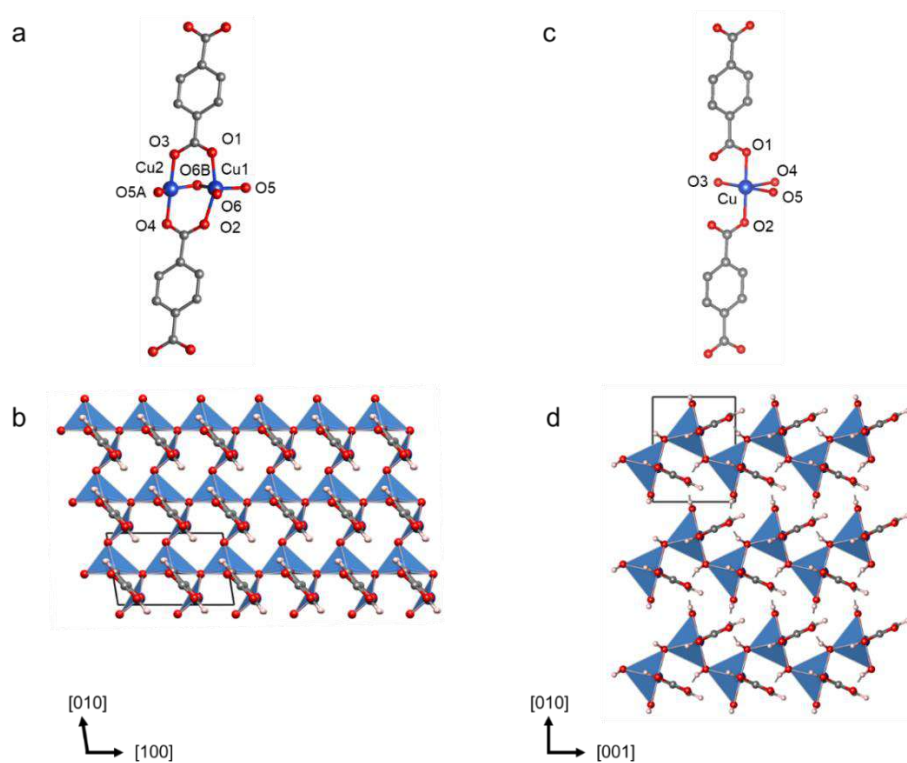


Figure S8. Coordinated environments of Cu in (a) Cu₂BDC and (c) CuBDC. The images of project along (b) Cu₂BDC [001] and (d) CuBDC [100]. A, (0, 1, 0) + (x, y, z) for O5; B, (1/2, 0, 0) + (x, y, z) for O6.

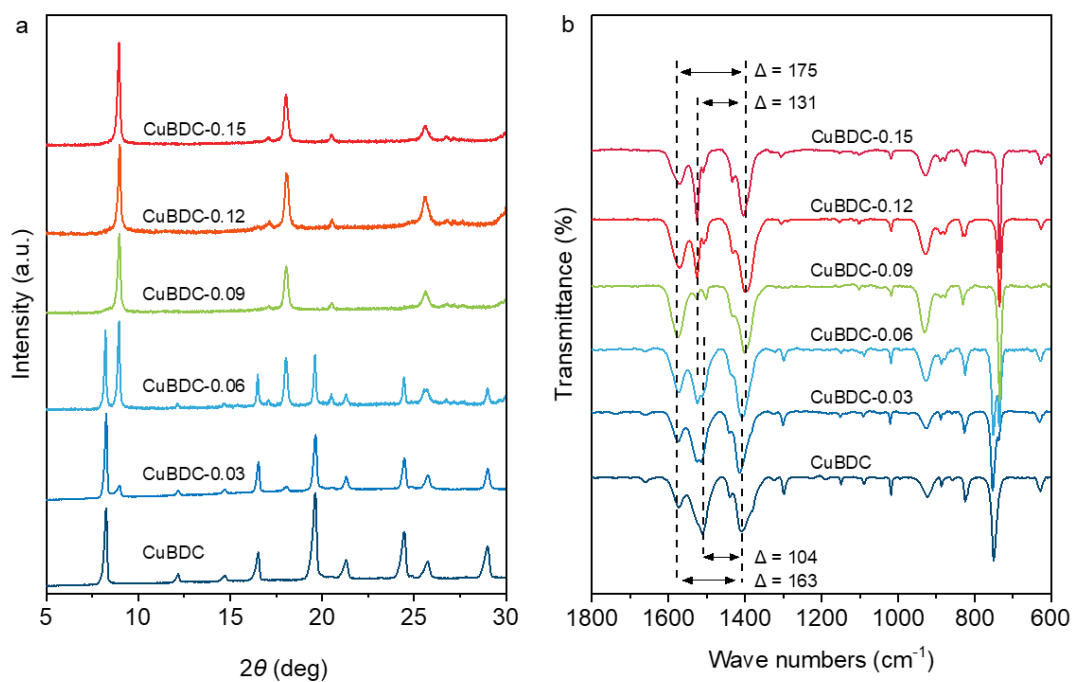


Figure S9. Structural characterization of CuBDC and the samples synthesized by different amount of LA cleaving CuBDC. (a) XRD patterns. (b) FTIR spectra.

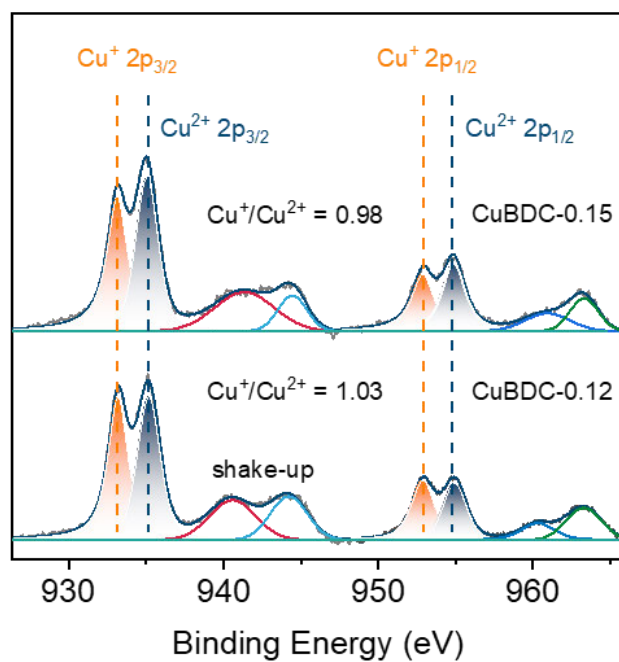


Figure S10. XPS analysis of the product with different LA (0.12 and 0.15 g) to cleave CuBDC.

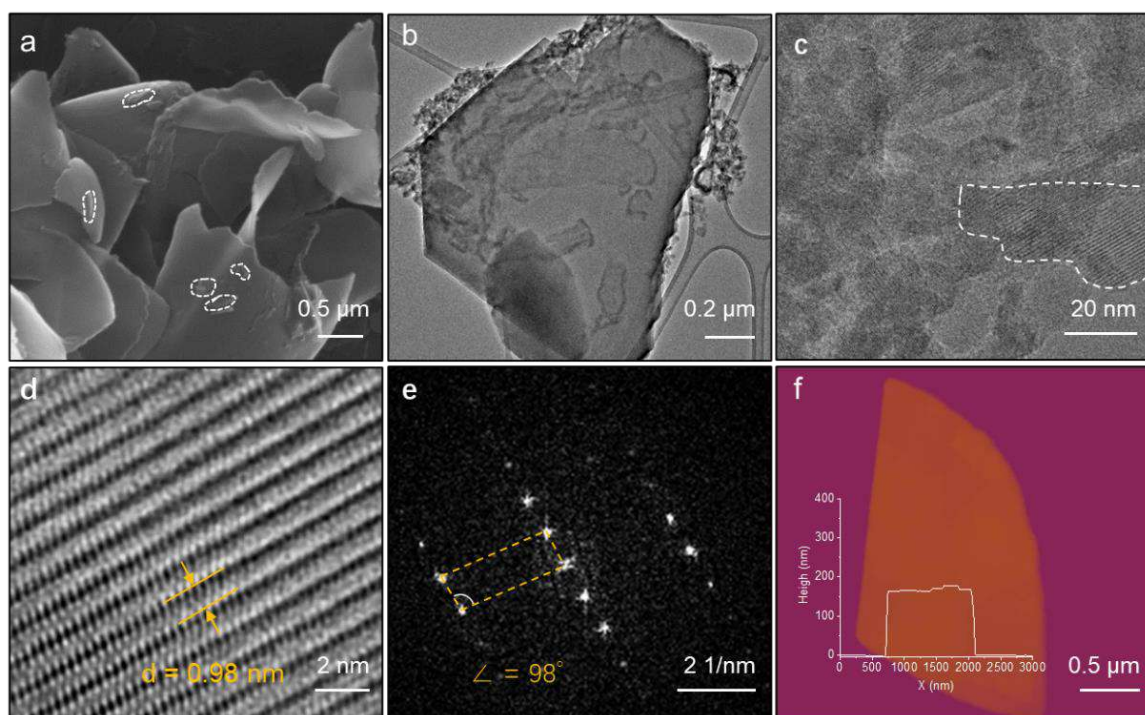


Figure S11. Characterization of CuBDC-0.06 transition sample. (a) SEM image; dashed circles show the existence of nanoparticles. (b) TEM image. (c, d) HRTEM images; panel d is enlarged image of dashed circles part in panel c. (e) FFT pattern. (f) AFM profile.

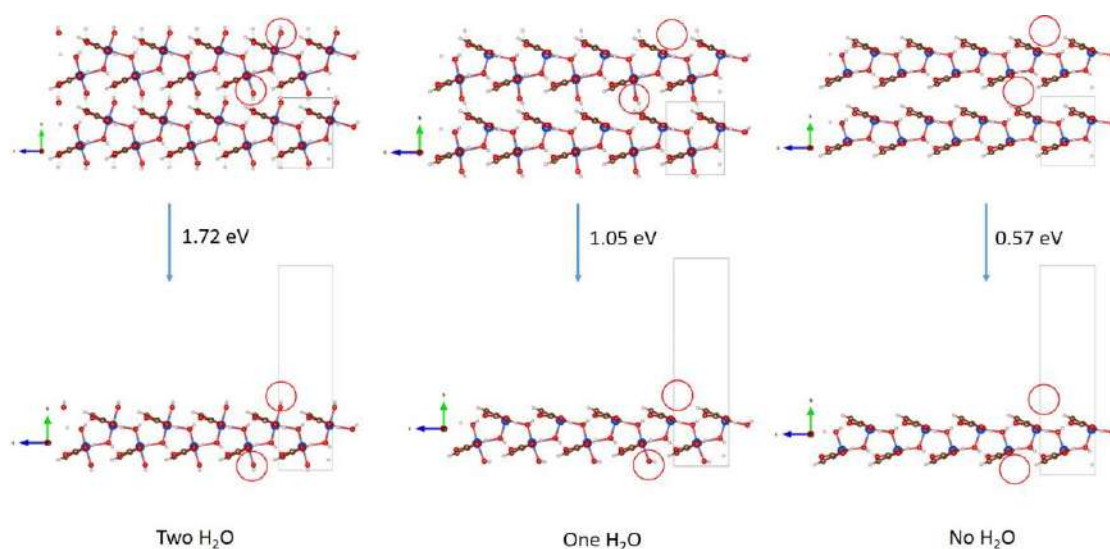


Figure S12. Structural models for CuBDC before (top) and following exfoliation (down) with different number of coordinated water and corresponding exfoliation energy. The positive value of exfoliation energy indicates this process is achieved with additional energy provided e.g. by sonication in the experiment. In addition, the fewer number of water in the framework, the smaller exfoliation energy, i.e. the more is the facile exfoliation.

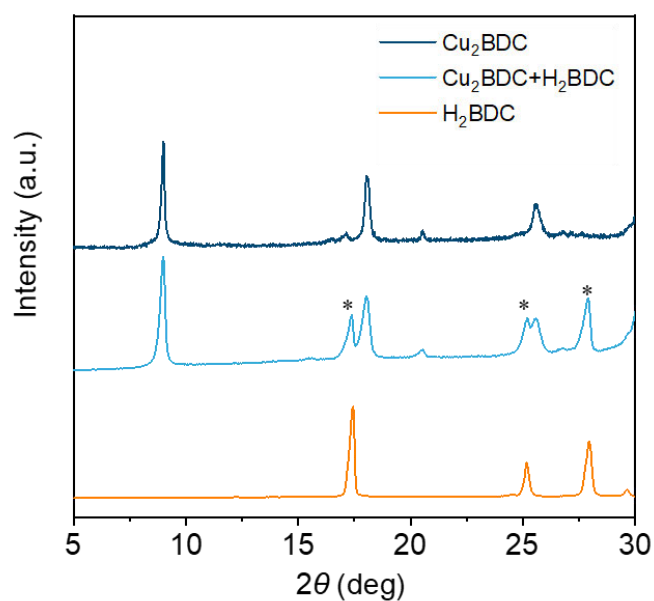


Figure S13. XRD patterns for Cu_2BDC washed with different solvent, and commercial H_2BDC . The labelled peaks (stars) are assigned to H_2BDC cleaved from CuBDC because H_2BDC is insoluble in water but soluble in DMF.

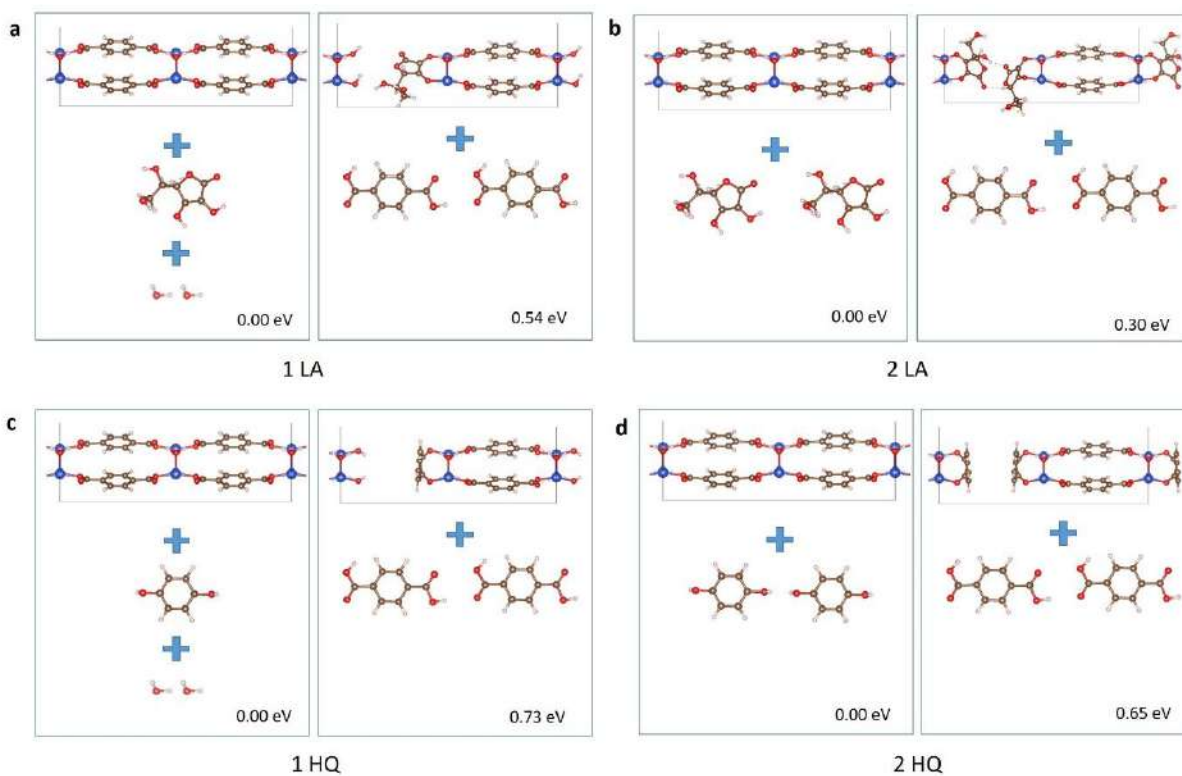


Figure S14. DFT-computed total energy of the system with clipping of H₂BDC from CuBDC by different numbers of LA and HQ molecules.

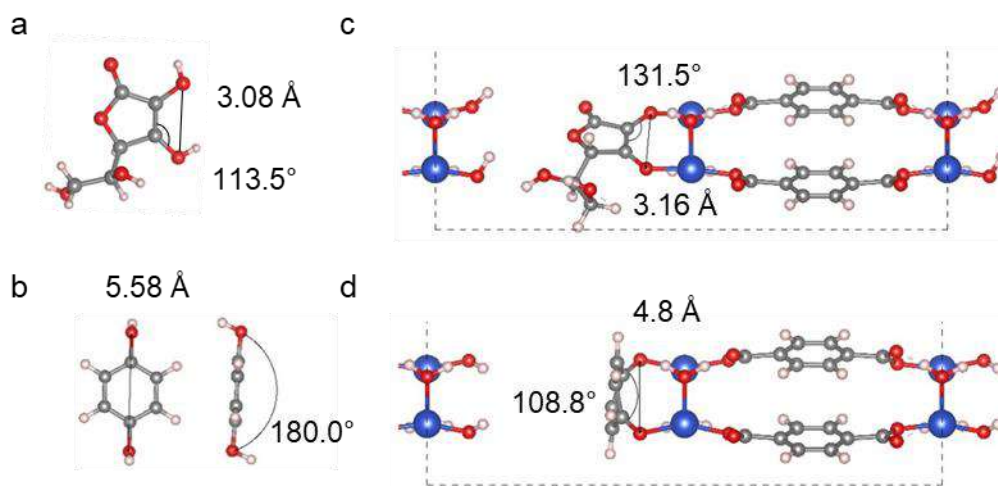


Figure S15. Molecular model of (a) LA and (b) HQ. The structural model of (c) LA and (d) HQ coordinated with CuBDC.

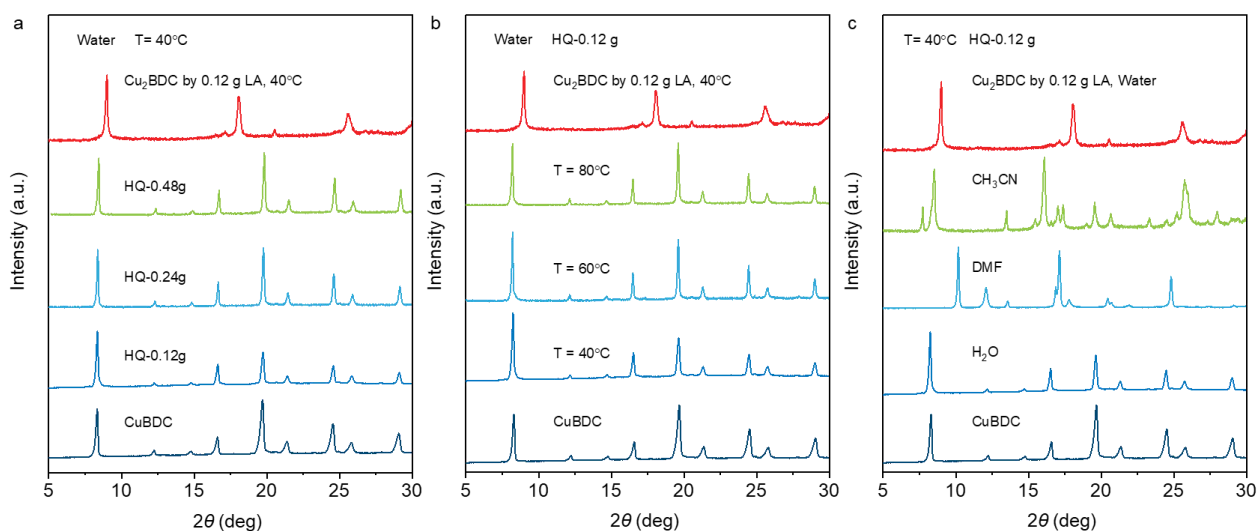


Figure S16. The XRD patterns of CuBDC after HQ cleaving under different conditions. Cu₂BDC and CuBDC work as reference samples. (a) different amount of HQ; (b) different temperatures; (c) different solutions.

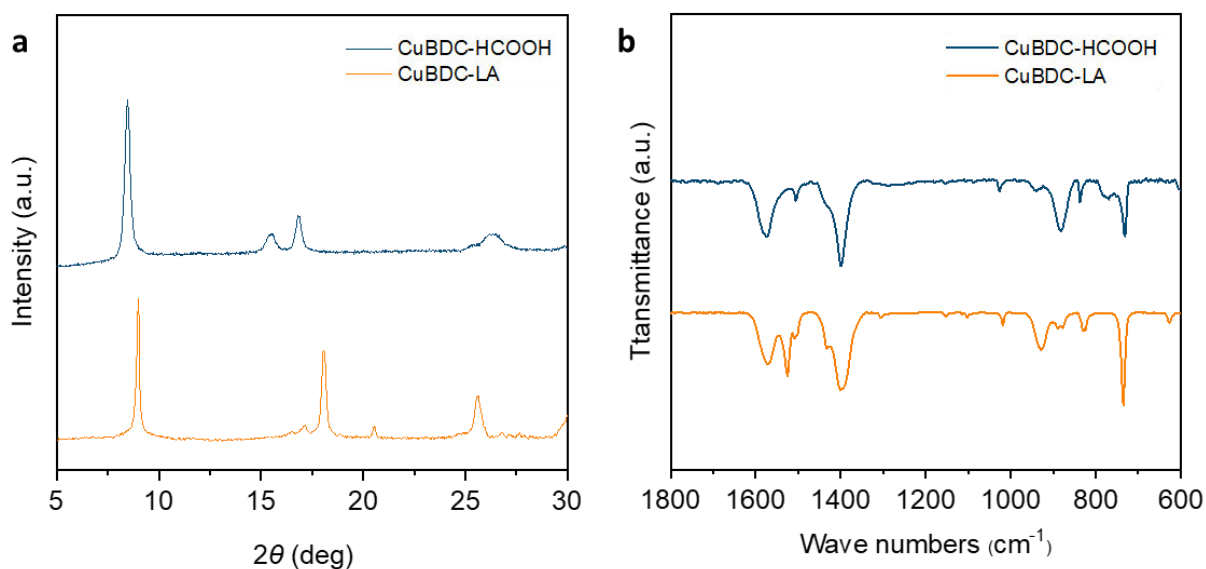


Figure S17. (a) XRD patterns and (b) FTIR spectra of CuBDC treated by HCOOH (CuBDC-HCOOH) and Cu₂BDC (CuBDC-LA).

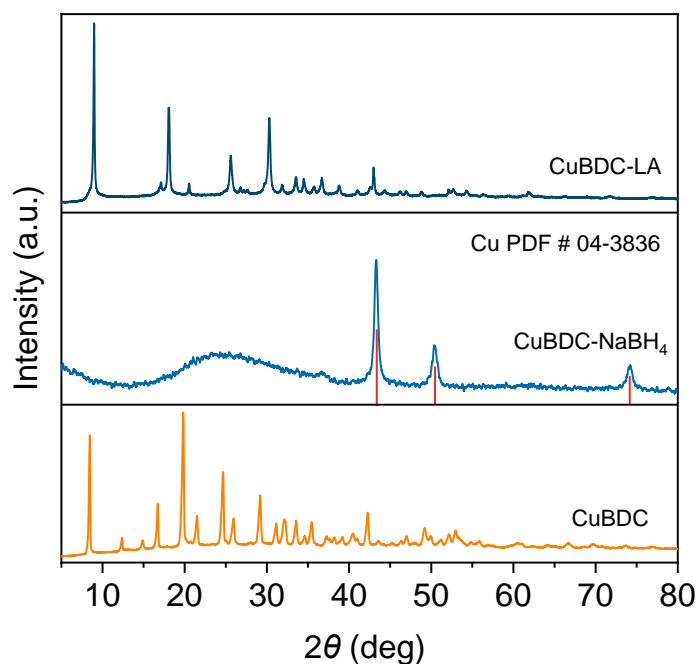


Figure S18. XRD patterns of CuBDC after NaBH₄ cleaving. CuBDC and CuBDC-LA (Cu₂BDC) work as the reference samples.

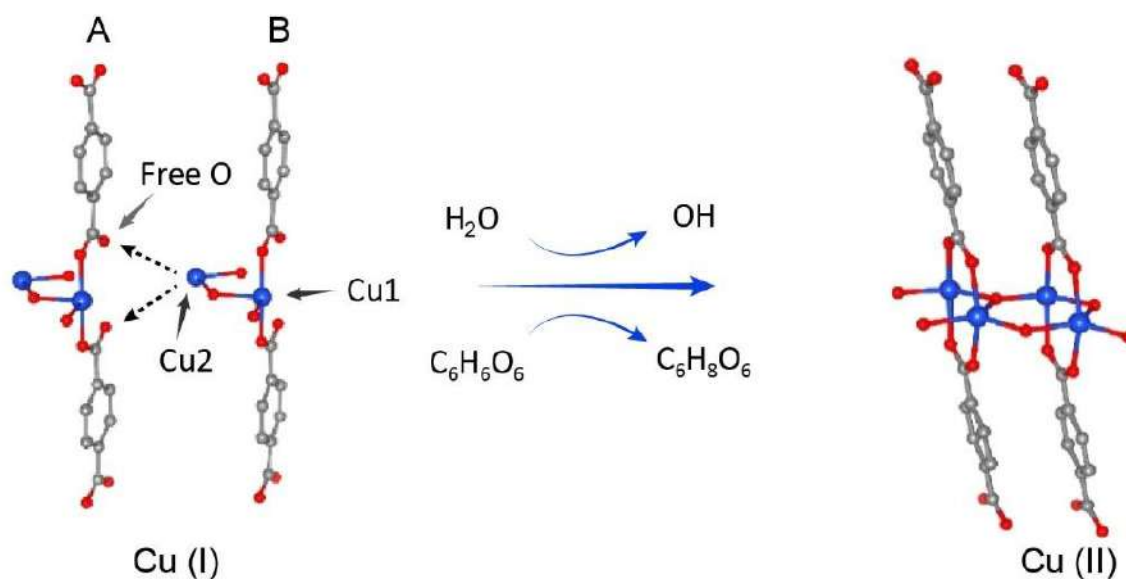


Figure S19. Proposed mechanism for Cu₂BDC·H₂O bridging with OH⁻ to form Cu₂(OH)₂BDC. Namely, oxidation of Cu^{I+} ion enables its coordination number to increase. This results in one Cu₂ atom in the layer B coordinating with two free oxygen atoms in layer A. Therefore, the coordination mode of Cu and carboxylate group convert from monodentate into bridging. Concomitantly H₂O provides the proton to facilitate C₆H₆O₆ reduction to C₆H₈O₆ and to yield active OH groups. These bridge three Cu atoms in the metal layer to form the Cu₂(OH)₂BDC structure.

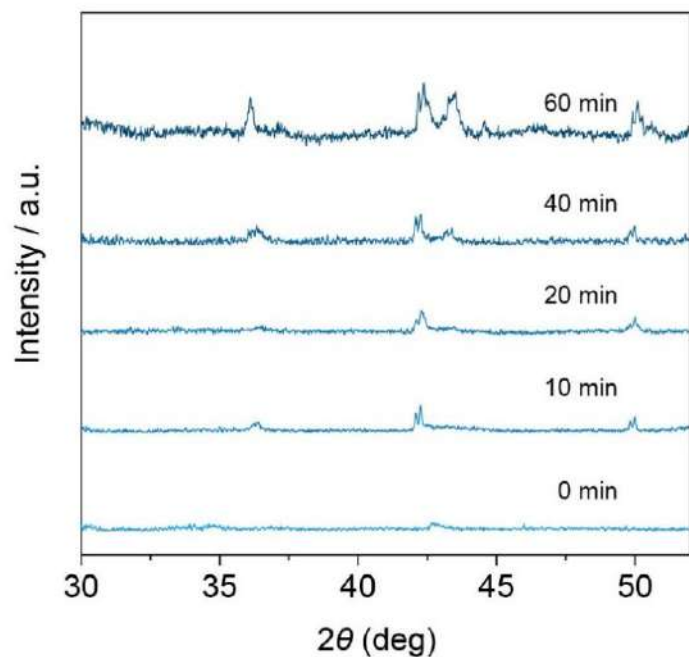


Figure S20. *Ex-situ* XRD patterns for Cu₂BDC derived samples under different reduction times at a constant potential of -1.30 V vs. RHE.

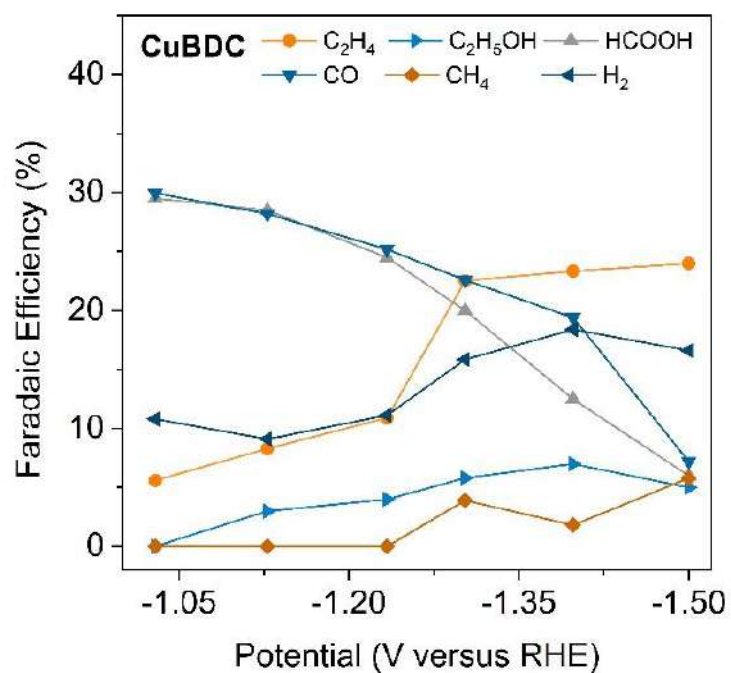


Figure S21. Faradaic efficiencies of CRR products for CuBDC derived samples over a range of applied potentials.

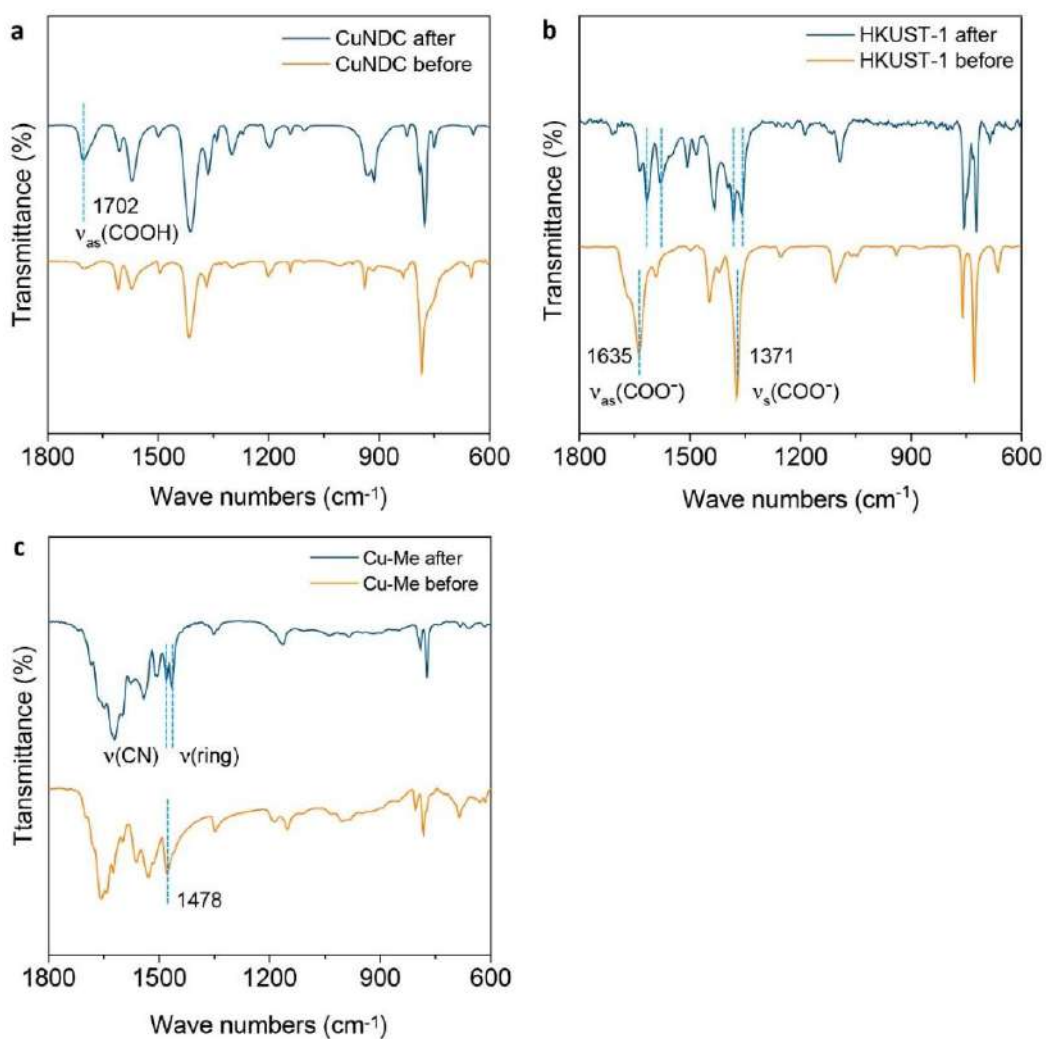


Figure S22. FTIR spectra of (a) CuNDC, (b) HKUST-1 and (c) Cu-Me samples before and after a LA treatment.

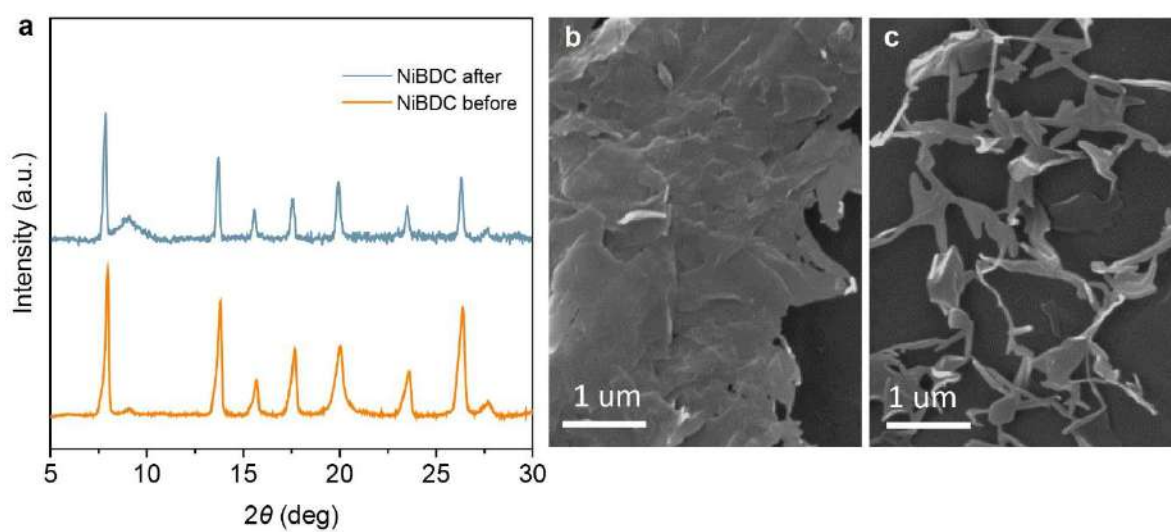


Figure S23. (a) XRD patterns for NiBDC before and after LA treatment. SEM images for (b) NiBDC before and (c) NiBDC after LA treatment.

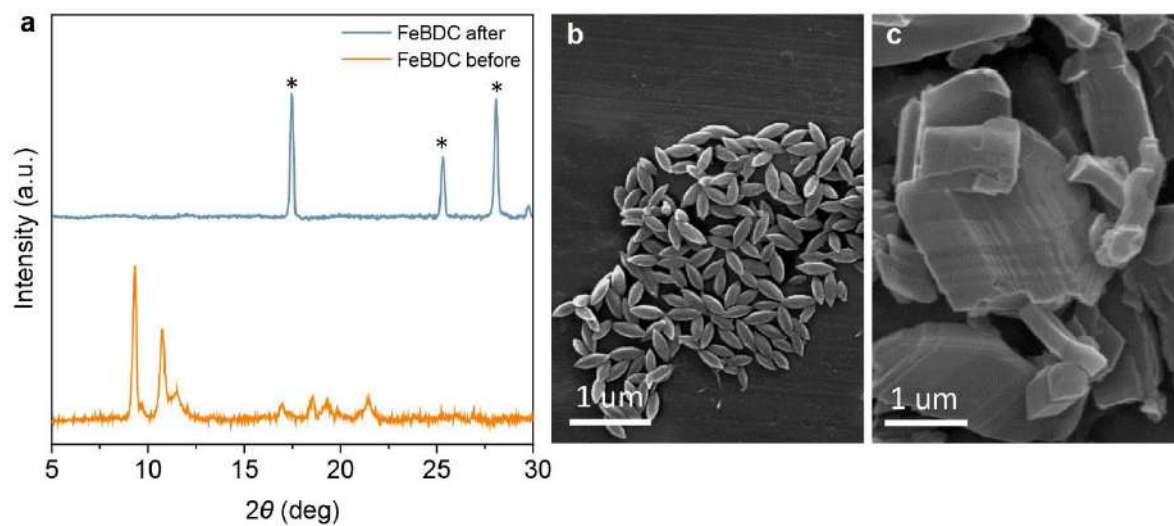


Figure S24. (a) XRD patterns for FeBDC before and after LA treatment. The labelled peaks (stars) are assigned to H_2BDC . SEM images for (b) FeBDC before and (c) FeBDC after LA treatment.

Table S1. Structure refinement parameters for Cu₂BDC.

Empirical formula	Cu ₂ C ₈ H ₇ O ₆
Formula weight	327
Crystal system	Triclinic
Space group	<i>P</i> 1
Unit cell dimensions (Å)	a = 7.0112603 b = 4.4221462 c = 9.9285706 α = 98.66481 β = 92.40965 γ = 98.74176
V (Å ³)	300.11987
Absorption coefficient (cm ⁻¹)	89.963
Crystal density (g/cm ³)	3.577
Cell Mass	646.418
Theta range (°)	5 - 80
R _{exp}	1.50%
R _w	2.73%
Goodness of fit	1.82

Table S2. CH₄ and C₂ products Faradaic efficiency comparison of the recently reported Cu electrocatalysts derived from other precursors.

Sample	Electrolyte	Potential (V vs RHE)	C ₂ FE (%) [*]	CH ₄ FE (%)	After CRR	Ref
Cu ₂ BDC	0.1 M KCl	-1.30	47.0	0.9	Cu ₂ O/Cu	This work
Cu phthalocyanine	0.5 M KCl	-1.60 (V vs Ag/AgCl)	25.0	4.0	Cu	8
Cu(II) complex ^a	0.1 M KHCO ₃	-1.00	8.4	--	Phen-Cu(I)	9
HKUST-1	0.5 M NaHCO ₃	-2.00 (V vs SCE)	12.0	--	Cu	10
Copper-porphyrin ^b	0.5 M KHCO ₃	-0.98	17.0	27.0	Cu	11
Cu ₂ O/CuHHTP ^c	0.1 M KCl/0.1 M KHCO ₃	-1.40	--	73.0	Cu	12
Cu-ade MOF ^d	0.1 M KHCO ₃	-1.60	23.0	50.0	Cu	13

a, 1,10-phenanthroline-Cu; b, porphyrin = 5,10,15,20-tetrakis(2,6-dihydroxyphenyl) porphyrin; c, HHTP = 2,3,6,7,10,11 hexahydroxytriphenylene; d, ade = adeninato/carboxylato. *, it is the total FE of C₂H₄ and C₂H₅OH. --, no data.

References

1. Nam, D. H.; Bushuyev, O. S.; Li, J.; De Luna, P.; Seifitokaldani, A.; Dinh, C. T.; Garcia de Arquer, F. P.; Wang, Y.; Liang, Z.; Proppe, A. H.; Tan, C. S.; Todorovic, P.; Shekhah, O.; Gabardo, C. M.; Jo, J. W.; Choi, J.; Choi, M. J.; Baek, S. W.; Kim, J.; Sinton, D.; Kelley, S. O.; Eddaoudi, M.; Sargent, E. H., *J. Am. Chem. Soc.* **2018**, *140*, 11378-11386.
2. Li, F. L.; Shao, Q.; Huang, X.; Lang, J. P., *Angew. Chem. Int. Ed.* **2018**, *57*, 1888-1892.
3. Gao, J.; Wang, J.; Qian, X.; Dong, Y.; Xu, H.; Song, R.; Yan, C.; Zhu, H.; Zhong, Q.; Qian, G.; Yao, J., *J. Solid State Chem.* **2015**, *228*, 60-64.
4. Kresse, G.; Joubert, D., *Phys. Rev. B* **1999**, *59*, 1758-1775.
5. Kresse, G.; Furthmuller, J., *Phys. Rev. B: Condens. Matter.* **1996**, *54*, 11169-11186.
6. Perdew, J. P.; Burke, K.; Ernzerhof, M., *Phys. Rev. Lett.* **1996**, *77*, 3865-3868.
7. Tkatchenko, A.; Scheffler, M., *Phys. Rev. Lett.* **2009**, *102*, 073005.
8. Kusama, S.; Saito, T.; Hashiba, H.; Sakai, A.; Yotsuhashi, S., *ACS Catal.* **2017**, *7*, 8382-8385.
9. Wang, J.; Gan, L. Y.; Zhang, Q. W.; Reddu, V.; Peng, Y. C.; Liu, Z. C.; Xia, X. H.; Wang, C.; Wang, X., *Adv. Energy Mater.* **2019**, *9*, 1803151.
10. Albo, J.; Vallejo, D.; Beobide, G.; Castillo, O.; Castano, P.; Irabien, A., *ChemSusChem* **2017**, *10*, 1100-1109.
11. Weng, Z. J., J.; Wu, Y.; Wu, Z.; Guo, X.; Materna, K. L.; Liu, W.; Batista, V. S.; Brudvig, G. W.; Wang, H., *J. Am. Chem. Soc.* **2016**, *138*, 8076-8079.
12. Yi, J. D.; Xie, R.; Xie, Z. L.; Chai, G. L.; Liu, T. F.; Chen, R. P.; Huang, Y. B.; Cao, R., *Angew. Chem. Int. Ed.* **2020**, *59*, 23641-23648.
13. Yang, F.; Chen, A.; Deng, P. L.; Zhou, Y.; Shahid, Z.; Liu, H.; Xia, B. Y., *Chem. Sci.* **2019**, *10*, 7975-7981.

Chapter 4 Stabilizing Cu²⁺ ions by solid solutions to promote CO₂ electroreduction to methane

4.1 Introduction and Significance

Cu serves as the only metal catalyst to achieve CRR with the generation of hydrocarbons and oxygenates. The previous report has confirmed that the *CO adsorption energy on Cu-based catalysts increases monotonically with the oxidation state. However, during CRR operation, a large overpotential is used to derive the catalytic reaction, which results in the reduction of various Cu-based catalysts to metal Cu⁰. Therefore, there is a lack of a platform to investigate the catalytic behavior of Cu²⁺ in CRR.

In this chapter, a solid-solution strategy is proposed to stabilize Cu²⁺ ions by incorporating them into CeO₂ matrix, which works as a self-sacrificing ingredient to protect Cu²⁺ active species. In situ spectroscopic characterization and density functional theory (DFT) calculations reveal that, compared with the conventional derived Cu catalysts with Cu⁰ or Cu¹⁺ active sites, the Cu²⁺ species in solid-solution (Cu-Ce-O_x) can significantly strengthen adsorption of *CO intermediate, facilitating its further hydrogenation to produce CH₄ instead of dimerization to C₂ products. As a result, different from most of the other Cu-based catalysts, Cu-Ce-O_x delivered a high faradaic efficiency for CH₄ of 67.8 % and as low as 3.6 % for C₂H₄.

The particular novelty of this work is:

1. New structure. We first report the solid-solution strategy to stabilize Cu²⁺ ions during CRR operation. Cu²⁺ ions are incorporated into CeO₂ matrix, which serves as a self-sacrificing ingredient to protect Cu²⁺ active sites.
2. New mechanism. In situ attenuated total reflectance infrared spectroscopy (ATR-IR) and DFT calculations confirmed that the stable Cu²⁺ active sites could

significantly enhance the initial *CO adsorption and promote the *CO hydrogenation to form *OCH₃, a crucial intermediate of CH₄ generation.

3. High selectivity. Cu-Ce-O_x delivered a high faradaic efficiency for CH₄ of 67.8% and as low as 3.6% for C₂H₄. The ratio of FE_{CH₄} to FE_{C₂H₄} for Cu-Ce-O_x is 31 times higher than that of the CuO supported on the surface of CeO₂ (CuO/CeO₂) and 22 times higher than that of the conventional oxide-derived Cu.

4.2 Stabilizing Cu²⁺ ions by Solid Solutions to Promote CO₂ Electroreduction to Methane

This chapter is included as a journal paper by Xianlong Zhou, Jieqiong Shan, Ling Chen, Bao Yu Xia, Tao Ling, Jingjing Duan, Yan Jiao, Yao Zheng, Shi-Zhang Qiao, Stabilizing Cu²⁺ ions by Solid Solutions to Promote CO₂ Electroreduction to Methane, Journal of the American Chemical Society, 2022, 144, 2079–2084.

Statement of Authorship

Title of Paper	Stabilizing Cu ²⁺ Ions by Solid Solutions to Promote CO ₂ Electroreduction to Methane
Publication Status	<input checked="" type="checkbox"/> Published <input type="checkbox"/> Accepted for Publication <input type="checkbox"/> Submitted for Publication <input type="checkbox"/> Unpublished and Unsubmitted work written in manuscript style
Publication Details	Xianlong Zhou, Jieqiong Shan, Ling Chen, Bao Yu Xia, Tao Ling, Jingjing Duan, Yan Jiao, Yao Zheng,* and Shi-Zhang Qiao*, Journal of the American Chemical Society, 2022, 144, 2079–2084.

Principal Author

Name of Principal Author (Candidate)	Xianlong Zhou		
Contribution to the Paper	Conducted material synthesis, carried out electrochemical tests and wrote the paper		
Overall percentage (%)	70		
Certification:	This paper reports on original research I conducted during the period of my Higher Degree by Research candidature and is not subject to any obligations or contractual agreements with a third party that would constrain its inclusion in this thesis. I am the primary author of this paper.		
Signature		Date	09/09/2022

Co-Author Contributions

By signing the Statement of Authorship, each author certifies that:

- the candidate's stated contribution to the publication is accurate (as detailed above);
- permission is granted for the candidate to include the publication in the thesis; and
- the sum of all co-author contributions is equal to 100% less the candidate's stated contribution.

Name of Co-Author	Jieqiong Shan		
Contribution to the Paper	Conducted in situ attenuated total reflectance infrared spectroscopy (ATR-IR) characterization and analysis		
Signature		Date	09/09/2022

Name of Co-Author	Ling Chen		
Contribution to the Paper	Conducted density functional theory (DFT) calculations		
Signature		Date	09/09/2022

Name of Co-Author	Bao Yu Xia		
Contribution to the Paper	Providing experiment conditions and constructive discussion		
Signature	_____	Date	09/09/2022

Name of Co-Author	Tao Ling		
Contribution to the Paper	Conducted TEM characterization and analysis		
Signature	_____	Date	09/09/2022

Name of Co-Author	Jingjing Duan		
Contribution to the Paper	Conducted in situ Raman characterization and analysis		
Signature	_____	Date	09/09/2022

Name of Co-Author	Yan Jiao		
Contribution to the Paper	Supervised density functional theory (DFT) calculations		
Signature	_____	Date	09/09/2022

Name of Co-Author	Yao Zheng		
Contribution to the Paper	Discussion of research plan, manuscript revision, and acted as corresponding author		
Signature	_____	Date	09/09/2022

Name of Co-Author	Shi-Zhang Qiao		
Contribution to the Paper	Supervised development of work, helped in manuscript evaluation and revision, and acted as corresponding author		
Signature	_____	Date	09/09/2022

Please cut and paste additional co-author panels here as required.

Stabilizing Cu²⁺ Ions by Solid Solutions to Promote CO₂ Electroreduction to Methane

Xianlong Zhou,[†] Jieqiong Shan,[†] Ling Chen, Bao Yu Xia, Tao Ling, Jingjing Duan, Yan Jiao, Yao Zheng,* and Shi-Zhang Qiao*



Cite This: *J. Am. Chem. Soc.* 2022, 144, 2079–2084



Read Online

ACCESS |



Metrics & More



Article Recommendations



Supporting Information

ABSTRACT: Copper is the only metal catalyst that can perform the electrocatalytic CO₂ reduction reaction (CRR) to produce hydrocarbons and oxygenates. Its surface oxidation state determines the reaction pathway to various products. However, under the cathodic potential of CRR conditions, the chemical composition of most Cu based catalysts inevitably undergoes electroreduction from Cu²⁺ to Cu⁰ or Cu¹⁺ species, which is generally coupled with phase reconstruction and the formation of new active sites. Since the initial Cu²⁺ active sites are hard to retain, there have been few studies about Cu²⁺ catalysts for CRR. Herein we propose a solid solution strategy to stabilize Cu²⁺ ions by incorporating them into a CeO₂ matrix, which works as a self sacrificing ingredient to protect Cu²⁺ active species. In situ spectroscopic characterization and density functional theory calculations reveal that compared with the conventionally derived Cu catalysts with Cu⁰ or Cu¹⁺ active sites, the Cu²⁺ species in the solid solution (Cu Ce O_x) can significantly strengthen adsorption of the *CO intermediate, facilitating its further hydrogenation to produce CH₄ instead of dimerization to give C₂ products. As a result, different from most of the other Cu based catalysts, Cu Ce O_x delivered a high Faradaic efficiency of 67.8% for CH₄ and a low value of 3.6% for C₂H₄.

Copper based catalysts have attracted wide attention as the only metal candidates to perform the electrocatalytic CO₂ reduction reaction (CRR) with generation of hydrocarbons and oxygenates.^{1,2} To date, most studies of Cu based catalysts have focused on producing various C₂ products, including ethylene, ethanol, and *n* propanol, while C₁ products (e.g., methane) are hard to obtain directly.³ The reason for this is that under the cathodic potential of CRR, Cu²⁺ species in catalysts can be inevitably electroreduced to Cu⁰ or Cu¹⁺ sites, forming the so called oxide derived Cu (OD Cu) catalysts.⁴ The mixture of Cu⁰ and Cu¹⁺ sites can significantly boost the thermodynamics of *CO dimerization, resulting in improved selectivity for C₂ products.^{5–10} Additionally, Peterson and Nørskov predicted that robust CH₄ generation would require relatively strong adsorption of *CO intermediates on the catalyst surface,¹¹ whereas weak adsorption facilitates the competing *CO dimerization.

Besides Cu⁰ or Cu¹⁺ species in OD Cu, Cu²⁺ has been extensively applied in other heterogeneous catalyses because it can easily bind CO and H₂O molecules.^{12,13} Given that the *CO adsorption energy in Cu based catalysts increases monotonically with the oxidation state,¹⁴ we hypothesized that a higher oxidation state of Cu²⁺ can facilitate *CO hydrogenation because of a stronger electrostatic interaction with it compared with the Cu⁰ or Cu¹⁺ counterparts. However, it remains a grand challenge to stabilize Cu²⁺ in catalysts under CRR operating conditions. The only report of Cu²⁺ stabilization was realized by the use of a metal–organic framework (MOF) with a specially designed ligand,^{15,16} while most inorganic copper oxides, nitrides, and sulfides and other MOF catalysts were electrochemically reduced to Cu⁰ or Cu¹⁺ species during CRR.^{17–20}

To address this, we incorporated Cu²⁺ ions into a CeO₂ matrix to form a Cu Ce O_x solid solution to stabilize Cu²⁺ during CRR operation. The rapid electron transport channel provided by Ce³⁺ in these solid solutions suppresses the accumulation of electrons around Cu²⁺ sites, thereby protecting them from electrochemical reduction. This strategy can ensure valence stability of Cu²⁺ during catalytic operation, which is different from previous studies that focused on reoxidizing lower valence state metal species back to the initial higher valence state.^{21,22} In situ attenuated total reflectance infrared (ATR IR) spectroscopy demonstrated that the stable Cu²⁺ active sites can significantly enhance the initial *CO adsorption and promote *CO hydrogenation to form *OCH₃, a crucial intermediate for CH₄ generation. As a result, Cu Ce O_x delivered a high Faradaic efficiency (FE) for CH₄ with significant suppression of the competing C₂ products (i.e., C₂H₄). This study of stabilization of Cu²⁺ benefits the understanding of its CRR mechanism and provides a valuable inspiration for the design of other high valence state metal ions to explore their catalytic activity.

Cu Ce O_x was synthesized via an electrospinning–calcination method coupled with chemical etching to remove the possible CuO nanoparticles that were phase separated from CeO₂ (Figure S1).²³ Powder X ray diffraction (XRD) patterns

Received: November 18, 2021

Published: January 28, 2022



showed that the main phase in Cu Ce O_x is a typical face centered cubic CeO_2 (Figure 1a), demonstrating the formation

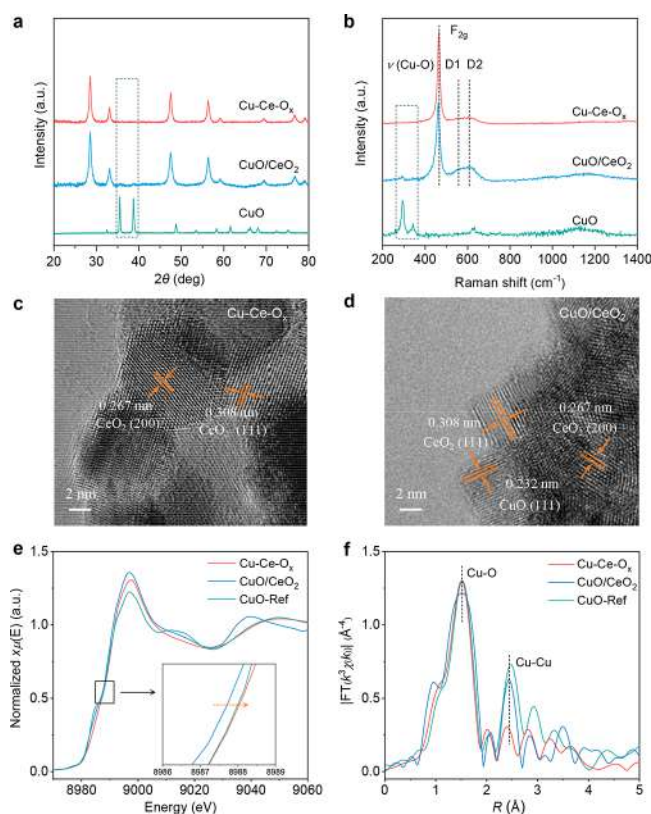


Figure 1. Structural characterizations of CuO/CeO_2 , Cu Ce O_x , and CuO . (a) XRD patterns. (b) Raman spectra. (c, d) HRTEM images. (e) Cu K edge XANES spectra. (f) Fourier transformed Cu K edge EXAFS spectra.

of a solid solution phase. By contrast, two weak diffraction peaks of CuO can be observed with the control sample, CuO/CeO_2 , which was prepared by an electrospinning–calcination method without an etching process. The Cu Ce O_x solid solution phase was also confirmed by Raman spectroscopy (Figure 1b). In addition, the bands at 500 to 600 cm^{-1} are assigned to a defect induced mode (D) resulting from the incorporation of CuO_x species into CeO_2 (Figures S2 and S3).²⁴ A lower intensity of them in Cu Ce O_x than in CuO/CeO_2 suggests that Cu species exist as Cu ions in the former but as CuO in the latter.^{25,26} The Cu content of Cu Ce O_x is 2.47 wt % as determined by inductively coupled plasma optical emission spectroscopy (ICP OES), which demonstrates a Cu/Ce atomic ratio of 0.08 (Table S1).

Transmission electron microscopy (TEM) images reveal that both Cu Ce O_x and CuO/CeO_2 consist of small nanocrystals with slightly different grain sizes (Figure S4). High resolution TEM (HRTEM) images confirm the presence of CuO clusters for CuO/CeO_2 , whereas no CuO is observed in Cu Ce O_x (Figure 1c,d). The energy dispersive X ray (EDX) element mappings further validate that Cu and Ce are uniformly distributed in the Cu Ce O_x framework (Figure S5). By contrast, the uneven distribution of Cu species in CuO/CeO_2 indicates the formation of CuO nanoparticles (Figure S6).

Cu K edge X ray absorption near edge structure (XANES) spectra display that Cu species in Cu Ce O_x exhibit an

oxidation state close to that of the CuO reference (Figure 1e). In the R space extended X ray absorption fine structure (EXAFS) spectra (Figure 1f), no Cu–Cu bond is observed in Cu Ce O_x , indicating that Cu^{2+} ions are monodispersed in the CeO_2 framework. This finding is also confirmed by Cu K edge wavelet transform (WT) EXAFS analysis (Figure S7). In a comparison with the two characteristic regions (Cu–O and Cu–Cu bonds) for CuO and CuO/CeO_2 , the absence of the corresponding signal for the Cu–Cu bond in Cu Ce O_x (CuO : 2.5 \AA^{-1}) strongly supports the atomic dispersion of Cu species in the CeO_2 matrix. Cu K edge EXAFS fitting further confirms that Cu ions in the solid solutions have the same coordination environment as CuO (Figure S8 and Table S2). In addition, a lack of medium range order around the Cu cations suggests that the Cu^{2+} ions are doped into the CeO_2 lattice,²⁷ in good agreement with the finding of the Raman spectra.

The CRR catalytic performances of CuO/CeO_2 and Cu Ce O_x were investigated in 1 M KOH solution by a flow cell (Figure S9). As shown in Figure 2a, at low potentials (below -1.0 V vs RHE), the main product with Cu Ce O_x is CH_4 with a maximum FE_{CH_4} of 67.8% achieved at -0.82 V vs RHE (with iR correction) with a total current density of 200 mA cm^{-2} . At

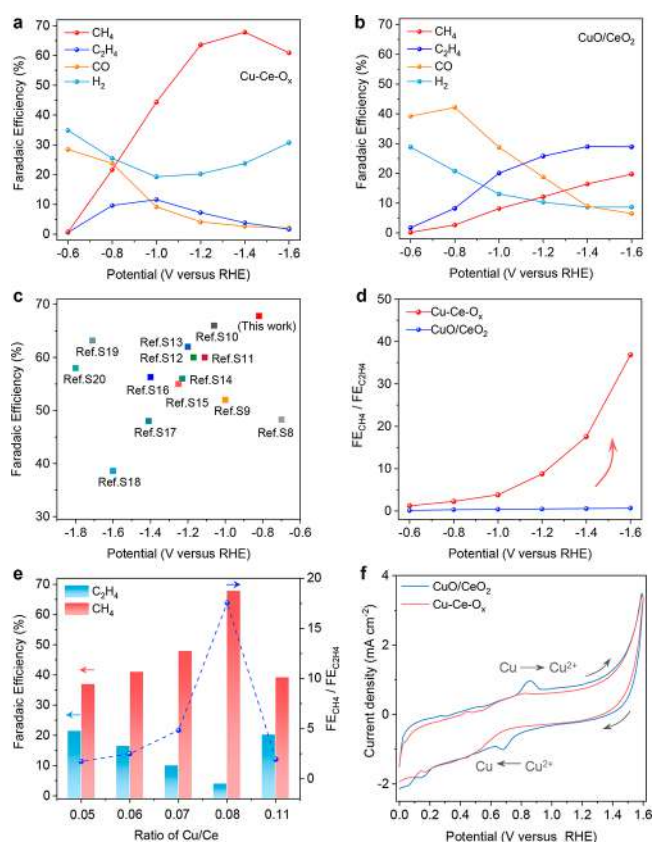


Figure 2. CRR performances of various samples. (a, b) FEs for CRR products at different potentials. CuO/CeO_2 can produce a few liquid products (e.g., formic acid and ethanol) under a more negative potential, which make the total FEs less than 100%. (c) FE_{CH_4} of Cu Ce O_x in comparison with other reported Cu based catalysts after iR correction (Table S3). (d) Ratios of FE_{CH_4} to $\text{FE}_{\text{C}_2\text{H}_4}$ for CuO/CeO_2 and Cu Ce O_x . (e) FEs for CRR products and ratios of FE_{CH_4} to $\text{FE}_{\text{C}_2\text{H}_4}$ on different Cu Ce O_x samples at -1.4 V vs RHE. (f) Cyclic voltammograms of Cu Ce O_x and CuO/CeO_2 after CRR.

the same time, strong C_2H_4 suppression ($FE_{C_2H_4} < 3.6\%$) can be observed. The long term stability of $Cu\ Ce\ O_x$ under a constant potential of $-1.4\ V$ vs RHE was evaluated in the flow reactor for more than 6 h with an average FE_{CH_4} of around 65% (Figure S10). By contrast, CuO/CeO_2 and CuO produce a mixture of CH_4 and C_2H_4 (Figures 2b and S11), which is similar to the widely reported OD Cu catalyst.^{28,29} Compared with the other reported Cu based materials, $Cu\ Ce\ O_x$ exhibits a remarkable CH_4 catalytic activity at a lower potential (Figure 2c). The maximum ratio of FE_{CH_4} to $FE_{C_2H_4}$ is 36.8 (at $-1.6\ V$ vs RHE), which is about 58 times higher than that of CuO/CeO_2 , unambiguously indicating higher CH_4 selectivity compared with C_2 products on $Cu\ Ce\ O_x$ (Figure 2d). Because the two samples have similar physical characteristics, such as particle size and surface area (Figure S12), the difference in CH_4 selectivity can be attributed to the intrinsic chemical characteristics (i.e., the existence of Cu^{2+} ions in $Cu\ Ce\ O_x$).

Therefore, we regulated the atomic ratio of Cu to Ce in a series of $Cu\ Ce\ O_x$ samples (Figure S13) to investigate the relationship between the concentration of Cu^{2+} and the CH_4 selectivity. At $-1.4\ V$ vs RHE, all of them (with $Cu/Ce = 0.05-0.11$) can exhibit FE_{CH_4} overwhelming $FE_{C_2H_4}$ (Figures 2e and S14). When Cu/Ce rises from 0.05 to 0.08, the ratio of FE_{CH_4} to $FE_{C_2H_4}$ increases 17 fold, indicating that a high concentration of Cu^{2+} in $Cu\ Ce\ O_x$ can significantly promote the CH_4 selectivity. However, a further increase of Cu/Ce to over 0.11 leads to a decrease in CH_4 selectivity. This change is possibly due to partial reduction of the Cu^{2+} to form OD Cu , in which the Cu^0/Cu^{1+} mixed interface can promote $*CO$ dimerization to yield C_2H_4 .^{9,28}

To reveal the origin of the different catalytic selectivity at $-1.4\ V$ vs RHE, we further performed cyclic voltammetry (CV) measurements to investigate the structural change of two samples during the CRR process. Figure 2f shows evident Cu^0/Cu^{2+} redox peaks in CuO/CeO_2 after CRR, similar to that of CuO (Figure S15), suggesting that CuO in CuO/CeO_2 has been electrochemically reduced to OD Cu . By contrast, there is no redox peak in the CV of $Cu\ Ce\ O_x$ as deep as $-1.6\ V$ vs RHE (Figures S16 and S17), confirming that its Cu^{2+} species remained unchanged during the process. Similar results apply for the other solid solution samples except for $Cu\ Ce\ O_x\ 0.11$, which shows a weak Cu^0/Cu^{2+} redox peak (Figure S16d).

In addition, we conducted spectroscopic characterizations to detect the possible phase transition and oxidation state change of these catalysts during CRR. Selected area electron diffraction (SAED) images and XRD patterns indicate no phase change for $Cu\ Ce\ O_x$ before and after the CRR process (Figure 3a,b). By contrast, the XRD pattern of after CRR CuO/CeO_2 exhibits the disappearance of peaks corresponding to CuO and the emergence of a Cu^0 signal (Figure S18), suggesting the reduction of CuO . This result is also supported by the HRTEM image and SAED images (Figures S19 and S20). X ray photoelectron spectroscopy (XPS) analysis also demonstrates that Cu^{2+} in $Cu\ Ce\ O_x$ remains unchanged in the CRR process, whereas Cu^0 was found in the sample of CuO/CeO_2 , suggesting the reduction of CuO (Figure 3c,d). In EDX, compared with the uneven Cu distribution in CuO/CeO_2 (Figure S21), uniform Cu species can be found in $Cu\ Ce\ O_x$ (Figure S22), further implying that no Cu nanoparticles were generated.

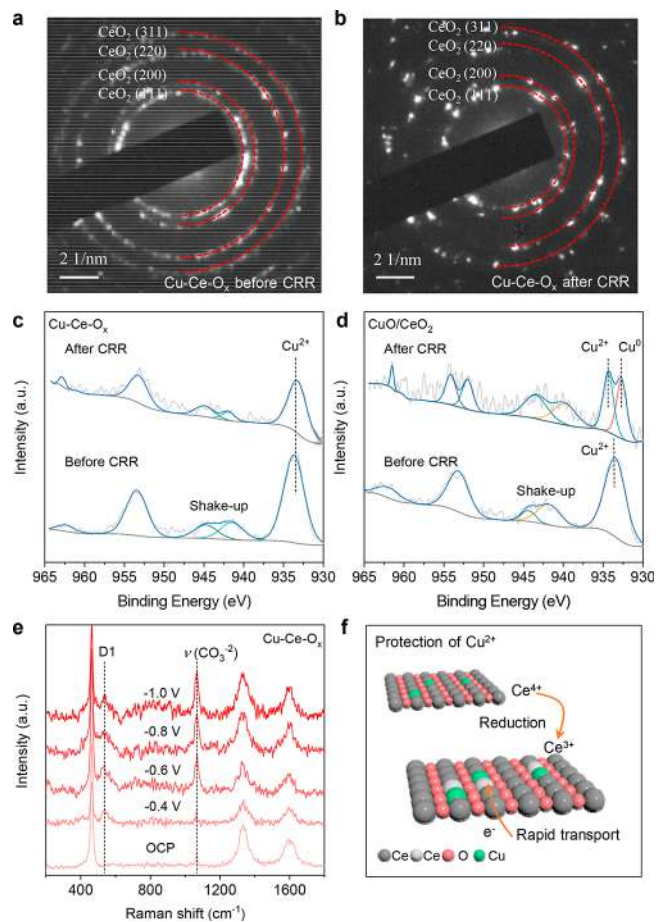


Figure 3. Stability investigation of $Cu\ Ce\ O_x$ and CuO/CeO_2 before and after CRR. (a, b) SAED patterns of $Cu\ Ce\ O_x$. (c, d) $Cu\ 2p$ XPS spectra. The fitted peaks at 932.50 and 933.40 eV are assigned to Cu^0 and Cu^{2+} species, respectively.³⁰ (e) In situ Raman spectra on $Cu\ Ce\ O_x$ collected at different potentials. (f) Scheme of the self sacrifice mechanism to protect Cu^{2+} .

We then conducted in situ Raman spectroscopy to study the mechanism of Cu^{2+} stability in $Cu\ Ce\ O_x$ during the CRR process. Figure 3e shows the appearance of a new peak at $\sim 560\ cm^{-1}$ that appeared during the negative scan, which can be ascribed to the D1 bond of defective CeO_2 . This peak originates from the electrochemical reduction of Ce^{4+} to Ce^{3+} with generation of an O^{2-} vacancy (Figure S23).³¹ The increase in Ce^{3+} concentration in $Cu\ Ce\ O_x$ after CRR is also confirmed by XPS analysis (Figure S24). Electrochemical impedance spectroscopy (EIS) results reveal that the solid solution after CRR has a lower charge transfer resistance, suggesting quicker electron transfer on its surface (Figure S25). Therefore, a CeO_2 self sacrifice mechanism is proposed to account for the stability of Cu^{2+} in $Cu\ Ce\ O_x$ (Figure 3f). First, during the CRR operation, the electron preferentially reduces Ce^{4+} in $Cu\ Ce\ O_x$ to Ce^{3+} . Meanwhile, the newly generated Ce^{3+}/Ce^{4+} couple works as a conductive network to improve the conductivity of the overall solid solution,³² which suppresses electron accumulation at the Cu^{2+} sites and prevents them from self reduction.

To elucidate the distinct CH_4 selectivity between $Ce-Cu-O_x$ and CuO/CeO_2 , we employed in situ ATR IR spectroscopy to identify their reactive species over the CRR process. First, compared with CuO/CeO_2 , a much stronger peak at 1955

Yan Jiao – School of Chemical Engineering and Advanced Materials, The University of Adelaide, Adelaide, SA 5005, Australia; [orcid.org/0000 0003 1329 4290](https://orcid.org/0000-0003-1329-4290)

Complete contact information is available at:
<https://pubs.acs.org/10.1021/jacs.1c12212>

Author Contributions

¹X.Z. and J.S. contributed equally.

Notes

The authors declare no competing financial interest.

ACKNOWLEDGMENTS

This work was financially supported by the Australian Research Council through Discovery Project Programs (FL170100154, FT200100062, and DP190103472). X.Z. acknowledges support from the Australian Government through Research Training Program Scholarships. The authors also gratefully acknowledge the staff at beamline 1W2B at the Beijing Synchrotron Radiation Facility (BSRF), China. DFT computations for this work were performed using supercomputing resources provided by the Phoenix HPC service at the University of Adelaide and the National Computational Infrastructure (NCI).

REFERENCES

- (1) Ross, M. B.; De Luna, P.; Li, Y.; Dinh, C. T.; Kim, D.; Yang, P.; Sargent, E. H. Designing materials for electrochemical carbon dioxide recycling. *Nat. Catal.* **2019**, *2* (8), 648–658.
- (2) Zheng, Y.; Vasileff, A.; Zhou, X.; Jiao, Y.; Jaroniec, M.; Qiao, S. Z. Understanding the Roadmap for Electrochemical Reduction of CO₂ to Multi Carbon Oxygenates and Hydrocarbons on Copper based Catalysts. *J. Am. Chem. Soc.* **2019**, *141* (19), 7646–7659.
- (3) Zhou, X.; Jin, H.; Xia, B. Y.; Davey, K.; Zheng, Y.; Qiao, S. Z. Molecular Cleavage of Metal Organic Frameworks and Application to Energy Storage and Conversion. *Adv. Mater.* **2021**, *33*, 2104341.
- (4) Lei, Q.; Zhu, H.; Song, K.; Wei, N.; Liu, L.; Zhang, D.; Yin, J.; Dong, X.; Yao, K.; Wang, N.; Li, X.; Davaasuren, B.; Wang, J.; Han, Y. Investigating the Origin of Enhanced C₂₊ Selectivity in Oxide / Hydroxide Derived Copper Electrodes during CO₂ Electroreduction. *J. Am. Chem. Soc.* **2020**, *142* (9), 4213–4222.
- (5) Wang, J.; Tan, H. Y.; Zhu, Y.; Chu, H.; Chen, H. M. Linking the Dynamic Chemical State of Catalysts with the Product Profile of Electrocatalytic CO₂ Reduction. *Angew. Chem., Int. Ed.* **2021**, *60* (32), 17254–17267.
- (6) Chou, T. C.; Chang, C. C.; Yu, H. L.; Yu, W. Y.; Dong, C. L.; Velasco Velez, J. J.; Chuang, C. H.; Chen, L. C.; Lee, J. F.; Chen, J. M.; Wu, H. L. Controlling the Oxidation State of the Cu Electrode and Reaction Intermediates for Electrochemical CO₂ Reduction to Ethylene. *J. Am. Chem. Soc.* **2020**, *142* (6), 2857–2867.
- (7) Wu, Z. Z.; Gao, F. Y.; Gao, M. R. Regulating the oxidation state of nanomaterials for electrocatalytic CO₂ reduction. *Energy Environ. Sci.* **2021**, *14* (3), 1121–1139.
- (8) Xiao, H.; Goddard, W. A.; Cheng, T.; Liu, Y. Cu metal embedded in oxidized matrix catalyst to promote CO₂ activation and CO dimerization for electrochemical reduction of CO₂. *Proc. Natl. Acad. Sci. U.S.A.* **2017**, *114* (26), 6685–6688.
- (9) Yuan, X.; Chen, S.; Cheng, D.; Li, L.; Zhu, W.; Zhong, D.; Zhao, Z. J.; Li, J.; Wang, T.; Gong, J. Controllable Cu⁰ Cu⁺ Sites for Electrocatalytic Reduction of Carbon Dioxide. *Angew. Chem., Int. Ed.* **2021**, *60* (28), 15344–15347.
- (10) Aran Ais, R. M.; Scholten, F.; Kunze, S.; Rizo, R.; Roldan Cuenya, B. The role of in situ generated morphological motifs and Cu(I) species in C₂₊ product selectivity during CO₂ pulsed electroreduction. *Nat. Energy* **2020**, *5* (4), 317–325.
- (11) Peterson, A. A.; Nørskov, J. K. Activity Descriptors for CO₂ Electroreduction to Methane on Transition Metal Catalysts. *J. Phys. Chem. Lett.* **2012**, *3* (2), 251–258.
- (12) Woertink, J. S.; Smeets, P. J.; Groothaert, M. H.; Vance, M. A.; Sels, B. F.; Schoonheydt, R. A.; Solomon, E. I. A [Cu₂O]²⁺ core in Cu ZSM 5, the active site in the oxidation of methane to methanol. *Proc. Natl. Acad. Sci. U.S.A.* **2009**, *106* (45), 18908–18913.
- (13) Xu, S.; Chansai, S.; Stere, C.; Inceesungvorn, B.; Goguet, A.; Wangkawong, K.; Taylor, S. F. R.; Al Janabi, N.; Hardacre, C.; Martin, P. A.; Fan, X. Sustaining metal organic frameworks for water gas shift catalysis by non thermal plasma. *Nat. Catal.* **2019**, *2* (2), 142–148.
- (14) Zhou, Y.; Che, F.; Liu, M.; Zou, C.; Liang, Z.; De Luna, P.; Yuan, H.; Li, J.; Wang, Z.; Xie, H.; Li, H.; Chen, P.; Bladt, E.; Quintero Bermudez, R.; Sham, T. K.; Bals, S.; Hofkens, J.; Sinton, D.; Chen, G.; Sargent, E. H. Dopant induced electron localization drives CO₂ reduction to C₂ hydrocarbons. *Nat. Chem.* **2018**, *10* (9), 974–980.
- (15) Zhang, Y.; Dong, L. Z.; Li, S.; Huang, X.; Chang, J. N.; Wang, J. H.; Zhou, J.; Li, S. L.; Lan, Y. Q. Coordination environment dependent selectivity of single site Cu enriched crystalline porous catalysts in CO₂ reduction to CH₄. *Nat. Commun.* **2021**, *12* (1), 6390.
- (16) Liu, Y.; Li, S.; Dai, L.; Li, J.; Lv, J.; Zhu, Z.; Yin, A.; Li, P.; Wang, B. The Synthesis of Hexaazatrinaphthylene Based 2D Conjugated Copper Metal Organic Framework for Highly Selective and Stable Electroreduction of CO₂ to Methane. *Angew. Chem., Int. Ed.* **2021**, *60* (30), 16409–16415.
- (17) De Luna, P.; Quintero Bermudez, R.; Dinh, C. T.; Ross, M. B.; Bushuyev, O. S.; Todorović, P.; Regier, T.; Kelley, S. O.; Yang, P.; Sargent, E. H. Catalyst electro redeposition controls morphology and oxidation state for selective carbon dioxide reduction. *Nat. Catal.* **2018**, *1* (2), 103–110.
- (18) He, C.; Duan, D.; Low, J.; Bai, Y.; Jiang, Y.; Wang, X.; Chen, S.; Long, R.; Song, L.; Xiong, Y. Cu_{2-x}S derived copper nanoparticles: A platform for unraveling the role of surface reconstruction in efficient electrocatalytic CO₂ to C₂H₄ conversion. *Nano Res.* **2021**, DOI: 10.1007/s12274-021-3532-7.
- (19) Zhao, C.; Luo, G.; Liu, X.; Zhang, W.; Li, Z.; Xu, Q.; Zhang, Q.; Wang, H.; Li, D.; Zhou, F.; Qu, Y.; Han, X.; Zhu, Z.; Wu, G.; Wang, J.; Zhu, J.; Yao, T.; Li, Y.; Bouwmeester, H. J. M.; Wu, Y. In Situ Topotactic Transformation of an Interstitial Alloy for CO Electroreduction. *Adv. Mater.* **2020**, *32* (39), 2002382.
- (20) Zhou, X.; Dong, J.; Zhu, Y.; Liu, L.; Jiao, Y.; Li, H.; Han, Y.; Davey, K.; Xu, Q.; Zheng, Y.; Qiao, S. Z. Molecular Scalpel to Chemically Cleave Metal Organic Frameworks for Induced Phase Transition. *J. Am. Chem. Soc.* **2021**, *143* (17), 6681–6690.
- (21) Sushkevich, V. L.; Palagin, D.; Ranocchiaro, M.; van Bokhoven, J. A. Selective anaerobic oxidation of methane enables direct synthesis of methanol. *Science* **2017**, *356* (6337), 523–527.
- (22) Jeon, H. S.; Timoshenko, J.; Rettenmaier, C.; Herzog, A.; Yoon, A.; Chee, S. W.; Oener, S.; Hejral, U.; Haase, F. T.; Roldan Cuenya, B. Selectivity Control of Cu Nanocrystals in a Gas Fed Flow Cell through CO₂ Pulsed Electroreduction. *J. Am. Chem. Soc.* **2021**, *143* (19), 7578–7587.
- (23) Li, R.; Yang, Y.; Sun, N.; Kuai, L. Mesoporous Cu Ce O_x Solid Solutions from Spray Pyrolysis for Superior Low Temperature CO Oxidation. *Chem. Eur. J.* **2019**, *25* (68), 15586–15593.
- (24) Li, L.; Chen, F.; Lu, J. Q.; Luo, M. F. Study of defect sites in Ce_{1-x}M_xO_{2-δ} (x = 0.2) solid solutions using Raman spectroscopy. *J. Phys. Chem. A* **2011**, *115* (27), 7972–7.
- (25) Gao, Y.; Zhang, Z.; Li, Z.; Huang, W. Understanding morphology dependent CuO_x-CeO₂ interactions from the very beginning. *Chin. J. Catal.* **2020**, *41* (6), 1006–1016.
- (26) Shan, W.; Shen, W.; Li, C. Structural Characteristics and Redox Behaviors of Ce_{1-x}Cu_xO_y Solid Solutions. *Chem. Mater.* **2003**, *15* (25), 4761–4767.
- (27) Wang, X.; Rodriguez, J. A.; Hanson, J. C.; Gamarrá, D.; Martínez Arias, A.; Fernández García, M. Unusual physical and chemical properties of Cu in Ce_{1-x}Cu_xO₂ oxides. *J. Phys. Chem. B* **2005**, *109* (42), 19595–603.

(28) Yang, P. P.; Zhang, X. L.; Gao, F. Y.; Zheng, Y. R.; Niu, Z. Z.; Yu, X.; Liu, R.; Wu, Z. Z.; Qin, S.; Chi, L. P.; Duan, Y.; Ma, T.; Zheng, X. S.; Zhu, J. F.; Wang, H. J.; Gao, M. R.; Yu, S. H. Protecting Copper Oxidation State via Intermediate Confinement for Selective CO₂ Electroreduction to C₂₊ Fuels. *J. Am. Chem. Soc.* **2020**, *142* (13), 6400–6408.

(29) Lee, S. Y.; Jung, H.; Kim, N. K.; Oh, H. S.; Min, B. K.; Hwang, Y. J. Mixed Copper States in Anodized Cu Electrocatalyst for Stable and Selective Ethylene Production from CO₂ Reduction. *J. Am. Chem. Soc.* **2018**, *140* (28), 8681–8689.

(30) Jung, H.; Lee, S. Y.; Lee, C. W.; Cho, M. K.; Won, D. H.; Kim, C.; Oh, H. S.; Min, B. K.; Hwang, Y. J. Electrochemical Fragmentation of Cu₂O Nanoparticles Enhancing Selective C–C Coupling from CO₂ Reduction Reaction. *J. Am. Chem. Soc.* **2019**, *141* (11), 4624–4633.

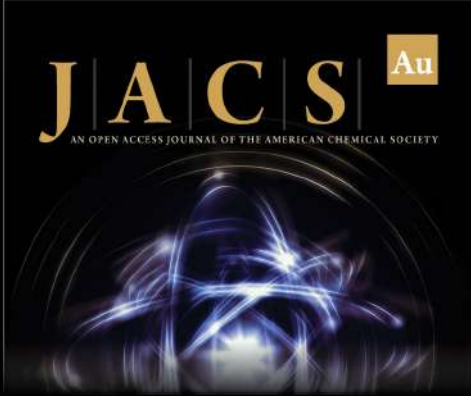
(31) Taniguchi, T.; Watanabe, T.; Sugiyama, N.; Subramani, A. K.; Wagata, H.; Matsushita, N.; Yoshimura, M. Identifying Defects in Ceria Based Nanocrystals by UV Resonance Raman Spectroscopy. *J. Phys. Chem. C* **2009**, *113* (46), 19789–19793.

(32) Kumar, M.; Yun, J. H.; Bhatt, V.; Singh, B.; Kim, J.; Kim, J. S.; Kim, B. S.; Lee, C. Y. Role of Ce³⁺ valence state and surface oxygen vacancies on enhanced electrochemical performance of single step solvothermally synthesized CeO₂ nanoparticles. *Electrochim. Acta* **2018**, *284*, 709–720.


(33) Katayama, Y.; Nattino, F.; Giordano, L.; Hwang, J.; Rao, R. R.; Andreussi, O.; Marzari, N.; Shao Horn, Y. An In Situ Surface Enhanced Infrared Absorption Spectroscopy Study of Electrochemical CO₂ Reduction: Selectivity Dependence on Surface C Bound and O Bound Reaction Intermediates. *J. Phys. Chem. C* **2019**, *123* (10), 5951–5963.


(34) Perez Gallent, E.; Figueiredo, M. C.; Calle Vallejo, F.; Koper, M. T. Spectroscopic Observation of a Hydrogenated CO Dimer Intermediate During CO Reduction on Cu(100) Electrodes. *Angew. Chem., Int. Ed.* **2017**, *56* (13), 3621–3624.


(35) Cheng, T.; Xiao, H.; Goddard, W. A., 3rd Full atomistic reaction mechanism with kinetics for CO reduction on Cu(100) from ab initio molecular dynamics free energy calculations at 298 K. *Proc. Natl. Acad. Sci. U.S.A.* **2017**, *114* (8), 1795–1800.



JACS Au
AN OPEN ACCESS JOURNAL OF THE AMERICAN CHEMICAL SOCIETY

 Editor-in-Chief
Prof. Christopher W. Jones
Georgia Institute of Technology, USA

Open for Submissions 

pubs.acs.org/jacsau  ACS Publications
Most Trusted. Most Cited. Most Read.

Supplementary Information

Stabilizing Cu²⁺ ions by Solid Solutions to Promote CO₂ Electroreduction to Methane

Xianlong Zhou,^{1#} Jieqiong Shan,^{1#} Ling Chen,¹ Bao Yu Xia,² Tao Ling,³ Jingjing Duan,⁴ Yan Jiao,¹
Yao Zheng,^{1*} Shi-Zhang Qiao^{1*}

¹ School of Chemical Engineering and Advanced Materials, The University of Adelaide, Adelaide, SA 5005, Australia.

² Key Laboratory of Material Chemistry for Energy Conversion and Storage (Ministry of Education), Hubei Key Laboratory of Material Chemistry and Service Failure, Wuhan; National Laboratory for Optoelectronics, School of Chemistry and Chemical Engineering, Huazhong University of Science and Technology (HUST), 1037 Luoyu Road, Wuhan 430074, China.

³ Key Laboratory for Advanced Ceramics and Machining Technology of Ministry of Education, Institute of New-Energy, School of Materials Science and Engineering, Tianjin University, Tianjin 300072, China.

⁴ Key Laboratory for Soft Chemistry and Functional Materials (Ministry of Education), School of Chemical Engineering, School of Energy and Power Engineering, Nanjing University of Science and Technology, Nanjing, 210094, China.

These authors contributed equally

*email: yao.zheng01@adelaide.edu.au; s.qiao@adelaide.edu.au

Materials Synthesis

Synthesis of CuO/CeO₂. Electrospinning was used to synthesize the precursors of solid solutions. 0.4 millimoles of Cu(NO₃)₂·3H₂O, 0.6 mmol of Ce(NO₃)₃·6H₂O, and 0.5 g of polyacrylonitrile (PAN) were dissolved in 6 mL of DMF under magnetic stirring for 4 h. Then, the mixed solution was transferred into a 10 mL plastic injection syringe. The electrospinning voltage was set as 18 kV, the distance between the nozzle and collector was 10 cm, the injection speed was 0.12 mm min⁻¹, then the precursors of solid solutions were obtained. CuO/CeO₂ powder was obtained after calcinating the precursors in air at 400 °C for 2 h at a heating rate of 2.0 °C min⁻¹.

Synthesis of Cu-Ce-O_x. A leaching strategy with concentrated NH₃·6H₂O (25-28%) was applied to synthesize Cu-Ce-O_x powder. In detail, the CuO/CeO₂ powders (0.2 g) were dispersed in 20 mL of concentrated NH₃·6H₂O. The mixture was vigorously stirred at 55 °C for 60 min. The catalyst was separated by centrifugation, and a blue filtrate could be obtained if there were CuO_x species on the catalyst surface. The leaching was repeated 6 times until the filtrate was colorless. The precipitates were washed with deionized water and ethanol for three times. Cu-Ce-O_x powder was obtained after freeze-drying for 24 h.

Synthesis of Cu-Ce-O_x-A. Preparation of solid solutions with different Cu mass percentages was similar to that of Cu-Ce-O_x. With the total mol of Cu(NO₃)₂·3H₂O and Ce(NO₃)₃·6H₂O kept as 1.0 mmol, we changed the mol mass of Cu(NO₃)₂·3H₂O from 0.05, 0.1, 0.2, 0.6 mmol to obtain different solid solution precursors. After the same chemical etching with concentrated NH₃·6H₂O, the Cu-Ce-O_x samples were obtained.

Synthesis of CuO and CeO₂. Preparation of CuO and CeO₂ was similar to that for CuO/CeO₂, in which 1 mmol of Ce(NO₃)₃·6H₂O or Cu(NO₃)₂·3H₂O and 0.5 g of PAN were used to obtain the mixed solution.

Materials Characterization

The phase and structure of as-synthesized samples were analyzed by a Philips PW-1830 X-Ray Diffractometer (XRD) using Cu K α radiation ($\lambda=1.5406$ Å, scan rate = 5° min⁻¹). Scanning electronic microscope (SEM) images and transmission electronic microscope (TEM) images were collected on a Hitachi New Generation SU8010 SEM and a JOEL 2100 TEM, respectively. Raman spectra were collected on a confocal Raman microscope (Horiba LabRAM HR Evolution) with a 633 nm solid laser as an excitation source (100 ~ 2000 cm⁻¹). XPS measurements were conducted on AXIS-ULTRA DLD-600W XPS (mono Al K α 1486.6 eV) and recorded by the hemispherical analyser with a step-size of 0.05 eV. The content of Cu and Ce in solid solutions was measured by inductively coupled plasma optical emission spectroscopy (ICP-OES, Agilent 730).

X-ray Absorption Spectroscopy (XAS) Analysis

Cu K-edge X-ray absorption spectroscopy analysis was carried out under ambient condition in fluorescence mode at beamline 1W2B in the Beijing Synchrotron Radiation Facility (BSRF), China. In the testing, it used a Si (111) double-crystal monochromator, and Cu-foil was used to calibrate the energy. Both the incident and fluorescence X-ray intensities were monitored using standard ion chambers and Ar-filled Lytle-type detector, respectively. The XAS raw data were background-subtracted, normalized, and Fourier-transformed using standard procedures with ATHENA.

Electrochemistry Measurement

Activity/selectivity measurement. The CO₂ reduction reaction (CRR) catalytic activity of different samples was investigated by a commercial flow cell (Gaossunion) in 1 M KOH solution. The volumes of anode and cathode chamber electrolyte were both 20 mL. To prepare the working electrode, 30 mg of catalyst was dispersed by sonication in 2.85 mL of isopropanol and 150 μL of 5 wt % of Nafion for 30 min. Next, inks were airbrushed onto a gas diffusion layer (GDL, Sigracet 29 BC) as the cathode electrode ($3 \times 1 \text{ cm}^2$, loading mass: 1.0 mg cm^{-2}). The reference and counter electrodes were Ag/AgCl (3.0 M KCl) and Pt foil ($3 \times 1 \text{ cm}$; 1 mm thickness) connected to a potentiostat (Gamry Interface 3000), respectively. An anion exchange membrane (FAB-PK-130) (Fuel Cell Store) was sandwiched between the two PTFE sheets to separate the chambers. In addition, 1 M KOH was circulated around the cathode and anode at a flow rate of 10.0 ml min^{-1} during the CRR. During this process and then testing, CO₂ was continuously purged at a rate of 20 μL min^{-1} . The resistance of 2.9 Ω was used to calculate the *iR*-correction. The gas products were self-injected into a gas chromatograph (Shimadzu GC-2014) equipped with TCD and methanizer/FID detectors.

Cyclic voltammetry. Cyclic voltammetry (CV) was used to detect Cu structure change of CuO/CeO₂ and Cu-Ce-O_x after CRR. Before CV measurements, we performed a chronograph voltage testing under -1.4 V vs RHE for 2 h to obtain samples. Then, CO₂ was turned off, and N₂ was continuously purged at a rate of 20 μL min^{-1} for 30 min to remove the gas products on the electrode surface. Additionally, the electrolyte was replaced with fresh 1 M KOH. Finally, we conducted CV measurements on the electrode with a scan rate of 20 mV s^{-1} .

XPS analysis of samples after CRR. We identified the Cu valence state of the solid solution after CRR by XPS analysis. When the CRR test was completed, the electrode was washed by deionized water and ethanol for three times. The sample after CRR was obtained after vacuum drying for 12 h, and sealed in a high-purity Ar-filled glove box to avoid oxidation in Air for further characterization.

Electrochemical impedance spectroscopy (EIS) was conducted also on the Gamry Interface 3000 electrochemical workstation in the frequency from 0.01 Hz to 100 kHz with a signal amplitude of 5 mV at -1.2 V vs RHE.

***In situ* Attenuated Total Reflectance Infrared (ATR-IR) Spectroscopy**

It was performed with a Thermo-Fisher Nicolet iS20 equipped with a liquid nitrogen-cooled HgCdTe (MCT) detector using a VeeMax III ATR accessory (Pike Technologies). A germanium prism (60°, PIKE Technologies) was mounted in a PIKE electrochemical three-electrode cell with an Ag/AgCl reference electrode (Pine Research) and a platinum-wire counter electrode. All ATR-IR measurements were acquired by averaging 64 scans at a spectral resolution of 4 cm⁻¹. Electrocatalyst ink was prepared by dispersing catalyst powder (20 mg) in a solution containing isopropanol (2.9 mL) and 5 wt % Nafion solution (100 μL) followed by ultrasonication for 1 hr. 50 μL of the catalyst ink was dropped onto the prism and left to dry slowly. The electrolyte was 0.1 M KHCO₃, which was constantly purged with CO₂ during the experiment. A CHI 760E electrochemical workstation (CH Instruments, USA) was connected for chronoamperometric tests from -0.6 to -1.8 V vs. Ag/AgCl stepwise. The spectra under open circuit potential (OCP) were recorded for comparison.

***In situ* Raman Spectroscopy**

In situ Raman was recorded on a HORIBA LabRAM HR Evolution Raman spectrometer. The measurement was carried out by utilizing a spectro-electrochemical flow cell through a quartz window to detect the cathode GDL. For each measurement, the Raman spectrum was accumulated by 2 acquisitions (20 s per acquisition). A syringe pump was used to pump 1 M KOH at a constant flow rate of 3 mL min⁻¹ over the GDL. CO₂ gas was introduced to the back of the GDL at a flow rate of 80 SCCM controlled by a mass flow controller (FMA-2617A-VOL, OMEGA). Working electrodes were formed from Airbrushed Cu-Ce-O_x deposited on a piece of GDL (2 × 2 cm², loading mass: 1.0 mg cm⁻²). Potentials were applied (in potential holds) with respect to an Ag/AgCl reference electrode and reported with respect to RHE. To be consistent with the electrolysis measurements, Raman spectra were obtained at 5 min after the potential was initially applied. Potential-dependent spectra were obtained at OCP, -0.4, -0.6, -0.8 and -1.0 V vs RHE. Nickel foam was used as the counter electrode.

Computational Methods

All DFT calculations were performed with the Vienna Ab Initio Simulation Package (VASP) code.¹ The Perdew-Burke-Ernzerhof (PBE) was employed for electron exchange-correlation.² Projector Augmented Wave (PAW) potentials were used to describe the ionic cores³. The atomic relaxations

were carried out with the quasi-Newton minimization scheme until the maximum force on any atom was below 0.03 eV/Å. The geometry optimizations were performed with a plane-wave cutoff of 400 eV. Irreducible 2×2×1 Monkhorst Pack k-point grid was used,⁴ with the centre shifted to the gamma point. The Fermi level was smeared with the Methfessel-Paxton approach with a smearing of 0.05 eV. Dipole corrections were included in all the calculations to minimize the inaccuracies in the total energy due to the simulated slab interactions. The dipole moment was calculated parallel to the z-direction.

The implicit solvent effect was considered by using VASPsol.⁵ The solvent dielectric constant was set to be 78.4 F/m, the width of dielectric cavity was 0.6 Å, the cutoff charge density was set to be 2.5×10⁻³ C/m³ and the effective cavity surface tension was 5.25×10⁻⁴ N/m.

The computational models were constructed based on 4×3×2 CeO₂ (111) supercell. To model the Cu-Ce-O_x solid-solution at low Cu content, one Ce atom on the top layer was replaced by a Cu atom. Topmost layer and adsorbates were free to move in all directions, with bottom layers fixed. The vertical separation between periodically repeated images was set to be at least 15 Å in all cases, to ensure no interaction between images.

The DFT-calculated electronic energies (E) are converted into free energies in the following way:

$$G = E + \text{ZPE} - \text{TS}$$

where ZPE is the zero-point energy correction and TS is the entropy correction at room temperature (300 K). All energy values were acquired in neutral environment (pH=7).

As the standard DFT functionals tended to over-delocalize electrons, DFT+U⁶ was employed with an effective U value of 5.0 eV for both Ce 4f-orbitals and Cu 3d-orbitals.⁷

Limiting potential (U_{limiting}) is used to describe the lowest potential requirement to eliminate the free energy difference of the potential-determining step (PDS), calculated as:

$$U_{\text{limiting}} = -\Delta G_{\text{max}}/e$$

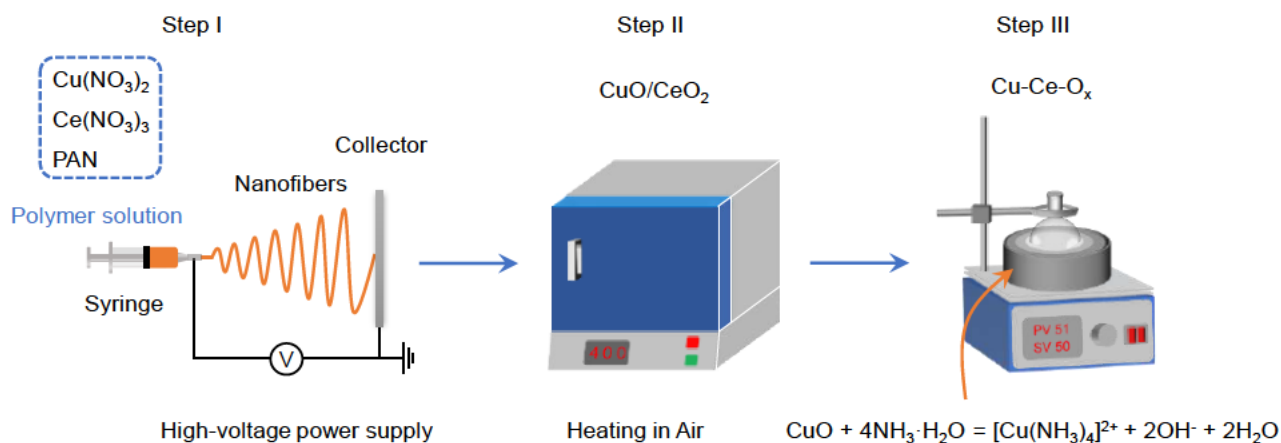


Figure S1. Synthetic route of solid solutions.

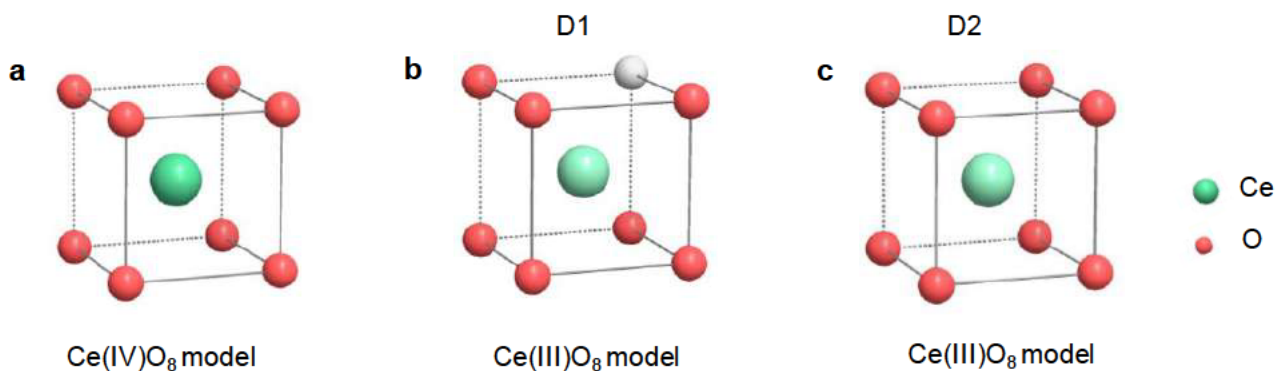


Figure S2. (a) The $\text{Ce}(\text{IV})\text{O}_8$ model and (b, c) defective complexes $\text{Ce}(\text{III})\text{O}_8$ models corresponding to D1 and D2 bands.

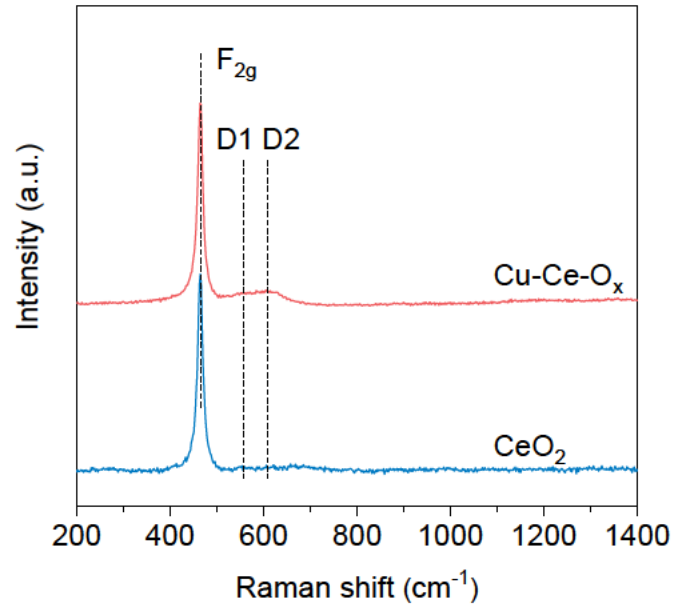


Figure S3. Raman spectra of Cu-Ce-O_x and CeO₂.

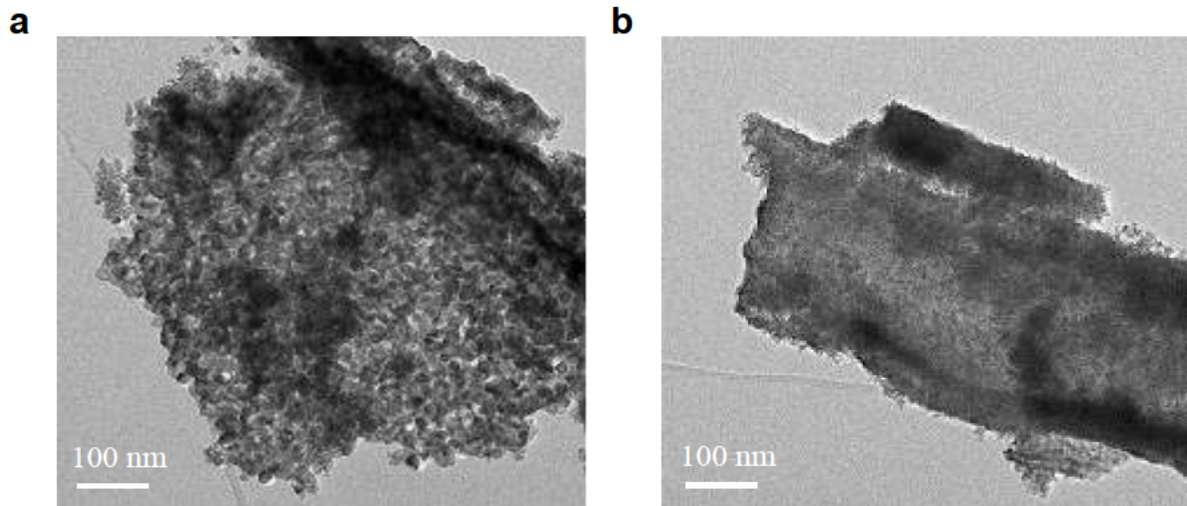


Figure S4. TEM images of (a) CuO/CeO₂ and (b) Cu-Ce-O_x.

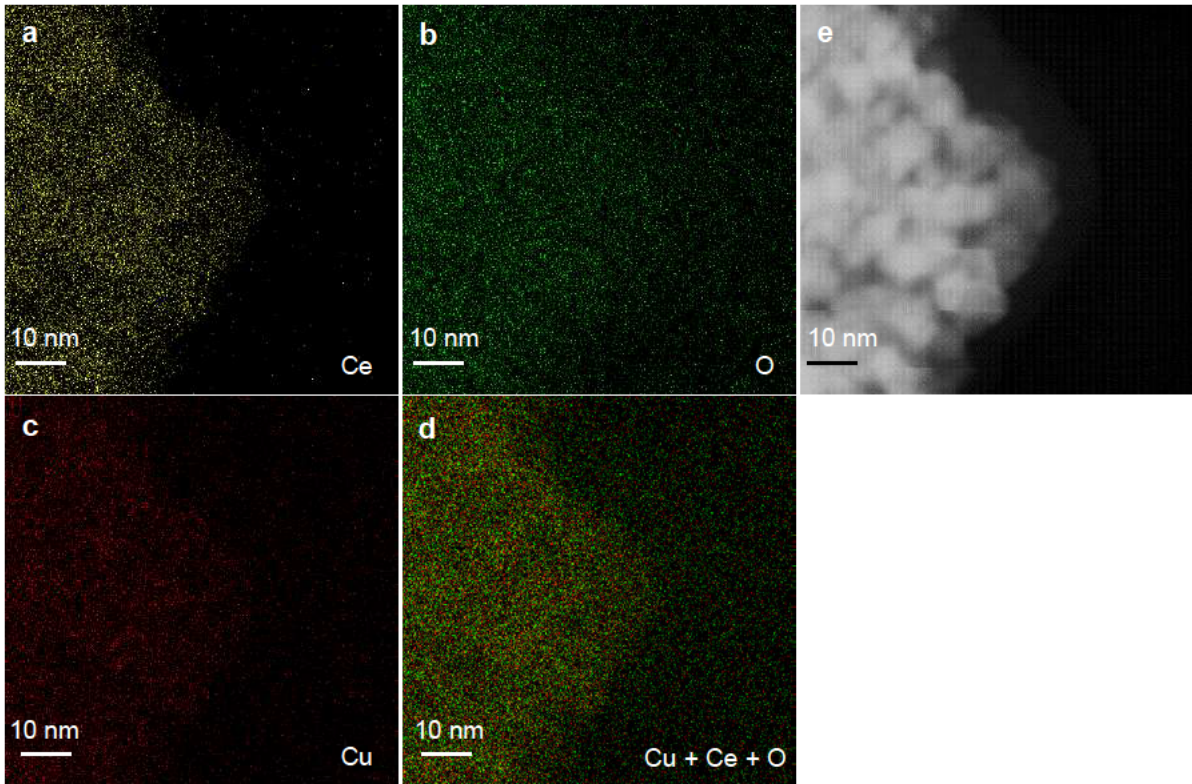


Figure S5. EDX elemental mapping images of Cu-Ce-O_x.

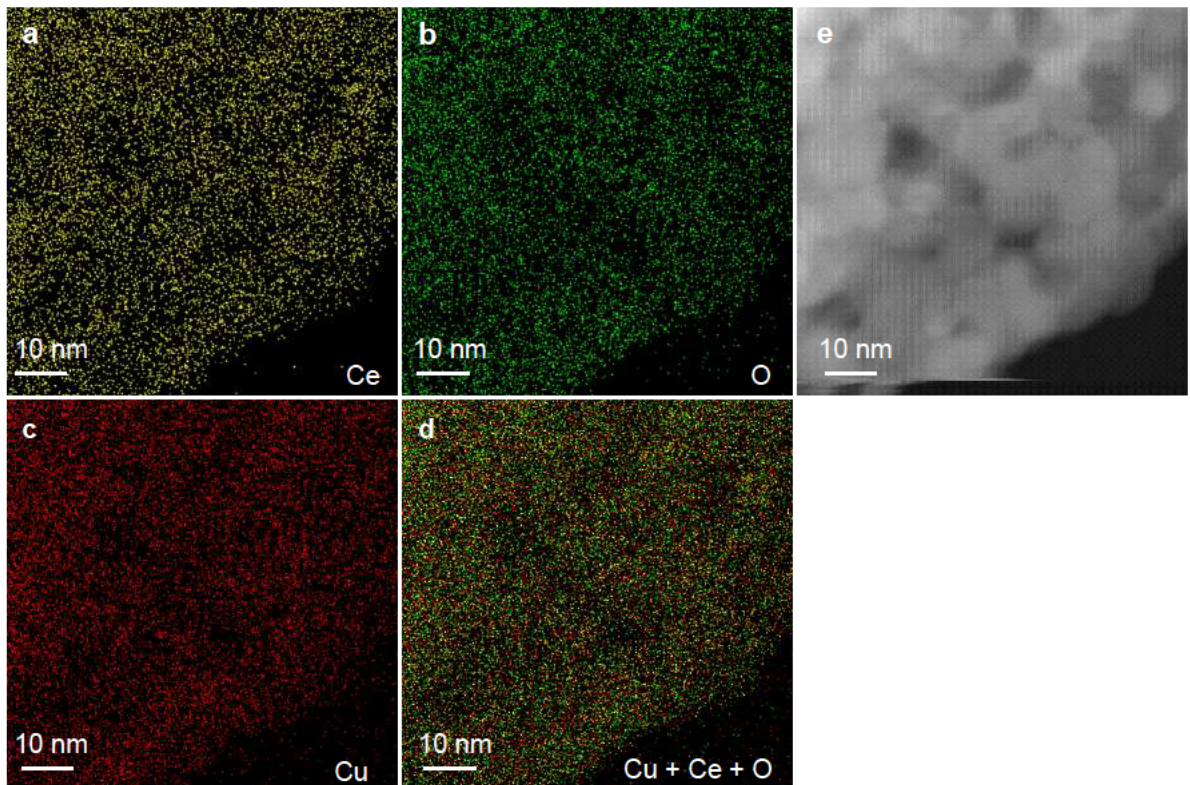


Figure S6. EDX elemental mapping images of CuO/CeO₂.

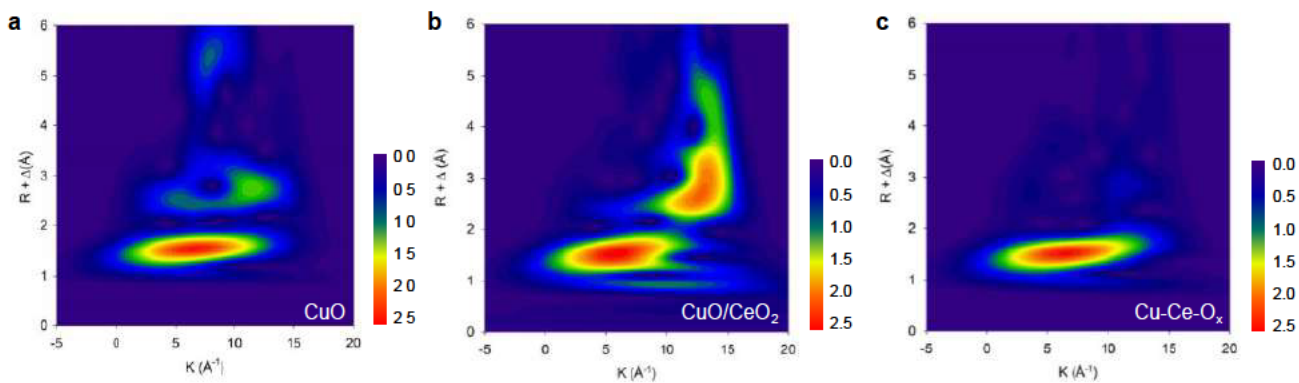


Figure S7. Cu K-edge WT-EXAFS of (a) CuO; (b) CuO/CeO₂; and (c) Cu-Ce-O_x.

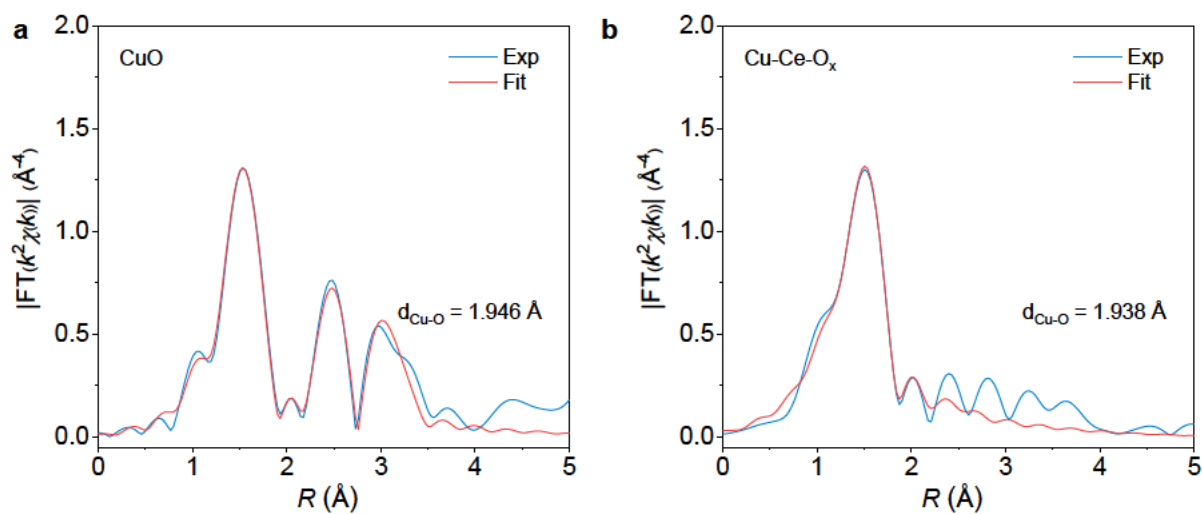


Figure S8. Fourier transformed magnitudes of experimental and fitting K-edge EXAFS spectra for (a) CuO and (b) Cu-Ce-O_x.

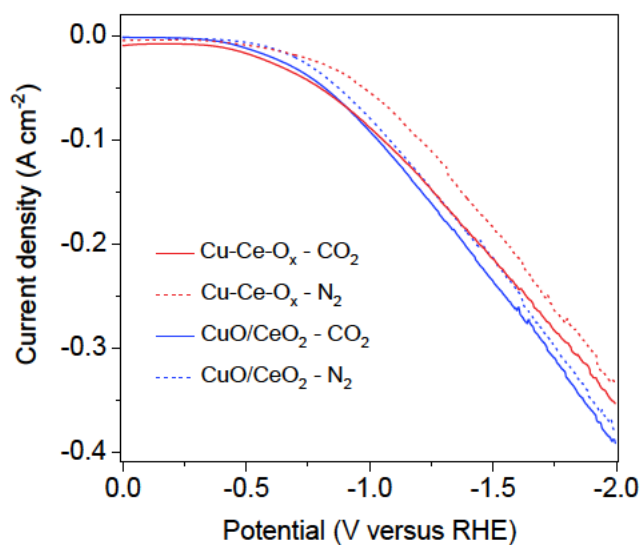


Figure S9. LSV curves of Cu-Ce-O_x and CuO/CeO₂ in N₂ or CO₂ atmosphere at a scan rate of 50 mVs⁻¹.

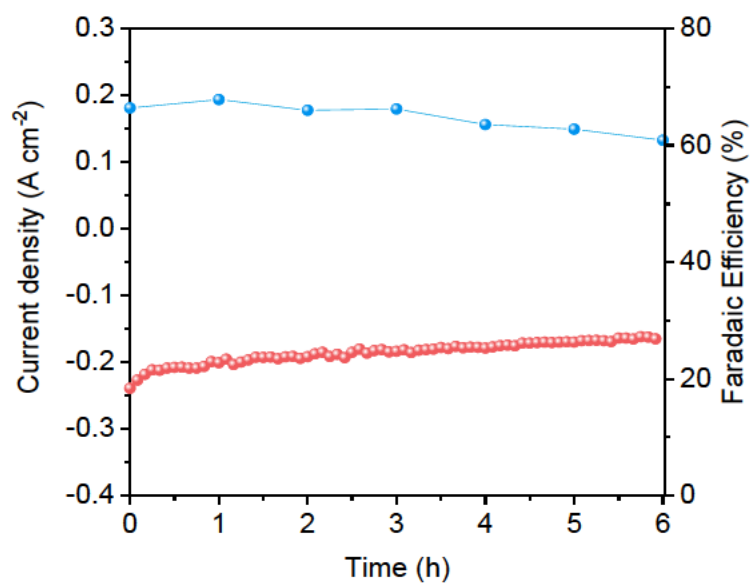


Figure S10. The time-dependent total current density and FE_{CH_4} for Cu-Ce-O_x recorded at -1.4 V vs RHE for 6 h.

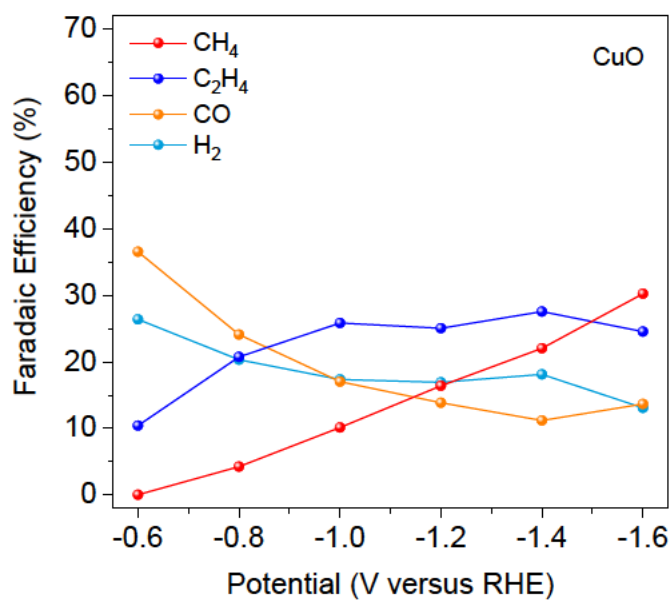


Figure S11. Faradaic efficiencies (FE) of CRR products for CuO over a range of applied potentials without iR correction.

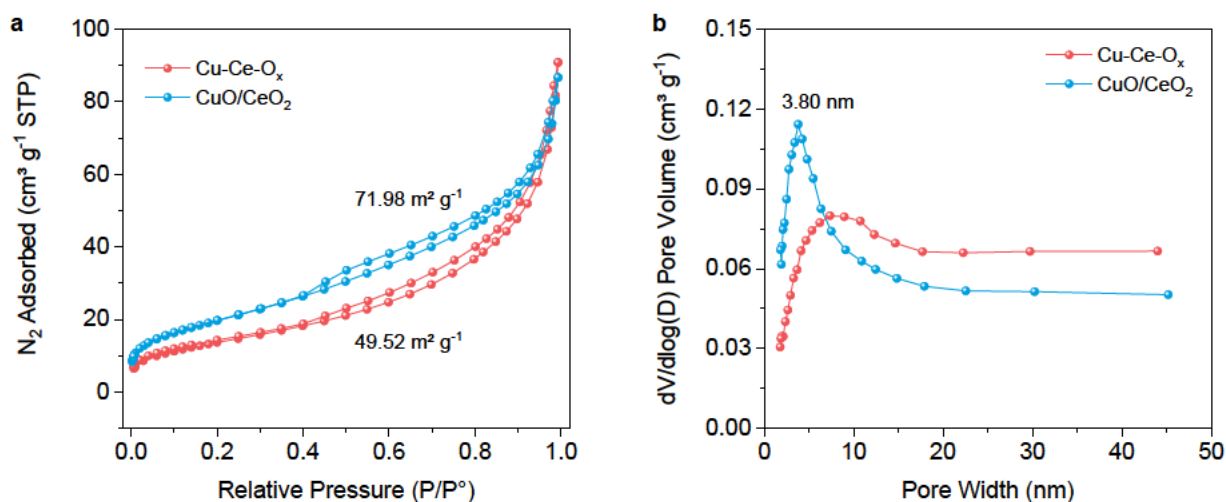


Figure S12. (a) The N_2 adsorption/desorption isotherms and (b) pore size distribution plots of Cu-

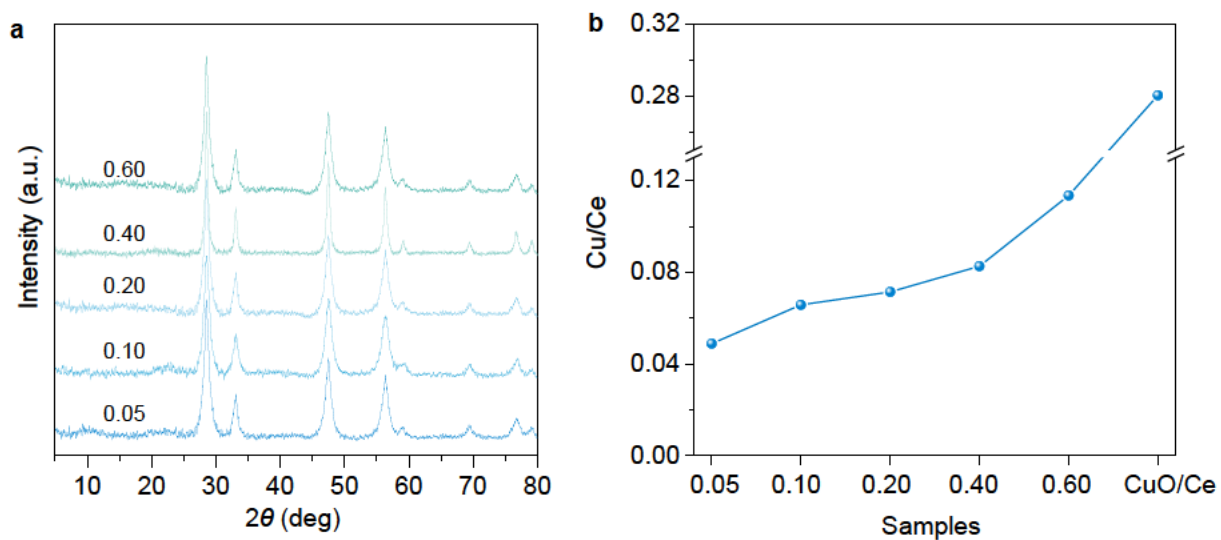


Figure S13. (a) The XRD patterns and (b) the Cu/Ce ratio calculated by ICP data for different samples. In panel a, we named the samples according to the molar percentage of $Cu(NO_3)_2 \cdot 3H_2O$ of $Ce(NO_3)_3 \cdot 6H_2O$ in the precursor. For instance, the sample name 0.10 refers to the adoption of 0.10 mmol of $Cu(NO_3)_2 \cdot 3H_2O$ and 0.90 mmol of $Ce(NO_3)_3 \cdot 6H_2O$.

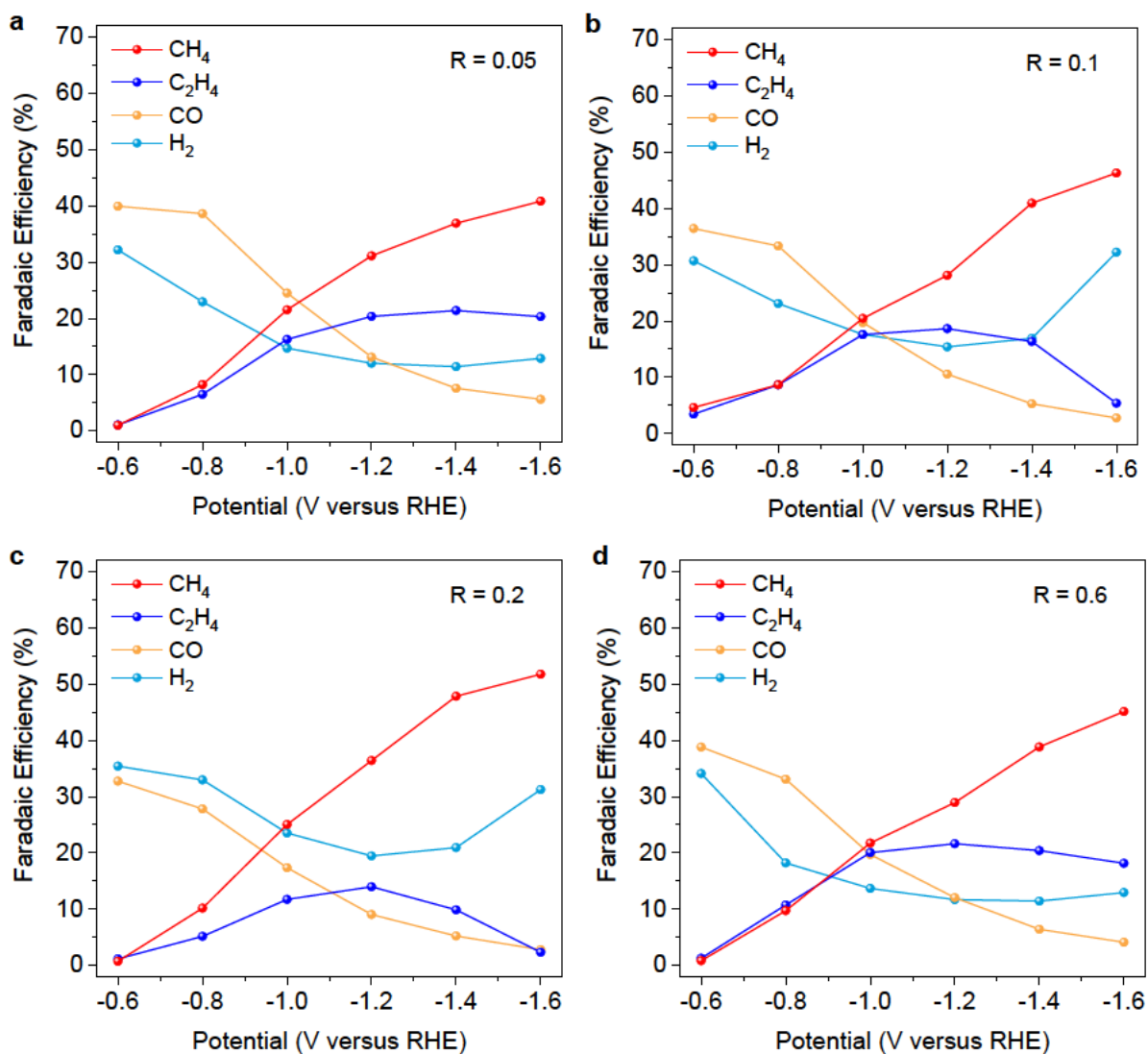


Figure S14. Faradaic efficiencies (FE) of CRR products for different solid solutions under a range of applied potentials without iR correction.

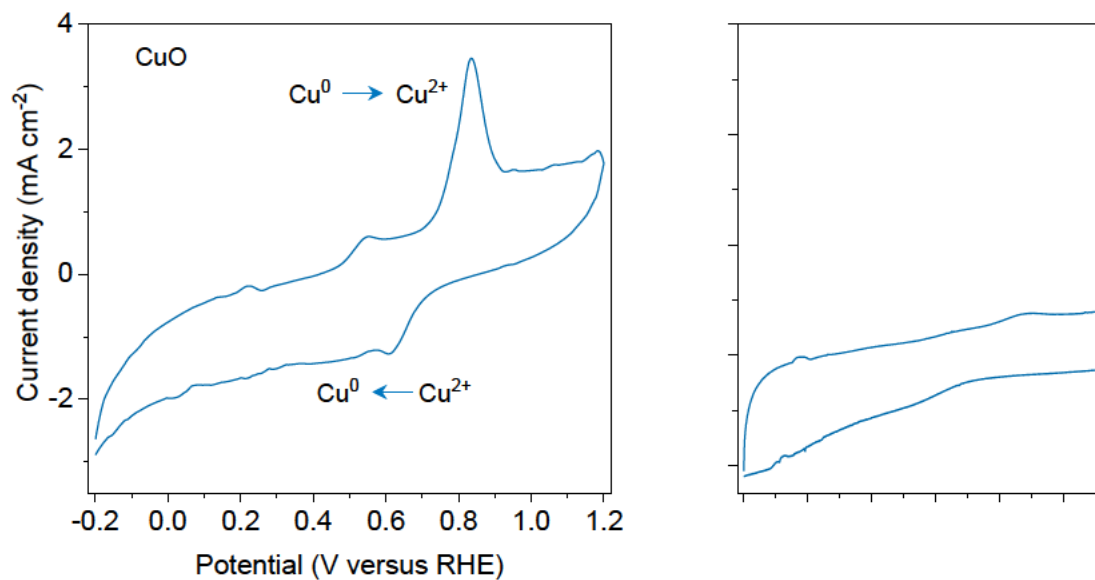


Figure S15. Cyclic voltammogram of CuO after CRR.

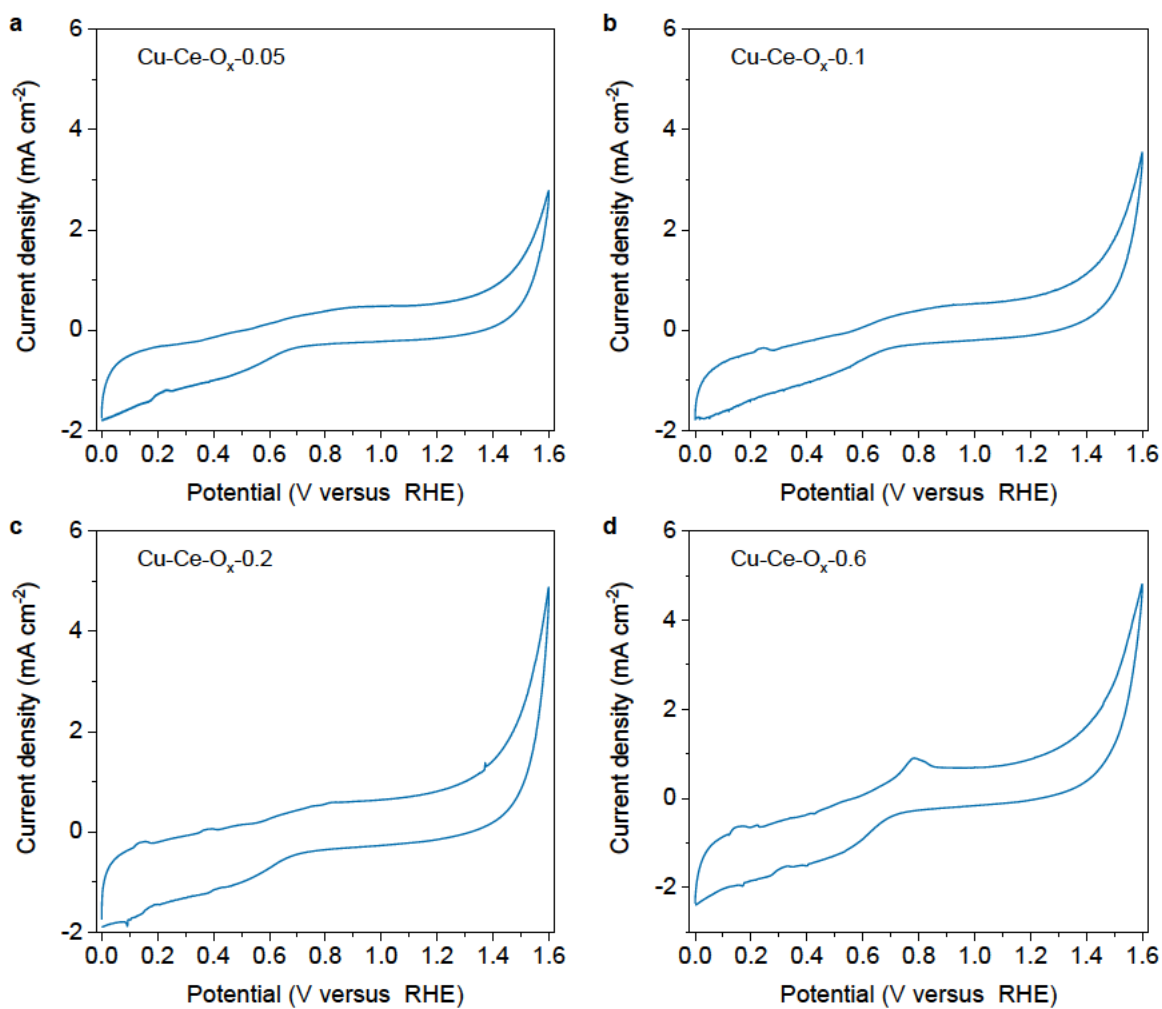


Figure S16. Cyclic voltammograms of different solid solutions after CRR.

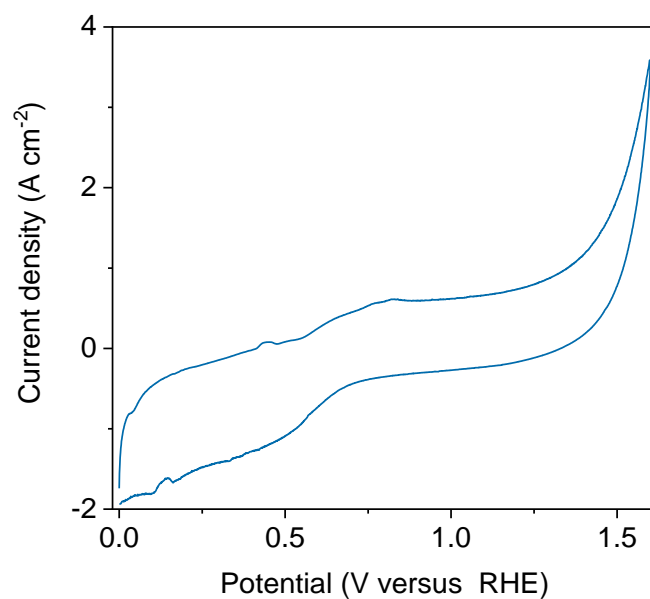


Figure S17. Cyclic voltammograms of Cu-Ce-O_x after CRR at -1.6 V vs RHE for 2h.

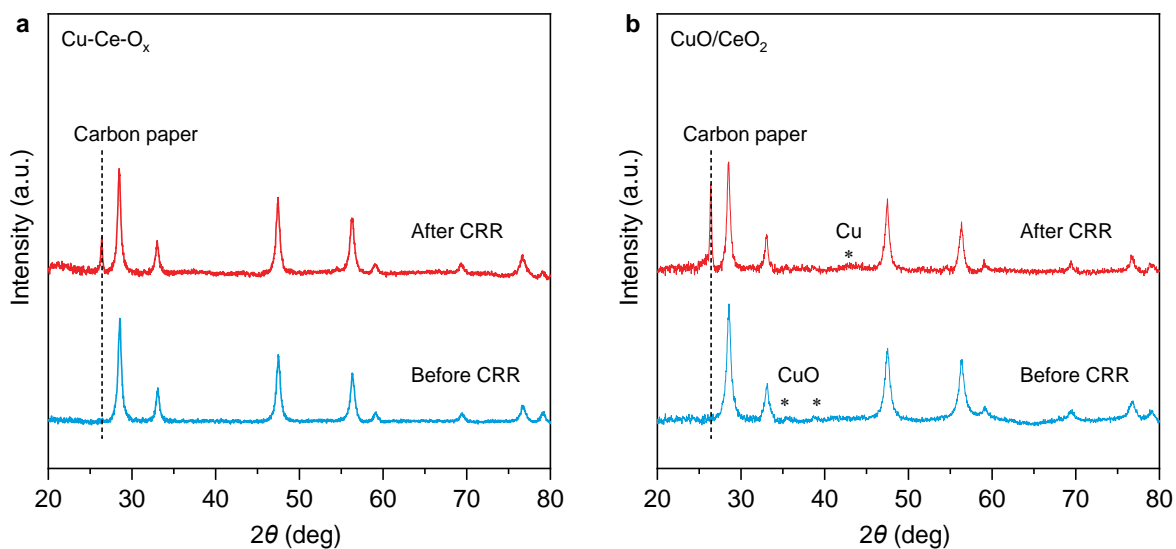


Figure S18. XRD patterns of (a) Cu-Ce-O_x and (b) CuO/CeO₂ before and after CRR.

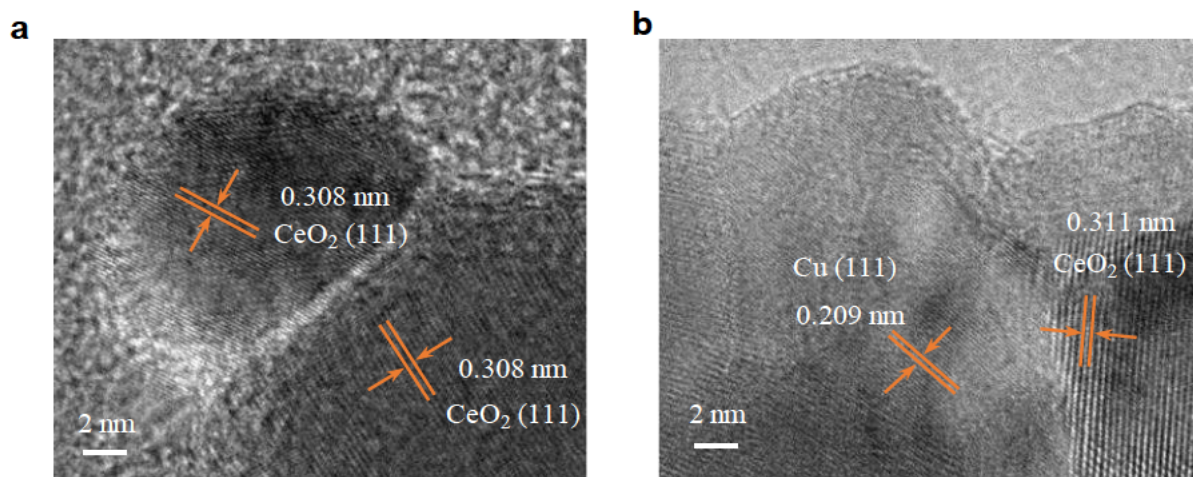


Figure S19. HRTEM images of (a) Cu-Ce-O_x and (b) CuO/CeO₂ after CRR.

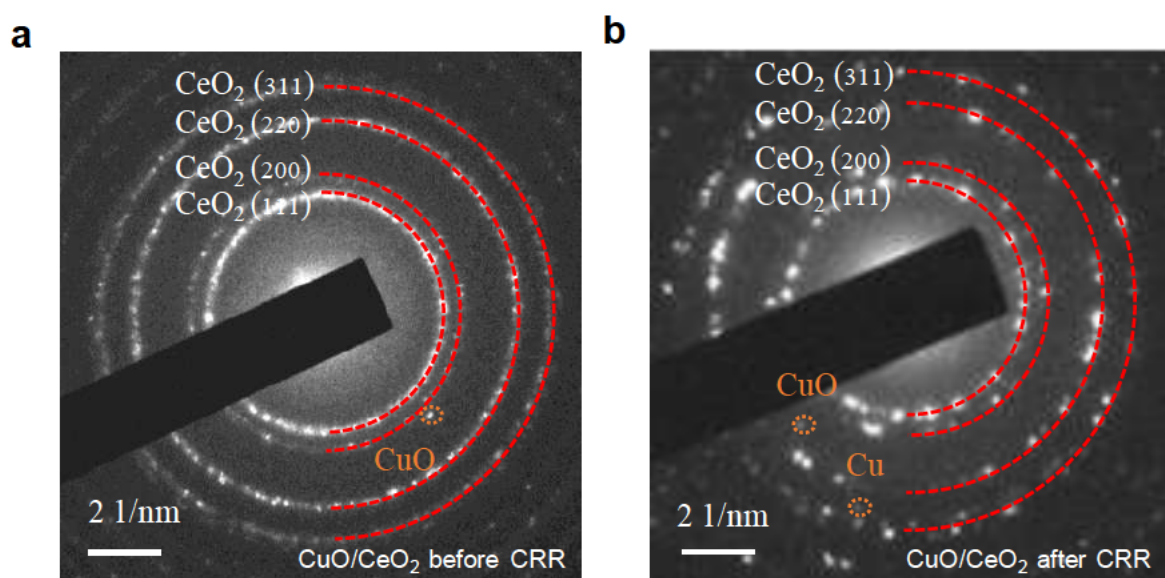


Figure S20. (a, b) SAED patterns of CuO/CeO₂ before and after CRR.

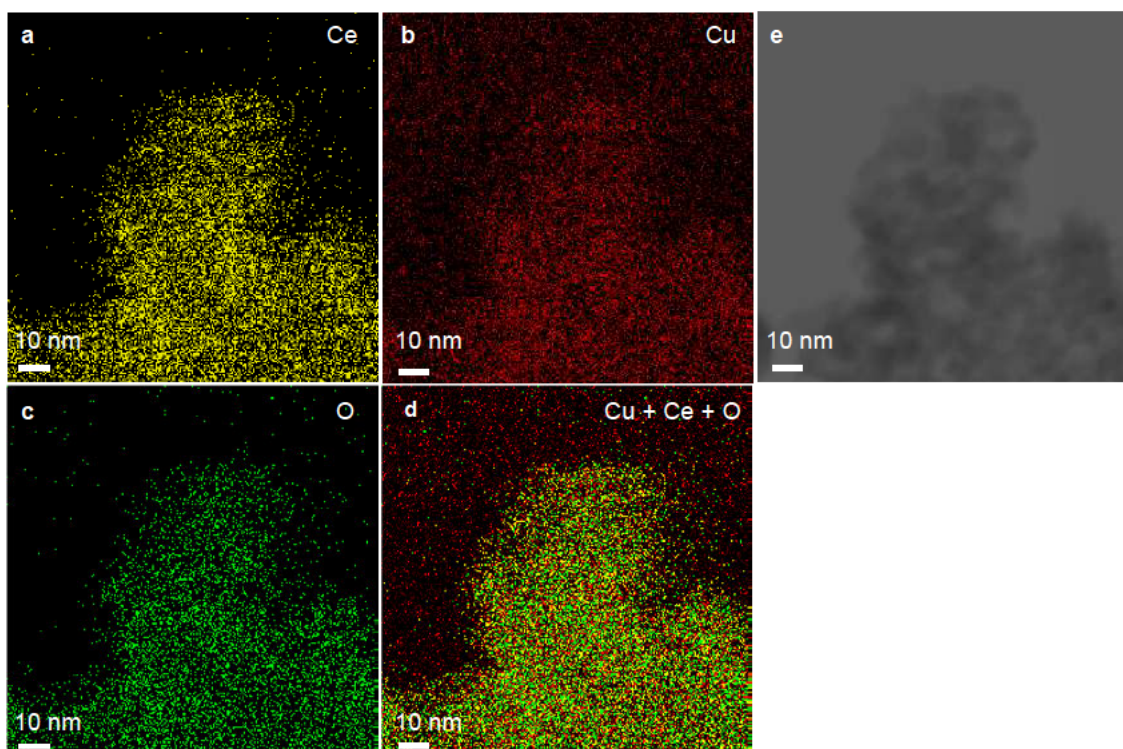


Figure S21. EDX elemental mapping images of CuO/CeO₂ sample after CRR.

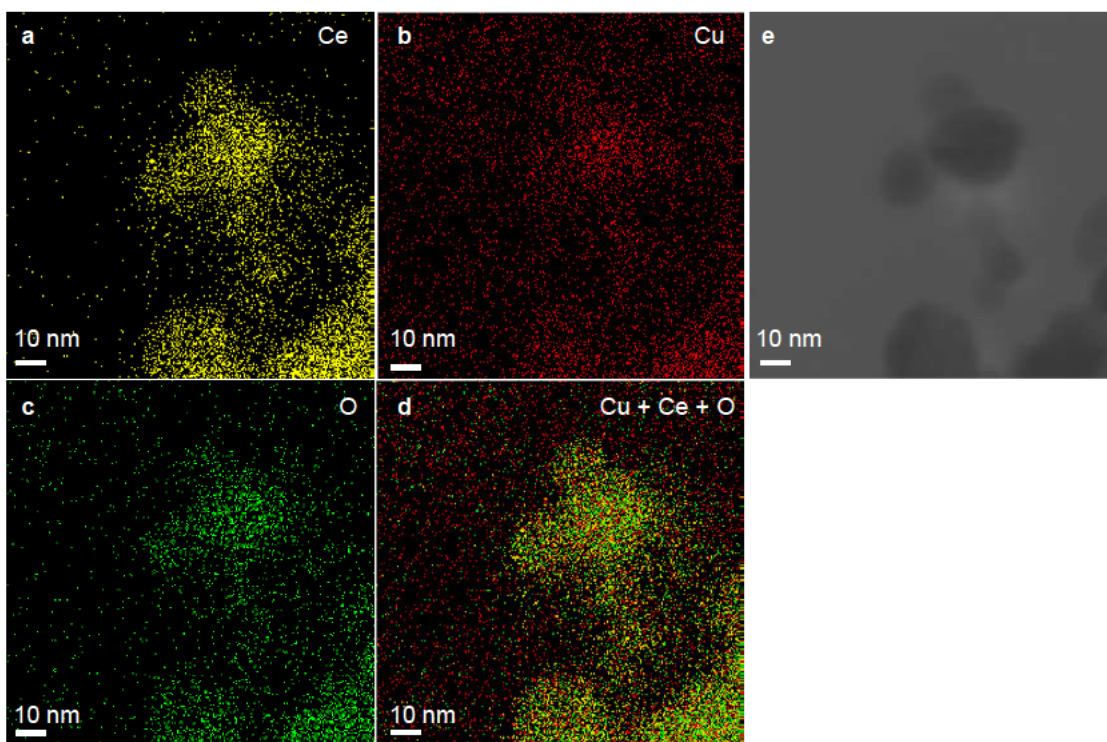


Figure S22. EDX elemental mapping images of Cu-Ce-O_x sample after CRR.

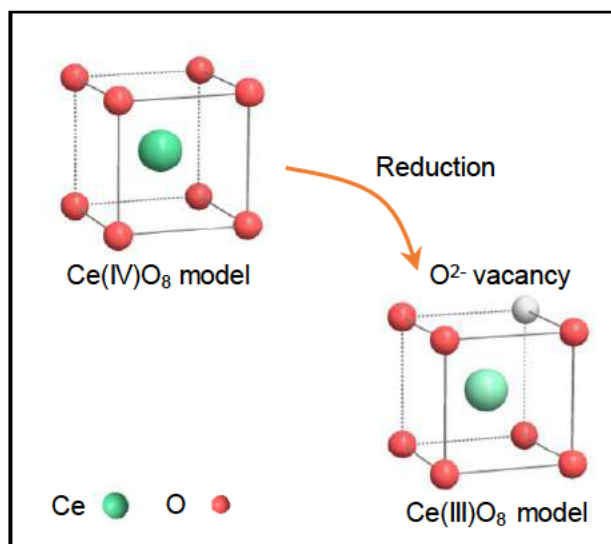


Figure S23. Scheme of the reduction of Ce^{4+} to Ce^{3+} with the formation of O^{2-} vacancy.

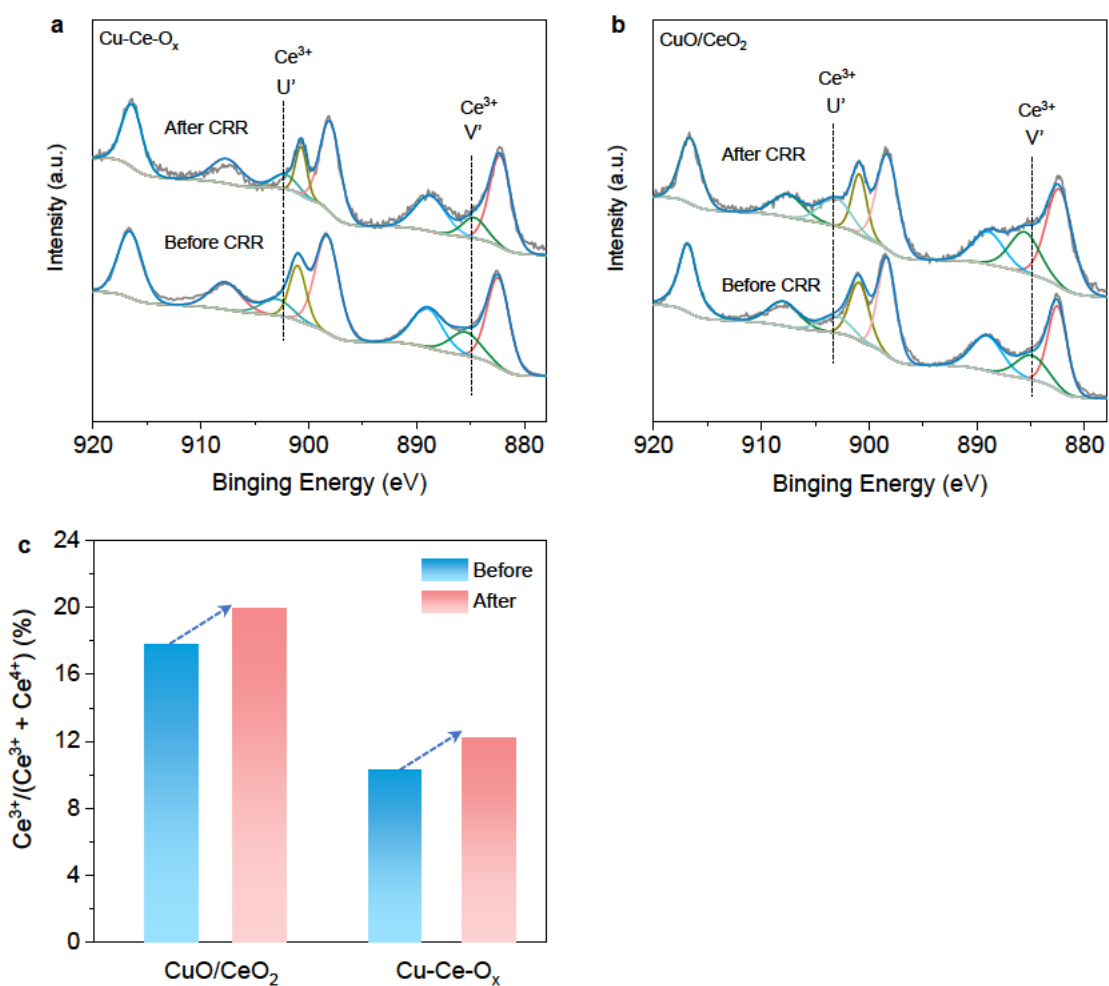


Figure S24. Ce 3d XPS spectra of (a) Cu-Ce-O_x and (b) CuO/CeO_2 before and after CRR. (c) The comparison of Ce^{3+} percentage in Cu-Ce-O_x and CuO/CeO_2 samples before and after CRR.

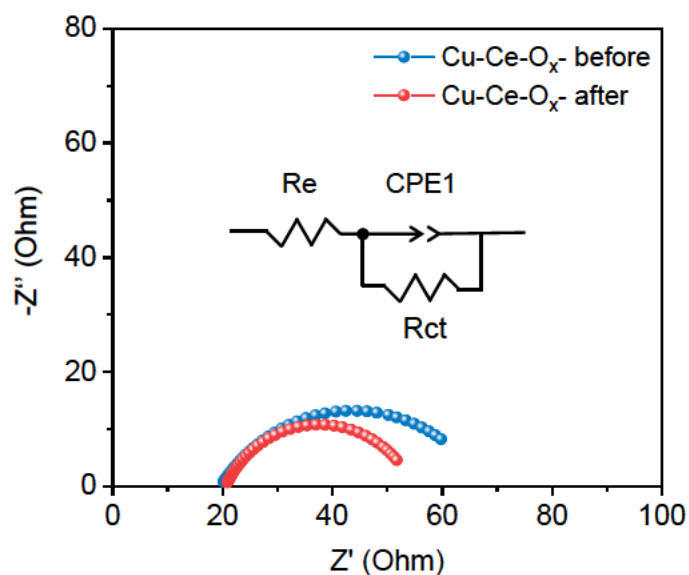


Figure S25. Nyquist plots of Cu-Ce-O_x-before and after CRR (at -1.2 V vs RHE for 60 min).

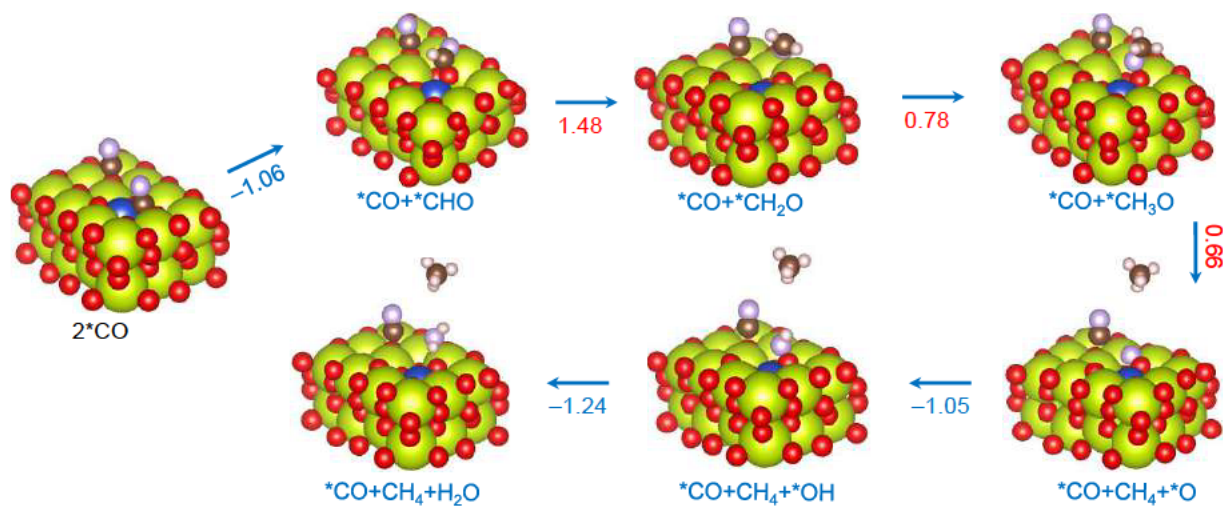


Figure S26. The atomic structures of intermediates along the CH₄ pathway and the energy changes for various catalytic steps. Yellow, copper; red, oxygen; orange, carbon; lavender, hydrogen. The number is the free energy change of each step (unit, eV).

Table S1. Atomic content of Cu-Ce-O_x and CuO/CeO₂

Sample	Cu content atom %	Ce content atom %	Atom ratio of Cu to Ce	Cu content wt %
Cu-Ce-O _x	2.47	65.03	0.08	2.47
CuO/CeO ₂	8.03	63.34	0.28	8.03

Table S2. Cu K-edge EXAFS Fitting Parameters ^a

Sample	Path	<i>N</i>	<i>r</i> (Å)	σ^2 (Å ²)	ΔE_0 (eV)	<i>R</i> (%)
CuO ^b	Cu-O	4	1.946	0.003	2.8	0.4
Cu-Ce-O _x ^c	Cu-O	4	1.938	0.003	2.5	0.3

^a *N*: coordination number; *r*: distance between absorber and backscatter atoms; σ^2 : Debye-Waller factor to account for thermal and structural disorders; ΔE_0 : inner potential correction; *R*: goodness of fit. Error bounds (accuracies) that characterize the structural parameters obtained by EXAFS spectroscopy were estimated as $N \pm 20\%$; $r \pm 1\%$; $\sigma^2 \pm 20\%$; $\Delta E_0 \pm 20\%$. ^b Fitting range: $2.6 \leq k$ (/Å) ≤ 12.5 and $1.0 \leq R$ (Å) ≤ 3.5 . ^c Fitting range: $2.5 \leq k$ (/Å) ≤ 12.4 and $1.0 \leq R$ (Å) ≤ 2.2 .

Table S3. CH₄ Faradaic efficiency comparison of the recently reported Cu electrocatalysts derived from other precursors.

Sample	Electrolyte	Potential (V vs RHE)	Current density (mA cm ⁻²)	CH ₄ FE (%)	Ref
Cu-Ce-O _x	1.0 M KOH	-0.82*	201.0	67.8	This work
Cu Nanoparticles	1.0 M KOH	-0.70	175.0	48.0	8
Cu-PzI ^a	1.0 M KOH	-1.0	287.2	52.0	9
CuPc ^b	1.0 M KHCO ₃	-1.06	13.0	66.0	10
CoO/Cu	1.0 M KHCO ₃	-1.11	225.0	60.0	11
Cu ₆₈ Ag ₃₂	0.5 M KHCO ₃	-1.17	--	60.0	12
Cu/Al ₂ O ₃	1.0 M KOH	-1.20	153.0	62.0	13
Au/Cu	1.0 M KHCO ₃	-1.23	200	56.0	14
Cu Nanowires	0.1 M KHCO ₃	-1.25	15.0	55.0	15
Cu/La ₂ CuO ₄	1.0 M KOH	-1.4	207.0	56.3	16
Cu	1.0 M KHCO ₃	-1.41	225.0	48.0	17
Cu-N-C	0.1 M KHCO ₃	-1.60	38.3	38.6	18
Cu ₂ O/Cu-MOF	0.1 M KHCO ₃	-1.71	13.3	63.2	19
Cu/CeO ₂	0.1 M KHCO ₃	-1.80	70.0	58.0	20

^a: Pz = pyrazole; ^b: Pc = phthalocyanine. --: no data. *, the potential (-0.82 V vs RHE) is calculated after IR correction.

Table S4. Free energy change of all proton-coupled electron transfer steps (PCTE) along CH₄ and C₂H₄ pathways after 2*CO adsorption on active sites of Cu-Ce-O_x; the energy unit is eV.

PCTE	Reaction along CH ₄ pathway	ΔG(U=0)
5 th	2CO(g) + * --- 2*CO	-1.54
6 th	2*CO + H --- *CO + *CHO	-1.06
7 th	*CO + *CHO + H --- *CO + *CH ₂ O	1.48
8 th	*CO + *CH ₂ O + H --- *CO + *CH ₃ O	0.78
9 th	*CO + *CH ₃ O + H --- *CO + CH ₄ + *O	0.66
10 th	*CO + CH ₄ + *O + H --- *CO + CH ₄ + *OH	-1.05
11 th	*CO + CH ₄ + *OH --- *CO + CH ₄ + H ₂ O	-1.24
PCTE	Reaction along C ₂ H ₄ pathway	ΔG(U=0)
5 th	2CO(g) + * --- 2*CO	-1.54
6 th	2*CO + H --- *CO-COH	1.25
7 th	*CO-COH + H --- *COH-COH	0.52
8 th	*COH-COH + H --- *C-COH + H ₂ O	-3.61
9 th	*C-COH + H ₂ O + H --- *CH-COH + H ₂ O	2.50
10 th	*CH-COH + H ₂ O + H --- *CH-C + 2H ₂ O	-0.09
11 th	*CH-C + 2H ₂ O + H --- *C-CH ₂ + 2H ₂ O	1.03
12 th	*C-CH ₂ + 2H ₂ O + H --- *CH-CH ₂ + 2H ₂ O	-1.44
13 th	*CH-CH ₂ + 2H ₂ O + H --- *CH ₂ -CH ₂ + 2H ₂ O	0.62

References

1. Kresse, G.; Furthmuller, J., Efficient iterative schemes for ab initio total-energy calculations using a plane-wave basis set. *Phys. Rev. B* **1996**, *54* (16), 11169-11186.
2. Perdew, J. P.; Burke, K.; Ernzerhof, M., Generalized gradient approximation made simple *Phys. Rev. Lett.* **1997**, *78* (7), 1396-1396.
3. Kresse, G.; Joubert, D., From ultrasoft pseudopotentials to the projector augmented-wave method. *Phys. Rev. B* **1999**, *59* (3), 1758-1775.
4. Monkhorst, H. J.; Pack, J. D., Special points for Brillouin-zone integrations. *Phys. Rev. B* **1976**, *13* (12), 5188-5192.
5. Wickramaratne, D.; Zahid, F.; Lake, R. K., Electronic and thermoelectric properties of few-layer transition metal dichalcogenides. *J. Chem. Phys.* **2014**, *140* (12), 124710.
6. Dudarev, S. L.; Botton, G. A.; Savrasov, S. Y.; Humphreys, C. J.; Sutton, A. P., Electron-energy-loss spectra and the structural stability of nickel oxide: An LSDA+U study. *Phys. Rev. B* **1998**, *57* (3), 1505-1509.
7. Cui, L.; Tang, Y.; Zhang, H.; Hector, L. G., Jr.; Ouyang, C.; Shi, S.; Li, H.; Chen, L., First-principles investigation of transition metal atom M (M = Cu, Ag, Au) adsorption on CeO₂(110). *Phys. Chem. Chem. Phys.* **2012**, *14* (6), 1923-1933.
8. Jeon, H. S.; Timoshenko, J.; Rettenmaier, C.; Herzog, A.; Yoon, A.; Chee, S. W.; Oener, S.; Hejral, U.; Haase, F. T.; Roldan Cuenya, B., Selectivity Control of Cu Nanocrystals in a Gas-Fed Flow Cell through CO₂ Pulsed Electroreduction. *J. Am. Chem. Soc.* **2021**, *143* (19), 7578-7587.
9. Wang, R.; Liu, J.; Huang, Q.; Dong, L. Z.; Li, S. L.; Lan, Y. Q., Partial Coordination-Perturbed Bi-Copper Sites for Selective Electroreduction of CO₂ to Hydrocarbons. *Angew. Chem. Int. Ed.* **2021**, *60* (36), 19829-19835.
10. Weng, Z.; Wu, Y.; Wang, M.; Jiang, J.; Yang, K.; Huo, S.; Wang, X. F.; Ma, Q.; Brudvig, G. W.; Batista, V. S.; Liang, Y.; Feng, Z.; Wang, H., Active sites of copper-complex catalytic materials for electrochemical carbon dioxide reduction. *Nat. Commun.* **2018**, *9* (1), 415.
11. Li, Y.; Xu, A.; Lum, Y.; Wang, X.; Hung, S. F.; Chen, B.; Wang, Z.; Xu, Y.; Li, F.; Abed, J.; Huang, J. E.; Rasouli, A. S.; Wicks, J.; Sagar, L. K.; Peng, T.; Ip, A. H.; Sinton, D.; Jiang, H.; Li, C.; Sargent, E. H., Promoting CO₂ methanation via ligand-stabilized metal oxide clusters as hydrogen-donating motifs. *Nat. Commun.* **2020**, *11* (1), 6190.
12. Chang, C. J.; Lin, S. C.; Chen, H. C.; Wang, J.; Zheng, K. J.; Zhu, Y.; Chen, H. M., Dynamic Reoxidation/Reduction-Driven Atomic Interdiffusion for Highly Selective CO₂ Reduction toward Methane. *J. Am. Chem. Soc.* **2020**, *142* (28), 12119-12132.

13. Chen, S.; Wang, B.; Zhu, J.; Wang, L.; Ou, H.; Zhang, Z.; Liang, X.; Zheng, L.; Zhou, L.; Su, Y. Q.; Wang, D.; Li, Y., Lewis Acid Site-Promoted Single-Atomic Cu Catalyzes Electrochemical CO₂ Methanation. *Nano Lett.* **2021**, *21* (17), 7325-7331.
14. Wang, X.; Ou, P.; Wicks, J.; Xie, Y.; Wang, Y.; Li, J.; Tam, J.; Ren, D.; Howe, J. Y.; Wang, Z.; Ozden, A.; Finfrock, Y. Z.; Xu, Y.; Li, Y.; Rasouli, A. S.; Bertens, K.; Ip, A. H.; Graetzel, M.; Sinton, D.; Sargent, E. H., Gold-in-copper at low *CO coverage enables efficient electromethanation of CO₂. *Nat. Commun.* **2021**, *12* (1), 3387.
15. Li, Y.; Cui, F.; Ross, M. B.; Kim, D.; Sun, Y.; Yang, P., Structure-Sensitive CO₂ Electroreduction to Hydrocarbons on Ultrathin 5-fold Twinned Copper Nanowires. *Nano Lett.* **2017**, *17* (2), 1312-1317.
16. Chen, S.; Su, Y.; Deng, P.; Qi, R.; Zhu, J.; Chen, J.; Wang, Z.; Zhou, L.; Guo, X.; Xia, B. Y., Highly Selective Carbon Dioxide Electroreduction on Structure-Evolved Copper Perovskite Oxide toward Methane Production. *ACS Catal.* **2020**, *10* (8), 4640-4646.
17. Wang, X.; Xu, A.; Li, F.; Hung, S. F.; Nam, D. H.; Gabardo, C. M.; Wang, Z.; Xu, Y.; Ozden, A.; Rasouli, A. S.; Ip, A. H.; Sinton, D.; Sargent, E. H., Efficient Methane Electrosynthesis Enabled by Tuning Local CO₂ Availability. *J. Am. Chem. Soc.* **2020**, *142* (7), 3525-3531.
18. Guan, A.; Chen, Z.; Quan, Y.; Peng, C.; Wang, Z.; Sham, T.-K.; Yang, C.; Ji, Y.; Qian, L.; Xu, X.; Zheng, G., Boosting CO₂ Electroreduction to CH₄ via Tuning Neighboring Single-Copper Sites. *ACS Energy Lett.* **2020**, *5* (4), 1044-1053.
19. Tan, X.; Yu, C.; Zhao, C.; Huang, H.; Yao, X.; Han, X.; Guo, W.; Cui, S.; Huang, H.; Qiu, J., Restructuring of Cu₂O to Cu₂O@Cu-Metal-Organic Frameworks for Selective Electrochemical Reduction of CO₂. *ACS Appl. Mater. Interfaces* **2019**, *11* (10), 9904-9910.
20. Wang, Y. F.; Chen, Z.; Han, P.; Du, Y. H.; Gu, Z. X.; Xu, X.; Zheng, G. F., Single-Atomic Cu with Multiple Oxygen Vacancies on Ceria for Electrocatalytic CO₂ Reduction to CH₄. *ACS Catal.* **2018**, *8* (8), 7113-7119.

Chapter 5 Tuning molecular electrophilicity of Cu-MOF catalysts to steer CO₂ electroreduction selectivity

5.1 Introduction and Significance

Cu is the only transition metal to achieve electrochemical CO₂ reduction (CRR) with generation of hydrocarbons and oxygenates. Meanwhile, its binding to CRR intermediate *CO is neither too weakly nor too strongly, resulting in its poor selectivity. To address this issue, different methods have been used to engineer the electronic structure of Cu-based catalysts. Therefore, those methods can improve the selectivity of one product. In addition, the protonation process of water also affects the CRR activity and selectivity. However, it is still challenging to regulate CRR selectivity in a broad product distribution on Cu by tuning the PCET process in CRR.

Here we employed a class of bipyridyl molecules (1,2-bis(4-pyridyl)ethane, 1,2-bis(4-pyridyl)benzene, 4,4'-bipyridine and trans-1,2-bis(4-pyridyl)ethylene) as linkers with different electrophilicity to steer Cu-MOFs' CRR selectivity. Density functional theory (DFT) calculations coupled with in-situ attenuated total reflectance infrared (ATR-IR) spectroscopy confirm that the electrophilicity of the linker can alter the catalyst's proton availability in PCET reactions. Catalyst with a low-electrophilicity linker exhibits fast proton transfer to *CO, which promotes its protonation to lead a high FE of 58.2% for CH₄. By contrast, a high-electrophilicity linker can stabilize *CO and favor its C-C coupling step, resulting in a high FE of 65.9% for C₂H₄.

The highlights of this work include:

1. New method. Linker's electrophilicity is used to tune catalyst's proton availability, which promotes or inhibits the critical proton-coupled electron transfer (PCET) process in CRR.
2. High selectivity. The linker with a low electrophilicity (1,2-bis(4-pyridyl)ethane)

can facilitate proton transfer to hydrogenate the *CO intermediates to generate CH₄ with a Faradaic efficiency (FE) of 58.2%; while the linker with a high electrophilicity (trans-1,2-bis(4-pyridyl)ethylene) can build stronger hydrogen bonds to stabilize *CO for further dimerization, realizing a C₂H₄ FE of 65.9%.

3. Structure-activity relationship. The combination of theoretical computation and in-situ spectroscopic characterizations established the relationship among the linker's electrophilicity, catalyst's proton availability, and its CRR pathway of CH₄ or C₂H₄.

5.2 Tuning Molecular Electrophilicity of Cu-MOF Catalysts to Steer CO₂ Electroreduction Selectivity

This chapter is included as a submitted manuscript by Xianlong Zhou, Jieqiong Shan, Huan Li, Bao Yu Xia, Yao Zheng, Shi-Zhang Qiao, Tuning Molecular Electrophilicity of Cu-MOF Catalysts to Steer CO₂ Electroreduction Selectivity.

Statement of Authorship

Title of Paper	Tuning Molecular Electrophilicity of Cu-MOF Catalysts to Steer CO ₂ Electroreduction Selectivity
Publication Status	<input type="checkbox"/> Published <input type="checkbox"/> Accepted for Publication <input checked="" type="checkbox"/> Submitted for Publication <input type="checkbox"/> Unpublished and Unsubmitted work written in manuscript style
Publication Details	Tuning Molecular Electrophilicity of Cu-MOF Catalysts to Steer CO ₂ Electroreduction Selectivity Xianlong Zhou, Jieqiong Shan, Bao Yu Xia,* Yao Zheng,* and Shi-Zhang Qiao*.

Principal Author

Name of Principal Author (Candidate)	Xianlong Zhou		
Contribution to the Paper	Conducted material synthesis, carried out electrochemical tests and wrote the paper		
Overall percentage (%)	80		
Certification:	This paper reports on original research I conducted during the period of my Higher Degree by Research candidature and is not subject to any obligations or contractual agreements with a third party that would constrain its inclusion in this thesis. I am the primary author of this paper.		
Signature		Date	09/09/2022

Co-Author Contributions

By signing the Statement of Authorship, each author certifies that:

- the candidate's stated contribution to the publication is accurate (as detailed above);
- permission is granted for the candidate to include the publication in the thesis; and
- the sum of all co-author contributions is equal to 100% less the candidate's stated contribution.

Name of Co-Author	Jieqiong Shan		
Contribution to the Paper	Conducted in situ attenuated total reflectance infrared spectroscopy (ATR-IR) characterization and analysis		
Signature		Date	09/09/2022

Name of Co-Author	Huan Li		
Contribution to the Paper	Conducted density functional theory (DFT) calculations		
Signature		Date	09/09/2022

Name of Co-Author	Bao Yu Xia		
Contribution to the Paper	Discussion of research plan, manuscript revision, and acted as corresponding author		
Signature	_____	Date	09/09/2022

Name of Co-Author	Yao Zheng		
Contribution to the Paper	Discussion of research plan, manuscript revision, and acted as corresponding author		
Signature	_____	Date	09/09/2022

Name of Co-Author	Shi-Zhang Qiao		
Contribution to the Paper	Supervised development of work, helped in manuscript evaluation and revision, and acted as corresponding author		
Signature	_____	Date	09/09/2022

Please cut and paste additional co-author panels here as required.

Tuning Molecular Electrophilicity of Cu-MOF Catalysts to Steer CO₂ Electroreduction Selectivity

Xianlong Zhou,^{1†} Jieqiong Shan,^{1†} Huan Li,¹ Bao Yu Xia,^{2*} Yao Zheng,^{1*} Shi-Zhang Qiao^{1*}

¹ School of Chemical Engineering and Advanced Materials, The University of Adelaide, Adelaide, SA 5005, Australia.

² Key Laboratory of Material Chemistry for Energy Conversion and Storage (Ministry of Education), Hubei Key Laboratory of Material Chemistry and Service Failure, Wuhan; National Laboratory for Optoelectronics, School of Chemistry and Chemical Engineering, Huazhong University of Science and Technology (HUST), 1037 Luoyu Road, Wuhan 430074, China.

Keywords: Molecular Electrophilicity; Cu-MOF; Proton transfer; CO₂ electroreduction; C1/C2 Selectivity

ABSTRACT: Cu is the only transition metal to achieve electrochemical CO₂ reduction (CRR) with generation of hydrocarbons and oxygenates. However, it is still a challenge to regulate CRR selectivity in a broad product distribution on Cu. Here we steered a series of Cu-based MOFs with different linker's electrophilicity to achieve a high CRR selectivity towards either CH₄ or C₂H₄. Molecular orbital analysis shows that linker's electrophilicity determines catalyst's proton availability, which promotes or inhibits the critical proton-coupled electron transfer (PCET) process in CRR. Consequently, the linker with a low electrophilicity (e.g., 1,2-bis(4-pyridyl)ethane) can facilitate proton transfer to hydrogenate the *CO intermediates to generate CH₄ with a Faradaic efficiency (FE) of 58.2%; while the linker with a high electrophilicity (e.g., trans-1,2-bis(4-pyridyl)ethylene) can build stronger hydrogen bonds to stabilize *CO for further dimerization, realizing a C₂H₄ FE of 65.9%. The combination of theoretical computation and in-situ spectroscopic characterizations established the relationship among the linker's electrophilicity, catalyst's proton availability, and its CRR pathway of either *CO hydrogenation or *CO-*COH dimerization. This work may provide new understanding of CRR selectivity by tuning PCET process but not materials engineering.

Electrochemical CO₂ reduction (CRR) in aqueous solutions can not only store renewable electricity obtained from intermittent solar or wind energy but also convert CO₂ into value-added chemicals or fuels.¹ Because Cu binds to CRR intermediates *CO neither too weakly nor too strongly, it is the only transition metal to deeply convert CO₂ to CH₄, C₂H₄ and C₂H₅OH.^{2a,2b} Unfortunately, this unique physicochemical property of Cu also results in a poor product selectivity. Various strategies, including alloy,³ oxide derived,⁴ and surface modification,⁵ have been developed to engineer Cu to obtain desired products. In general, these Cu-based catalysts exhibit a high selectivity for one product, such as CO, CH₄ or C₂H₄. For example, Ma et al. reported Cu(OH)X (X=F, Cl, Br, I) derived Cu with the highest Faradaic efficiency (FE) of 65.0% for C₂H₄.⁶ However, these catalysts displayed a low selectivity for CH₄. Likewise, although Cu-Au alloy can achieve a high CH₄ FE of 56.0%, a high selectivity for C₂H₄ cannot be obtained on this catalyst family.⁷ Therefore, it remains to be a great challenge to tune CRR in a broad product distribution with a high selectivity for one specific product.

It is widely accepted that *CO-*COH coupling is the rate-determining step of C₂H₄ generation, while that of CH₄ generation is the hydrogenation of *CO to *CHO.⁸ For example, Li et al. utilized a library of molecules to stabilize atop-bound *CO intermediate, thereby realizing a high FE for C₂H₄.⁹ Chen et al. promoted water splitting to supply high concentration of active protons and achieved a high CO₂-to-CH₄ selectivity.¹⁰ Based on findings, we hypothesize that stabilizing *CO intermediate without fast proton transfer on Cu surface can promote *CO dimerization to C₂H₄, while a facile proton transfer can directly hydrogenate *CO to CH₄. These two proton-coupled electron transfers (PCET) processes are critical steps to

steer the reaction pathway towards desired products. The PCET process has been widely studied in homogeneous catalysis but not yet in heterogeneous CRR. Metal-organic frameworks (MOFs), composed of metal nodes and organic linkers, provide a great platform for tuning the coordination environment of metal active centers to optimize the adsorption of *CO.¹¹ More importantly, linker's electrophilicity affects the electrocatalyst's proton availability, which promotes or inhibits the PCET process of either hydrogenation or dimerization. Therefore, different from electronic structure engineering in conventional catalysts, it provides an alternative and insightful way to steer CRR selectivity in Cu-based MOFs.^{2a,12}

As a proof-of-concept, here we employed a class of bipyridyl molecules (1,2-bis(4-pyridyl)ethane (bpa), 1,2-bis(4-pyridyl)benzene (dpb), 4,4'-bipyridine (bpy) and trans-1,2-bis(4-pyridyl)ethylene (bpe)) as linkers with different electrophilicity to steer Cu-MOFs' CRR selectivity. Density functional theory (DFT) calculations coupled with in-situ attenuated total reflectance infrared (ATR-IR) spectroscopy confirm that the electrophilicity of linker can alter the catalyst's proton availability in PCET reactions. Catalyst with a low-electrophilicity linker exhibits fast proton transfer to *CO, which promotes its protonation to lead a high FE of 58.2% for CH₄. By contrast, a high-electrophilicity linker can stabilize *CO and favor its C-C coupling step, resulting in a high FE of 65.9% for C₂H₄.

Cu-based MOFs were synthesized with CuCl and bipyridyl molecules in acetonitrile. Cu(bpy)Cl was firstly investigated as its structure has been identified by Yaghi.¹³ As illustrated in **Figure 1a**, two Cu atoms are bridged with two chlorine ligands, and each atom is coordinated to two bpy linkers to form a slightly distorted tetrahedron. The power X-ray diffraction (XRD) pattern of Cu(bpy)Cl

matches well with the simulated one (**Figure 1b**). To investigate the effect of linker's electrophilicity on Cu-MOFs, we chose four linkers (bpa, dpb, bpy and bpe) with two identical pyridyl groups but distinct carbon-carbon linking structures. Since molecule's electrophilicity is relative to its lowest unoccupied molecular orbital (LUMO) position,¹⁴ we first used density functional theory (DFT) to calculate the projected density of states of N 2p orbitals (N_{2p}) in different linkers (**Figure S1**). It is revealed that the electrophilicity of four linkers increases in sequence from bpa to bpe (**Figure 1c**). As a result, pyridine (Py) in the linker could be initially protonated to form pyridinium ions (PyH^*) intermediate during the electrochemical reaction,¹⁵ in which H^* can participate in the PCET process.¹⁶ Therefore, the proton availability of these Cu-MOFs is a critical factor in determining the PCET process. Based on the classical Brønsted-Lowry acid-base theory, the proton availability of PyH^* depends on the molecule's electrophilicity (**Figure 1d**). If the electrophilicity is low, the proton can be easily transferred to the $^*\text{CO}$ intermediate, favoring its hydrogenation (top). On the contrary, the molecule with high electrophilicity cannot implement this transfer,

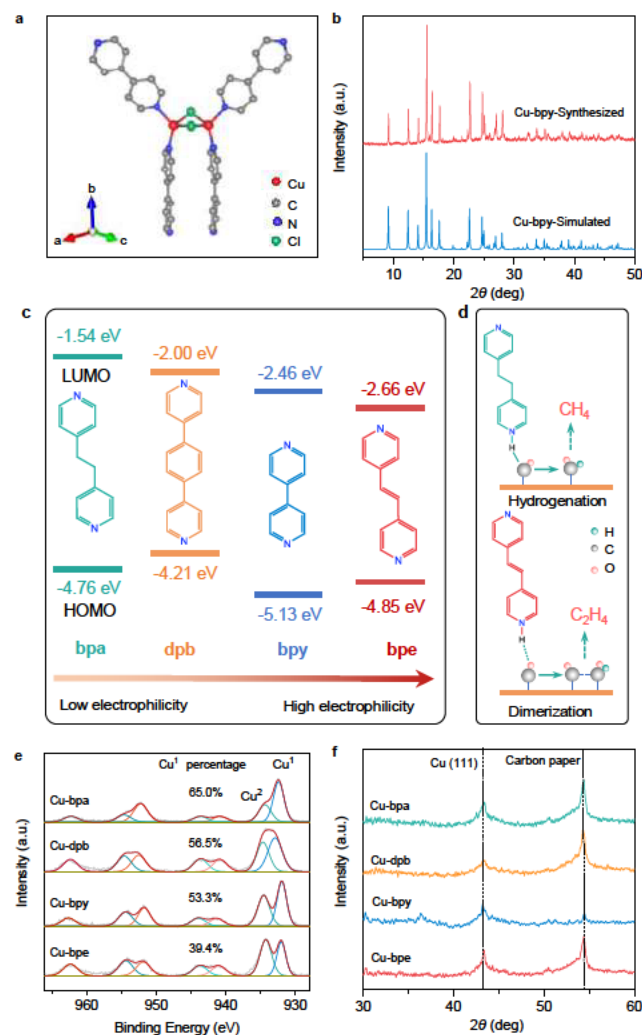


Figure 1. (a) Structural model of Cu-bpy; (b) XRD patterns of synthesized and simulated Cu-bpy; (c) The energy levels of N 2p in each molecule. (d) Schematic illustration of two PCET processes: hydrogenation (top) and dimerization (bottom). (e) Cu 2p XPS spectra for various Cu-MOFs. (f) The XRD patterns of various Cu-MOFs after CRR.

Based on this theoretical analysis, we then synthesized the other three Cu-Y MOFs (**Figure S2**, Y= dpb, bpy and bpe) with the same

morphology (**Figure S3**). X-ray photoelectron spectroscopy (XPS) analysis demonstrates that there are two Cu species of Cu^{1+} and Cu^{2+} in Cu-Y (**Figure 1e**).¹⁷ It is worth noting that a decreased percentage of Cu^{1+} in Cu-Y can be observed with the increase of electrophilicity of linker. This is because the linker with the high electrophilicity facilitates electronic transfer from metal to pyridine-N and results in the formation of Cu^{2+} .¹⁴ Fourier-transform infrared spectroscopy (FTIR) further indicates that the character peak of C=N bond in bipyridyl molecules decreases from 1614 to 1603 cm^{-1} with the decreased linker electrophilicity due to electron transfer from metal atoms to organic molecules (**Figure S4**). As shown in **Figure 1f** and **Figure S5**, Cu-Y samples have been reduced to Cu metals after CRR. It should be noted that FTIR results display the character peak of C=N bond in Cu-bpy, confirming the formation of a bpy-modified Cu catalyst after CRR (**Figure S6**).

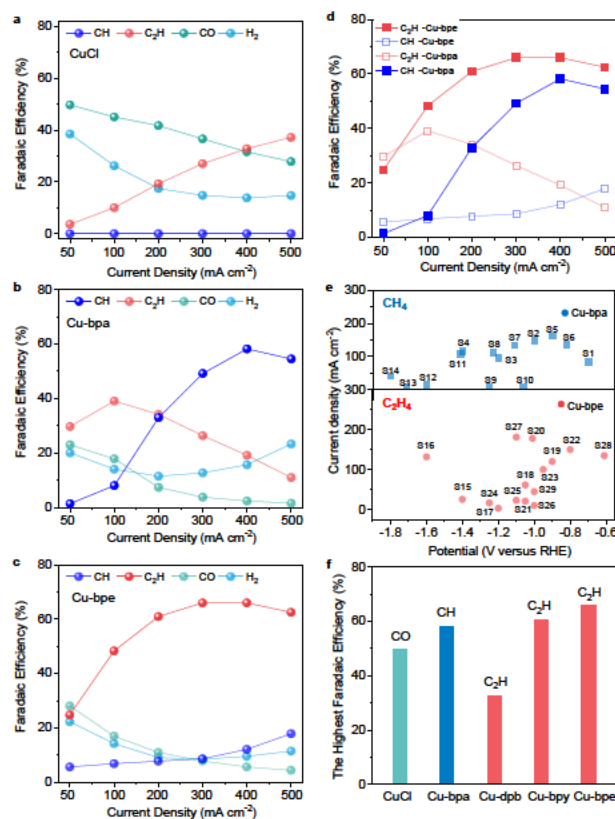


Figure 2. CRR performances of various samples at different current densities. (a-c) FEs for CRR products on various samples; (d) $\text{FE}_{\text{C}_2\text{H}_4}$ and FE_{CH_4} for Cu-bpa and Cu-bpe; (e) FE_{CH_4} of Cu-bpa and $\text{FE}_{\text{C}_2\text{H}_4}$ of Cu-bpe in comparison with other reported Cu-based catalysts after iR correction (Table S1, S2); and (f) Their highest FE of distinct CRR products at 50, 400, 400, 500, and 300 mA cm^{-2} , respectively.

The CRR catalytic performances of the traditional CuCl and Cu-based MOFs were investigated in 1 M KOH solution by using a flow cell (**Figure S7**). As shown in **Figure 2a**, there is no dominant CRR product for CuCl, which is similar with widely reported oxide derived Cu.¹ When the linker with lower electrophilicity (e.g., bpa) was introduced, Cu exhibited a strikingly different CRR performance with that of CuCl (**Figure 2b**). At large current densities ($> 200 \text{ mA cm}^{-2}$), the FEs for CH_4 are significantly higher than those of C_2H_4 , and a maximum FE_{CH_4} of 58.2% can be achieved at 400 mA cm^{-2} . With the catalyst containing high-electrophilicity linkers (e.g., Cu-bpe), high FEs for C_2H_4 up to 65.9% can be achieved at 300 mA cm^{-2} (**Figure 2c**). For Cu-dpb, which electrophilicity locates between Cu-bpa and Cu-bpy, the hydrocarbon product is a mixture of CH_4

and C_2H_4 (Figure S8, S9). Therefore, we can conclude that the linker with low electrophilicity favors the CH_4 formation, whereas the linker with high electrophilicity benefits the C_2H_4 generation (Figure 2d). It is worth mentioning that the performance of Cu-bpa and Cu-bpe are among the highest current densities ever reported for CH_4 and C_2H_4 , respectively, at a low potential zone (Figure 2e). Therefore, in our Cu-MOF catalysts, the CRR products can be tuned in a wide distribution, whilst a high FE for one specific product (CH_4 or C_2H_4) can be achieved simultaneously (Figure 2f).

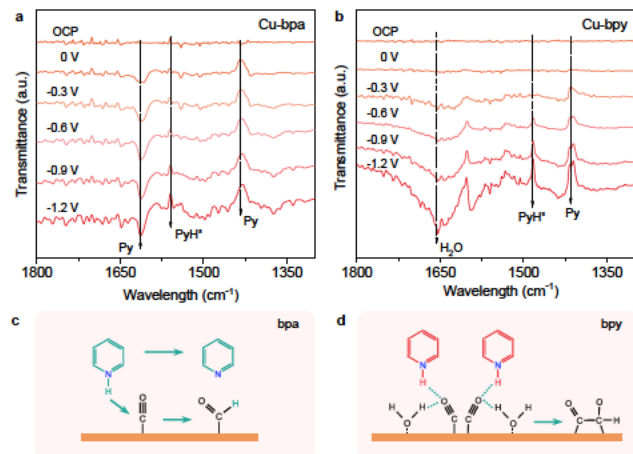


Figure 3. In situ ATR-IR spectra on (a) Cu-bpa and (b) Cu-bpy at different potentials of CRR. Schematic illustration for (c, d) dehydrogenation of PyH^* in bpa and bpy.

To elucidate the distinct selectivity of four samples, we employed in-situ ATR-IR spectroscopy to analyze the surface structure of catalysts over the CRR process. First, compared with Cu-bpy, a negative peak at 1613 cm^{-1} and a positive peak at 1431 cm^{-1} are observed in Cu-bpa (Figure 3a), which belongs to Py in the bpa linker. The peak at 1560 cm^{-1} is assigned to PyH^* .¹⁸ By contrast, in addition to the peaks of PyH^* and Py, an interface water peak can also be observed at 1654 cm^{-1} (Figure 3b), similar to those of CuCl, Cu-dpb and Cu-bpe (Figure S10). This difference suggests that the proton resulted from PyH^* participates in the PCET process of CRR on Cu-bpa to hydrogenate *CO , but not on Cu-bpy (Figure 3c, 3d). In addition, the interface water peak of Cu-bpy indicates the formation of a strong hydrogen bonding.¹⁹ The previous report has demonstrated that the hydrogen bonding can stabilize *CO intermediates and increase its coverage, thereby enhancing the dimerization for C_2H_4 formation,²⁰ which agrees well with our electrochemical observations.

We then investigated the critical intermediates in CRR to understand the influence of catalysts' proton availability on the PCET processes. A CHO^* intermediate at 1505 cm^{-1} can be clearly observed on Cu-bpa with potential being applied (Figure 4a). This intermediate can be further hydrogenation via a series of PCET reactions to form *OCH_3 , which is the final intermediate in the generation of CH_4 .²¹ By contrast, Cu-bpy exhibited two strong peaks at 1595 and 1190 cm^{-1} (Figure 4b), which are corresponding to $OCCOH^*$ for the formation of C_2H_4 . This was derived from the dimerization of two *CO and then further hydrogenation.²² The linear relationships between the integral area of these two intermediates and potentials show that the slope of *OCH_3 is nearly twice that of $OCCOH^*$ on Cu-bpa, whereas the slope of *OCH_3 is one-sixth that of $OCCOH^*$ on Cu-bpy (Figure 4c, d, Figure S11). The higher slope of $OCCOH^*$ was also observed on Cu-dpb and Cu-bpe. (Figure S12).

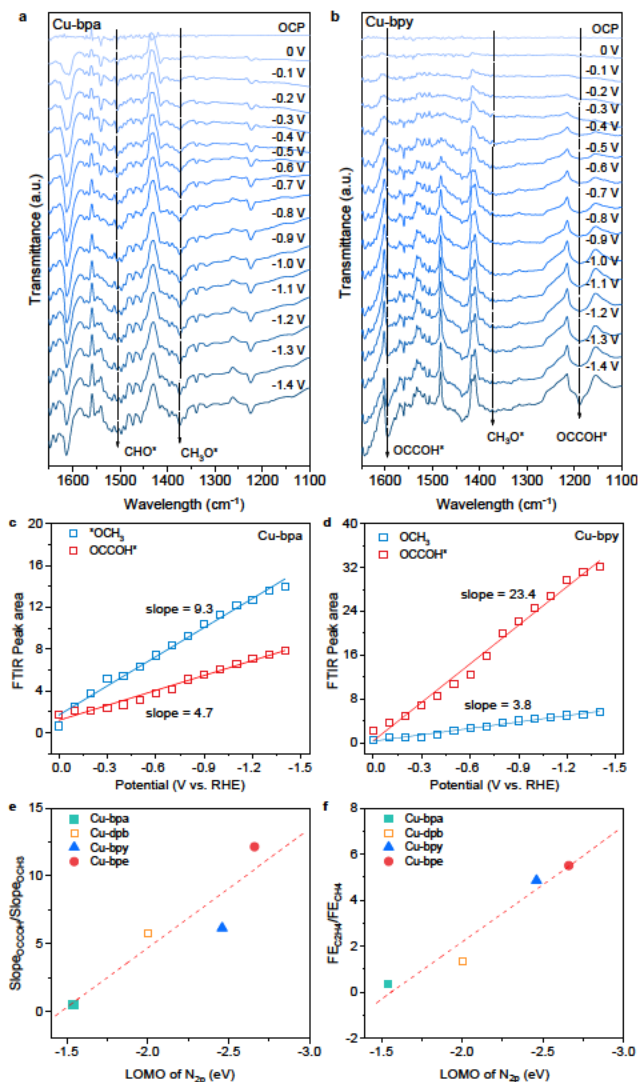


Figure 4. In situ ATR-IR spectra on (a) Cu-bpa and (b) Cu-bpy at different potentials of CRR. (c, d) The integrated peak area of *OCH_3 and $OCCOH^*$ on Cu-bpa and Cu-bpy under different potentials. (e) The relationship between the ratio of catalyst's $slope_{OCCOH^*}$ to $slope_{^*OCH_3}$ in ATR-IR spectra and linker's electrophilicity (quantified by its LOMO of N_{2p}). (f) The relationship between the ratio of catalyst's $FE_{C_2H_4}$ to FE_{CH_4} and linker electrophilicity.

We compared the slope ratio of $OCCOH^*$ to *OCH_3 for Cu-bpa, Cu-dpb, Cu-bpy, and Cu-bpe, which increases from 0.5 to 5.7, 6.2 and 12.2, respectively, with the increase of linker electrophilicity (Figure 4e). This suggests that the linker with a higher electrophilicity favors the formation of $OCCOH^*$ while inhibit that of *OCH_3 . The trend explains the intrinsic reason that Cu-bpa generates CH_4 as the dominant product while Cu-bpe produces C_2H_4 . Therefore, the relationship between the ratio of $FE_{C_2H_4}$ to FE_{CH_4} on four catalysts and their electrophilicity (quantified by the LOMO of N_{2p}) can be built (Figure 4f). The observed relationship confirms that the selectivity of CH_4 and C_2H_4 can be readily regulated by linker electrophilicity in Cu-MOFs, i.e., the linker with a low electrophilicity (e.g., bpa) favors CH_4 , while the linker with a high electrophilicity (bpe) can facilitate C_2H_4 formation.

In summary, we developed a molecular engineering strategy to widely regulate CRR selectivity of CH_4 and C_2H_4 on MOF-derived-Cu. Based on the DFT computation, electrochemical results and in-

situ ATR-IR spectroscopy analysis, we explicitly revealed the regulation mechanism by tuning the linker's electrophilicity and proton availability to alter the critical PCET processes in CRR. We found the linker with low electrophilicity can promote proton transfer from PyH* to *CO intermediates to facilitate formation of CH₄. By contrast, the linker with high electrophilicity can build strong hydrogen bond, and stabilize the *CO dimer, thereby favoring the C₂H₄ formation. This finding provides new insights into steering CRR selectivity on Cu-based catalysts by tuning the PCET process, which could also guide the catalyst design for other proton-involving electrochemical reactions.

ASSOCIATED CONTENT

The Supporting Information is available free of charge via the Internet at <http://pubs.acs.org>.

Detailed computational and experimental methods.

AUTHOR INFORMATION

Corresponding Author

*Bao Yu Xia Email: byxia@hust.edu.cn

*Yao Zheng Email: yao.zheng01@adelaide.edu.au

*Shi-Zhang Qiao Email: s.qiao@adelaide.edu.au

Author Contributions

†X.Z. and J.S. contributed equally.

Notes

The authors declare no competing financial interest.

ACKNOWLEDGMENT

This work received funding from the Australian Research Council through the Discovery Project programs (FL170100154, FT200100062, DP220102596 and DP190103472). X. Zhou acknowledges support from the Australian Government through Research Training Program Scholarships. DFT computations within this research were undertaken with the assistance of resources and services from the National Computational Infrastructure (NCI), which the Australian Government supports.

REFERENCES

- (1) Wang, G.; Chen, J.; Ding, Y.; Cai, P.; Yi, L.; Li, Y.; Tu, C.; Hou, Y.; Wen, Z.; Dai, L., Electrocatalysis for CO₂ conversion: from fundamentals to value-added products. *Chem. Soc. Rev.* **2021**, *50* (8), 4993-5061.
- (2) (a) Tabassum, H.; Yang, X.; Zou, R.; Wu, G., Surface engineering of Cu catalysts for electrochemical reduction of CO₂ to value-added multi-carbon products. *Chem Catal.* **2022**, *2* (7), 1561-1593; (b) Nitopi, S.; Bertheussen, E.; Scott, S. B.; Liu, X.; Engstfeld, A. K.; Horch, S.; Seger, B.; Stephens, I. E. L.; Chan, K.; Hahn, C.; Nørskov, J. K.; Jaramillo, T. F.; Chorkendorff, I., Progress and Perspectives of Electrochemical CO₂ Reduction on Copper in Aqueous Electrolyte. *Chem. Rev.* **2019**, *119* (12), 7610-7672.
- (3) Lee, C. W.; Yang, K. D.; Nam, D. H.; Jang, J. H.; Cho, N. H.; Im, S. W.; Nam, K. T., Defining a Materials Database for the Design of Copper Binary Alloy Catalysts for Electrochemical CO₂ Conversion. *Adv. Mater.* **2018**, *30* (42), e1704717.
- (4) Yang, P. P.; Zhang, X. L.; Gao, F. Y.; Zheng, Y. R.; Niu, Z. Z.; Yu, X.; Liu, R.; Wu, Z. Z.; Qin, S.; Chi, L. P.; Duan, Y.; Ma, T.; Zheng, X. S.; Zhu, J. F.; Wang, H. J.; Gao, M. R.; Yu, S. H., Protecting Copper Oxidation State via Intermediate Confinement for Selective CO₂ Electroreduction to C₂. *Fuels. J. Am. Chem. Soc.* **2020**, *142* (13), 6400-6408.
- (5) Wakerley, D.; Lamaison, S.; Ozanam, F.; Menguy, N.; Mercier, D.; Marcus, P.; Fontecave, M.; Mougél, V., Bio-inspired hydrophobicity

promotes CO₂ reduction on a Cu surface. *Nat. Mater.* **2019**, *18* (11), 1222-1227.

(6) Ma, W.; Xie, S.; Liu, T.; Fan, Q.; Ye, J.; Sun, F.; Jiang, Z.; Zhang, Q.; Cheng, J.; Wang, Y., Electrocatalytic reduction of CO₂ to ethylene and ethanol through hydrogen-assisted C-C coupling over fluorine-modified copper. *Nat. Catal.* **2020**, *3* (6), 478-487.

(7) Wang, X.; Ou, P.; Wicks, J.; Xie, Y.; Wang, Y.; Li, J.; Tam, J.; Ren, D.; Howe, J. Y.; Wang, Z.; Ozden, A.; Finrock, Y. Z.; Xu, Y.; Li, Y.; Rasouli, A. S.; Bertens, K.; Ip, A. H.; Graetzel, M.; Sinton, D.; Sargent, E. H., Gold-in-copper at low *CO coverage enables efficient electromethanation of CO₂. *Nat. Commun.* **2021**, *12* (1), 3387.

(8) Zheng, Y.; Vasileff, A.; Zhou, X.; Jiao, Y.; Jaroniec, M.; Qiao, S. Z., Understanding the Roadmap for Electrochemical Reduction of CO₂ to Multi-Carbon Oxygenates and Hydrocarbons on Copper-based Catalysts. *J. Am. Chem. Soc.* **2019**, *141* (19), 7646-7659.

(9) Li, F.; et al, Molecular tuning of CO₂-to-ethylene conversion. *Nature* **2020**, *577* (7791), 509-513.

(10) Chen, S.; Zhang, Z.; Jiang, W.; Zhang, S.; Zhu, J.; Wang, L.; Ou, H.; Zaman, S.; Tan, L.; Zhu, P.; Zhang, E.; Jiang, P.; Su, Y.; Wang, D.; Li, Y., Engineering Water Molecules Activation Center on Multisite Electrocatalysts for Enhanced CO₂ Methanation. *J. Am. Chem. Soc.* **2022**, *144* (28), 12807-12815.

(11) Zhou, X.; Jin, H.; Xia, B. Y.; Davey, K.; Zheng, Y.; Qiao, S. Z., Molecular Cleavage of Metal-Organic Frameworks and Application to Energy Storage and Conversion. *Adv. Mater.* **2021**, *33* (51), 2104341.

(12) Vasileff, A.; Xu, C.; Jiao, Y.; Zheng, Y.; Qiao, S.-Z., Surface and Interface Engineering in Copper-Based Bimetallic Materials for Selective CO₂ Electroreduction. *Chem* **2018**, *4* (8), 1809-1831.

(13) Yaghi, O. M.; Li, G., Mutually Interpenetrating Sheets and Channels in the Extended Structure of [Cu(4,4'-bpy)Cl]. *Angew. Chem. Int. Ed.* **1995**, *34* (2), 207-209.

(14) Sprague-Klein, E. A.; Ho-Wu, R.; Nguyen, D.; Coste, S. C.; Wu, Y.; McMahon, J. J.; Seideman, T.; Schatz, G. C.; Van Duyne, R. P., Modulating the Electron Affinity of Small Bipyridyl Molecules on Single Gold Nanoparticles for Plasmon-Driven Electron Transfer. *J. Phys. Chem. C* **2021**, *125* (40), 22142-22153.

(15) Uchida, T.; Mogami, H.; Yamakata, A.; Sasaki, Y.; Osawa, M., Hydrogen evolution reaction catalyzed by proton-coupled redox cycle of 4,4'-bipyridine monolayer adsorbed on silver electrodes. *J. Am. Chem. Soc.* **2008**, *130* (33), 10862-10863.

(16) Ertem, M. Z.; Konezny, S. J.; Araujo, C. M.; Batista, V. S., Functional Role of Pyridinium during Aqueous Electrochemical Reduction of CO₂ on Pt(111). *J. Phys. Chem. Lett.* **2013**, *4* (5), 745-748.

(17) Ahmed, A.; Robertson, C. M.; Steiner, A.; Whittles, T.; Ho, A.; Dhanak, V.; Zhang, H., Cu(I)Cu(II)BTC, a microporous mixed-valence MOF via reduction of HKUST-1. *RSC Adv.* **2016**, *6* (11), 8902-8905.

(18) Dunwell, M.; Yan, Y.; Xu, B., In Situ Infrared Spectroscopic Investigations of Pyridine-Mediated CO₂ Reduction on Pt Electrocatalysts. *ACS Catal.* **2017**, *7* (8), 5410-5419.

(19) Ataka, K.-i.; Yotsuyanagi, T.; Osawa, M., Potential-Dependent Reorientation of Water Molecules at an Electrode/Electrolyte Interface Studied by Surface-Enhanced Infrared Absorption Spectroscopy. *J. Phys. Chem.* **1996**, *100* (25), 10664-10672.

(20) Ahn, S.; Klyukin, K.; Wakeham, R. J.; Rudd, J. A.; Lewis, A. R.; Alexander, S.; Carla, F.; Alexandrov, V.; Andreoli, E., Poly-Amide Modified Copper Foam Electrodes for Enhanced Electrochemical Reduction of Carbon Dioxide. *ACS Catal.* **2018**, *8* (5), 4132-4142.

(21) Zhou, X.; Shan, J.; Chen, L.; Xia, B. Y.; Ling, T.; Duan, J.; Jiao, Y.; Zheng, Y.; Qiao, S. Z., Stabilizing Cu²⁺ Ions by Solid Solutions to Promote CO₂ Electroreduction to Methane. *J. Am. Chem. Soc.* **2022**, *144* (5), 2079-2084.

(22) Perez-Gallent, E.; Figueiredo, M. C.; Calle-Vallejo, F.; Koper, M. T., Spectroscopic Observation of a Hydrogenated CO Dimer Intermediate During CO Reduction on Cu(100) Electrodes. *Angew. Chem. Int. Ed.* **2017**, *56* (13), 3621-3624.

Supplementary Information

Tuning Molecular Electrophilicity of Cu-MOF Catalysts to Steer CO₂ Electroreduction Selectivity

Xianlong Zhou,^{1#} Jieqiong Shan,^{1#} Huan Li,¹ Bao Yu Xia,^{2*} Yao Zheng,^{1*} Shi-Zhang Qiao^{1*}

¹ School of Chemical Engineering and Advanced Materials, The University of Adelaide, Adelaide, SA 5005, Australia.

² Key Laboratory of Material Chemistry for Energy Conversion and Storage (Ministry of Education), Hubei Key Laboratory of Material Chemistry and Service Failure, Wuhan; National Laboratory for Optoelectronics, School of Chemistry and Chemical Engineering, Huazhong University of Science and Technology (HUST), 1037 Luoyu Road, Wuhan 430074, China.

These authors contributed equally

*Email: byxia@hust.edu.cn; yao.zheng01@adelaide.edu.au; s.qiao@adelaide.edu.au

Materials Synthesis

Synthesis of Cu-MOFs.

0.25 g of CuCl powder was dispersed in 25 mL of acetonitrile with sonication for 5 min. 2.5 mmol of organic linker (1,2-bis(4-pyridyl)ethane, 1,2-bis(4-pyridyl)benzene, 4,4'-bipyridine and trans-1,2-bis(4-pyridyl)ethylene) was dissolved in 5 mL of acetonitrile with 10 min sonication. Then, the solution with organic linker was added into the solution with CuCl. Following magnetic stirring for 60 min, the precipitate was washed respectively with acetonitrile and deionized water three times. All samples were obtained following freeze-drying for 24 h.

Materials Characterization

The phase and structure of as-synthesized samples were analyzed by a Philips PW-1830 X-Ray Diffractometer (XRD) using Cu K α radiation ($\lambda=1.5406 \text{ \AA}$, scan rate = 5° min^{-1}). Transmission electronic microscope (TEM) images were collected on a JOEL 2100 TEM. XPS measurements were conducted on AXIS-ULTRA DLD-600W XPS (mono Al K α 1486.6 eV) and recorded by the hemispherical analyser with a step-size of 0.05 eV. FTIR spectra were collected on a Nicolet 6700 spectrometer.

Electrochemistry Measurement

Activity/selectivity measurement. The CO₂ reduction reaction (CRR) catalytic activity of different samples was investigated by a commercial flow cell (Gaossunion) in 1 M KOH solution. The volume of anode and cathode chamber electrolyte was both 15 mL. To prepare the working electrode, 25 mg of catalyst was dispersed by sonication in 2.85 mL of isopropanol and 150 μL of 5 wt % of Nafion for 60 min. Next, inks were airbrushed onto a gas diffusion layer (GDL, Sigracet 29 BC) as the cathode electrode ($3 \times 1 \text{ cm}^2$, loading mass: 1.0 mg cm^{-2}). The reference and counter electrodes were Ag/AgCl (3.0 M KCl) and Pt foil ($3 \times 1 \text{ cm}$; 1 mm thickness) connected to a potentiostat (Gamry Interface 3000), respectively. An anion exchange membrane (FAB-PK-130) (Fuel Cell Store) was sandwiched between the two PTFE sheets to separate the chambers. In addition, 1 M KOH was circulated around the cathode and anode at a flow rate of 10.0 ml min^{-1} during the CRR. During this process and then testing, CO₂ was continuously purged at a rate of $20 \mu\text{L min}^{-1}$. The gas products were self-injected into a gas chromatograph (Shimadzu GC-2014) equipped with TCD and methanizer/FID detectors. The resistance of 1.9Ω had been used to calculate the iR-correction.

XPS analysis of samples after CRR. We identify the Cu valence state of solid solution after CRR by XPS analysis. When we completed the CRR test, the electrode was washed by deionized water and ethanol for three times. The sample after CRR was obtained after vacuum drying for 12 h. Then,

it was further sealed in a high-purity Ar-filled glove box. Finally, we can identify the Cu valent state of the sample after CRR by XPS analysis.

XRD analysis of samples after CRR. We identify the phase of catalysts after CRR by XPS analysis. When we completed the CRR test, the electrode was washed by deionized water and ethanol for three times. Then, the sample after CRR was obtained after vacuum drying for 12 h. Finally, we can identify the Cu valent state of the sample after CRR by XRD analysis.

***In situ* Attenuated Total Reflectance Infrared (ATR-IR) Spectroscopy**

It was conducted by using a Thermo-Fisher Nicolet iS20 equipped with a liquid nitrogen-cooled HgCdTe (MCT) detector using a VeeMax III ATR accessory (Pike Technologies). A germanium prism (60°, PIKE Technologies) was mounted in a PIKE electrochemical three-electrode cell with a platinum-wire counter electrode and an Ag/AgCl reference electrode (Pine Research). All ATR-IR measurements were acquired by averaging 64 scans at a spectral resolution of 4 cm⁻¹. Electrocatalyst ink was prepared by dispersing catalyst powder (10 mg) in a solution containing isopropanol (1.5 mL) and 5 wt % Nafion solution (50 μL) followed by ultrasonication for 60 min. 50 μL of the catalyst ink was dropped onto the prism and left to dry slowly. The electrolyte was 0.1 M KHCO₃, which was constantly purged with CO₂ during the experiment. A CHI 760E electrochemical workstation (CH Instruments, USA) was connected for chronoamperometric tests from -0.6 to -2.1 V vs. Ag/AgCl stepwise. Meanwhile, the spectra under open circuit potential (OCP) were recorded for comparison.

Computational Section.

All calculations in this work were carried out using density functional theory (DFT) method as implemented in the VASP code. The electronic exchange-correlation energy was modeled using the Perdew-Burke-Ernzerhof (PBE) functional within the generalized gradient approximation (GGA). The projector augmented wave (PAW) method was used to describe the ionic cores. For the plane-wave expansion, a 450-eV kinetic energy cut-off was used after testing a series of different cut-off energies. A Monkhorst-Pack 2×4×2 k-point grid was used to sample the Brillouin zone. The convergence criterion for the electronic structure iteration was set to be 10⁻⁴ eV, and that for geometry optimizations was set to be 0.01 eV Å⁻¹ on force. A Gaussian smearing of 0.1 eV was applied during the geometry optimization for the total energy computations.

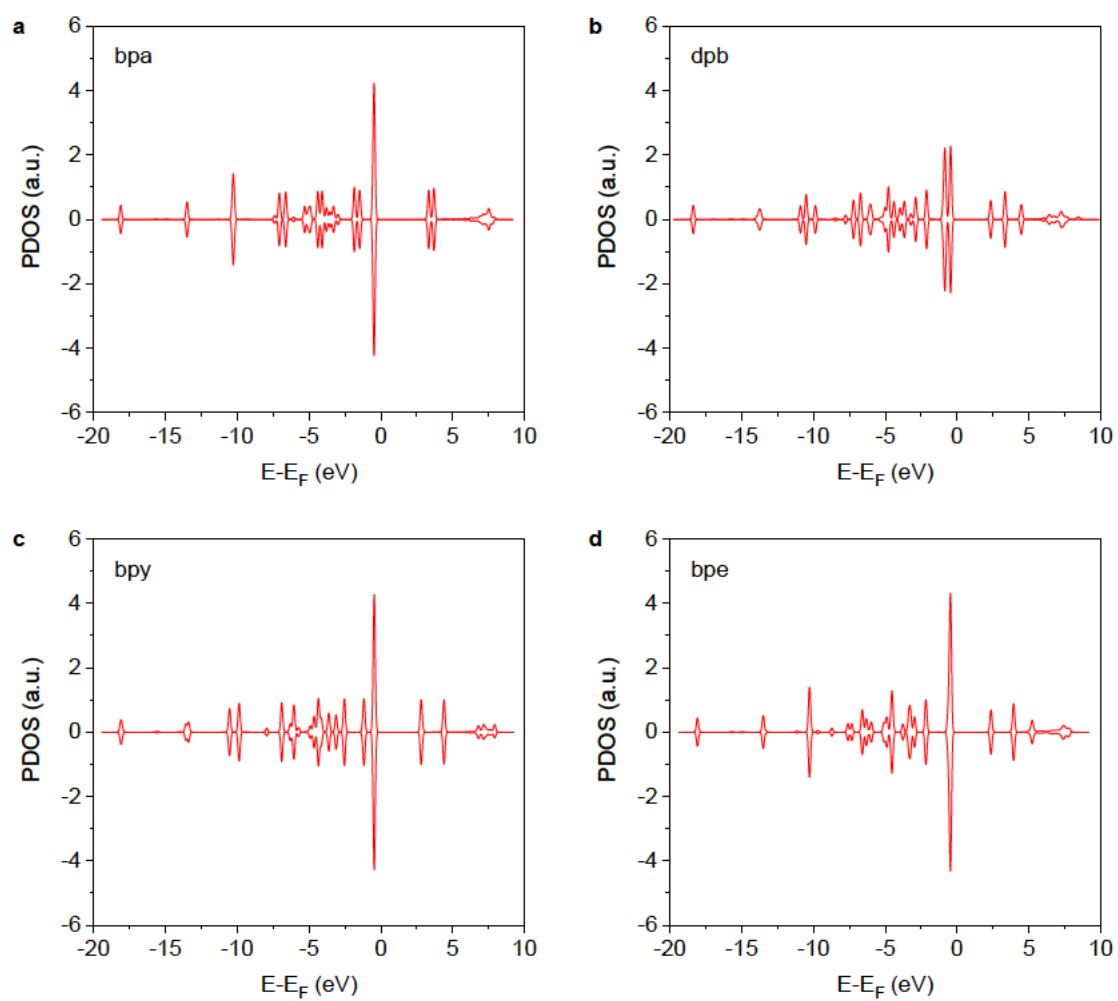


Figure S1. Projected density of states (PDOS) of N 2p in (a) bpa, (b) dpb, (c) bpy and (d) bpe.

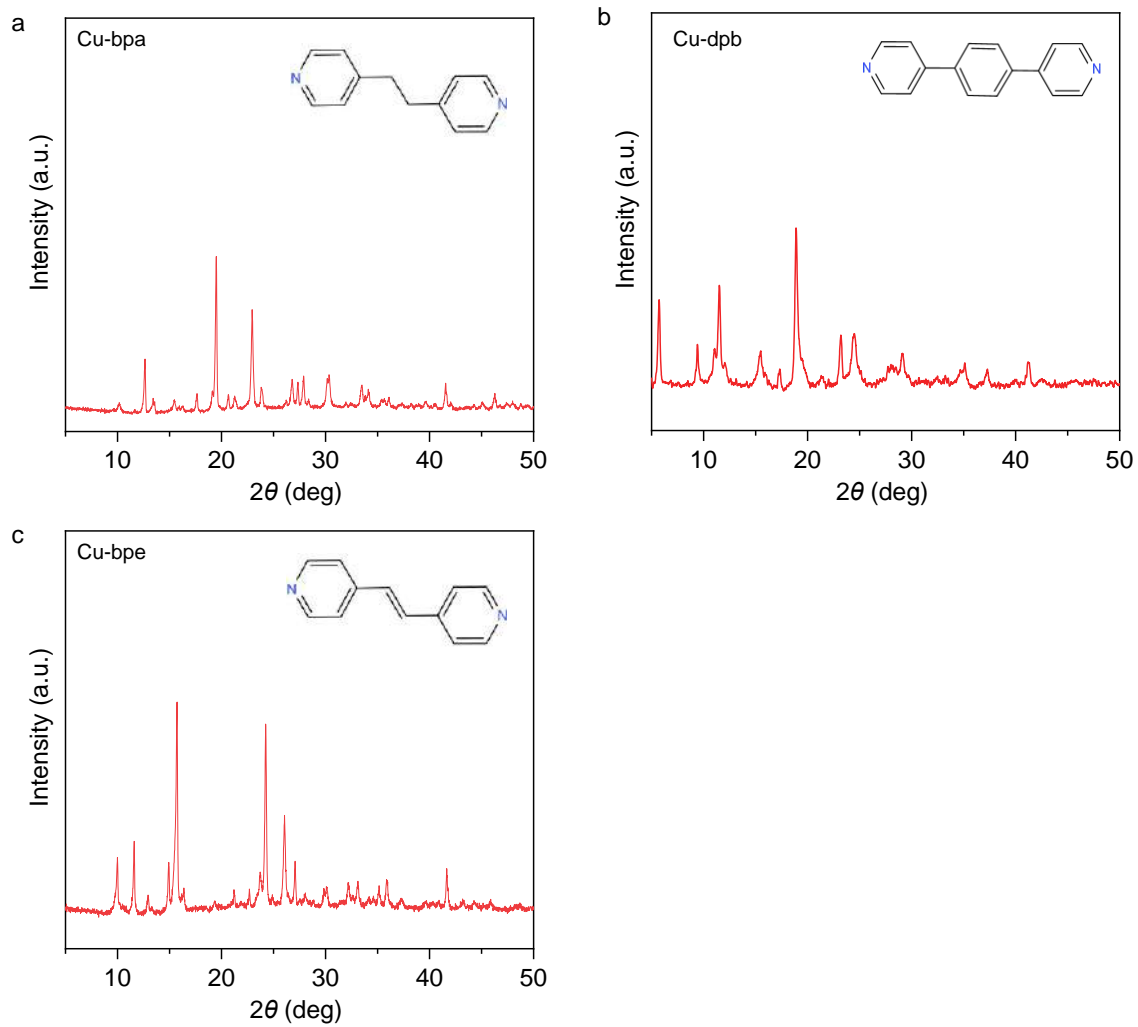


Figure S2. The XRD patterns of (a) Cu-bpa; (b) Cu-dpb and (c) Cu-bpe.

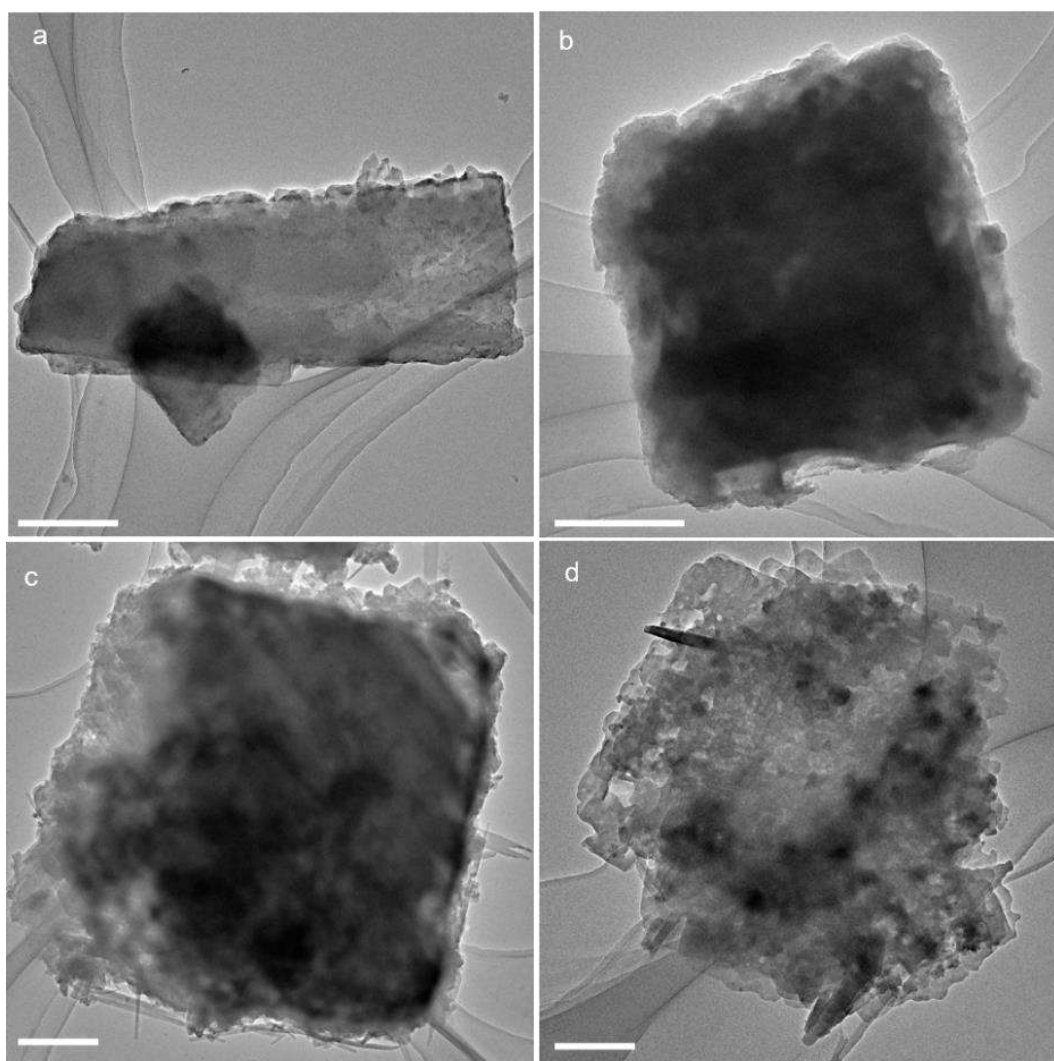


Figure S3. TEM images of (a) Cu-bpa; (b) Cu-dpb; (c) Cu-bpy; and (d) Cu-bpe. The scale bars are 500, 500, 500, and 250 nm, respectively.

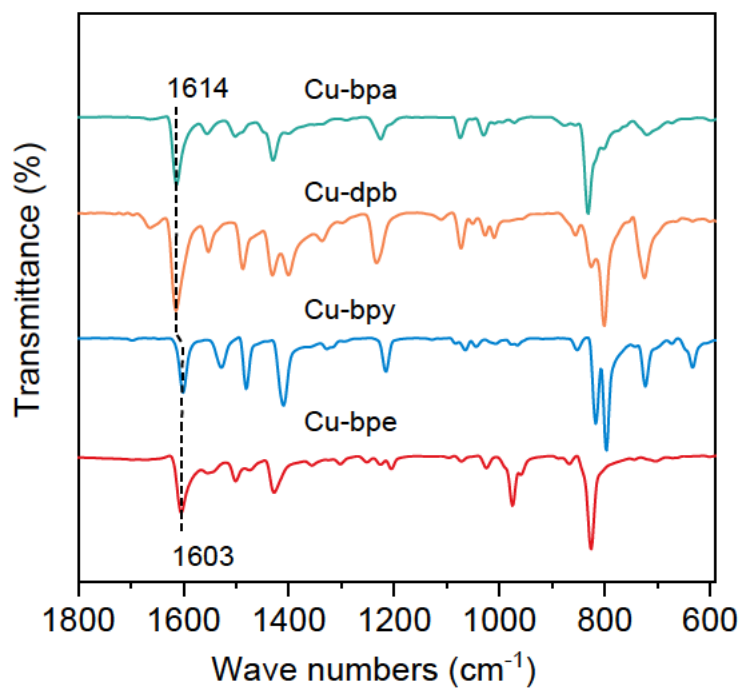


Figure S4. FTIR spectra of various Cu-MOFs.

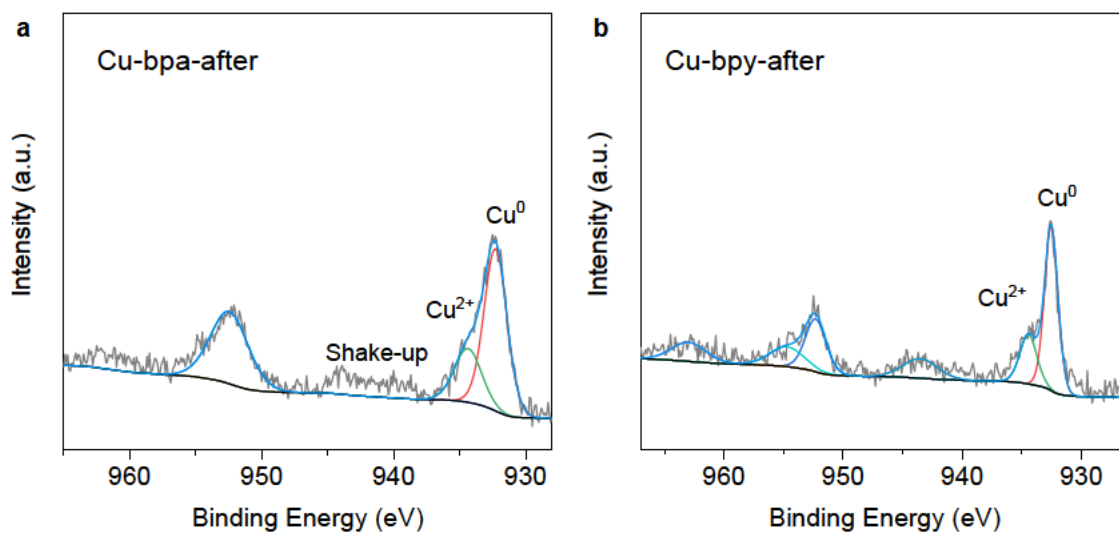


Figure S5. Cu 2p XPS spectra of (a) Cu-bpa and (c) Cu-bpy after CRR.

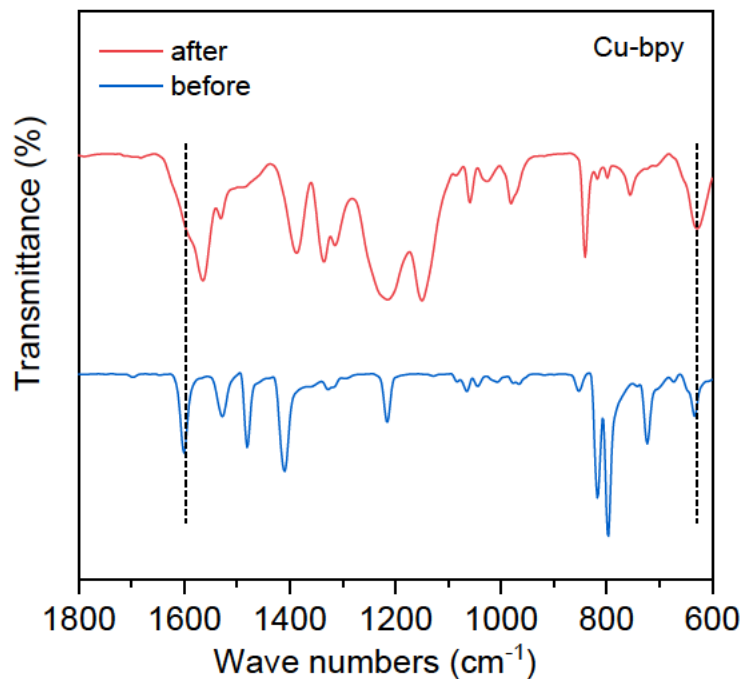


Figure S6. FTIR spectra of Cu-bpy before and after CRR.

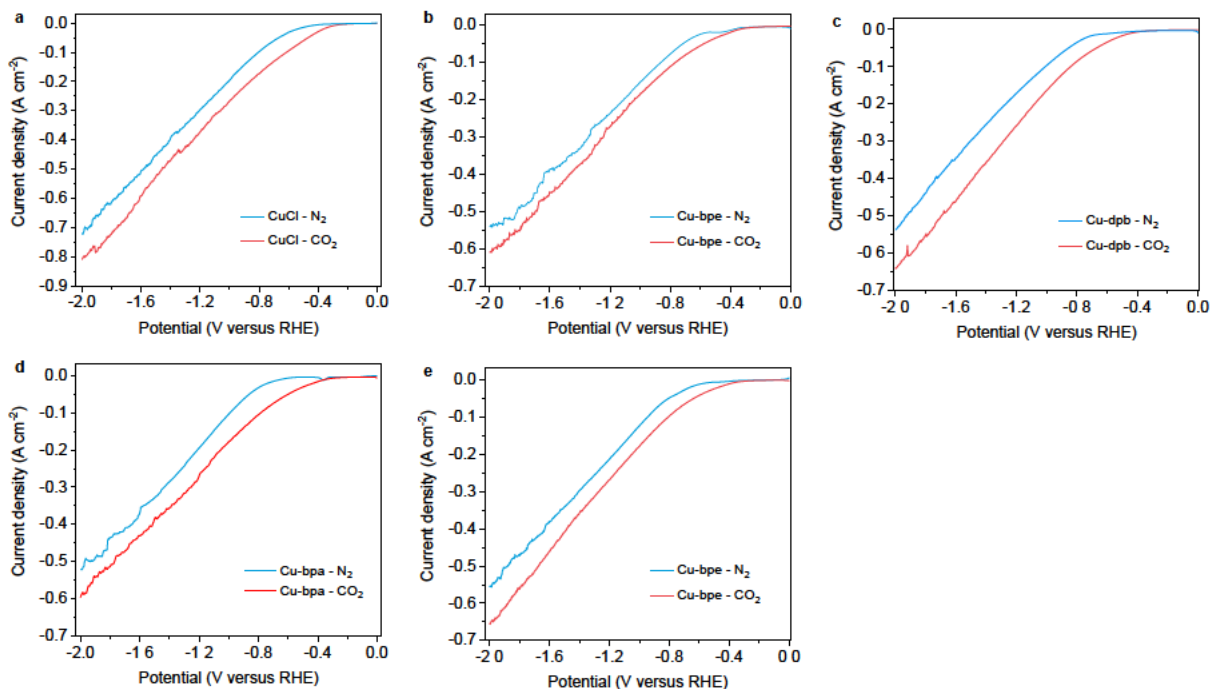


Figure S7. Linear sweep voltammetry (LSV) curves of different samples in N_2 or CO_2 atmosphere with a scan rate of 50 mVs^{-1} .

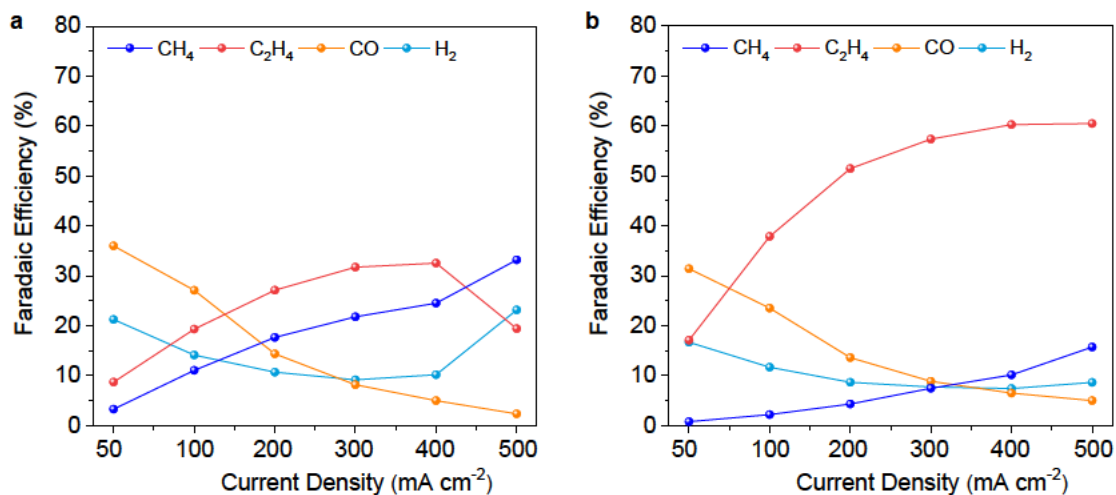


Figure S8. Faradaic efficiencies (FE) of CRR products on (a) Cu-dpb and (b) Cu-bpy over a range of applied current densities.

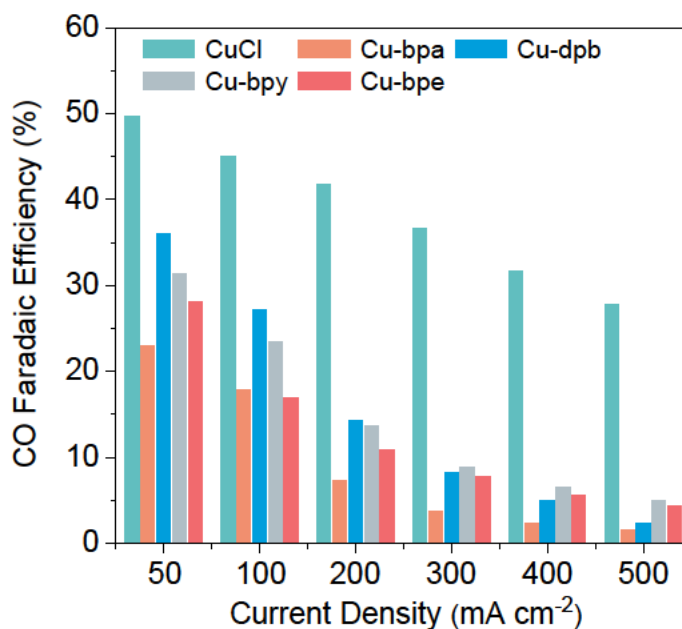


Figure S9. Faradaic efficiencies (FE) of CO on CuCl and Cu-MOFs over a range of applied current densities.

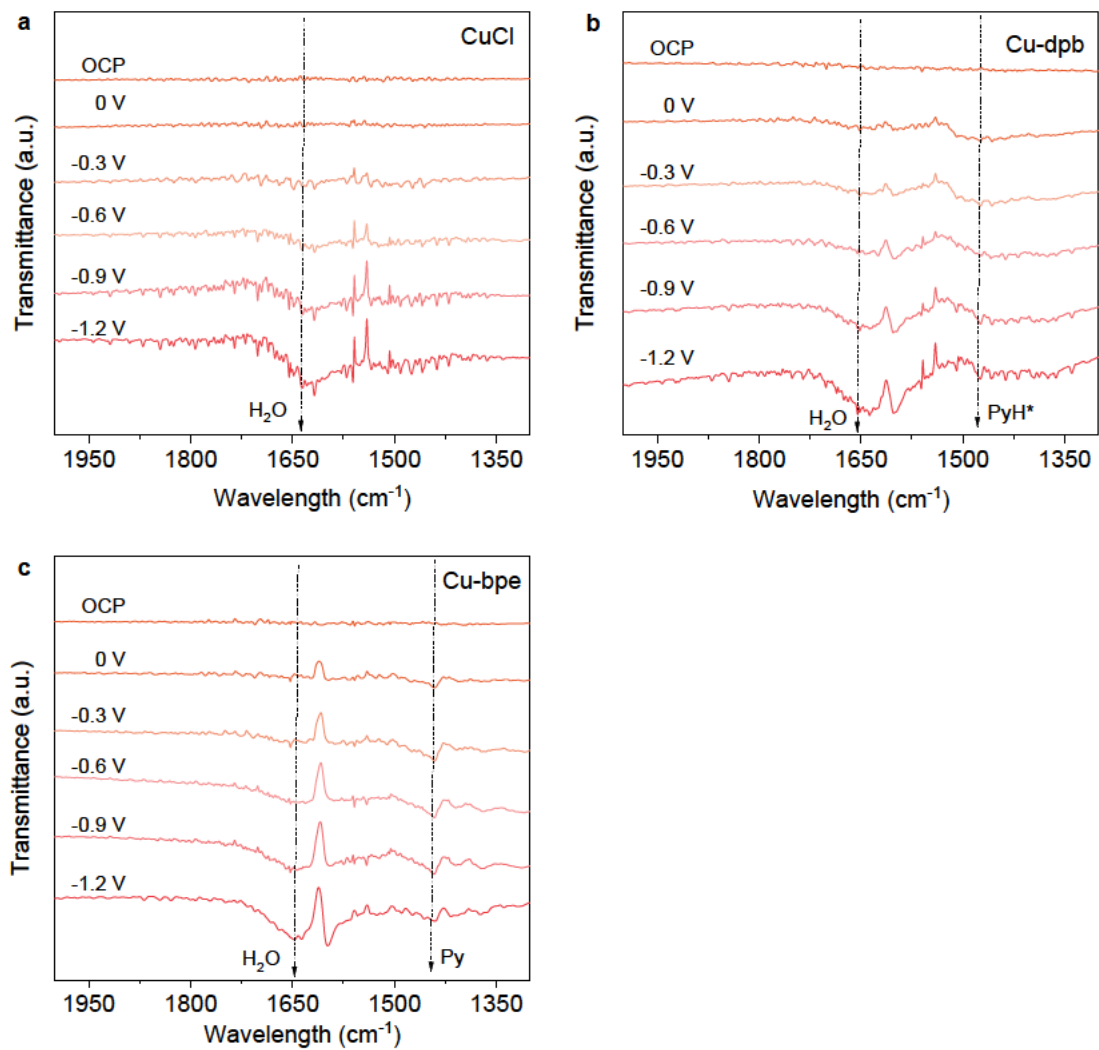


Figure S10. In-situ ATR-IR spectra on (a) CuCl, (b) Cu-dpb and (c) Cu-bpe at different potentials of CRR.

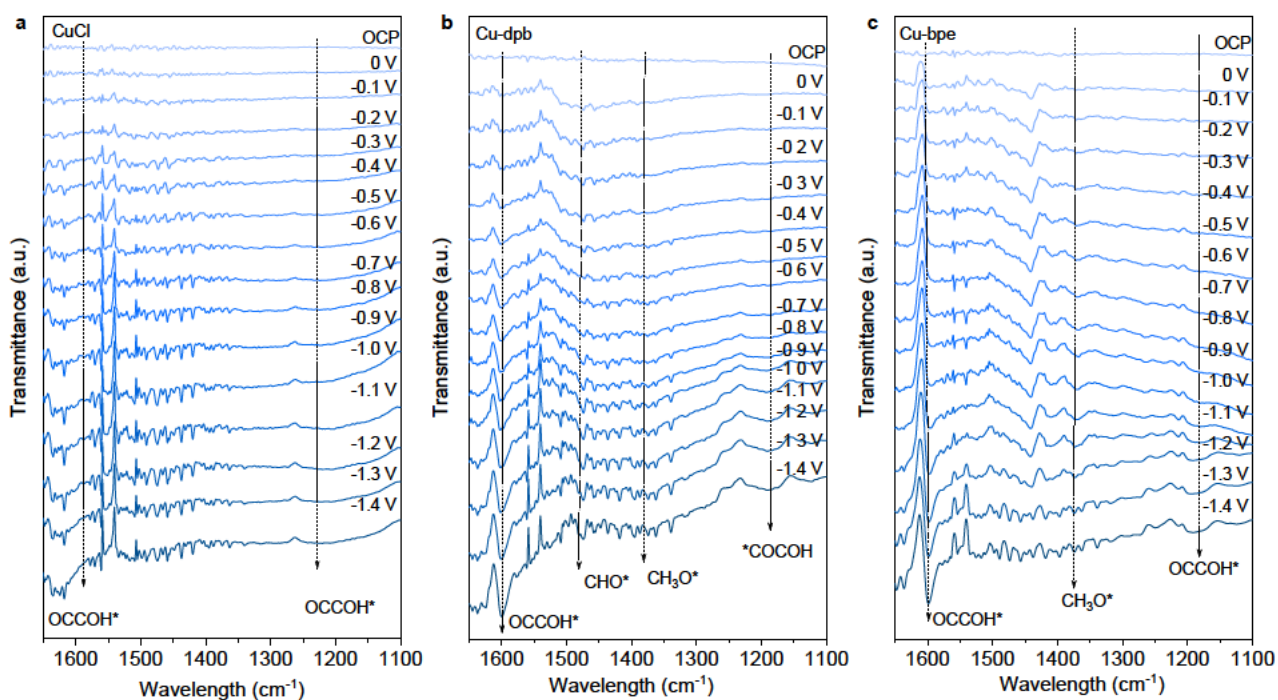


Figure S11. In-situ ATR-IR spectra on (a) CuCl, (b) Cu-dpb and (c) Cu-bpe at different potentials of CRR.

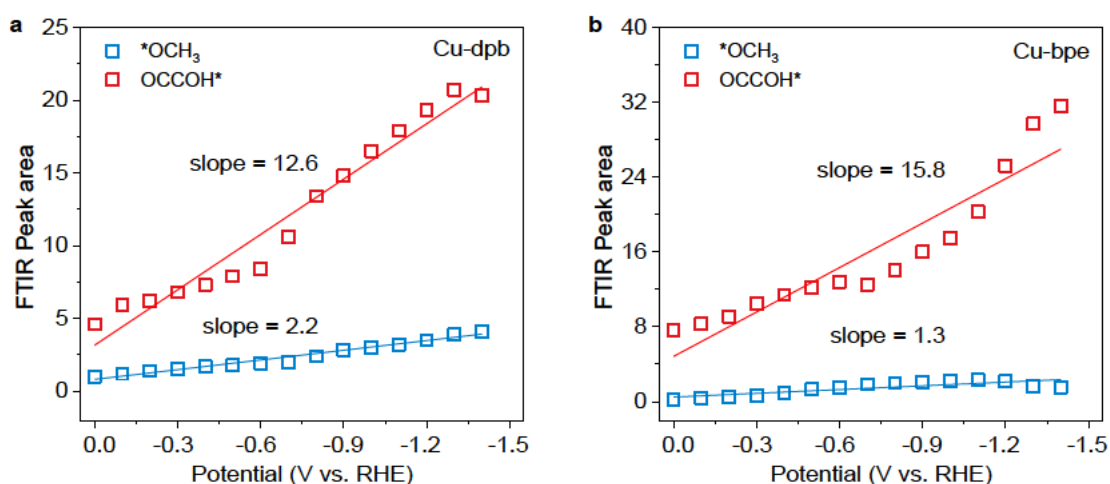


Figure S12. The integrated peak area of $^*\text{OCH}_3$ and OCCOH^* on (a) Cu-dpb and (b) Cu-bpe at different potentials of CRR.

Table S1. CH₄ Faradaic efficiency and current density comparison of the recently reported Cu electrocatalysts derived from other precursors.

Sample	Electrolyte	Potential (V vs RHE)	CH ₄ FE (%)	CH ₄ current density (mA cm ⁻²)	Ref
Cu-bpa	1.0 M KOH	-0.83	58.2	232.8	This work
Cu particles	1.0 M KOH	-0.70	48.0	84.0	1
Cu-PzI ^a	1.0 M KOH	-1.00	52.0	149.3	2
Cu/Al ₂ O ₃	1.0 M KOH	-1.20	62.0	94.86	3
Cu/La ₂ CuO ₄	1.0 M KOH	-1.40	56.3	116.5	4
Cu-DBC ^b	1.0 M KOH	-0.90	80.0	162.4	5
Cu-Ce-O _x	1.0 M KOH	-0.82	67.8	136.2	6
CoO/Cu	1.0 M KHCO ₃	-1.11	60.0	135.0	7
Au/Cu	1.0 M KHCO ₃	-1.23	56.0	112.0	8
Cu Nanowires	0.1 M KHCO ₃	-1.25	55.0	8.2	9
CuPc ^c	1.0 M KHCO ₃	-1.06	66.0	8.5	10
Cu	1.0 M KHCO ₃	-1.41	48.0	108.0	11
Cu-N-C	0.1 M KHCO ₃	-1.60	38.6	14.8	12
Cu ₂ O/Cu-MOF	0.1 M KHCO ₃	-1.71	63.2	8.4	13
Cu/CeO ₂	0.1 M KHCO ₃	-1.80	58.0	40.6	14

^a: Pz = pyrazole; ^b: DBC = dibenzo-[g,p]chrysene-2,3,6,7,10,11,14,15octaol; ^c: Pc = phthalocyanine.

Table S2. C₂H₄ Faradaic efficiency and current density comparison of the recently reported Cu electrocatalysts.

Sample	Electrolyte	Potential (V vs RHE)	C ₂ H ₄ FE (%)	C ₂ H ₄ current density (mA cm ⁻²)	Ref
Cu-bpe	1.0 M KOH	-0.85	65.9	263.6	This work
NCDs/Cu/CuO ^a	0.5 M KHCO ₃	-1.40	56.6	25.5	15
Ag@Cu	1.0 M KOH	-1.60	43.9	131.7	16
Cu-HITP ^b	0.1 M KHCO ₃	-1.20	51.0	3.1	17
AgI/CuO	1.0 M KOH	-1.05	45.0	61.5	18
Cu ₂ O ^c	1.0 M KHCO ₃	-0.90	40.0	120.0	19
CuO	0.5 M KCl	-1.01	71.2	178.0	20
Cu ₂ O	0.1 M KHCO ₃	-1.05	52.3	20.9	21
Cutr ^c	1.0 M KHCO ₃	-0.80	50.0	150.0	22
Cu	0.1 M KHCO ₃	-0.95	58.6	100.0	23
Cu ₃ (HITP) ₂	0.1 M KHCO ₃	-1.25	63.0	16.5	24
Cu nanowires	1.0 M KHCO ₃	-1.10	57.7	23.1	25
Cu ₄ (OH) ₆ FCl	0.1 M KHCO ₃	-1.00	36.3	10.1	26
Cu/Al ₂ O ₃	5.0 M KOH	-1.10	60.4	181.2	27
Cu ₂ O	1.0 M KOH	-0.61	38.0	134.9	28
OBC ^d	0.1 M KHCO ₃	-1.00	45.0	44.7	29

^a: NDC = -NH₂-modified carbon dots; ^b: HITP = 2,3,6,7,10,11-hexaiminotriphenylene; ^c: trc = 1,2,4-triazole; ^d: OBC = Oxygen-bearing copper.

References

- (1) Jeon, H. S.; Timoshenko, J.; Rettenmaier, C.; Herzog, A.; Yoon, A.; Chee, S. W.; Oener, S.; Hejral, U.; Haase, F. T.; Roldan Cuenya, B., Selectivity Control of Cu Nanocrystals in a Gas-Fed Flow Cell through CO₂ Pulsed Electroreduction. *J. Am. Chem. Soc.* **2021**, *143* (19), 7578-7587.
- (2) Wang, R.; Liu, J.; Huang, Q.; Dong, L. Z.; Li, S. L.; Lan, Y. Q., Partial Coordination-Perturbed Bi-Copper Sites for Selective Electroreduction of CO₂ to Hydrocarbons. *Angew. Chem. Int. Ed.* **2021**, *60* (36), 19829-19835.
- (3) Chen, S.; Wang, B.; Zhu, J.; Wang, L.; Ou, H.; Zhang, Z.; Liang, X.; Zheng, L.; Zhou, L.; Su, Y. Q.; Wang, D.; Li, Y., Lewis Acid Site-Promoted Single-Atomic Cu Catalyzes Electrochemical CO₂ Methanation. *Nano Lett.* **2021**, *21* (17), 7325-7331.
- (4) Chen, S.; Su, Y.; Deng, P.; Qi, R.; Zhu, J.; Chen, J.; Wang, Z.; Zhou, L.; Guo, X.; Xia, B. Y., Highly Selective Carbon Dioxide Electroreduction on Structure-Evolved Copper Perovskite Oxide toward Methane Production. *ACS Catal.* **2020**, *10* (8), 4640-4646.
- (5) Zhang, Y.; Dong, L. Z.; Li, S.; Huang, X.; Chang, J. N.; Wang, J. H.; Zhou, J.; Li, S. L.; Lan, Y. Q., Coordination environment dependent selectivity of single-site-Cu enriched crystalline porous catalysts in CO₂ reduction to CH₄. *Nat. Commun.* **2021**, *12* (1), 6390.
- (6) Zhou, X.; Shan, J.; Chen, L.; Xia, B. Y.; Ling, T.; Duan, J.; Jiao, Y.; Zheng, Y.; Qiao, S. Z., Stabilizing Cu²⁺ Ions by Solid Solutions to Promote CO₂ Electroreduction to Methane. *J. Am. Chem. Soc.* **2022**, *144* (5), 2079-2084.
- (7) Li, Y.; Xu, A.; Lum, Y.; Wang, X.; Hung, S. F.; Chen, B.; Wang, Z.; Xu, Y.; Li, F.; Abed, J.; Huang, J. E.; Rasouli, A. S.; Wicks, J.; Sagar, L. K.; Peng, T.; Ip, A. H.; Sinton, D.; Jiang, H.; Li, C.; Sargent, E. H., Promoting CO₂ methanation via ligand-stabilized metal oxide clusters as hydrogen-donating motifs. *Nat. Commun.* **2020**, *11* (1), 6190.
- (8) Wang, X.; Ou, P.; Wicks, J.; Xie, Y.; Wang, Y.; Li, J.; Tam, J.; Ren, D.; Howe, J. Y.; Wang, Z.; Ozden, A.; Finrock, Y. Z.; Xu, Y.; Li, Y.; Rasouli, A. S.; Bertens, K.; Ip, A. H.; Graetzel, M.; Sinton, D.; Sargent, E. H., Gold-in-copper at low *CO coverage enables efficient electromethanation of CO₂. *Nat. Commun.* **2021**, *12* (1), 3387.
- (9) Li, Y.; Cui, F.; Ross, M. B.; Kim, D.; Sun, Y.; Yang, P., Structure-Sensitive CO₂ Electroreduction to Hydrocarbons on Ultrathin 5-fold Twinned Copper Nanowires. *Nano Lett.* **2017**, *17* (2), 1312-1317.
- (10) Weng, Z.; Wu, Y.; Wang, M.; Jiang, J.; Yang, K.; Huo, S.; Wang, X. F.; Ma, Q.; Brudvig, G. W.; Batista, V. S.; Liang, Y.; Feng, Z.; Wang, H., Active sites of copper-complex catalytic materials for electrochemical carbon dioxide reduction. *Nat. Commun.* **2018**, *9* (1), 415.
- (11) Wang, X.; Xu, A.; Li, F.; Hung, S. F.; Nam, D. H.; Gabardo, C. M.; Wang, Z.; Xu, Y.; Ozden, A.; Rasouli, A. S.; Ip, A. H.; Sinton, D.; Sargent, E. H., Efficient Methane Electrosynthesis Enabled by Tuning Local CO₂ Availability. *J. Am. Chem. Soc.* **2020**, *142* (7), 3525-3531.

- (12) Guan, A.; Chen, Z.; Quan, Y.; Peng, C.; Wang, Z.; Sham, T.-K.; Yang, C.; Ji, Y.; Qian, L.; Xu, X.; Zheng, G., Boosting CO₂ Electroreduction to CH₄ via Tuning Neighboring Single-Copper Sites. *ACS Energy Lett.* **2020**, *5* (4), 1044-1053.
- (13) Tan, X.; Yu, C.; Zhao, C.; Huang, H.; Yao, X.; Han, X.; Guo, W.; Cui, S.; Huang, H.; Qiu, J., Restructuring of Cu₂O to Cu₂O@Cu-Metal-Organic Frameworks for Selective Electrochemical Reduction of CO₂. *ACS Appl. Mater. Interfaces* **2019**, *11* (10), 9904-9910.
- (14) Wang, Y. F.; Chen, Z.; Han, P.; Du, Y. H.; Gu, Z. X.; Xu, X.; Zheng, G. F., Single-Atomic Cu with Multiple Oxygen Vacancies on Ceria for Electrocatalytic CO₂ Reduction to CH₄. *ACS Catal.* **2018**, *8* (8), 7113-7119.
- (15) Zhou, Y. J.; Qi, H. H.; Wu, J.; Huang, H.; Liu, Y.; Kang, Z. H., Amino Modified Carbon Dots with Electron Sink Effect Increase Interface Charge Transfer Rate of Cu-Based Electrocatalyst to Enhance the CO₂ Conversion Selectivity to C₂H₄. *Adv. Funct. Mater.* **2022**, *32* (22), 2113335.
- (16) Zhong, Y. Z.; Kong, X. D.; Song, Z. M.; Liu, Y.; Peng, L. P.; Zhang, L.; Luo, X.; Zeng, J.; Geng, Z. G., Adjusting Local CO Confinement in Porous-Shell Ag@Cu Catalysts for Enhancing C-C Coupling toward CO₂ Electroreduction. *Nano Lett.* **2022**, *22* (6), 2554-2560.
- (17) Zhao, Z.-H.; Zhu, H.-L.; Huang, J.-R.; Liao, P.-Q.; Chen, X.-M., Polydopamine Coating of a Metal–Organic Framework with Bi-Copper Sites for Highly Selective Electroreduction of CO₂ to C₂₊ Products. *ACS Catal.* **2022**, 7986-7993.
- (18) Yang, R.; Duan, J.; Dong, P.; Wen, Q.; Wu, M.; Liu, Y.; Li, H.; Zhai, T., In Situ Halogen-Ion Leaching Regulates Multiple Sites on Tandem Catalysts for Efficient CO₂ Electroreduction to C₂₊ Products. *Angew. Chem. Int. Ed.* **2022**, *61* (21), e202116706.
- (19) Wu, Z. Z.; Zhang, X. L.; Niu, Z. Z.; Gao, F. Y.; Yang, P. P.; Chi, L. P.; Shi, L.; Wei, W. S.; Liu, R.; Chen, Z.; Hu, S.; Zheng, X.; Gao, M. R., Identification of Cu(100)/Cu(111) Interfaces as Superior Active Sites for CO Dimerization During CO₂ Electroreduction. *J. Am. Chem. Soc.* **2022**, *144* (1), 259-269.
- (20) Liu, W.; Zhai, P.; Li, A.; Wei, B.; Si, K.; Wei, Y.; Wang, X.; Zhu, G.; Chen, Q.; Gu, X.; Zhang, R.; Zhou, W.; Gong, Y., Electrochemical CO₂ reduction to ethylene by ultrathin CuO nanoplate arrays. *Nat. Commun.* **2022**, *13* (1), 1877.
- (21) Jiang, Y.; Wang, X.; Duan, D.; He, C.; Ma, J.; Zhang, W.; Liu, H.; Long, R.; Li, Z.; Kong, T.; Loh, X. J.; Song, L.; Ye, E.; Xiong, Y., Structural Reconstruction of Cu₂O Superparticles toward Electrocatalytic CO₂ Reduction with High C₂₊ Products Selectivity. *Adv. Sci.* **2022**, *9* (16), e2105292.
- (22) Huang, D.-S.; Zhu, H.-L.; Zhao, Z.-H.; Huang, J.-R.; Liao, P.-Q.; Chen, X.-M., A Stable and Low-Cost Metal-Azolate Framework with Cyclic Tricopper Active Sites for Highly Selective CO₂ Electroreduction to C₂₊ Products. *ACS Catal.* **2022**, 8444-8450.
- (23) Zhang, G.; Zhao, Z. J.; Cheng, D.; Li, H.; Yu, J.; Wang, Q.; Gao, H.; Guo, J.; Wang, H.; Ozin, G. A.; Wang, T.; Gong, J., Efficient CO₂ electroreduction on facet-selective copper films with high conversion rate. *Nat. Commun.* **2021**, *12* (1), 5745.

- (24) Sun, H.; Chen, L.; Xiong, L.; Feng, K.; Chen, Y.; Zhang, X.; Yuan, X.; Yang, B.; Deng, Z.; Liu, Y.; Rummeli, M. H.; Zhong, J.; Jiao, Y.; Peng, Y., Promoting ethylene production over a wide potential window on Cu crystallites induced and stabilized via current shock and charge delocalization. *Nat. Commun.* **2021**, *12* (1), 6823.
- (25) Lyu, Z.; Zhu, S.; Xie, M.; Zhang, Y.; Chen, Z.; Chen, R.; Tian, M.; Chi, M.; Shao, M.; Xia, Y., Controlling the Surface Oxidation of Cu Nanowires Improves Their Catalytic Selectivity and Stability toward C₂₊ Products in CO₂ Reduction. *Angew. Chem. Int. Ed.* **2021**, *60* (4), 1909-1915.
- (26) Li, M.; Ma, Y.; Chen, J.; Lawrence, R.; Luo, W.; Sacchi, M.; Jiang, W.; Yang, J., Residual Chlorine Induced Cationic Active Species on a Porous Copper Electrocatalyst for Highly Stable Electrochemical CO₂ Reduction to C₂₊. *Angew. Chem. Int. Ed.* **2021**, *60* (20), 11487-11493.
- (27) Li, H.; Yu, P.; Lei, R.; Yang, F.; Wen, P.; Ma, X.; Zeng, G.; Guo, J.; Toma, F. M.; Qiu, Y.; Geyer, S. M.; Wang, X.; Cheng, T.; Drisdell, W. S., Facet-Selective Deposition of Ultrathin Al₂O₃ on Copper Nanocrystals for Highly Stable CO₂ Electroreduction to Ethylene. *Angew. Chem. Int. Ed.* **2021**, *60* (47), 24838-24843.
- (28) Yang, P. P.; Zhang, X. L.; Gao, F. Y.; Zheng, Y. R.; Niu, Z. Z.; Yu, X.; Liu, R.; Wu, Z. Z.; Qin, S.; Chi, L. P.; Duan, Y.; Ma, T.; Zheng, X. S.; Zhu, J. F.; Wang, H. J.; Gao, M. R.; Yu, S. H., Protecting Copper Oxidation State via Intermediate Confinement for Selective CO₂ Electroreduction to C₂₊ Fuels. *J. Am. Chem. Soc.* **2020**, *142* (13), 6400-6408.
- (29) Zhang, W.; Huang, C.; Xiao, Q.; Yu, L.; Shuai, L.; An, P.; Zhang, J.; Qiu, M.; Ren, Z.; Yu, Y., Atypical Oxygen-Bearing Copper Boosts Ethylene Selectivity toward Electrocatalytic CO₂ Reduction. *J. Am. Chem. Soc.* **2020**, *142* (26), 11417-11427.

Chapter 6 Regulating interface water structure by solvation effects to promote electrochemical C-C coupling reactions

6.1 Introduction and Significance

During CRR process, water serves not only as a proton source but also as a solvent environment, whose structure can determine catalyst activity and selectivity. Cu is a unique electrocatalyst that can achieve CRR with the generation of hydrocarbons and oxygenates. It should be noted that CRR is a proton-coupled electron transfer (PCET) process, and its activity and selectivity are dependent not only on the conventional electronic structure of the catalyst but also on the availability of protons. However, it is still a challenge to regulate the interfacial water structure of Cu catalyst to steer its CRR selectivity.

Here we employed dimethyl sulfoxide (DMSO) as an electrolyte additive to tune the solvation structure of K ions to promote *CO dimerization to generate C₂H₄. The ¹H chemical shift confirms that replacing part of H₂O in KOH solution with DMSO can strengthen hydrogen bonds in the electrolyte. In-situ Raman spectroscopy suggests that the stronger hydrogen bonds form more 4-coordinated hydrogen-bonded water on the catalyst surface during CRR operation. In addition, in-situ attenuated total reflectance infrared (ATR-IR) spectroscopy confirms that, due to the addition of DMSO, the adsorption ability of *CO is significantly increased, favoring C-C coupling step, resulting in a three-fold higher ratio of FE_{C₂H₄} to FE_{CO}.

The particular novelty of this work is:

1. New method. We engineer the solvation structure of K⁺ ions through the introduction of DMSO to replace part of H₂O in the electrolyte to tune interfacial water structure on the catalyst surface to steer CRR selectivity.
2. Tuning interfacial water. In situ spectroscopic characterizations reveal that solvated

K ions in the mixed solvent can form a higher percentage of 4-coordinated hydrogen-bonded water on the surface of Cu catalyst, consequently building stronger hydrogen bonds to stabilize *CO and fast its dimerization.

3. High selectivity. Due to the addition of DMSO, the adsorption ability of *CO is significantly increased, favoring C-C coupling step to C₂H₄, resulting in a three-fold higher ratio of FEC_{2H4} to FE_{CO}.

6.2 Regulating interfacial water structure by solvent effects to facilitate electrochemical C-C coupling reactions

This chapter is included as a submitted manuscript by Xianlong Zhou, Jieqiong Shan, Yilong Zhu, Min Zheng, Bao Yu Xia, Yan Jiao, Yao Zheng, Shi-Zhang Qiao, Solvent effects regulating interfacial water structure of Cu catalysts to facilitate electrochemical C-C coupling reactions.

Statement of Authorship

Title of Paper	Stabilizing Cu ²⁺ Ions by Solid Solutions to Promote CO ₂ Electroreduction to Methane
Publication Status	<input type="checkbox"/> Published <input type="checkbox"/> Accepted for Publication <input type="checkbox"/> Submitted for Publication <input checked="" type="checkbox"/> Unpublished and Unsubmitted work written in manuscript style
Publication Details	Solvent effects regulating interfacial water structure of Cu catalyst to promote electrochemical C-C coupling reactions, Xianlong Zhou, Jieqiong Shan, Min Zheng, Bao Yu Xia, Yao Zheng, Shi-Zhang Qiao

Principal Author

Name of Principal Author (Candidate)	Xianlong Zhou		
Contribution to the Paper	Conducted material synthesis, carried out electrochemical tests and wrote the paper		
Overall percentage (%)	70		
Certification:	This paper reports on original research I conducted during the period of my Higher Degree by Research candidature and is not subject to any obligations or contractual agreements with a third party that would constrain its inclusion in this thesis. I am the primary author of this paper.		
Signature		Date	09/09/2022

Co-Author Contributions

By signing the Statement of Authorship, each author certifies that:

- the candidate's stated contribution to the publication is accurate (as detailed above);
- permission is granted for the candidate to include the publication in the thesis; and
- the sum of all co-author contributions is equal to 100% less the candidate's stated contribution.

Name of Co-Author	Jieqiong Shan		
Contribution to the Paper	Conducted in situ attenuated total reflectance infrared spectroscopy (ATR-IR) and Raman characterization		
Signature		Date	09/09/2022

Name of Co-Author	Min Zheng		
Contribution to the Paper	FTIR testing		
Signature		Date	09/09/2022

Name of Co-Author	Bao Yu Xia		
Contribution to the Paper	Providing experiment conditions and constructive discussion		
Signature		Date	09/09/2022

Name of Co-Author	Yao Zheng		
Contribution to the Paper	Discussion of research plan, manuscript revision, and acted as corresponding author		
Signature		Date	09/09/2022

Name of Co-Author	Shi-Zhang Qiao		
Contribution to the Paper	Supervised development of work, helped in manuscript evaluation and revision, and acted as corresponding author		
Signature		Date	09/09/2022

Please cut and paste additional co-author panels here as required.

Regulating Interfacial Water Structure by Solvent Effects to Promote Electrochemical C-C Coupling Reactions

Xianlong Zhou,¹ Jieqiong Shan,¹ Min Zheng,¹ Bao Yu Xia², Yao Zheng,^{1*} Shi-Zhang Qiao^{1*}

¹ School of Chemical Engineering and Advanced Materials, The University of Adelaide, Adelaide, SA 5005, Australia.

² Key Laboratory of Material Chemistry for Energy Conversion and Storage (Ministry of Education), Hubei Key Laboratory of Material Chemistry and Service Failure, Wuhan; National Laboratory for Optoelectronics, School of Chemistry and Chemical Engineering, Huazhong University of Science and Technology (HUST), 1037 Luoyu Road, Wuhan 430074, China.

Keywords: Solvation structure; interfacial water; CO₂ electroreduction; C-C coupling; proton-coupled electron transfer

ABSTRACT: During the aqueous electrochemical CO₂ reduction (CRR) process, water molecules serve not only as a proton source but also a solvent environment, whose structure at the interfacial electrolyte/electrode can determine catalyst's activity and selectivity. Here we engineer the solvation structure of metal cations by organic solvent additive to tune the interfacial water structure, which can facilitate the proton-coupled electron transfer (PCET) process of CO₂ activation and increase the absorption ability for *CO intermediate, thereby promoting the C-C coupling reaction during CRR. Dimethyl sulfoxide (DMSO) serves as an electrolyte additive to tune the solvation structure of K ions in KOH electrolyte because it can preferentially solvate with K ions over the water molecules. In situ spectroscopic characterizations reveal that solvated DMSO with the electrostatic effect of K ions can form a higher percentage of 4-coordinated hydrogen-bonded water on the surface of conventional Cu catalyst. This water can build stronger hydrogen bonds to stabilize *CO and fast its dimerization to form C₂H₄. This work may provide a more general understanding of CRR selectivity by tuning interfacial water structure to steer PCET process rather than materials engineering.

Electrochemical CO₂ reduction powered by reversible electricity provides an attractive technique for achieving carbon-emissions-neutral processes.¹ It can transform CO₂ into various value-added chemicals or fuels, including methane (CH₄), carbon monoxide (CO), methanol (CH₃OH), ethene (C₂H₄), or ethanol (C₂H₅OH).² Cu is the only metal element to electrochemically catalyze CO₂ into hydrocarbons and oxygenates due to its binding to CRR intermediate *CO neither too weakly nor too strongly.³ Unfortunately, this unique physicochemical property of Cu also results in poor selectivity, heavily impeding their practical applications for CRR. Currently, tuning the electronic structure of Cu can significantly improve its absorption ability of intermediates and then promote electrosynthesis of the desired reduction products.⁴ For example, Zhou et al. synthesized boron-doped Cu to stabilize its oxidation state, thereby increasing *CO adsorption energy and facilitating its dimerization to multi-carbon hydrocarbons.⁵ It should be noted that CRR contains a series of proton-coupled electron transfer (PCET) process; therefore its activity and selectivity are dependent not only on the conventional electronic structure of the catalyst but also on the availability of protons.⁶ Currently, there are two typical ways to alter the availability of protons to tune CRR selectivity of the Cu catalyst, i.e., pH of electrolyte, and source of the proton. Specifically, at pH = 1, the C1 pathway undergoes through the *COH intermediate to form CH₄, while the C₂ pathways are kinetically suppressed. By contrast, at pH = 12, the C1 pathway is blocked, while the *CO-*CO dimerization pathway is both thermodynamically and kinetically favorable.⁷ On the other hand, our recent research suggests that tuning of linker's electrophilicity can alter Cu-MOF catalyst's proton availability and consequently, favoring CRR pathway of either *CO hydrogenation to CH₄ or *CO-*COH dimerization to C₂H₄.

Recent studies confirm that water plays critical roles in electrocatalysis and aqueous battery on solid/liquid interfaces, such as providing proton resources and solvation environments.^{8a, 8b} Wang et al. added a thin layer of protic ionic liquids to the surface of metallic catalysts (Au/C and Pt/C) and tuned interfacial hydrogen bonds in aqueous solution to result in favorable PCET kinetics, thereby boosting the intrinsic oxygen-reduction reaction (ORR) activity.⁹ In aqueous Zn batteries, a solid preferential hydrogen bonding effect between the organic solvent and H₂O can be formed to reduce the H₂O activity and hinder deprotonation of the electrolyte. As a result, this mixed solvent can suppress side reactions and boost the zinc dissolution/deposition.^{10a, 10b} Likewise, the deprotonation of water can also have effects on the activity and selectivity of Cu-based catalysts in CRR by regulation of the PCET process.¹¹ Therefore, we hypothesize that tuning of the solvation structure of metal cations builds strong hydrogen bonds to stabilize *CO intermediate, promoting *CO dimerization to generate C₂H₄. However, there are few studies on manipulating the solvent structure of metal cations to tune the interaction between hydrogen bonds and CRR intermediates.

As a proof-of-concept, here we employed dimethyl sulfoxide (DMSO) as an electrolyte additive to tune the solvation structure of K ions to promote *CO dimerization to generate C₂H₄. The H¹ chemical shift confirms that replacing part of H₂O in KOH solution with DMSO can strengthen hydrogen bonds in the electrolyte. In situ Raman spectroscopy suggests that the stronger hydrogen bonds form more 4-coordinated hydrogen-bonded water on the catalyst surface during CRR operation. Furthermore, in-situ attenuated total reflectance infrared (ATR-IR) spectroscopy confirms that, due to the addition of DMSO, the adsorption ability of *CO is significantly

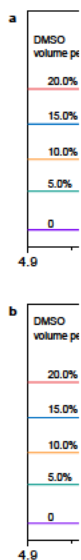


Figure 1 and (b) vent. (c) (d) Snap in MD si

DMSO tion stru potassiu portantly ter (18.0 ions and resonanc infrared the inter: decrease (D₂O, Fi tween D can rebu when KC typically increases (**Figure 1b**), suggesting that the stronger hydrogen bonds result from the solvent effects of metal cations. It should be noted that the H¹chemical shift gradually enlarges with the addition of DMSO, indicating that we can adjust the strength of hydrogen bonds by altering the volume ratio of DMSO to H₂O.¹⁴ In addition, we also tuned cations and anions to alter hydrogen bond network of electrolyte(**Figure S2**), and found that their increases of H¹chemical shift are smaller than that of DMSO, suggesting its higher efficiency to alter hydrogen bond network. The FTIR spectroscopy further identified water structure change in the mixed solution due to the introduction of DMSO (**Figure 1c**).^{15a, 15b} The results show that the area ratio of 4-coordinated hydrogen-bonded water (4-HB-H₂O) to 2-HB-H₂O in the DMSO/H₂O mixed solution slightly increases from 2.95 to 3.16, suggesting generation of stronger hydrogen bond, which is also supported by molecular dynamics simulation (**Figure 1d**).

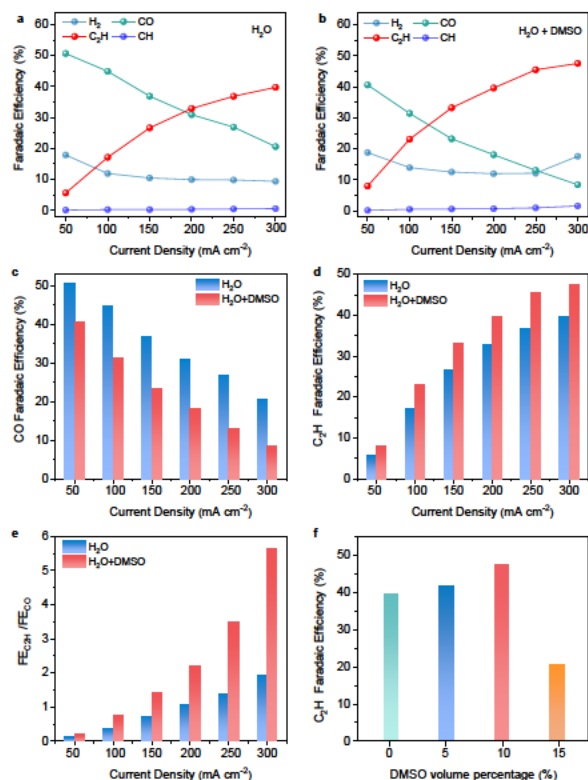


Figure 2. CRR performances of Cu₂O in 1 M KOH with distinct solvent composition at different current densities. FEs for CRR products in (a) pure water and (b) the DMSO/H₂O mixed electrolyte. FEs for (c) CO and (d) C₂H₄. (e) the ratio of FE_{C₂H₄} to FE_{CO}. (f) FEs for C₂H₄ at 300 mA cm⁻² in different volume percentage of DMSO.

Then, the most common Cu₂O as the model catalyst was synthesized using a previous method.¹⁶ Its phase and morphology were analyzed by power X-ray diffraction (XRD) patterns (**Figure S3**) and scanning electron microscopy (SEM) images (**Figure S4**), respectively. Transmission electron microscopy image further confirmed the synthesized Cu₂O with polyhedral structure (**Figure S5**), matching well with the previous one.¹⁷ The CRR catalytic performances of Cu₂O were investigated in different electrolytes by a flow cell (**Figure S6**). As shown in **Figure 2a**, at low current densities (below 200 mA cm⁻²), the main product with Cu₂O in 1 M KOH is CO with a maximum FE_{CO} of 50.6% achieved at 50 mA cm⁻². When the current density further increases, the main product is converted to C₂H₄, and the maximum FE_{C₂H₄} of 39.7% is performed at 300 mA cm⁻². When DMSO replaced H₂O in the electrolyte, we find that the product distribution is unchanged (**Figure 2b**). It should be noted that FE_{C₂H₄} surpasses FE_{CO} at a lower current density than pure water, indicating a higher C-C coupling efficiency in the mixed electrolyte. Consequently, at 300 mA cm⁻², the maximum FE_{C₂H₄} of 47.5% can be achieved.

We further compare their FE_{CO} and FE_{C₂H₄}, respectively, and find that FE_{CO} is significantly decreased after the introduction of DMSO at all current densities, while FE_{C₂H₄} is the opposite (**Figure 2c, 2d**). To highlight the selectivity change of Cu₂O in two electrolytes, we calculated the ratio of FE_{C₂H₄} to FE_{CO} (**Figure 2e**). The results show that the C-C coupling efficiency in the DMSO/H₂O mixed electrolyte is significantly higher than that of H₂O with a maximum FE_{C₂H₄}/FE_{CO} of 3.0 achieved at 300 mA cm⁻². In addition, we tune the volume ratio of DMSO to H₂O to investigate CRR catalytic behaviors of Cu₂O in different electrolytes (**Figure S7**). The results

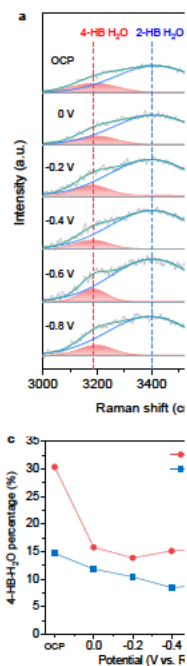


Figure 3. The in situ Raman spectroscopy of KHCO_3 with (a) pure the solvent. (c) The structure. (d) Schematic illustration in 1 M KHCO_3 using solvent, respectively.

We then conducted in situ ATR-IR spectroscopy on the interface H_2O structure of DMSO during CRR. The CO_2 is dominant in the water structure in the previous report.^{15b} By contrast, 4-HB- H_2O is foremost in the bulk electrolyte. This change in water structure results from the potential to build an electrochemical double layer on the surface of the electrode. With the potential decreasing, the percentage of 4-HB- H_2O is slightly down, suggesting forming a stable interface H_2O layer on the catalyst surface. When part of H_2O in the electrolyte was replaced by DMSO (Figure 3b), the percentage of 4-HB- H_2O typically increases at open circuit potential (OCP), indicating that DMSO can promote to form stronger hydrogen bonds than water during CRR. We further analyzed the percentage ratio of 4-HB- H_2O to 2-HB- H_2O , and found that the percentage of 4-HB- H_2O in the mixed electrolyte is always higher than that of pure water over the CRR process (Figure 3c). Therefore, we can propose a scheme to present the interface water structure change on the catalyst surface after the introduction of DMSO. During CRR operation, the interface water structure at the outer Helmholtz plane (OHP) is 2-HB- H_2O due to the weak interaction between water with water (Figure 3d). When one of water molecules is replaced by DMSO, due to the interaction between water with DMSO increasing (Figure 3e),^{10a} the percentage of 4-HB- H_2O is enlarged with the formation of a stronger hydro-

gen bond network on the catalyst surface. Notably, the higher percentage of 4-HB- H_2O can remain at various application potentials.

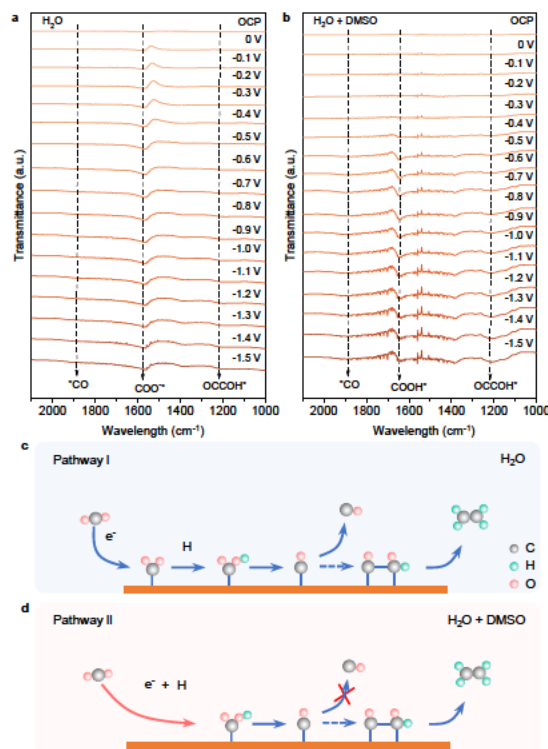


Figure 4. In situ ATR-IR spectra on Cu_2O at different potentials of CRR in CO_2 -saturated 1.0 M KHCO_3 using (a) pure water and (b) DMSO/ H_2O mixed solution as solvent. Schematic illustration for CRR pathway on Cu_2O in 1 M KOH using (c) pure water and (d) DMSO/ H_2O mixed solution as solvent.

To elucidate the different catalytic activity of Cu_2O in the pure water and mixed electrolytes, in situ ATR-IR spectroscopy was employed to identify their reactive species over the CRR process. First, a strong peak at 1568 cm^{-1} in pure water is assigned to the COO^* intermediate (Figure 4a), resulting in the first electron transfer to the CO_2 molecule. On the other hand, the peak at 1640 cm^{-1} belongs to the COOH^* intermediate in the mixed electrolyte (Figure 4b). It means that DMSO can alter the PCET pathway for CO_2 activation. Specifically, simultaneous electron and proton transfer proceed in the mixed electrolyte, whereas they are done step-by-step in pure water (Figure 4c, 4d).¹⁸ Second, compared with pure water, a slightly stronger peak at 1890 cm^{-1} corresponding to the bridge-adsorbed CO ($\text{CO}_{\text{bridge}}$) can be obtained on Cu_2O in the mixed electrolyte during the negative scan. It suggests that the stronger hydrogen bond network caused by the addition of DMSO on Cu_2O surface can exhibit a greater ability to stabilize the $^*\text{CO}$ intermediate than pure water, which is confirmed by the previous report.¹⁹ In the end, a weak peak at 1218 cm^{-1} in pure water is assigned to OCCOH^* , a critical intermediate for C_2H_4 . By contrast, the peak is stronger in the DMSO/ H_2O mixed electrolyte, indicating a higher C-C efficiency on Cu_2O catalyst. This result is consistent with its catalytic performance in two different electrolytes.

To rule out the structural changes of Cu_2O resulted from DMSO during CRR operation, we used various characterizations to investigate the phase and morphology of catalyst in different electrolytes after CRR operation. Firstly, there is no phase transition for Cu_2O in two electrolytes as shown in Figure S8, which is similar to the previous report.¹⁷ Then, we used SEM coupled with TEM to detect the

catalyst morphology and found that the polyhedral structure of Cu₂O can remain well (Figure S9, S10). We further employed FTIR to detect possible organic composition derived from the decomposition of DMSO. The results show no additional peak is observed on the Cu₂O surface after CRR in the mixed electrolyte (Figure S11). In addition, we also consider the pH change, which is detected by in situ Raman, on the surface of the catalyst resulting from DMSO.²⁰ The results confirm that the introduction of DMSO can not alter the local pH of the Cu₂O surface (Figure S12). Therefore, we can conclude that improving CRR activity and selectivity belongs to DMSO tuning interfacial water structure of Cu₂O rather than other factors.

In summary, we have developed a new strategy to tune PCET process of the catalyst during CRR to improve its activity and selectivity by utilizing the solvent effect of metal cations in the electrolyte. Based on the results of NMR and in situ spectroscopy, we explicitly revealed that high-donor-number organic molecules can form a stronger hydrogen bonding network in the mixed electrolyte, which can alter the PCET process of CO₂ activation and enhance the adsorption ability of *CO intermediate, thereby significantly improving the efficacy of C-C coupling to C₂H₄. Our findings suggest the possibility of tuning interfacial water structure to steer electrocatalyst's activity and selectivity, which could also guide the study of other catalysis for other water-involving electrochemical reactions.

ASSOCIATED CONTENT

The Supporting Information is available free of charge via the Internet at <http://pubs.acs.org>.

Detailed computational and experimental methods.

AUTHOR INFORMATION

Corresponding Author

*Yao Zheng Email: yao.zheng01@adelaide.edu.au

*Shi-Zhang Qiao Email: s.qiao@adelaide.edu.au

Notes

The authors declare no competing financial interest.

ACKNOWLEDGMENT

This work received funding from the Australian Research Council through the Discovery Project programs (FL170100154, FT200100062, DP220102596 and DP190103472). X. Zhou acknowledges support from the Australian Government through Research Training Program Scholarships.

REFERENCES

- (1) Wang, G.; Chen, J.; Ding, Y.; Cai, P.; Yi, L.; Li, Y.; Tu, C.; Hou, Y.; Wen, Z.; Dai, L., Electrocatalysis for CO₂ conversion: from fundamentals to value-added products. *Chem. Soc. Rev.* **2021**, *50* (8), 4993-5061.
- (2) Zhou, X.; Jin, H.; Xia, B. Y.; Davey, K.; Zheng, Y.; Qiao, S. Z., Molecular Cleavage of Metal-Organic Frameworks and Application to Energy Storage and Conversion. *Adv. Mater.* **2021**, *33* (51), 2104341.
- (3) Zheng, Y.; Vasileff, A.; Zhou, X.; Jiao, Y.; Jaroniec, M.; Qiao, S. Z., Understanding the Roadmap for Electrochemical Reduction of CO₂ to Multi-Carbon Oxygenates and Hydrocarbons on Copper-based Catalysts. *J. Am. Chem. Soc.* **2019**, *141* (19), 7646-7659.
- (4) Vasileff, A.; Xu, C.; Jiao, Y.; Zheng, Y.; Qiao, S.-Z., Surface and Interface Engineering in Copper-Based Bimetallic Materials for Selective CO₂ Electroreduction. *Chem* **2018**, *4* (8), 1809-1831.
- (5) Zhou, Y.; Che, F.; Liu, M.; Zou, C.; Liang, Z.; De Luna, P.; Yuan, H.; Li, J.; Wang, Z.; Xie, H.; Li, H.; Chen, P.; Bladt, E.; Quintero-Bermudez, R.;

Sham, T.-K.; Bals, S.; Hofkens, J.; Sinton, D.; Chen, G.; Sargent, E. H., Dopant-induced electron localization drives CO₂ reduction to C₂ hydrocarbons. *Nat. Chem.* **2018**, *10* (9), 974-980.

(6) Zhou, X.; Liu, H.; Xia, B. Y.; Ostrikov, K.; Zheng, Y.; Qiao, S. Z., Customizing the microenvironment of CO₂ electrocatalysis via three-phase interface engineering. *SmartMat* **2022**, *3* (1), 111-129.

(7) Schouten, K. J. P.; Pérez Gallent, E.; Koper, M. T. M., The influence of pH on the reduction of CO and CO₂ to hydrocarbons on copper electrodes. *J. Electrochem. Soc.* **2014**, *716*, 53-57.

(8) (a) Tang, C.; Zheng, Y.; Jaroniec, M.; Qiao, S. Z., Electrocatalytic Refinery for Sustainable Production of Fuels and Chemicals. *Angew. Chem. Int. Ed.* **2021**, *60* (36), 19572-19590; (b) Gonella, G.; Backus, E. H. G.; Nagata, Y.; Bonthuis, D. J.; Loche, P.; Schlaich, A.; Netz, R. R.; Kühnle, A.; McCrum, I. T.; Koper, M. T. M.; Wolf, M.; Winter, B.; Meijer, G.; Campen, R. K.; Bonn, M., Water at charged interfaces. *Nat. Rev. Chem.* **2021**, *5* (7), 466-485.

(9) Wang, T.; Zhang, Y. R.; Huang, B. T.; Cai, B.; Rao, R. R.; Giordano, L.; Sun, S. G.; Shao-Horn, Y., Enhancing oxygen reduction electrocatalysis by tuning interfacial hydrogen bonds. *Nat. Catal.* **2021**, *4* (9), 753-762.

(10) (a) Nian, Q.; Zhang, X.; Feng, Y.; Liu, S.; Sun, T.; Zheng, S.; Ren, X.; Tao, Z.; Zhang, D.; Chen, J., Designing Electrolyte Structure to Suppress Hydrogen Evolution Reaction in Aqueous Batteries. *ACS Energy Lett.* **2021**, *6* (6), 2174-2180; (b) Cao, L.; Li, D.; Hu, E.; Xu, J.; Deng, T.; Ma, L.; Wang, Y.; Yang, X. Q.; Wang, C., Solvation Structure Design for Aqueous Zn Metal Batteries. *J. Am. Chem. Soc.* **2020**, *142* (51), 21404-21409.

(11) Chu, A. T.; Surendranath, Y., Aprotic Solvent Exposes an Altered Mechanism for Copper-Catalyzed Ethylene Electrosynthesis. *J. Am. Chem. Soc.* **2022**.

(12) Mahler, J.; Persson, I., A study of the hydration of the alkali metal ions in aqueous solution. *Inorg. Chem.* **2012**, *51* (1), 425-38.

(13) Huang, B.; Myint, K. H.; Wang, Y.; Zhang, Y.; Rao, R. R.; Sun, J.; Mui, S.; Katayama, Y.; Corchado Garcia, J.; Fraggadakis, D.; Grossman, J. C.; Bazant, M. Z.; Xu, K.; Willard, A. P.; Shao-Horn, Y., Cation-Dependent Interfacial Structures and Kinetics for Outer-Sphere Electron-Transfer Reactions. *J. Phys. Chem. C* **2021**, *125* (8), 4397-4411.

(14) Hao, J.; Yuan, L.; Ye, C.; Chao, D.; Davey, K.; Guo, Z.; Qiao, S. Z., Boosting Zinc Electrode Reversibility in Aqueous Electrolytes by Using Low-Cost Antisolvents. *Angew. Chem. Int. Ed.* **2021**, *60* (13), 7366-7375.

(15) (a) Ataka, K.-i.; Yotsuyanagi, T.; Osawa, M., Potential-Dependent Reorientation of Water Molecules at an Electrode/Electrolyte Interface Studied by Surface-Enhanced Infrared Absorption Spectroscopy. *J. Phys. Chem.* **1996**, *100* (25), 10664-10672; (b) Wang, Y. H.; Zheng, S.; Yang, W. M.; Zhou, R. Y.; He, Q. F.; Radjenovic, P.; Dong, J. C.; Li, S.; Zheng, J.; Yang, Z. L.; Attard, G.; Pan, F.; Tian, Z. Q.; Li, J. F., In situ Raman spectroscopy reveals the structure and dissociation of interfacial water. *Nature* **2021**, *600* (7887), 81-85.

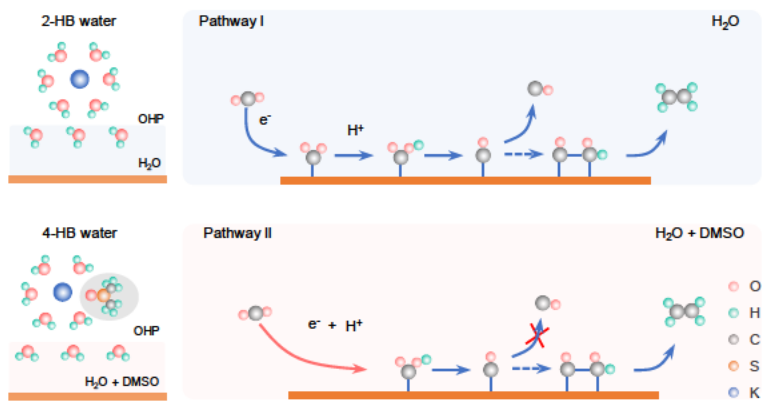
(16) Wu, Z. Z.; Zhang, X. L.; Niu, Z. Z.; Gao, F. Y.; Yang, P. P.; Chi, L. P.; Shi, L.; Wei, W. S.; Liu, R.; Chen, Z.; Hu, S.; Zheng, X.; Gao, M. R., Identification of Cu(100)/Cu(111) Interfaces as Superior Active Sites for CO Dimerization During CO₂ Electroreduction. *J. Am. Chem. Soc.* **2022**, *144* (1), 259-269.

(17) Gao, Y.; Wu, Q.; Liang, X.; Wang, Z.; Zheng, Z.; Wang, P.; Liu, Y.; Dai, Y.; Whangbo, M. H.; Huang, B., Cu₂O Nanoparticles with Both {100} and {111} Facets for Enhancing the Selectivity and Activity of CO₂ Electroreduction to Ethylene. *Adv. Sci.* **2020**, *7* (6), 1902820.

(18) Firet, N. J.; Smith, W. A., Probing the Reaction Mechanism of CO₂ Electroreduction over Ag Films via Operando Infrared Spectroscopy. *ACS Catal.* **2016**, *7* (1), 606-612.

(19) Li, J.; Li, X.; Gunathunge, C. M.; Waegle, M. M., Hydrogen bonding steers the product selectivity of electrocatalytic CO reduction. *Proc. Natl. Acad. Sci. U.S.A.* **2019**, *116* (19), 9220-9229.

(20) Zheng, M.; Wang, P.; Zhi, X.; Yang, K.; Jiao, Y.; Duan, J.; Zheng, Y.; Qiao, S. Z., Electrocatalytic CO₂-to-C₂⁺ with Ampere-Level Current on Heteroatom-Engineered Copper via Tuning *CO Intermediate Coverage. *J. Am. Chem. Soc.* **2022**, *144* (32), 14936-14944.



Supplementary Information

Solvent effects regulating interfacial water structure of Cu catalyst to promote electrochemical C-C coupling reactions

Xianlong Zhou,^{1#} Jieqiong Shan,^{1#} Yilong Zhu,¹ Min Zheng, Bao Yu Xia,² Yan Jiao,¹ Yao Zheng,¹
Shi-Zhang Qiao¹

¹ School of Chemical Engineering and Advanced Materials, The University of Adelaide, Adelaide, SA 5005, Australia.

² Key Laboratory of Material Chemistry for Energy Conversion and Storage (Ministry of Education), Hubei Key Laboratory of Material Chemistry and Service Failure, Wuhan; National Laboratory for Optoelectronics, School of Chemistry and Chemical Engineering, Huazhong University of Science and Technology (HUST), 1037 Luoyu Road, Wuhan 430074, China.

These authors contributed equally

*Email: yao.zheng01@adelaide.edu.au; s.qiao@adelaide.edu.au

Materials Synthesis

Synthesis of Cu₂O.

The synthesis of the Cu₂O sample was carried out according to the previous method. In detail, 4.0 g of polyvinylpyrrolidone (PVP, Mr = 30000) was dissolved in 45 mL of deionized water (DIW), followed by stirring until the mixture was completely dissolved. CuCl₂·2H₂O (0.1 mol L⁻¹; 5 mL) was added dropwise to the above aqueous solution. The resulting solution was heated in a water bath at 55 °C. Then, NaOH aqueous solution (2 mol L⁻¹; 5 mL) was added. After stirring for 0.5 h, ascorbic acid solution (0.6 mol L⁻¹; 6 mL) was added dropwise. The reaction solution was stirred at 55 °C for additional 180 min. The resulting precipitate was collected by centrifugation and rinsed at least three times with plenty of DIW and ethanol. Finally, the brick red powder was obtained following freeze-drying for 24 h.

Materials Characterization

The phase and structure of as-synthesized samples were analysed by a Philips PW-1830 X-Ray Diffractometer (XRD) using Cu K α radiation ($\lambda=1.5406$ Å, scan rate = 5° min⁻¹). Scanning electron microscope (SEM) images were collected on a Hitachi New Generation SU8010 field emission SEM. Transmission electronic microscope (TEM) images were collected on a JOEL 2100 TEM. Raman spectra were a HORIBA Scientific Raman spectroscopy instrument. FTIR spectra were collected on a Nicolet 6700 spectrometer.

Electrochemistry Measurement

Activity/selectivity measurement. The CO₂ reduction reaction (CRR) catalytic activity of different samples was investigated by a commercial flow cell (Gaossunion) in 1 M KOH solution. The volume of anode and cathode chamber electrolyte was both 15 mL. To prepare the working electrode, 25 mg of catalyst was dispersed by sonication in 2.85 mL of isopropanol and 150 μ L of 5 wt % of Nafion for 60 min. Next, inks were airbrushed onto a gas diffusion layer (GDL, Sigracet 29 BC) as the cathode electrode (3×1 cm², loading mass: 1.0 mg cm⁻²). The reference and counter electrodes were Ag/AgCl (3.0 M KCl) and Pt foil (3×1 cm; 1 mm thickness) connected to a potentiostat (Gamry Interface 3000), respectively. An anion exchange membrane (FAB-PK-130) (Fuel Cell Store) was sandwiched between the two PTFE sheets to separate the chambers. In addition, 1 M KOH was circulated around the cathode and anode at a flow rate of 10.0 ml min⁻¹ during the CRR. During this process and then testing, CO₂ was continuously purged at a rate of 20 μ L min⁻¹. The gas products were self-injected into a gas chromatograph (Shimadzu GC-2014) equipped with TCD and methanizer/FID detectors.

XRD analysis of samples after CRR. We identify the phase and structure of catalysts in the flow cell after CRR by XPD analysis. When we completed the CRR test, the electrode was washed by deionized water and ethanol for three times. Then, the sample after CRR was obtained after vacuum drying for 12 h. Finally, we can identify the phase of the sample after CRR by XRD analysis. In addition, the sample was also investigated by other methods, including **SEM** and **FTIR**.

TEM analysis of samples after CRR. We investigate the structure of catalysts in the H-type cell after CRR by TEM analysis. When we completed the CRR test, the electrode was washed by deionized water and ethanol for three times. Then, the sample after CRR was obtained after vacuum drying for 12 h. Finally, we can identify structure of the sample after CRR by TEM analysis.

In situ Attenuated Total Reflectance Infrared (ATR-IR) Spectroscopy

It was conducted by using a Thermo-Fisher Nicolet iS20 equipped with a liquid nitrogen-cooled HgCdTe (MCT) detector using a VeeMax III ATR accessory (Pike Technologies). A germanium prism (60°, PIKE Technologies) was mounted in a PIKE electrochemical three-electrode cell with a platinum-wire counter electrode and an Ag/AgCl reference electrode (Pine Research). All ATR-IR measurements were acquired by averaging 64 scans at a spectral resolution of 4 cm⁻¹. Electrocatalyst ink was prepared by dispersing catalyst powder (10 mg) in a solution containing isopropanol (1.5 mL) and 5 wt % Nafion solution (50 µL) followed by ultrasonication for 60 min. 50 µL of the catalyst ink was dropped onto the prism and left to dry slowly. The electrolyte was 0.1 M KHCO₃, which was constantly purged with CO₂ during the experiment. A CHI 760E electrochemical workstation (CH Instruments, USA) was connected for chronoamperometric tests from -0.6 to -2.1 V vs. Ag/AgCl stepwise. Meanwhile, the spectra under open circuit potential (OCP) were recorded for comparison.

In situ Raman Spectroscopy

In situ Raman was recorded on a HORIBA Scientific Raman spectroscopy instrument (laser excitation at 532 nm) using a screen-printed chip electrode from Pine Research Instrumentation. Ten microliters of the ink gel were added to the printed electrode before dried at room temperature. For each measurement, the Raman spectrum was accumulated by 2 acquisitions (20 s per acquisition). To be consistent with the electrolysis measurements, Raman spectra were obtained at 5 min after the potential was initially applied. Potential-dependent spectra were obtained at OCP, 0, -0.2, -0.4, -0.6, -0.8 and -1.0 V vs RHE.

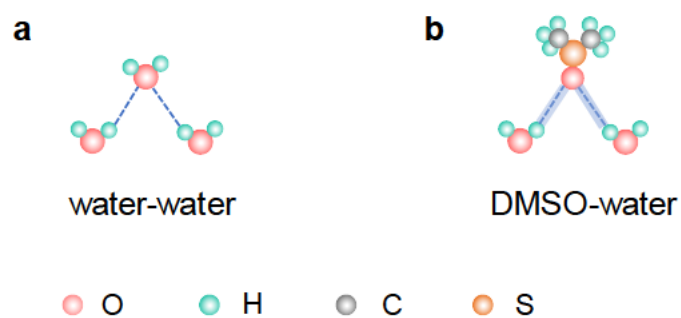


Figure S1. H-bond patterns between (a) water and water molecules, (b) water and DMSO molecules.

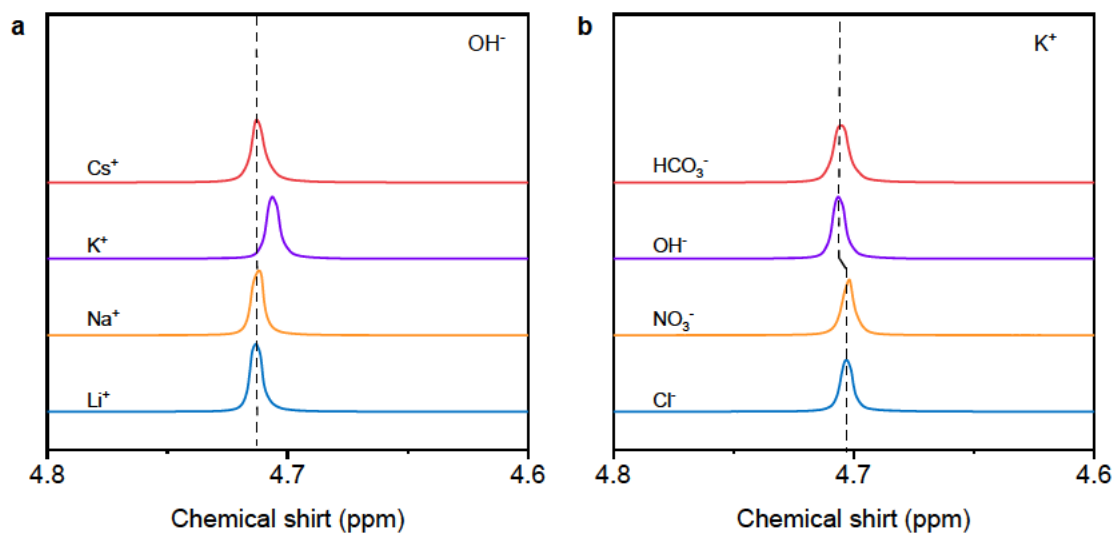


Figure S2. The ¹H chemical shifts of different electrolytes.

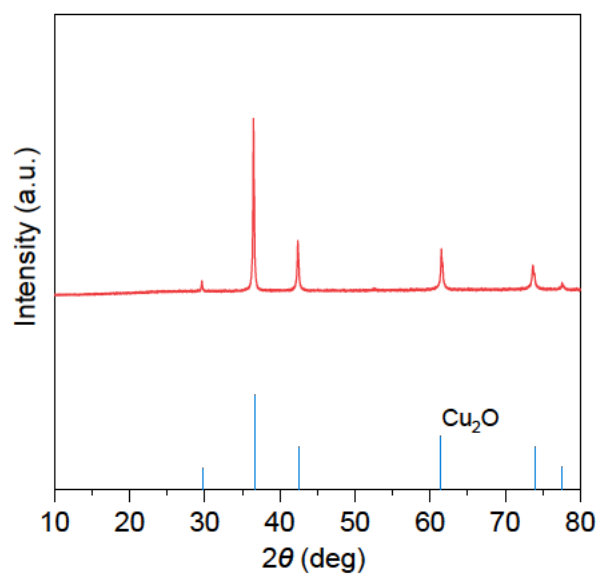


Figure S3. XRD patterns of Cu₂O.

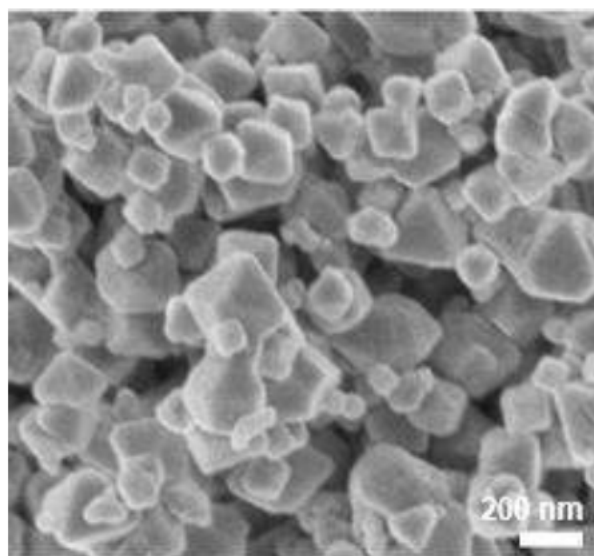


Figure S4. SEM image of Cu₂O.

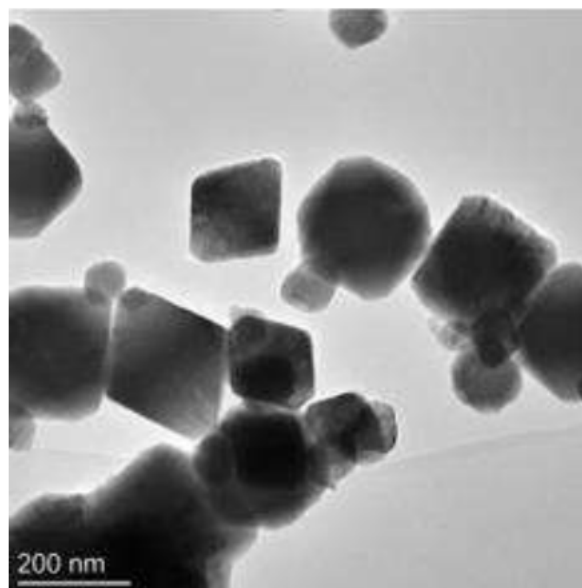


Figure S5. TEM image of Cu₂O.

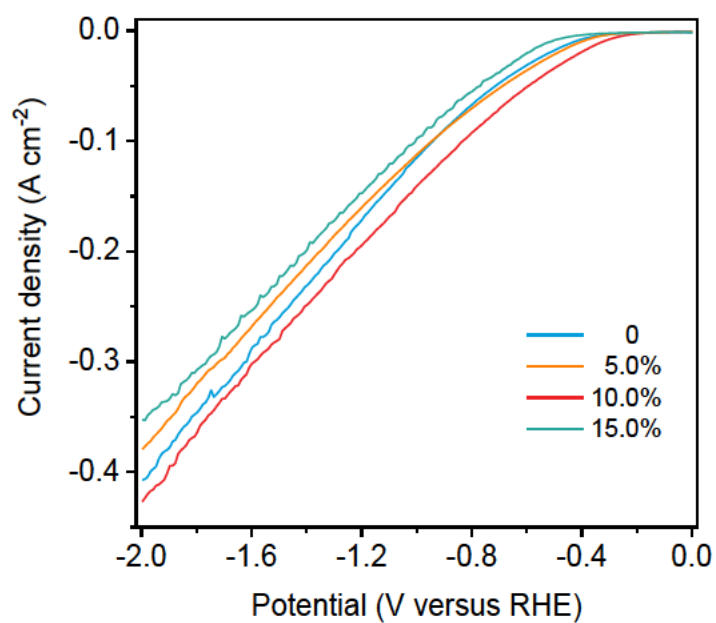


Figure S6. Linear sweep voltammetry (LSV) curves of CO₂ atmosphere with a scan rate of 50 mVs⁻¹ in 1 M KOH using different solutions.

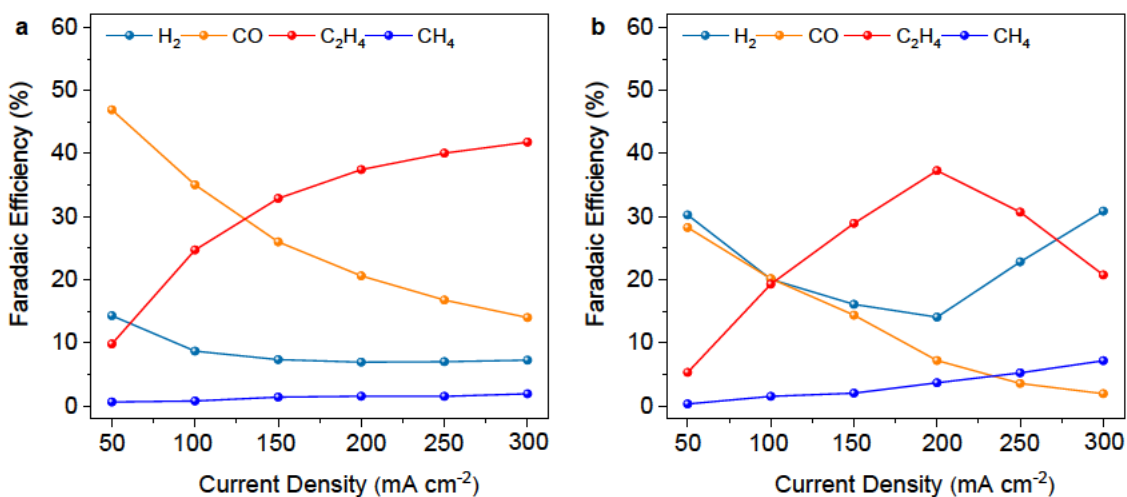


Figure S7. Faradaic efficiencies (FE) of CRR products on Cu₂O over a range of applied current densities in different electrolyte by tuning DMSO percentage in the mixed solution. (a) 5% and (b) 15%.

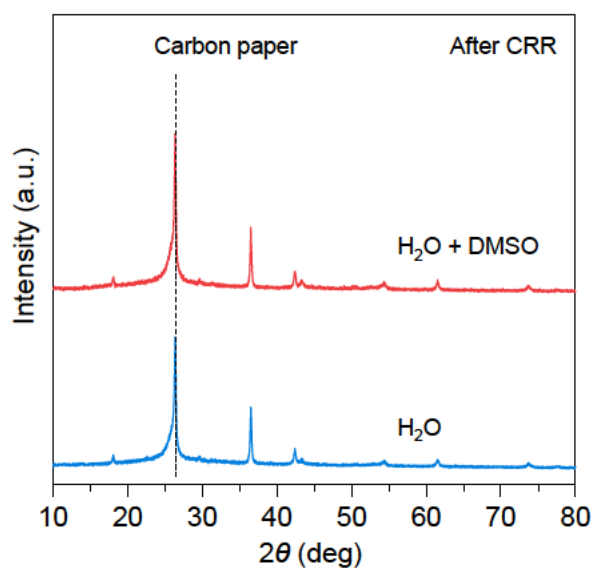


Figure S8. XRD pattern of Cu₂O after CRR in different electrolytes. (a) 90% H₂O+10% DMSO and (b) H₂O.

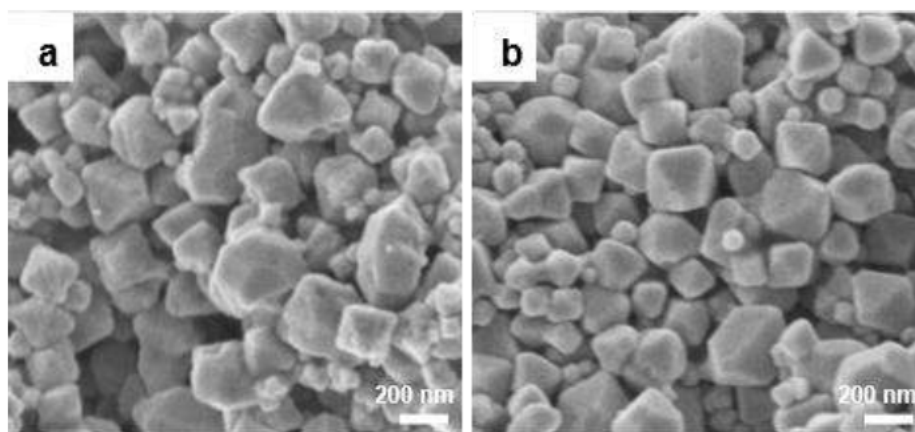


Figure S9. SEM images of Cu₂O after CRR in different electrolytes. (a) H₂O and (b) 90% H₂O+10% DMSO.

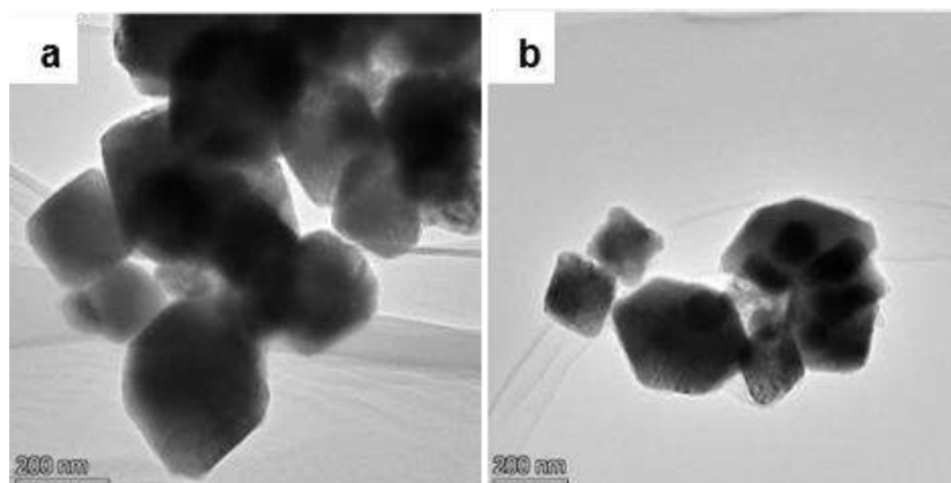


Figure S10. TEM images of Cu₂O after CRR in different electrolytes. (a) H₂O and (b) 90% H₂O+10% DMSO.

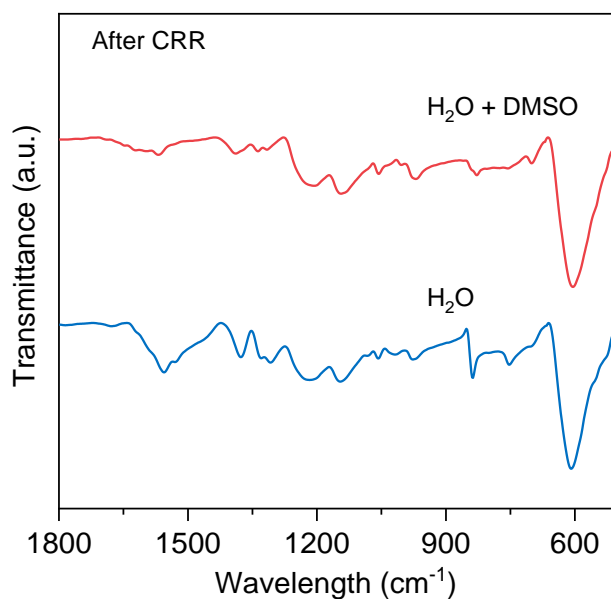


Figure S11. FTIR spectra on Cu₂O after CRR in different electrolytes, i.e., 90% H₂O+10% DMSO and pure H₂O.

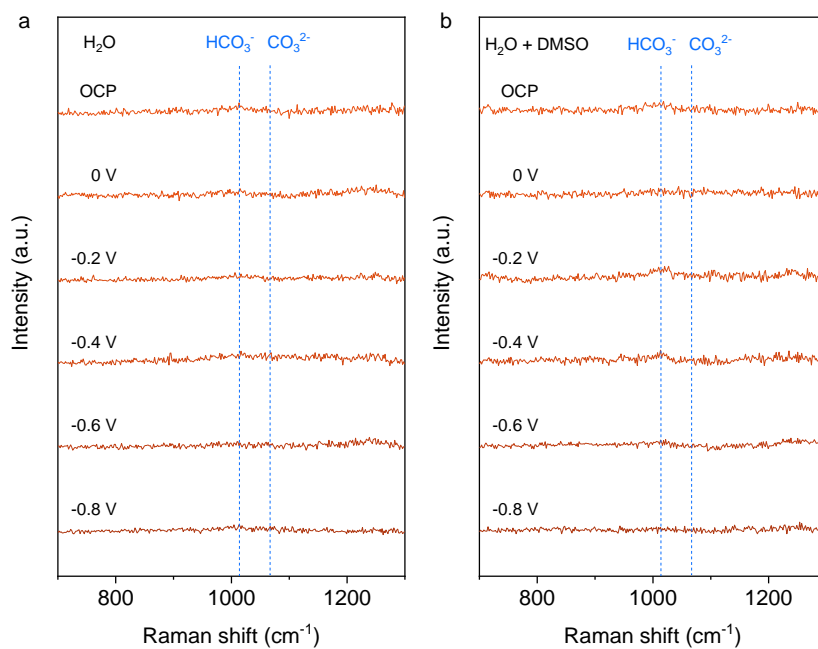


Figure S12. In situ Raman spectra on Cu₂O collected at different potentials in different electrolytes. (a) H₂O and (b) 90% H₂O+10% DMSO.

Chapter 7 Conclusion and perspectives

7.1 Conclusion

This thesis intends to fabricate high-performance Cu-based catalysts for CRR and understand regulation of their CRR activity by steering PCET process and the role of interfacial water structure. The following conclusions can be drawn from the work in this thesis:

1. Molecular cleavage of CuBDC can complete the phase transition and fabricate a new MOF that consists of Cu^{1+} and Cu^{2+} atoms in the framework of Cu_2BDC . During CRR operation, they are reduced into target $\text{Cu}^{1+}/\text{Cu}^0$ species, which present a higher FE of C2 products (ethylene and ethanol) than that of CuBDC-derived sample.
2. The solid-solution strategy is able to stabilize Cu^{2+} against electrochemical reduction during CRR. The Cu^{2+} in Cu-Ce-O_x can enhance the absorption stability of $^*\text{CO}$ intermediate, which in turn promotes its further hydrogenation and suppresses the dimerization, thereby significantly improving the selectivity of CH_4 .
3. The linker with low electrophilicity can promote proton transfer from PyH^* to $^*\text{CO}$ intermediates to facilitate formation of CH_4 . By contrast, the linker with high electrophilicity can build strong hydrogen bond, and stabilize the $^*\text{CO}$ dimer, thereby favoring the C_2H_4 formation.
4. The high-donor-number organic molecules can form a stronger hydrogen bonding network in the mixed electrolyte through tuning interfacial water structure, altering the PCET process of CO_2 activation and enhance the adsorption ability of $^*\text{CO}$ intermediate, thereby significantly improving the efficacy of C-C coupling to C_2H_4 .

7.2 Perspectives

It is a great improvement of Cu-based catalyst activity and selectivity through catalyst

design and electrolyte engineering. Due to different strategies, we can build the Cu₂O/CuO structure, stabilize Cu²⁺ as the active sites, tune the PCET process and the solvent structure of metal cations to improve the adsorption ability of intermediates, thereby steering CRR selectivity. However, a number of issues remain as follows:

1. Flow cell has been widely used to investigate the CRR activity in this thesis because this cell can decrease the thickness of diffusion layer and provide an industrial current density. However, electrode flooding is a great challenge for its industrial application. It usually leads to the destruction of the gas diffusion layer during CRR operation, resulting in the instability of the electrode. There is still a big gap to overcome for industrial application. Therefore, more studies should be investigated to improve the stability of the electrode in the flow cell.
2. The previous reference has confirmed that at pH = 12, the *CO-*CO dimerization pathway is both thermodynamically and kinetically favorable, while the C₁ pathway is blocked. Therefore, a strong base solution (1M KOH) is widely used to improve the C₂ product selectivity of Cu-based catalysts. It can lead to the consumption of a large amount of CO₂ with the formation of K₂CO₃, reducing CO₂ utilization efficiency. Therefore, an acid electrolyte is favorable. However, the efficiency of C-C coupling is significantly lower than that of the base solution. Therefore, a high-performance Cu-based catalyst in the acid electrolyte needs to be developed.
3. The DFT calculations provide promising methods for understanding the catalytic process. Based on the catalyst design, we can investigate the effects of various strategies on catalytic activity and selectivity at the atomic or molecular scale. Because of the complexity of the catalyst interface during CRR, the DFT calculations can provide more opportunities to investigate the interface science of CRR than experiments. However, there are few theoretical researches on the surface

and interface change of the catalysts by simulation of their local environments. Therefore, investigative research will need to be directed to revealing the relationship between the real local environment and catalytic behaviors.

4. Water serves not only as a proton source but also as a solvent environment, whose structure can determine catalyst activity and selectivity. Therefore, investigating water structure is a crucial issue for developing high-performance CRR electrocatalysts. Indeed, it is tough to detect the interfacial water structure because the information resulting from its change is relatively weak. In addition, the intermediates during CRR operation can also affect various in situ characterizations processes. Therefore, an advanced technology sensitive to the water interfacial structure should be provided to address this issue, such as in situ sum frequency generation (SFG) vibrational spectrometer.
5. Currently, the ion exchange membranes in the flow cell can not work more than 100 h. To achieve industrial-level CO₂ reduction, it needs to develop ion exchange membranes with a long-term stability. In addition, products separation and purification with a low cost also need to be addressed in the further research.

In all, with the rapid development of artificial intelligence and more advanced in situ characterization techniques, more challenges will be solved in the future, ultimately achieving a thorough understanding and full control of Cu-based catalyst CRR.

Appendix I: Publications during PhD Candidature

1. **Xianlong Zhou**, Jieqiong Shan, Yilong Zhu, Min Zheng, Bao Yu Xia, Yan Jiao, Yao Zheng, Shi-Zhang Qiao, Regulating interfacial water structure by solvent effects to promote electrochemical C-C coupling reactions. (*In preparation*)
2. **Xianlong Zhou**, Jieqiong Shan, Huan Li, Bao Yu Xia, Yao Zheng, Shi-Zhang Qiao, Tuning Molecular Electrophilicity of Cu-MOF Catalysts to Steer CO₂ Electroreduction Selectivity. *J. Am. Chem. Soc.* (*Under revision*)
3. **Xianlong Zhou**, Jieqiong Shan, Ling Chen, Bao Yu Xia, Tao Ling, Jingjing Duan, Yan Jiao, Yao Zheng, Shi-Zhang Qiao, Stabilizing Cu²⁺ ions by Solid Solutions to Promote CO₂ Electroreduction to Methane. *J. Am. Chem. Soc.* 2022, 144, 2079-2084.
4. **Xianlong Zhou**, Juncai Dong, Yihan Zhu, Lingmei Liu, Yan Jiao, Huan Li, Yu Han, Kenneth Davey, Qiang Xu, Yao Zheng, Shi-Zhang Qiao, Molecular Scalpel to Chemically Cleave Metal-Organic Frameworks for Induced Phase Transition. *J. Am. Chem. Soc.* 2021, 143, 6681-6690.
5. **Xianlong Zhou**, Huanyu Jin, Bao Yu Xia, Kenneth Davey, Yao Zheng, Shi-Zhang Qiao, Molecular Cleavage of Metal-Organic Frameworks and Application to Energy Storage and Conversion. *Adv. Mater.* 2021, 33, 2104341.
6. **Xianlong Zhou**, Hao Liu, Bao Yu Xia, Kostya (Ken) Ostrikov, Yao Zheng, Shi-Zhang Qiao, Customizing the Microenvironment of CO₂ Electrocatalysis via Three-phase Interface Engineering. *SmartMat.* 2022, 3, 111. (*Invited review*)
7. Yao Zheng, Anthony Vasileff, **Xianlong Zhou**, Yan Jiao, Mietek Jaroniec, and Shi-Zhang Qiao, Understanding the Roadmap for Electrochemical Reduction of CO₂ to Multi-Carbon Oxygenates and Hydrocarbons on Copper-based Catalysts. *J. Am. Chem. Soc.* 2019, 141, 7646-7659.
8. Laiquan Li, Cheng Tang, Yao Zheng, Bingquan Xia, **Xianlong Zhou**, Haolan Xu, and Shi-Zhang Qiao, Tailoring Selectivity of Electrochemical Hydrogen Peroxide Generation by Tunable Pyrrolic-Nitrogen-Carbon. *Adv. Energy Mater.* 2020, 10, 2000789.